The brittle-to-viscous transition in experimentally deformed quartz gouge

Inauguraldissertation

zur
Erlangung der Würde eines Doktors der Philosophie
vorgelegt der
Philosophisch-Naturwissenschaftlichen Fakultät
der Universität Basel

von

Bettina Richter
aus Wernigerode (Deutschland)

Basel, 2017

Genehmigt von der Philosophisch-Naturwissenschaftlichen Fakultät auf Antrag von

Prof. Dr. Renée Heilbronner
(Fakultätsverantwortliche)

Prof. Dr. Hugues Raimbourg
(Korreferent)

Basel, den 23.05.2017

Prof. Dr. Martin Spiess
(Dekan der Philisophisch-Naturwissenschaftlichen Fakultät)

An experiment is a question which science poses to Nature,
and a measurement is the recording of Nature's answer.

Max Planck

Kurzfassung

Die vorliegende Arbeit befasst sich mit dem Übergang von spröder zu viskoser Deformation in polykristallinem Quarz. Der Fokus liegt hierbei auf dem Bereich, in dem bruchhafte und kristallplastische Prozesse nebeneinander wirken und letztere zunehmend dominieren. Dieser fließende Übergang wird von einer Vielzahl von Parametern (z. B. Temperatur, Umlagerungsdruck, Verformungsrate, Korngröße) beeinflusst, die Auswirkungen auf die aktiven Deformationsmechanismen haben.

Mit Hilfe von Deformationsexperimenten im Griggs-Apparat wird der Einfluss von Temperatur, Umlagerungsdruck, Verformungsrate und Scherverformung analysiert. Fein gemahlenes Quarzpulver (Korngröße unter 100 µm), welches ursprünglich von einem natürlichen Einkristall stammt, wird als Ausgangsmaterial verwendet. Das Pulver simuliert fein gemahlenes Material, wie es in Störungszonen entstehen kann und bei Reaktivierung eben dieser verformt wird. Einige Proben werden vor der Verformung für 20 h bei 1000 °C und 1,5 - 1,6 GPa Umlagerungsdruck getempert. Die Experimente werden bei Temperaturen zwischen 500 °C und 1000 °C und Umlagerungsdrücken von 0,5 GPa bis 1,5 GPa durchgeführt. Die konstante Scherverformungsrate variiert zwischen $3{\cdot}10^{-3}\,s^{-1}$ und $2{\cdot}10^{-6}\,s^{-1}$. Bei einigen Experimenten wird die Verformungsrate stufenweise verändert („strain rate stepping“). Die Proben werden anschließend hinsichtlich der mikrostrukturellen und texturellen Entwicklung mittels Licht- und Rasterelektronenmikroskopie untersucht.

Da es in einigen Proben zur Bildung von Coesit, einem Hochdruckpolymorph von Quarz, kommt, wird die Beziehung des Spannungszustandes innerhalb der Probe zum thermodynamischen Druck, der den Phasenübergang von Quarz zu Coesit bestimmt, untersucht. Sowohl das Wachstum von Coesit als auch die Rückumwandlung zu Quarz werden innerhalb eines Experiments beobachtet und mit zunehmender beziehungsweise abnehmender Differentialspannung korreliert. Der Druck-Temperatur-Bereich des Stabilitätsfeld von Coesit wird jedoch weder von der Differentialspannung noch vom Umlagerungsdruck oder der mittleren Spannung erreicht. Nur die maximale Hauptspannung liegt oberhalb des Phasenübergangs, was im Gegensatz zu der häufigen Annahme steht, dass die mittlere Spannung als Äquivalent für den thermodynamischen Druck gesehen werden kann.

Bei hohen Umlagerungsdrücken (P_c) ist keine eindeutige Temperaturabhängigkeit der Spannung zu erkennen für Temperaturen unter 650 °C. Für höhere Temperaturen nimmt die Differentialspannung ($\Delta\sigma$) mit zunehmender Temperatur ab. Zwischen 650 °C und 700 °C

bei 1,5 GPa Umlagerungsdruck und $2{,}5{\cdot}10^{-5}\,s^{-1}$ tritt die größte Abnahme des Differentialspannungsabfall auf. Diese korreliert mit dem Unterschreiten des Goetze-Kriteriums ($\Delta\sigma = P_c$). Der Reibungskoeffizient (μ) hat bei Temperaturen unterhalb von 700 °C eine sehr geringe Temperaturabhängigkeit und liegt bei $\mu \sim 0{,}45$. Zwischen 700 °C und 1000 °C zeigt er hingegen eine starke inverse Temperaturabhängigkeit für $2{,}5{\cdot}10^{-5}\,s^{-1}$ und $2{,}5{\cdot}10^{-4}\,s^{-1}$. Für langsamere Verformungsraten ($4{\cdot}10^{-6}\,s^{-1}$) liegt der Reibungskoeffizient bei sehr niedrigen Werten ($\mu < 0,1$) und zeigt eine geringe Abhängigkeit von der Temperatur. Eine positive Druckabhängigkeit ist bei 650 °C zwischen 1,0 GPa und 1,5 GPa vorhanden. Bei 700 °C ist die Druckabhängigkeit ambivalent. Für 800 °C ist keine Druckabhängigkeit zwischen 1,0 GPa und 1,5 GPa zu erkennen. Eine negative Druckabhängigkeit wird bei niedrigeren Umlagerungsdrücken deutlich. Folglich dominieren spröde Deformationsmechanismen, die überwiegend vom Umlagerungsdruck abhängen und relativ unabhängig von der Temperatur sind, bei niedrigen Temperaturen und Umlagerungsdrücken. Die zunehmende Bedeutung von kristallplastischen Prozessen wird durch eine zunehmende Temperaturabhängigkeit und Druckunabhängigkeit illustriert.

Niedriggradige Proben sowie Proben bei 0,5 GPa Umlagerungsdruck sind durch heterogene Deformation geprägt, welche durch die Ausbildung von Scherbändern in Riedel-Geometrie gekennzeichnet ist. Durchgehende Brüche treten nicht auf. Vielmehr wird die Bruchausbreitung gehemmt und kataklastisches Fließen überwiegt. Mit zunehmender Temperatur entwickelt sich die Mikrostruktur hin zu einen S-C'-Gefüge. Ab 700 °C entsteht eine durchgehende Foliation, die durch leicht elongierte, rekristallisierte Körner gebildet wird. Proben, deren Differentialspannung oberhalb des Goetze-Kriteriums liegen, bilden ein S-C'-Gefüge aus, welches bei einem hohen Grad an Verformung beständig ist. Proben mit Differentialspannungen unterhalb des Goetze-Kriteriums haben bereits im Bereich der maximalen Scherspannung ein S-C'-Gefüge, welches mit zunehmender Verformung in Form von Dislokationskriechen von Rekristallisaten überprägt wird. Die durchschnittliche Größe der rekristallisierten Körner nimmt mit zunehmender Temperatur beständig zu (1,8 µm bei 700 °C; 10,1 µm bei 1000 °C für 1,5 GPa und $2{,}5{\cdot}10^{-5}\,s^{-1}$). Bereits bei 600 °C entstehen in feinkörnigem Material Zonen in C'-Orientierung mit kleinen, idiomorphen Körnern, die durch Lösungs-Fällungs-Kriechen gebildet werden. Mit zunehmender Temperatur werden diese Bereiche breiter.

Eine zufällige kristallographische Vorzugsregelung, wie sie im Ausgangsmaterial vorhanden ist, besteht weiterhin in niedriggradigen Proben und bei niedrigen Umlagerungsdrücken. Mit leicht dominierenden kristallplastischen Prozessen und der Entwicklung eines S-C'-Gefüge beginnt sich eine periphere Vorzugsorientierung der *c*-Achsen auszubilden. Bei 700 °C und 800 °C sind die *c*-Achsen von einem peripheren Maximum geprägt, welches für S-C'-Gefüge entgegengesetzt zum Schersinn rotiert ist. Mit zunehmender Verformung und der Entstehung einer ausgeprägten Foliation rotiert das Maximum mit dem Schersinn. Die *a*-Achsen liegen in einem kleinen Winkel ($\sim$10 °) zur Scherzonengrenze. Neben dem peri-

pheren Maximum der *c*-Achsen entwickelt sich bei 900 °C ein zweites, zentrales Maximum. Bei 1000 °C ist nur noch das zentrale Maximum vorhanden.

Die Differentialspannung getemperter Proben ist deutlich höher als ohne diese Vorbehandlung. Dabei besteht der wesentliche Unterschied der Materialien in der Korngrößenverteilung. Das Ausgangsmaterial hat ein breites Korngrößenspektrum. Durch Tempern wird dieses Spektrum verringert auf Kosten der kleinsten und größten Fraktion. Folglich ist Lösungs-Fällungs-Kriechen, welches bevorzugt in feinkörnigem Material initiiert wird, geringer ausgeprägt.

Spannungskoeffizienten und Aktivierungsenergien von Fließgesetzen, die kristallplastische Verformung beschreiben, sind mit Hilfe der mechanischen Daten bestimmt. Hohe Spannungskoeffizienten ($n = 6{,}4 \pm 1{,}3$) bei 650 °C sind ein Hinweis darauf, dass kristallplastische Prozesse nicht dominieren und folglich Fließgesetze nicht angewendet werden können („power law breakdown“). Zwischen 800 °C und 1000 °C ist der Spannungskoeffizient konstant bei $n = 1{,}9 \pm 0{,}7$ mit einer dazugehörigen Aktivierungsenergie von 170 ± 72 kJ/mol. Dieser Wert ist zu niedrig für theoretische und häufig genutzte experimentelle Werte von Dislokationskriechen sowie zu hoch für Diffusionskriechen.

Die einsetzende Dominanz von viskosen Prozessen ist häufig von einem S-C'-Gefüge gekennzeichnet, wobei das Vorhandensein von C'-Scherbänder nicht unbedingt ein Hinweis für fortgeschrittene Verformung und die Überprägung früherer Foliationen ist („crenulation“). Vielmehr können C'-Bändern bereits bei geringer Verformung, ohne vorherige Foliation, auftreten und sind häufig mit Lösungs-Fällungs-Kriechen assoziiert. Im viskosdominierten Bereich tritt sowohl Dislokationskriechen als auch Lösungs-Fällungs-Kriechen auf. Der ratenlimitierende Schritt bleibt offenbar zwischen 800 °C und 1000 °C unverändert. Korngrößenabhängige Diffusionsprozesse sind vorwiegend in den feinkörnigen Bereichen aktiv, wohingegen Dislokationskriechen korngrößenunabhängig ist und in größeren Körner vorherrscht.

Abstract

This study investigates the transition from brittle to viscous deformation in polycrystalline quartz. It focuses on the semi-brittle field and the transition to dominating viscous processes. The transition is influenced by several parameters (e.g. temperature, confining pressure, strain rate, grain size) that affect operating deformation mechanisms.

The influence of temperature, confining pressure, shear-strain rate and shear strain is analysed with the help of deformation experiments in a Griggs apparatus. The starting material is a crushed quartz (grain size below 100 µm) originated from a natural single crystal. This powder simulates fine-grained crushed material within fault zones that can be deformed while the fault zone is reactivated. Some samples are hot pressed for 20 h at 1000 °C and 1.5-1.6 GPa confining pressure before deformation starts. Experiments are conducted at temperatures between 500 °C and 1000 °C and confining pressures of 0.5 GPa to 1.5 GPa. The shear-strain rate varies between $3{\cdot}10^{-3}\,s^{-1}$ and $2{\cdot}10^{-6}\,s^{-1}$. Experiments are performed at constant shear-strain rates except for some strain-rate-stepping experiments. Afterwards, the microstructural evolution and the textural evolution are analysed using light microscopy and scanning electron microscopy.

Coesite, a high-pressure polymorph of quartz, is formed in some samples. Therefore, the relationship between the stress state in the sample and the thermodynamic pressure, which determines the phase transformation of quartz to coesite, is analysed. The formation of coesite as well as the back transformation to quartz is observed in a single sample and related to increasing and decreasing differential stresses, respectively. But the *PT* range of the stability field of coesite is not reached by differential stress nor confining pressure or mean stress. Only the maximum principal stress is above the quartz-to-coesite phase transformation, which is in contrast to the common assumption of considering the mean stress as equivalent for the thermodynamic pressure.

At high confining pressure the temperature dependence of stress is ambiguous for temperatures below 650 °C. For higher temperatures, differential stress ($\Delta\sigma$) decreases with increasing temperature. The largest decrease occurs between 650 °C and 700 °C at 1.5 GPa confining pressure and $2.5{\cdot}10^{-5}\,s^{-1}$, which correlates with falling below the Goetze criterion ($\Delta\sigma = P_c$). Similar to stress, the friction coefficient (μ) slightly depends on temperature below 700 °C and it is approximately 0.45. A strong inverse temperature dependence is indicated between 700 °C and 1000 °C at $2.5{\cdot}10^{-5}\,s^{-1}$ and $2.5{\cdot}10^{-4}\,s^{-1}$. Lower shear-strain

rates ($4{\cdot}10^{-6}\,s^{-1}$) are characterised by low friction coefficients ($\mu < 0.1$) and small temperature dependence. At 650 °C a positive pressure dependence is observed between 1.0 GPa and 1.5 GPa whereas the pressure dependence is ambiguous at 700 °C. No pressure dependence occurs at 800 °C between 1.0 GPa and 1.5 GPa confining pressure but a decrease of P_c to 0.5 GPa appears to cause strengthening. Hence, brittle deformation mechanisms dominate at low temperatures and confining pressures. They mainly depend on confining pressure or rather normal stress. Temperature slightly affects these processes. Increasing temperature dependence and pressure independence indicate an increasing amount of crystal plastic processes.

Heterogeneous deformation dominates in low-grade samples and at low confining pressures. It is characterised by Riedel geometry but through-going fractures do not exist. Crack propagation is inhibited and cataclastic flow is predominant. With increasing temperature or confining pressure, the microstructure evolves into an S-C' fabric. At 700 °C and high shear strain, a penetrative foliation is established by slightly elongated recrystallised grains. The S-C' fabric persists at high shear strain for samples with differential stresses above the Goetze criterion. Samples with differential stresses below the Goetze criterion already establish an S-C' fabric at peak stress. With increasing strain by predominantly dislocation creep, recrystallisation overprints the S-C' fabric. The mode of recrystallised grain sizes increases with increasing temperature (1.8 µm at 700 °C; 10.1 µm at 1000 °C for 1.5 GPa and $2.5{\cdot}10^{-5}\,s^{-1}$). Already at 600 °C, small, equiaxed grains form by dissolution-precipitation processes in fine-grained material in C' orientation. These zones widen with increasing temperature and they are common in samples with S-C' fabric.

A random crystallographic preferred orientation (CPO) exists in the undeformed material and persists at low temperatures or low confining pressure. *C*-axes develop a peripheral CPO with increasing crystal plasticity and the development of an S-C' fabric. At 700 °C and 800 °C, a peripheral maximum occurs that is rotated anticlockwise with the sense of shear in S-C' fabrics. The maximum rotates with the sense of shear with increasing shear strain and the development of a penetrative foliation. The *a*-axes form a girdle that is slightly inclined ($\sim$10 °) with respect to the shear zone boundary. A central *c*-axes maximum evolves at 900 °C next to the peripheral maximum. At 1000 °C, only the central maximum exists.

The differential stress of hot pressed samples is significantly higher than stresses of samples without hot pressing. The grain size distribution is the main difference between these materials. The initial powder has a broad grain size range. This range decreases with hot pressing at the expanse of the smallest and largest fraction. Hence, dissolution-precipitation processes are less effective because they are initiated in fine-grained zones.

Flow laws are used to relate crystal plasticity in experiments with natural conditions. A high stress exponent ($n = 6.4 \pm 1.3$) at 650 °C indicates power law breakdown. A stress exponent of $n = 1.9 \pm 0.7$ is calculated between 800 °C and 1000 °C. The corresponding activation energy is 170 ± 72 kJ/mol. The stress exponent is below the theoretical value and

often used experimentally determined stress exponents for dislocation creep as well as above values for diffusion creep.

The transition from semi-brittle deformation to viscous dominated deformation is often marked by an S-C' fabric. The occurrence of C' shear bands is not necessarily an indication for high shear strain and crenulation of an earlier foliation. In fact, C' bands can be generated at low shear strain without an initial foliation. They are often associated with dissolution-precipitation processes. In the viscous dominated field, dislocation creep as well as dissolution-precipitation processes occur. Apparently, the rate limiting step is unchanged between 800 °C and 1000 °C. Grain size sensitive diffusion processes are active in fine-grained material while grain size insensitive dislocation creep dominates in larger grains.

Contents

List of figures

List of tables

1 Introduction

Over the past 60 years, several studies on deformation processes in quartz have been conducted covering natural rocks, experimentally deformed single crystals and polycrystalline material at brittle and viscous conditions. Yet, the transition from cataclastic dominated deformation to crystal plastic dominated deformation as well as the interaction of deformation mechanism is not fully understood.

In this chapter, the motives for further deformation experiments on quartz and the importance of the brittle-to-viscous transition are presented. It is explained to what extent rock deformation experiments are a helpful approach to separate processes involved in deformation. The basics of the most important deformation mechanism at the brittle-to-viscous transition are outlined.

1.1 Motivation

Quartz - as one of the most abundant minerals in the continental crust - has been intensively studied in experiments [e.g. Carter et al., 1964; Hobbs, 1968; Hirth and Tullis, 1992] and nature [Menegon et al., 2008; Stipp et al., 2002; Kilian et al., 2011]. Due to crystal plastic behaviour of quartz in a broad range of the upper and middle continental crust, quartz rheology is often used to simulate crustal behaviour [e.g. Fliervoet et al., 1997; Kohlstedt et al., 1995]. However, crustal rocks are predominantly polymineralic aggregates and the rheological behaviour is influenced by interactions of minerals (e.g. feldspar, quartz, calcite). Yet, in contrast to most other rock-forming minerals, quartz has a simple chemical composition of silica tetrahedras (SiO_2) and it is less influenced by metamorphic reaction compared to e.g. feldspar. Therefore, mechanical behaviour and microstructural evolution are caused by rheological factors rather than chemical variations.

Despite a large database of rheological parameters of quartz at various external conditions, there is a lack of data at the transition between semi-brittle conditions and crystal plastic behaviour.

Primarily, deformation is localised in fault zones in the lithosphere. These fault zones occur on all scales - from kilometre-scaled fault zones between tectonic plates down to micrometre-scaled fractures between grains. Potential displacement correlates with scale. Accumulated energy can be slowly released (e.g. viscous flow, aseismic creep) or cause

abrupt failure (e.g. earthquake). The magnitude of stored energy depends on the potential for the deviatoric stress build up. According to strength envelopes for the crust of the Earth, the highest differential stresses occur in the semi-brittle flow regime [e.g. Brace and Kohlstedt, 1980; Kohlstedt et al., 1995; Pec et al., 2012a], which is limited by the onset of viscous deformation processes (lower boundary = brittle-ductile transition) and pure viscous deformation processes (upper boundary = brittle-plastic transition; terminology after Rutter [1986]). Hence, large earthquakes are likely to originate and it is necessary to understand the stress build up on micrometre scale influenced by interactions of deformation mechanisms in this zone. As a result, there is the possibility that high stresses and thereby the origin of earthquakes can extend to viscous dominated regions.

Fault zones are frequently reactivated and the deformed material is overprinted by renewed deformation. Thus, the rheological behaviour of intact rocks only applies to new fault zones and crushed material simulates fault gouge that is reactivated. Reactivated faults are expected to be weaker than the intact rock [Keulen, 2006] but there is evidence for stronger material after deformation [e.g. Di Toro and Pennacchioni, 2005].

How can high stresses persist in previously crushed material? How intense is the effect of annealing of crushed material? How do deformation mechanisms operate side by side and to what extent?

1.2 Rock deformation experiments

Rock deformation is influenced by various physical (e.g. temperature, pressure, strain rate) and chemical (e.g. water content, oxygen fugacity) parameters. In natural samples, it is difficult to separate the effect of each parameter. In addition, the time span of deformation ranges from milliseconds up to millions of years and the samples are seldom directly accessible after deformation.

Several rock deformation apparatuses (e.g. gas apparatus, piston cylinder apparatus, multi anvil apparatus) have been designed to study the effect of different parameters on deformation in a somewhat controlled environment. They use different confining media: solid confining medium enables high confining pressures and long experimental duration but the uncertainties of stress values depend on the strength of the confining medium, liquid confining medium improves the stress resolution, gas medium provides low stress uncertainties and allows pore fluid control but it is reduced to low confining pressures. An outline of the development of deformation apparatuses can be found in e.g. Paterson [1990]; Tullis and Tullis [1986]. Although quartz tends to be viscous in natural rocks under low-grade conditions, it needs to be deformed at high pressures and temperatures in experiments to achieve crystal plasticity. Therefore, Griggs apparatuses, developed in the 1960's [Griggs, 1967; Green et al., 1970], are used to study viscous deformation in quartz. The rheological behaviour

is analysed as a function of controlled temperature, confining pressure and to some extent stress or strain rate.

Previous studies of quartz focused on coaxial deformation of single crystals [e.g. Hobbs, 1968; Vernooij et al., 2006] or quartzites [e.g. Tullis et al., 1973; Kronenberg and Tullis, 1984; Hirth and Tullis, 1992] but the resulting strains were rather small. By changing the sample assembly to shear geometry, higher final strains (up to a shear strain of 8) could be achieved [Dell'Angelo and Tullis, 1989; Muto et al., 2011; Heilbronner and Tullis, 2002; Heilbronner and Tullis, 2006]. Furthermore, pure shear - as produced with coaxial experiments - seldom occurs in nature. A combination of pure and simple shear is more likely to simulate natural deformation. Torsion experiments that can produce even higher shear strains (up to 20) can only be performed - up to date - in gas apparatuses [e.g. Schmocker et al., 2003], in which experiments are performed at low confining pressures (<500 MPa).

1.3 Deformation mechanisms

Deformation behaviour of quartz is characterised by various processes that can be subdivided into brittle and viscous deformation mechanisms. Inferences can be drawn about the active mechanism on the basis of typical microstructures. At the brittle-to-viscous transition, cataclastic flow, dislocation creep and dissolution-precipitation processes are assumed to be active [Evans et al., 1990; Hirth and Tullis, 1994].

Cataclastic flow is characterised by microcracking and movement of fragments, in which fracture formation depends on normal stress. Hence, strength increases and crack growth and propagation is suppressed with increasing confining pressure [Lockner, 1995]. Subcritical cracks dominate and frictional sliding is less pronounced. Microcracking is homogeneously distributed and macroscopic localisation is prevented [Schmocker et al., 2003]. Fragments resulting from fracturing are passively rotated. Hirth and Tullis [1989] describe cataclastic flow as a transient phenomenon that is marked by changes in porosity. It is a complex interaction of porosity reduction due to compaction and dilatancy due to fracturing [Paterson and Wong, 2005; Lockner, 1995].

Viscous deformation is characterised by crystal plasticity due to the motion of lattice defects and grain boundary sliding. Thereby, dislocations (line defects) produce typical structures. A detailed description of the basics of dislocations can be found in Hull and Bacon [2011]. Dislocations are moved by either glide in the glide plane or climb out of the glide plane. A critical shear stress is necessary to move dislocations, whereby the velocity depends i.a. on temperature and type of dislocations (edge or screw dislocation). Strain is effectively produced by moving dislocations (glissile). The Orowan equation relates the strain rate to the amount of dislocations and the velocity [e.g. Kohlstedt and Hansen, 2015]. Immobile dislocations (sessile) do not contribute to the strain. A certain dislocation density is necessary to produce strain on the microscale. Dislocations themselves can be observed

with transmission electron microscopy (TEM). The onset of dislocation creep is indicated by microstructures e.g. undulatory extinction, kinks, twinning and deformation lamellae [e.g. Carter et al., 1964; Hobbs, 1968; Green et al., 1970; Tullis et al., 1973]. Hirth and Tullis [1992] subdivided this dislocation creep in three regimes depending on accompanying recrystallisation processes.

Besides dislocation creep, diffusive mass transfer processes (e.g. dissolution-precipitation) contribute to crystal plasticity. In this case, ions move through the lattice. The rate depends on the flow velocity of the ions as well as the dissolution rate and precipitation rate. The slowest step is rate limiting. Fluids enhance this process [Tullis and Yund, 1982] by increasing silica transport, dissolution and precipitation. Typical microstructures produced by dissolution-precipitation involve small, equiaxed grains and the lack of dislocations [e.g. Trepmann et al., 2007; den Brok, 1992]. For geometrical reason, diffusion processes are often accompanied by grain boundary sliding [Kohlstedt and Hansen, 2015]. Dislocation creep depends on dislocation densities and velocity whereas grain size is less important. However, grain size sensitive dissolution-precipitation is more favourable in small grains.

At semi-brittle conditions, these deformation mechanisms can be active next to each other and probably interact. There is evidence for crack formation at dislocation pile-ups [Wong, 1990; Evans and Kohlstedt, 1995] as well as dislocations initiated at crack tips [e.g. Trepmann et al., 2007; Vernooij et al., 2006; FitzGerald et al., 1991]. Trepmann et al. [2007] related recrystallisation to high stress and high dislocation densities. Also, there are indications that the coefficient of friction decreases with increasing involvement of dissolution-precipitation [Chester and Higgs, 1992; Chester, 1995].

Besides microstructural evidence for individual deformation mechanism, textures can be related to different deformation mechanisms. Crystallographic preferred orientations (CPO) are caused by intracrystalline deformation (e.g. dislocation creep). A random CPO is attributed to deformation processes involving rigid body rotation. Diffusional mass transfer processes can produce a CPO [Bons and den Brok, 2000], which is often less pronounced than for dislocation creep.

1.4 Extrapolation to nature

The extrapolation to natural conditions is one of the main challenges for deformation experiments. In nature, strain by crystal plasticity is generally produced by low strain rates over long periods of time. Hence, experiments are performed at higher temperatures to compensate for reasonable higher strain rates in the laboratory. The same deformation mechanisms are assumed for nature and experiments based on similar microstructures. Only few examples of crystal plasticity are known for similar orders of strain rates in nature as in experiments [e.g. Linde et al., 1996].

In general, creep behaviour is extrapolated to natural conditions using constitutive flow laws [Ji and Xia, 2002]:

$$\dot{\varepsilon} = A \cdot f_{H_2O}^{m} \cdot \sigma^{n} \cdot d_{equ}^{M} \cdot exp(-\frac{Q}{R \cdot T}) \tag{1.1}$$

with $\dot{\varepsilon}$ - strain rate, σ - differential stress, n - stress exponent, d_{equ} - representative diameter, M - grain size exponent, Q - activation energy, R - universal gas constant, T - absolute temperature, A - material-dependent factor, f - fugacity, m - water fugacity exponent. Diffusion creep is characterised by an inverse grain-size dependence and stress is directly related to strain. For dislocation creep dominated by dislocation climb, a relationship between stress and strain is assumed that obeys a grain size insensitive power law. Towards lower temperatures or higher stresses, dislocation creep is controlled by dislocation glide instead of climb and the stress-strain dependence is exponential and indicated by a power law breakdown [Evans and Kohlstedt, 1995].

In general, stress highly depends on the accuracy and precision of the apparatus. Hence, it is crucial to determine external factors like the pressure dependence of the water fugacity [Kronenberg and Tullis, 1984]. These extrapolations depend on the rate-limiting step of the dominant deformation mechanism. They only apply to a single mechanism, which is seldom the case in deformed rocks. Rather, several mechanisms interact at the same time.

1.5 (Non-)hydrostatic conditions

Deformation itself is characterised by a non-hydrostatic stress state. Some studies indicate that deformation influences kinetics of mineral reactions and phase transformations [e.g. de Ronde and Stünitz, 2007]. Most of the experimental studies focusing on kinetics or pressure-temperature conditions of phase transformations are performed under hydrostatic conditions where thermodynamics are well defined [Gibbs, 1906]. But thermodynamics under non-hydrostatic conditions are less understood and highly debated [e.g. Kamb, 1959; Paterson, 1973; Shimizu, 1992]. The difficulty of relating pressure - a scalar value - and stress - a tensor - is an ongoing topic. Stüwe and Sandiford [1994] proposed the use of the mean stress as equivalent for the thermodynamic pressure. Yet, this approach neglects the anisotropy of the stress magnitude. Recent studies [e.g. Wheeler, 2014; Tajčmanová et al., 2015; Schmalholz and Podladchikov, 2014] analyse the effect of non-hydrous, direction-dependent stress states on mineral reactions based on i.a. observations in deformation experiments [Hirth and Tullis, 1994; Green, 1972].

In order to quantify the influence of deformation on kinetics and mineral reaction, the influence of non-hydrostatic stress states needs to be understood.

1.6 Structure of this thesis

In the course of this thesis, I have performed a set of deformation experiments on a crushed quartz single crystal examining a broad range of temperatures and confining pressures (500 °C - 1000 °C, 500 MPa - 1500 MPa). The displacement rate varies between 10^{-6} and 10^{-9} m s^{-1}. The experiments simulate the conditions of a continental fault zone where the material deforms at the transition between semi-brittle flow and dislocation creep. The evaluation of mechanical data and the analysis of texture and microstructure allow to draw conclusions about the interaction of cataclastic and crystal plastic deformation mechanisms.

Chapter two and **chapter three** focus on the experimental and analytical methods. At first, the experimental procedure including the preparation of the starting material and the data processing are described. Detailed characteristics of the deformation apparatuses have been examined in previous studies [e.g. Pec, 2014]. Hence, this chapter focuses on improvements, especially in the data processing. The third chapter briefly summarises texture determination, microstructural analysis methods and the Raman spectroscopy method. It is also referred to earlier studies that have established these methodologies [e.g. CIP in van Daalen et al., 1999] as well as an extraordinary textbook on image analysis [Heilbronner and Barrett, 2014].

Chapter four focuses on the formation of coesite in several samples. The presence of this high-pressure silica phase is linked to the pressure and stress state in the sample. Thereby, the importance of the mean stress as driving force for pressure-dependent phase transformations or mineral reactions is re-evaluated. In addition, the effect of deformation on kinetics is reconsidered.

Chapter five presents the mechanical data of the experiments and derived rheological characteristics (e.g. friction coefficient, stress exponent, activation energy). The effect of temperature, confining pressure and shear-strain rate on the mechanical behaviour and the microstructural evolution is described. Different initial grain size distributions were used, whereby the influence on deformation mechanisms and recrystallisation is analysed. Based on microstructural observations and rheological parameters, the experiments are extrapolated to common natural strain rates.

Chapter six presents microstructure and texture evolution at the semi-brittle-to-viscous transition. The onset of dissolution-precipitation at semi-brittle conditions along developing shear bands is investigated. In addition, transitional microstructural features are analysed that evolve to core-mantle structures.

Chapter seven summarises previous results and provides general conclusions including an outlook for future work.

The **Appendix** includes experimental conditions of all experiments. Additional observations in the microstructure are presented and detailed microstructural features of high

quality samples are shown. In addition, an elaborated description of the laboratory workflow, prepared in the course of this thesis, is provided.

Chapter four, five and six are written as manuscripts for publication. Therefore, some parts, especially in the methodology, are repeated.

2 | Experimental method

This chapter will describe the starting material, the deformation apparatus, the experimental procedure and the data processing. All experiments are performed in a Griggs-type solid medium deformation apparatus. Most of them are constant displacement experiments, some are performed with changing displacement rates and others include a hot-pressing stage prior to deformation. The differences in the experimental runs will be described. During the work on this thesis the rigS6 programme by Renée Heilbronner is improved on the basis of Pec [2014] and new calibrations and corrections are implemented.

2.1 Starting material

The starting material is prepared from a single quartz crystal grown hydrothermally in an alpine cleft (Aar Massiv, Switzerland). This material was used in previous studies on single crystals [e.g. Tarantola et al., 2010; Thust, 2014]. The inhomogeneous crystal has large, milky parts, which contain many fluid inclusions, and clearer parts with few inclusions (Fig. 2.1a). The H_2O-rich fluid inclusions (5-200 µm) contain nearly all of the water [Tarantola et al., 2010]. The quartz itself is almost dry and the water amount is close to the detection limit of fourier transform infrared spectroscopy (FTIR) measurements [Thust, 2014].

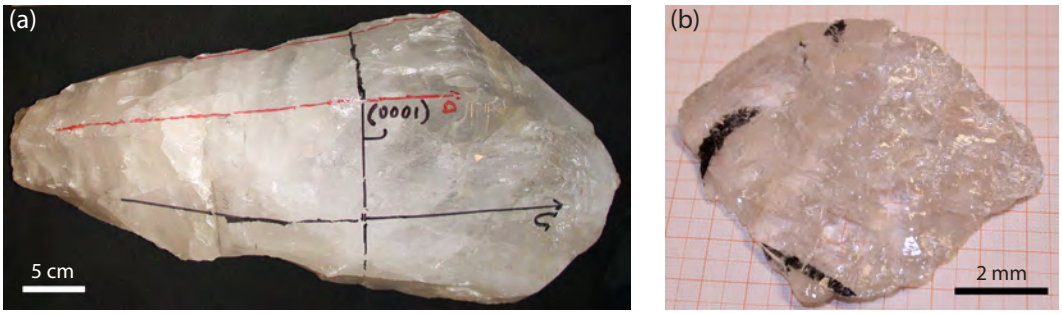

Fig. 2.1: a) Quartz single crystal with fluid-rich parts ('milky') and fluid-poor parts (clear). (Photograph by Anja Thust) (b) Part of the quartz crystal with less fluid inclusion. Areas with black marks are not used for the powder preparation.

For this study parts of the single crystal with few fluid inclusions are used (Fig. 2.1b). The crystal fragments are broken into small pieces with a hammer and screened with a 100-µm sieve. The coarser fraction is repeatedly pestled and sieved until the overall grain size is

less than 100 µm. Then the powder is washed with distilled water to remove the very fine-grained fraction. Afterwards the powder is dried at ∼120 °C. For one experiment, the fraction between 7-11 µm is used. For this, some powder is sieved with a 40-µm sieve, repeatedly pestled and filtrated at first with filter paper < 11 µm and then with < 7 µm paper followed by drying. In general, most of the fluid inclusions, especially the larger ones, decrepitated during the crushing process.

The polycrystalline quartz powder consists of sharp-edged splinters of which many are highly elongated. Although a 100-µm sieve is used, several elongated grains have long axis above 100 µm (Fig. 2.2a). The grain size distribution of the powder is measured with a LS 13 320 laser diffraction particle size analyser that measures only the long axis of a particle. The distribution ranges from 0.2 µm up to 300 µm including a large fraction above 100 µm (Fig. 2.2b). The mean length is about 65 µm and the mode ranges between 90 and 95 µm. These values emphasise the heterogeneous character of the grains with respect to form and size but do not represent a grain size distribution with respect to the diameter.

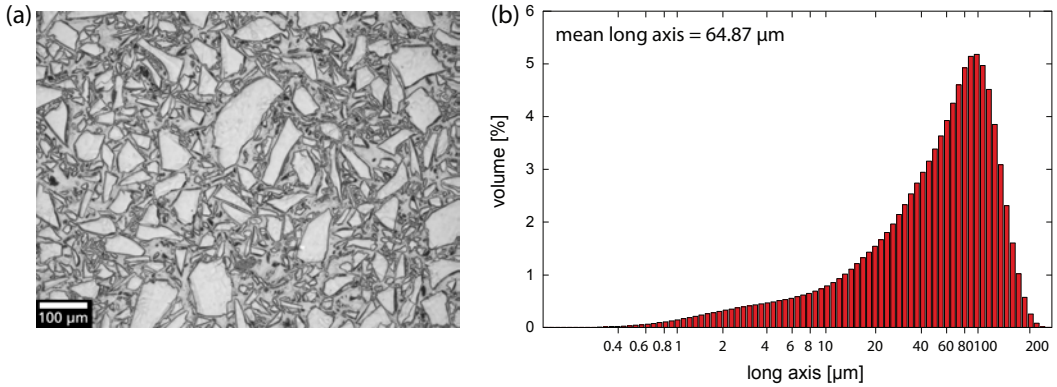

Fig. 2.2: (a) Micrograph of quartz powder illustrating the sharp edges of most of the grains. Note that several highly elongated grains occur (reflected light). (b) Long axis measured with a particle analyser. A left-skewed distribution with long axis up to 300 µm is shown.

2.2 Experimental procedure

All 57 experiments were performed in the rock deformation laboratory at the University of Tromsø, Norway. Both of the available Griggs-type apparatuses were used for this study (see appendix B for details). Only 34 experiments provided good results (no broken pressure vessels, lead leaks, salt leaks or other difficulties). A detailed description of the deformation apparatus, the experimental procedure and the characteristics of the deformation apparatuses can be found in Pec [2014]. Only minor changes in the sample preparation and experimental procedure were made to those routines.

The following paragraphs will briefly illustrate the experimental procedure and focus on special treatment and changes in the data processing. In addition, the behaviour of both rigs during an experimental run and their response to pressurisation is compared.

2.2.1 Deformation apparatus

A Griggs-type deformation apparatus consists of a steel frame that holds a load cell (Fig. 2.3 and 2.4). This load cell measures the force on the force piston (often referred to as "σ_1 piston") on a sample chamber. Therefore, a pressure vessel containing the sample chamber is placed at the lowermost steel plate. A hydraulic ram is attached to the middle steel plate whereby a force is applied to the solid confining medium, which surrounds the sample chamber inside the pressure vessel, and a confining pressure is built up (Fig. 2.5a). The load cell is attached to the upper steel plate and the force is transmitted to the sample via a force ram, which is driven into the sample assembly. A motor and a gear system that are mounted on top of the steel frame control the movement of this force ram. The movement is measured with a direct current displacement transducer (DC-DT, resolution $\sim$1 µm). The movement of the hydraulic ram that builds up the confining pressure is controlled by an oil pumping system, which can be operated manually or automatically (Fig. 2.5b).

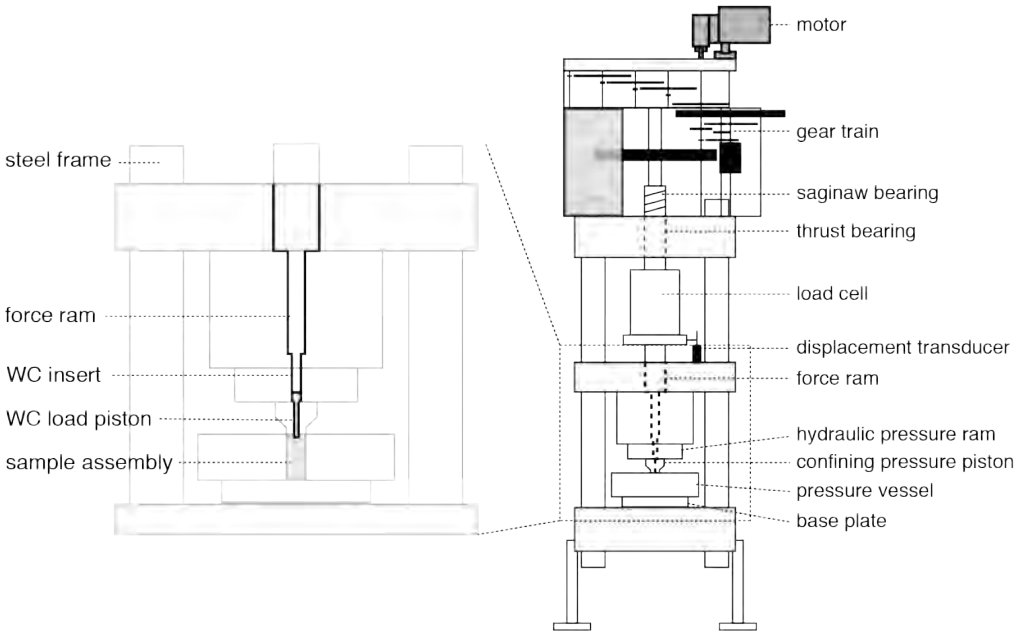

Fig. 2.3: Sketch of a Griggs apparatus [after Holyoke and Kronenberg, 2010].

The hydraulic ram and the pressure vessel are constantly cooled with two separate water circuits connected to a single main circuit. Therefore, temperature changes in one pressure vessel influence the cooling efficiency of the other vessel. Fortunately, the temperature in the laboratory is relatively constant with respect to differences between day and night as well as seasonal variations.

The control unit (Fig. 2.6) regulates the velocity of the motors and the temperature generated by the furnace and monitors force, confining pressure and displacement. In addition, force, confining pressure and displacement are constantly recorded digitally as well as with an analog chart recorder. Some emergency shutdowns are implemented in the control unit to

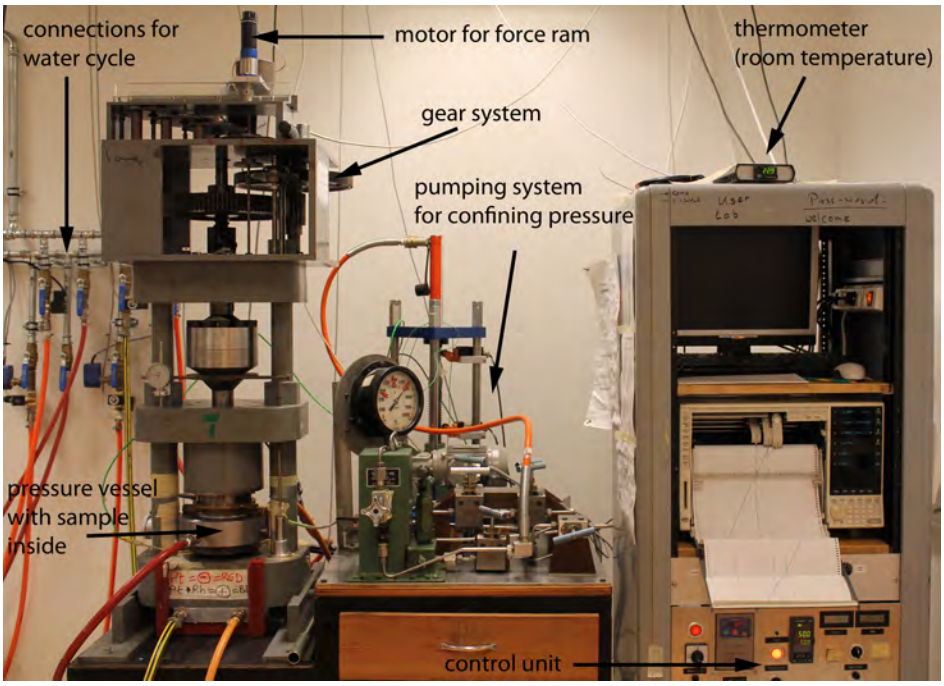

Fig. 2.4: Rig 1 in the deformation lab.

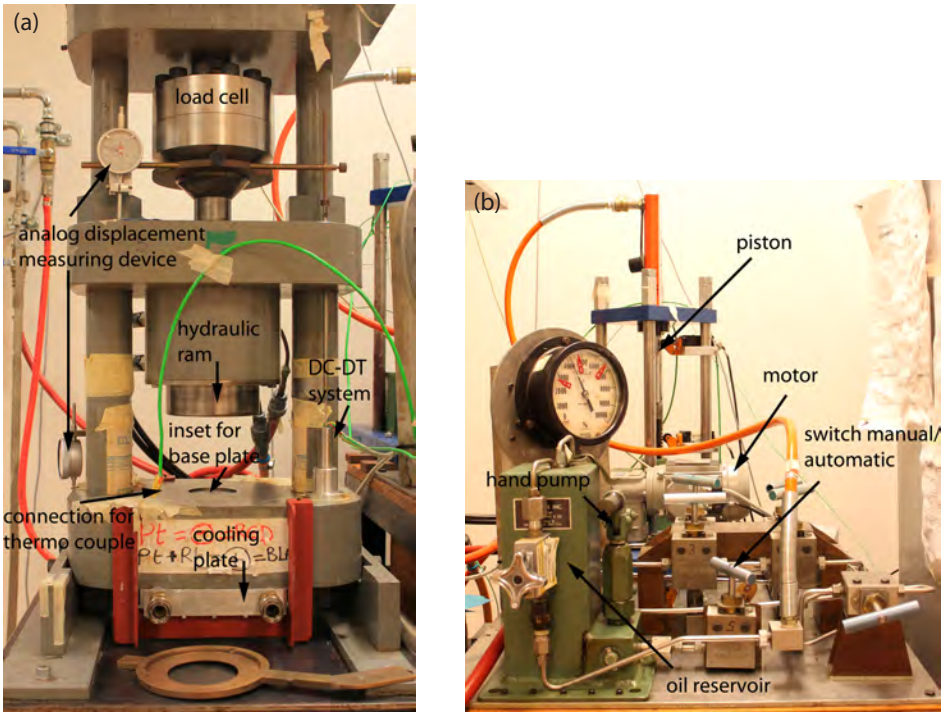

Fig. 2.5: Rig 1 (a) Details of the apparatus. Note the additional cooling plate below the lower steel plate. (b) Pumping system for the oil ram that builds up the confining pressure.

ensure safety, e.g. if a water cycle is intermitted or the temperature signal is disconnected or fluctuates intensely the furnace and the motors are stopped.

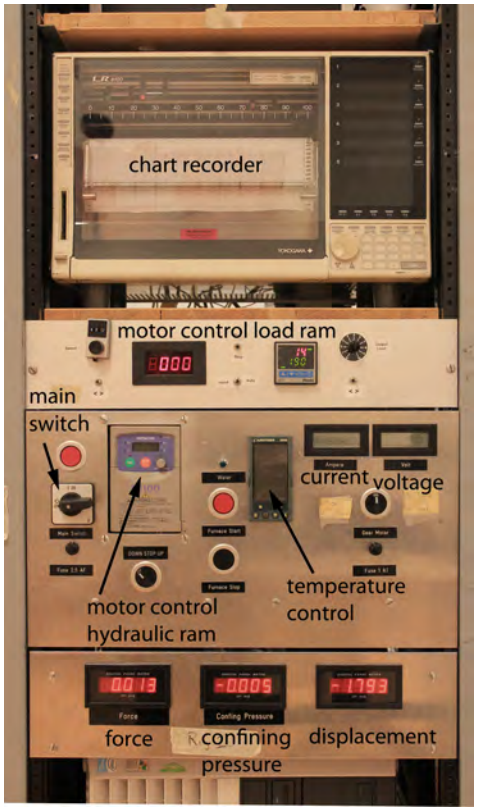

Fig. 2.6: Control panel of the Griggs apparatus (rig 1). PC that additionally records the data is not shown.

The setup of both apparatuses is very similar and the same sample assembly is used. Due to a slightly thinner steel frame the first rig is suitable for larger pressure vessels than the second one. The main difference is a second, more precise displacement transducer (digital linear transformation measurement system, LTM, resolution 0.1 µm) that is installed at rig 2 (Fig. 2.7). Furthermore, rig 2 uses an original load cell whereas rig 1 has a new one and the oil pumps for the confining pressure are of different generations. In addition, a cooling plate below the base plate of the steel frame of rig 1 was installed in the course of this study (Fig. 2.5a). Therefore, the water-cooling is more efficient and high-temperature experiments are predominantly performed on this rig.

2.2.2 Sample assembly

The well-established sample assembly for shear experiments used in Pec [2014] is used in this study. A platinum jacket (thickness 0.15 mm, purity 99.95 %) with weld-sealed platinum cups at the top and bottom contains the sample (Fig. 2.8). A thin nickel foil (thickness 0.025 mm) is placed at the inner surface of the jacket. The jacket contains $\sim$ 0.1 g quartz powder (Fig. 2.9) that is placed on top of a 45° pre-cut alumina (Al_2O_3) forcing block. A brass die is used to compact the quartz powder manually. A small amount of water (0.2 µl equals 0.2 wt%) is added to the powder with a pipette and a second pre-cut alumina forcing block is placed on top of the powder. Between the nickel foil and the forcing blocks, there

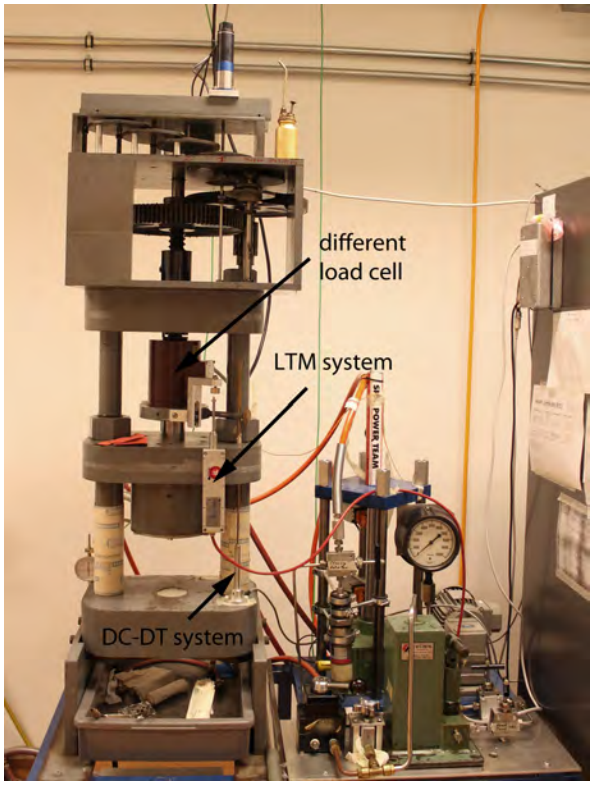

Fig. 2.7: Rig 2 in the deformation lab. The additional LTM system is marked.

is still some space and small amounts of powder can end up in this free space during the sample preparation. Hence, the material between the forcing blocks, that will be deformed, can be reduced. This loss of material should be considered, especially if significant amounts of powder are removed from the zone between the forcing blocks.

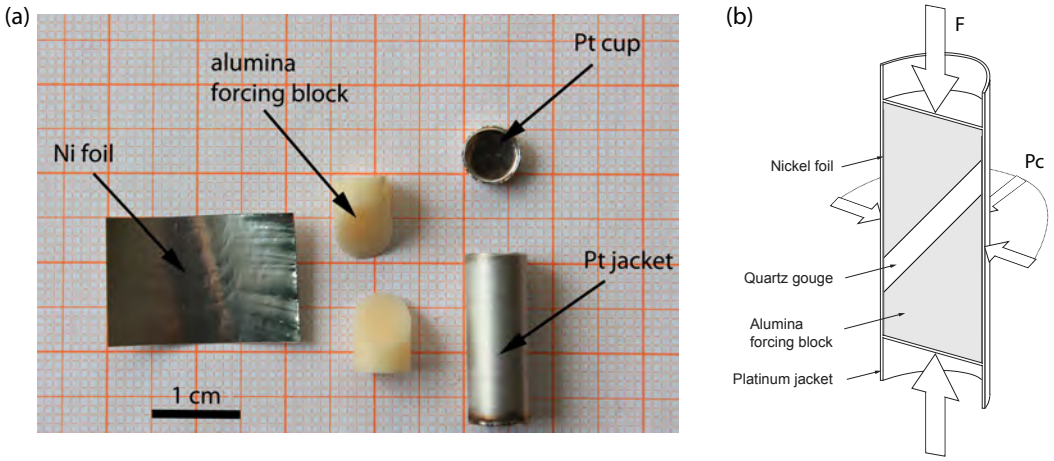

Fig. 2.8: (a) Pieces of the sample chamber (quartz powder not shown). (b) Sketch of the sample chamber.

Sodium chloride (NaCl, purity 99.5 %), which acts as confining medium, surrounds the platinum jacket. A carbon furnace, which is placed in between the inner and outer salt pieces, is used as heating unit (Fig. 2.10). In later experiments (from 422br onwards) the length of the furnace (35.3 mm) is slightly reduced compared with the furnace (35.7 mm) used in Pec [2014] and the first experiments of this study. The heating characteristics are not affected by this reduction but additional 0.4 mm of space is available for other parts of the

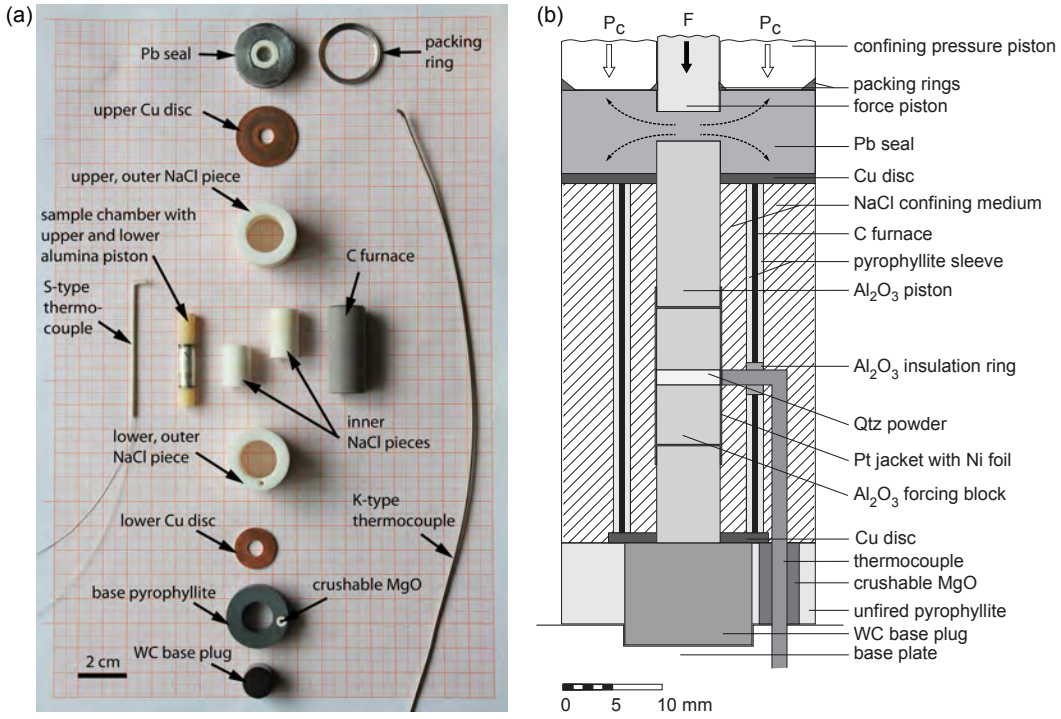

Fig. 2.9: (a) Individual pieces of the sample assembly. Sample chamber is already weld-sealed. Both types of thermocouples are shown. (b) Schematic sample assembly inside a pressure vessel.

assembly. More importantly, the whole sample assembly is shortened and the force piston and confining pressure piston (often referred to as "σ_3 piston") can be placed more inside the pressure vessel (see section 2.2.3). Thereby, their position is more stable and tilting during the initial compaction is reduced. Copper discs (thickness 1 mm) are placed on top and below the furnace to enable a connection of the furnace with the outer electric circuit. The lower copper disc sits above a tungsten carbide piston, which is surrounded by pyrophyllite. A lead piece with a salt inset is above the upper copper disc. The temperature in the centre of the sample assembly, close to the platinum jacket, is controlled by a thermocouple (TC). Above 800 °C an S-type (Pt-Pt/Rh) thermocouple is used. A K-type (Cr-Al) thermocouple is used for lower temperature. The later one is more robust and less fragile during sample preparation and pressurisation than the S-type. But the material starts to corrode or melt at temperatures above 800 °C. When all pieces are assembled, the outer salt pieces and the lead piece are wrapped in Teflon tape.

Everything is renewed for each sample except for the tungsten carbide piston and the upper copper disc. A step-by-step description of preparing individual pieces and building the sample assembly can be found in appendix E.

2.2.3 Mounting the sample assembly in the Griggs apparatus

The sample assembly is mounted on a base plate before a pressure vessel is placed on top of it (Fig. 2.11a). The base plate is isolated with paper from the pressure vessel to prevent a short circuit. The sample assembly is encapsuled on top by the lead piece

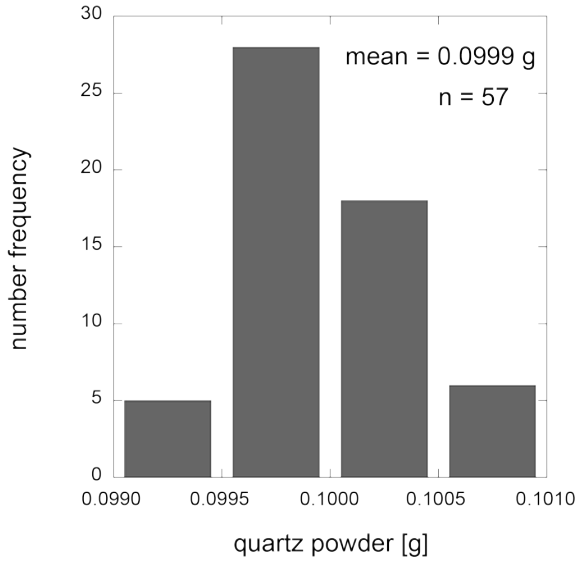

Fig. 2.10: Weight distribution of quartz powder that is filled in the sample chamber.

(Fig. 2.11b) and a large packing ring (Fig. 2.12a) seals it. The packing ring prevents the lead from extruding between the pressure vessel and the piston for the confining pressure. Another, smaller, packing ring seals the lead from the space between the force piston and the piston for the confining pressure (Fig. 2.10b, Fig. 2.12b). These two pistons and the small packing ring are placed on top of the lead piece together with an upper cooling plate, which is mounted on the pressure vessel (Fig. 2.13a). The lower side of the base plate as well as the thermocouple are isolated with tape (Fig. 2.13b). Afterwards the pressure vessel is placed on the lowermost steel plate of the rig and the water tubes, the electricity cable and the thermocouple are connected (Fig. 2.14).

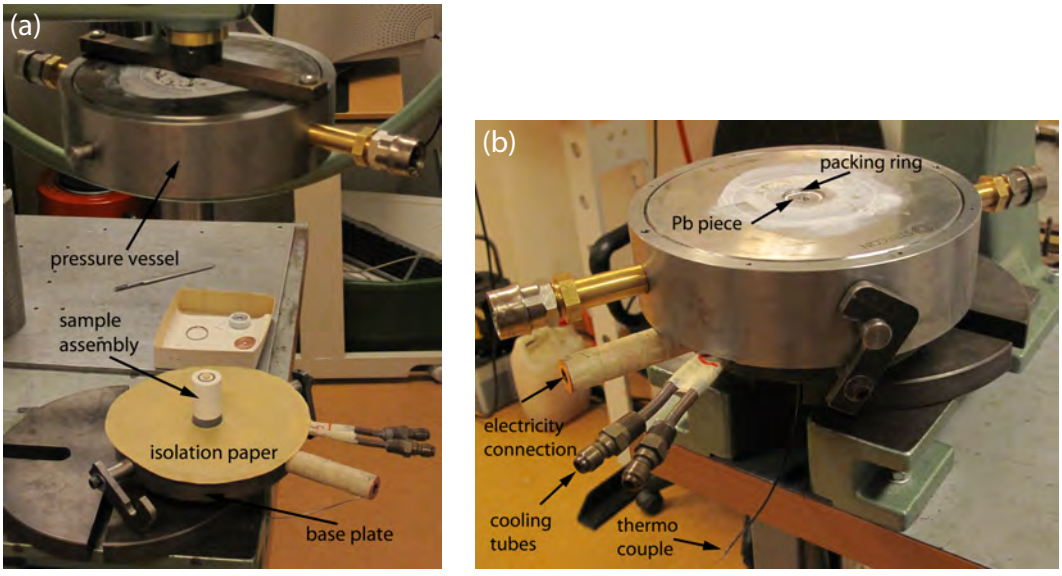

Fig. 2.11: (a) Inserting the sample assembly in the pressure vessel. Sample assembly is placed in the centre of the base plate and a sheet of paper is used for isolating the pressure vessel from the base plate. (Photograph by Leif Tokle) (b) The pressure vessel is placed onto the base plate in such a way that the sample assembly fits into the hole without any damage. The large packing ring is put in place on top of the lead piece. (Photograph by Leif Tokle)

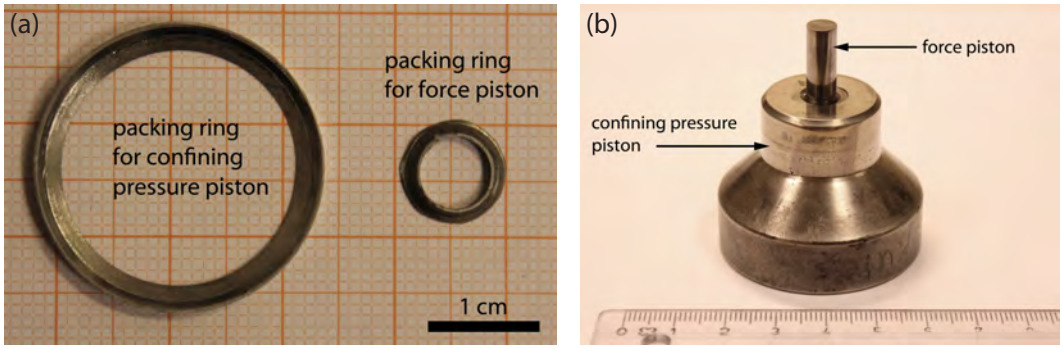

Fig. 2.12: (a) Both packing rings that are used for sealing the lead piece. (b) Pistons for applying force and confining pressure to the sample.

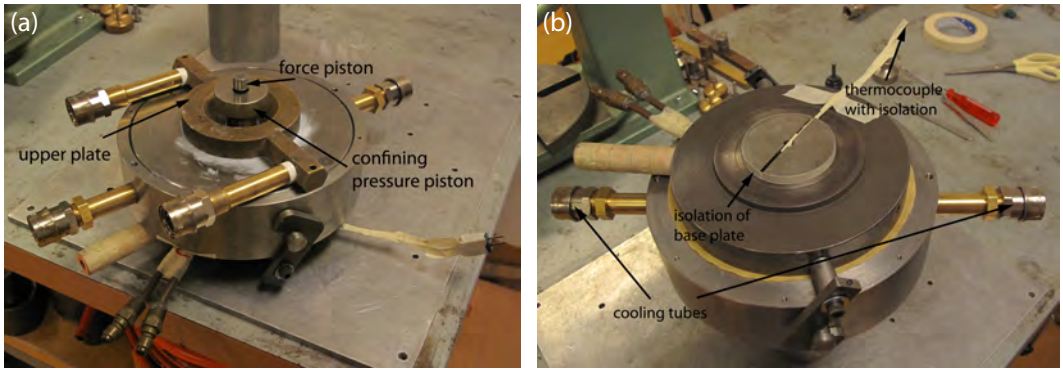

Fig. 2.13: (a) Completed pressure vessel with upper cooling plate and placed pistons. (Photograph by Leif Tokle) (b) Base plate upside down after the sample has been place in the pressure vessel. The isolation with tape of the base plate and the thermocouple is visible. (Photograph by Leif Tokle)

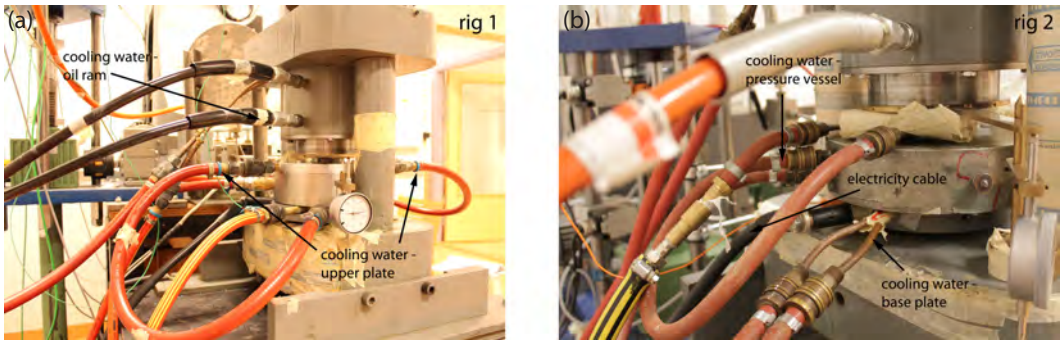

Fig. 2.14: Thermocouple and electricity cable for the furnace as well as the tubes for the cooling water cycle of the pressure vessel are connected.

2.2.4 Experimental run

A typical experimental run (Fig. 2.15) starts with increasing pressure and temperature of the sample to the required pressure and temperature conditions (I - pressurisation). When the conditions are reached the motor for the force ram is set to a specific displacement rate (II - run-in). After the run-in, the force increases significantly when the load on the sample is increased (III - loading). At peak stress the actual deformation in the shear zone starts (IV - deformation). Quenching and depressurisation conclude the experiment (IV).

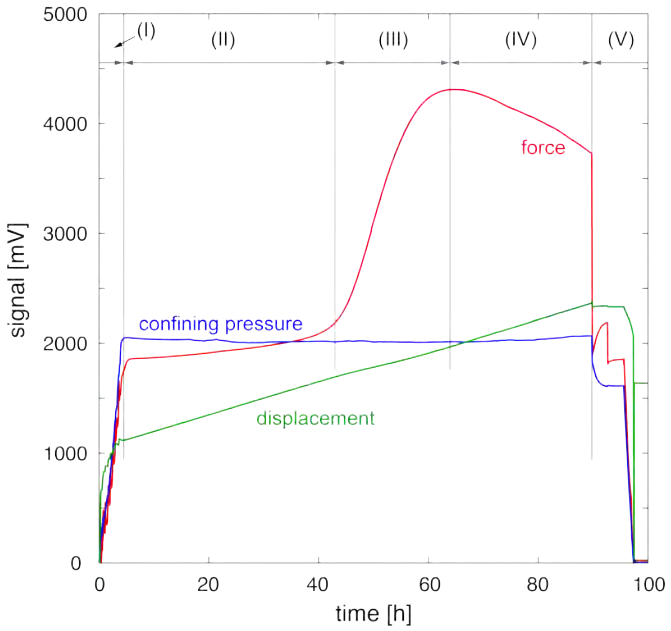

Fig. 2.15: Digital signal-time record of a normal run (452br). I - pressurisation, II - run-in, III - loading, IV - deformation, V - quenching and depressurisation.

2.2.4.1 Pressurisation

All samples are slowly pressurised and heated to deformation conditions (5-9 h). The confining pressure is manually increased to ~150 MPa with the oil pump to prevent the added water in the sample chamber from evaporating. Then, the furnace is started and heated to 100 °C (heating rate 20 °C min^{-1}). At 200 MPa and 100 °C, the manual pumping of the confining pressure and the manual advancement of the force ram are switched to automatic motor control. Temperature and pressure are increased in alternating steps of 100 °C and 100-300 MPa in a similar way for experiments at similar conditions. The increase is carried out in such a way that the conditions remain in the α-quartz field as long as possible (Fig. 2.16)

The output of the furnace increases with higher temperature (Fig. 2.17), whereby the values of rig 1 generally are higher than the values of rig 2. The differences are due to smaller diameters of the water tubes at most of the pressure vessels in rig 2 causing a less efficient cooling of the Griggs apparatus. Rig 1 has an additional cooling plate that improves the cooling. Furthermore, the temperature of the cooling water varies, which can also affect the cooling efficiency.

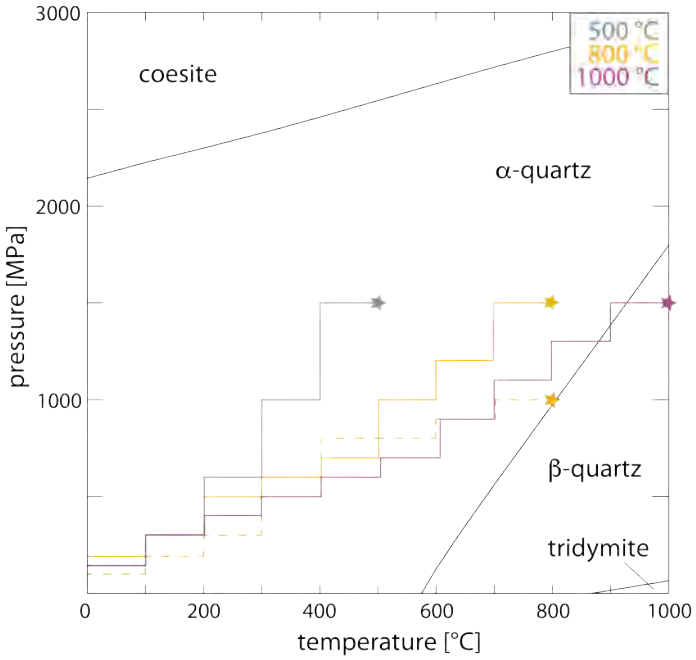

Fig. 2.16: Schematic path of pressure and temperature increase during pressurisation for different experiments. Most of the experiments start in the α-quartz field.

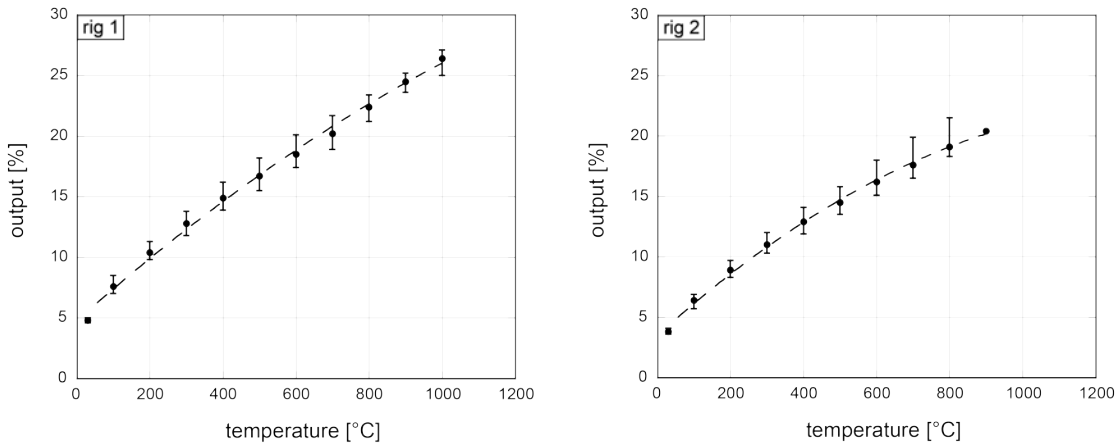

Fig. 2.17: Output of the furnace during pressurisation for rig 1 (left) and rig 2 (right). The output of rig 2 is significantly lower than that of rig 1, especially at higher temperatures, due to less efficient cooling (see text for details).

2.2.4.2 Different experimental types

By turning on the motor of the force ram with a specific rate a conventional experiment with a constant displacement rate of the force ram is started. At first, the piston of the force drives through the lead piece (run-in). When the force piston hits the upper alumina piston in the sample assembly (hit point) the load on the sample is increased and deformation starts. After loading to peak stress the shear zone is deformed intensively until the desired shear strain is reached. During the run-in, the force increases gently. At the end of the run-in, when the force piston is close to the upper alumina piston, the slope increases until it is as steep as the loading part. Hence, the hit point is not well defined and has to be constructed (see section 2.4).

A set of experiments performed at 1.5 GPa includes a hot-pressing state prior to deformation (Fig. 2.18a). Therefore, the sample is pressurised to slightly higher confining pressures (15.5 - 1.6 GPa) and heated to 1000 °C. The sample rests at these conditions for 20 h (IIa in Fig. 2.18a). The hot-pressing stage simulates annealing of the gouge material. Afterwards, the temperature is decreased to the required deformation temperature. Thereby the confining pressure decreases, too (∼1.5 GPa). Once, the deformation temperature is reached the motor of the force ram is started and the experiment continues as a conventional experiment.

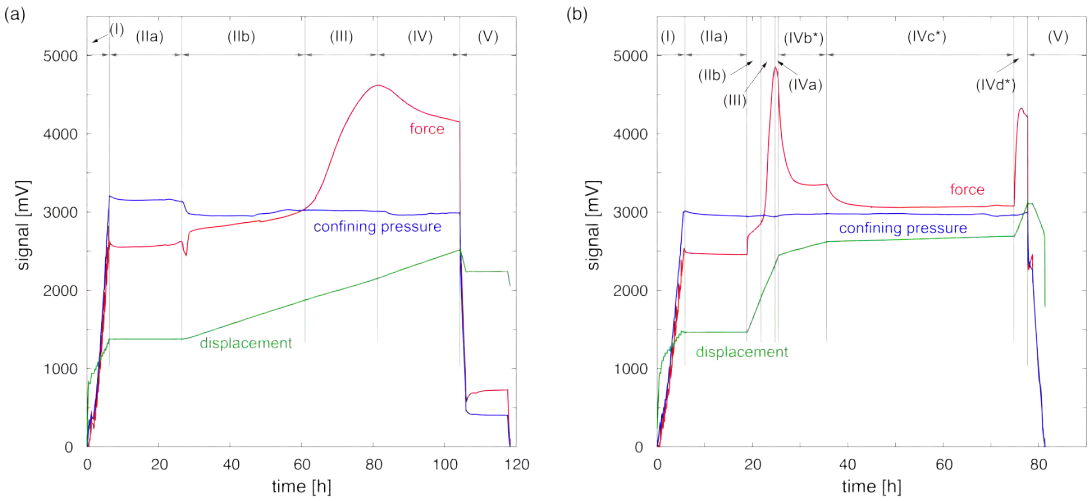

Fig. 2.18: Run of (a) experiments including hot-pressing (e.g. 419br) and (b) strain-rate-stepping experiments (e.g. 482br). I - pressurisation, IIb - run-in, III - loading, IV - deformation, V - quenching and depressurisation.

Another set of experiments is conducted at varying displacement rates (Fig. 2.18b). After the pressurisation, the sample rests at deformation conditions for some time to get similar time spans as in conventional experiments before the hit point (IIa in Fig. 2.18b). Then the motor of the force is set to the fastest, desired displacement rate and started. When the peak stress has been reached and some deformation has taken place the displacement rate is reduced to the next slower displacement rate by rearranging the gears of the gear system (Fig. 2.4). When steady state of the force is reached the displacement rate is further

reduced. After steady-state conditions at the slowest displacement rate, the displacement rate is increased to the fastest rate again. Then, the experiment is stopped.

2.2.4.3 End of experiment

The experiment is stopped by quenching the sample to 200 °C within two or three minutes (cooling rates 150-300 °C min^{-1}) and retreating the force piston in such a way that it is at a slightly higher level (∼200 MPa) than the confining pressure. The sample is slowly depressurised to ∼250 MPa, followed by the decrease of pressure and temperature to room conditions. The depressurisation takes place slowly with the force at slightly higher levels than the confining pressure to prevent any damage in the sample.

The pressure vessel is disconnected from the cooling system and the electricity. Base plate and upper plate are demounted from the vessel. Subsequently, the sample assembly is removed from the pressure vessel and disassembled and the expendables are carefully removed from the sample chamber (Fig. 2.19). Thin sections are made from the samples (chapter 3).

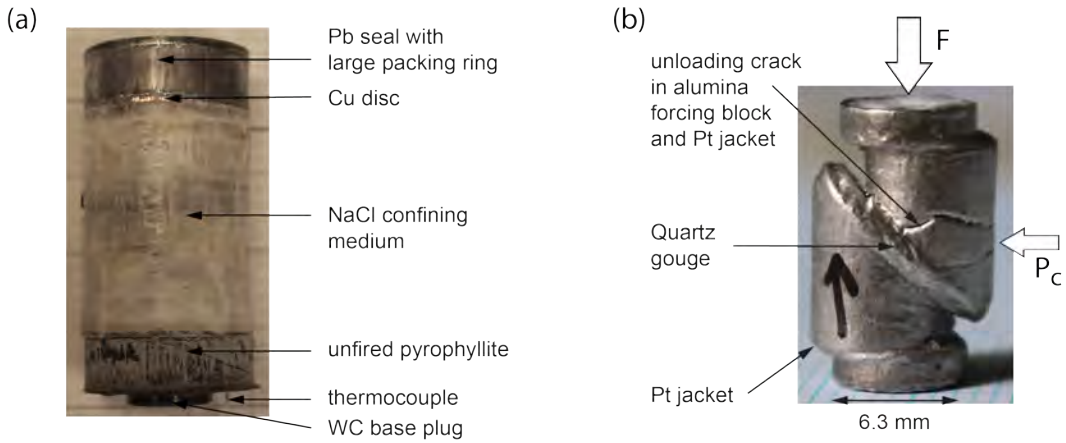

Fig. 2.19: Sample assembly after removing from the pressure vessel. (a) The whole assembly is highly compacted and needs to be separated with a scalpel. (b) After the salt is removed from the sample chamber the shear deformation in the shear zone is visible.

2.3 Limits and variations of the sample assembly

Some parts of the sample assembly are prone to be damaged during experiments. The tungsten carbide piston is used for several experiments but it often cracks during the depressurisation of high-temperature experiments even though the stresses are relatively low in these experiments. But the results are not affected by this cracking due to unloading. In contrast, the alumina forcing blocks can deform during high-stress experiments, especially if the sample was exposed to high temperatures before. This deformation can be recorded in the mechanical data and cannot be clearly separated from deformation in quartz (e.g. 415br).

For the first experiments (338br - 380br), additional platinum discs were used between the forcing blocks and the platinum cups (Fig. 2.20, Tab. B-2). Originally, this additional amount of platinum was meant to improve the movement of the alumina pistons along this surface, especially under high stresses. Unfortunately, the added material increases the potential of tilting between the alumina pistons whereby the load is applied on a smaller, possibly varying area. The resulting stress-strain curves illustrate these instabilities and show unrealistically high stresses. The deformation that occurs in the shear zone cannot be clearly related to the applied load. Therefore, the use of extra platinum discs was discontinued in experiments from 381br onwards and most of the experiments with two platinum discs are not used for further evaluation.

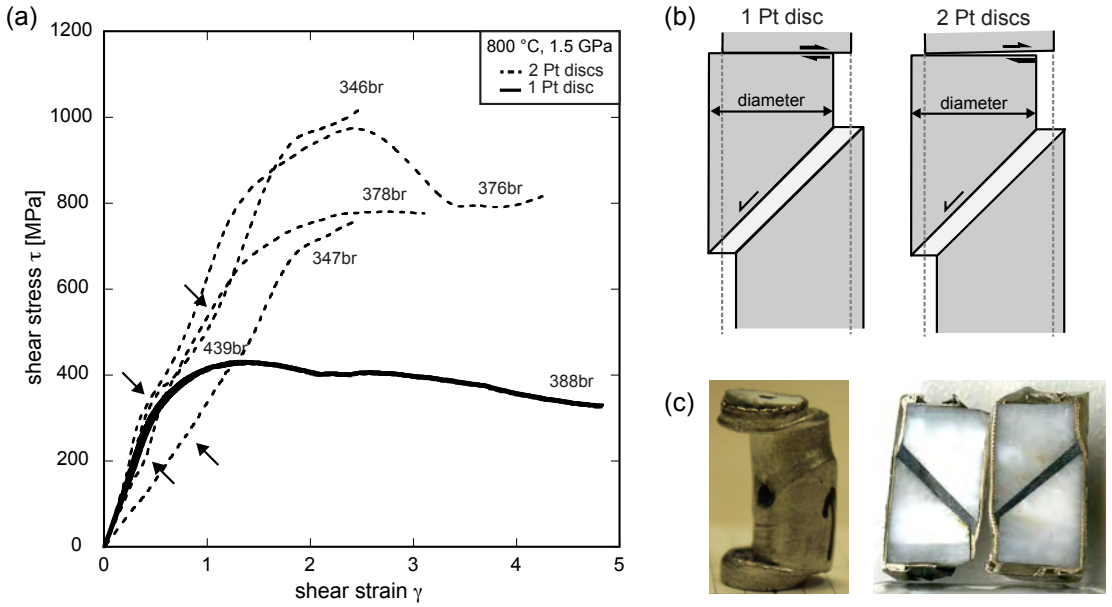

Fig. 2.20: Effect of two Platinum discs. (a) Stress-strain curves at 800 °C and 1.5 GPa confining pressure (solid line - 1 disc, dashed line - 2 discs). Arrows indicate potential instabilities. (b) Schematic sample chamber with 1 or 2 Platinum discs under deformation. (c) Sample chamber of 376br. The whole sample chamber slips along the doubled Platinum discs due to tilting. The thickness of the shear zone is highly irregular.

Several samples, especially at higher temperature, include carbon (see appendix C.1 for details), which does not exist in the original quartz single crystal. Carbon infiltration during the crushing process can be excluded. The only possible carbon source in the sample assembly is the carbon furnace. Therefore, carbon must diffuse into the platinum jacket during the experimental run. To prevent this diffusion, small amounts of hematite are mixed with NaCl of the inner salt piece that surrounds the sample jacket. The hematite is reduced to magnetite (hematite-magnetite buffer, Equation 2.1) during an experiment and should exhibit carbon from infiltrating the jacket by oxidation to carbon dioxide (Equation 2.2).

$$6Fe_2O_3 \rightleftarrows 4Fe_3O_4 + O_2 \tag{2.1}$$

$$C + O_2 \rightleftarrows CO_2 \tag{2.2}$$

The hematite is reduced to magnetite that can be measured in the salt after deformation and the colour changes from red hematite to black magnetite (Fig. 2.21). But carbon still infiltrates the jacket. The amount of hematite mixed with NaCl cannot be increased further since the rheological characteristics of the salt have to be maintained (e.g. compressibility, melting point). Hence, the hematite-bearing salt is only used in three experiments (Appendix B) as the buffering effect is not very efficient.

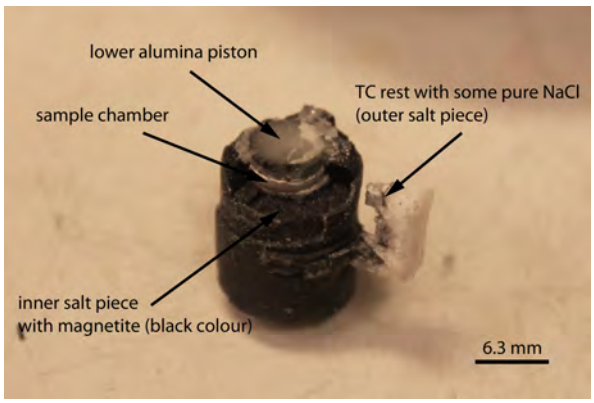

Fig. 2.21: Sample chamber (345br) that is still surrounded by salt. The black colour results from hematite transforming to magnetite during the experimental run.

2.4 Data processing and analysis

During an experiment, an external load cell measures the force applied to the force piston. The displacement of this piston compared to the steel frame of the rig is recorded by a DC-DT or LTM. The oil pressure of the hydraulic ram is measured and equals the confining pressure (P_c) . All these data are recorded by an analogue recorder and digitally recorded at a frequency of 1 Hz with LabVIEW (Fig. 2.22). The data are analysed with a modified version of the Fortran-based rigS6 programme by Renée Heilbronner (www.earth.unibas.ch/micro), which is similar to the MATLAB-based RIG programme by Pec [2014]. Details on renewed area correction and displacement-dependent correction can be found in Heilbronner et al. [2015].

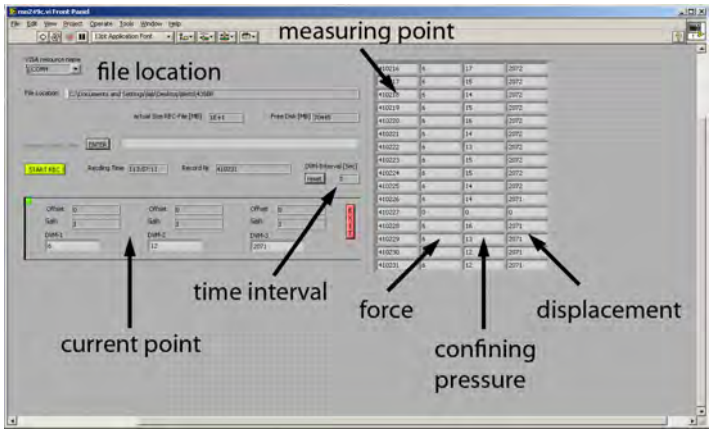

Fig. 2.22: Screenshot of LabVIEW while recording an experiment.

The starting point of the actual experiment, the hit point, has to be determined because it is not clearly visible in the record. The load curve is extrapolated to lower force levels.

The force level of the first bending point after starting the force motor (beginning of run-in) is used as reference line and the intersection of this reference line and the extrapolation of the load curve is considered as hit point (Fig. 2.23).

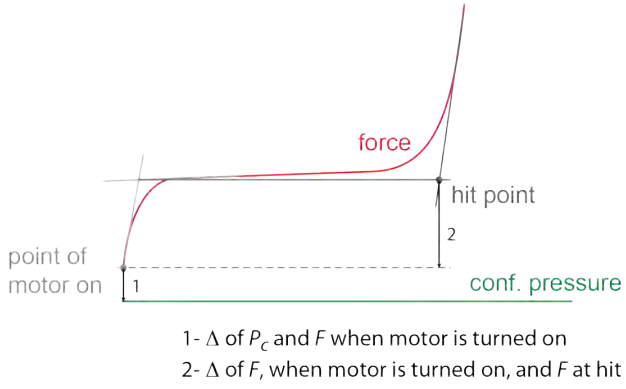

Fig. 2.23: Construction of the hit point.

The confining pressure and the force are not at the same level after pressurisation (see Fig. 2.24) if the later is transformed to stress (σ_1). This difference is independent of the deformation temperature (Fig. 2.24a). But it is indicated that $\sigma_1 > P_c$ for experiments performed in rig 1 while experiments performed in rig 2 show the opposite trend. After turning on the force motor after pressurisation, the force increases strongly in a short period of time before the slope decreases and the actual run-in starts. The amount of increase is independent of temperature, too (Fig. 2.24b), and a difference between both rigs is not visible. The effect of confining pressure on the amount of increase of σ_1 is not clear due to small data sets at low confining pressures (Fig. 2.24c). At about 1.5 GPa confining pressure, several samples have a large difference between hit point and starting the motor. Hence, these values have a relatively broad range ($\sim$70 - 600 MPa). A comparison of the σ_1 increase before hit point and the difference between σ_1 and P_c after pressurisation illustrates the different behaviour of the rigs after pressurisation (Fig. 2.24d). Yet, the increase of σ_1 before the hit point is independent of the rig.

Until now, all experiments have been considered. Excluding experiments with failing pressure vessels, salt or lead leaks or strange mechanical data due to additional Pt discs (Appendix B) eliminates most of the outliers (Fig. 2.25). The difference in both rigs after pressurisation that is independent of temperature is confirmed (Fig. 2.25b) as well as the independence of the increase in σ_1 of the confining pressure (Fig. 2.25c). Except for two remaining outliers (rig 2), the increase of σ_1 is similar for both rigs and clusters around 150 MPa whereupon rig 2 tends to slightly higher values than rig 1. The reason for the discrepancy between both rigs in unknown but it could be attributed to the different loading cells. The difference between confining pressure and σ_1 at hit point is presumably due to strain-rate-dependent processes in the lead and does not represent a real difference in stresses in the sample.

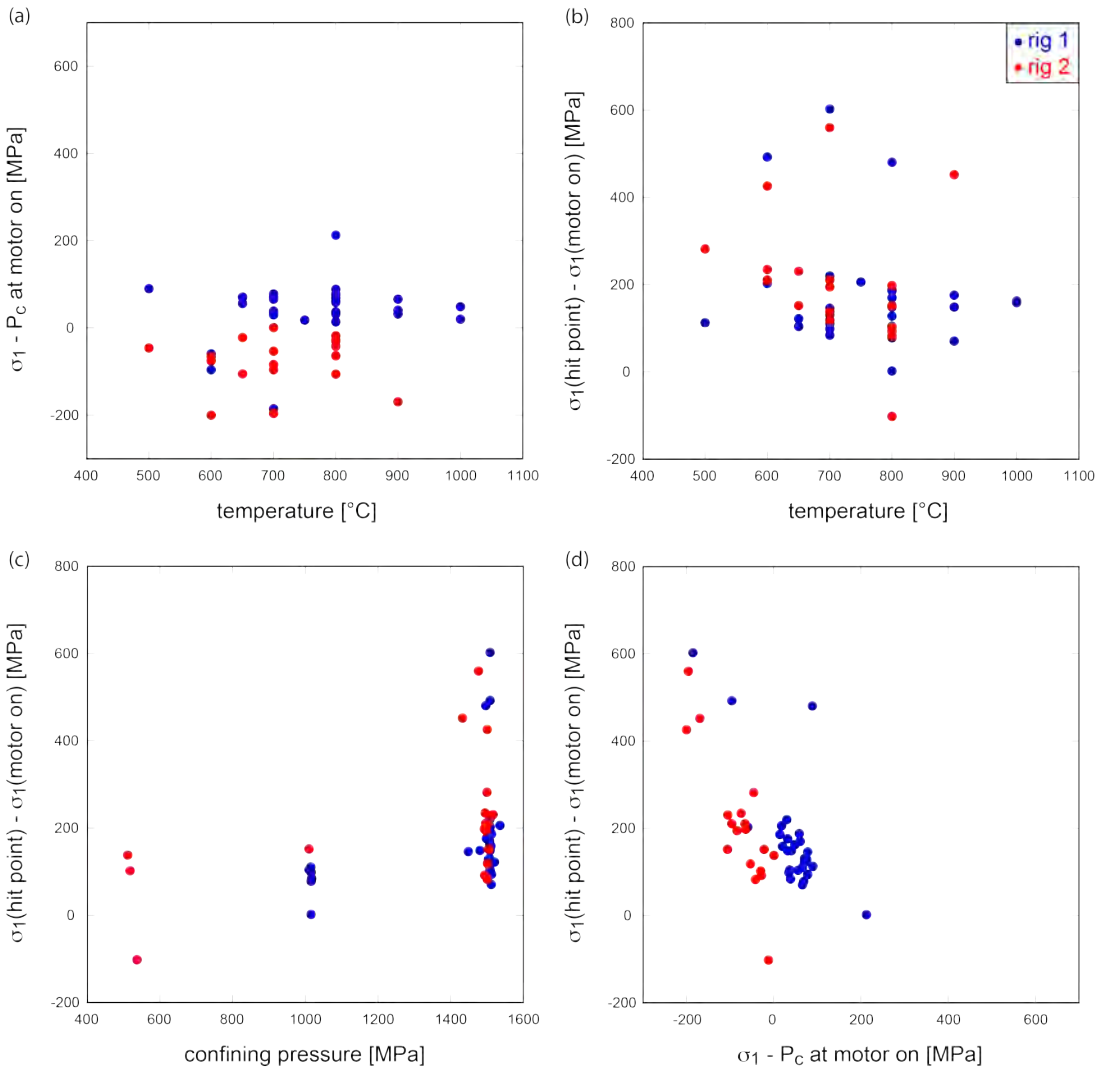

Fig. 2.24: Stress relations before hit point for all experiments. (a) Difference between force (translated to σ_1) and confining pressure when the force motor is started after pressurisation (force motor on) versus deformation temperature. (b) Difference between σ_1 at hit point and σ_1 at force motor on versus deformation temperature. (c) Difference between σ_1 at hit point and σ_1 at force motor on versus confining pressure. (d) Difference between σ_1 at hit point and σ_1 at force motor on versus difference between force (translated to σ_1) and confining pressure at force motor on.

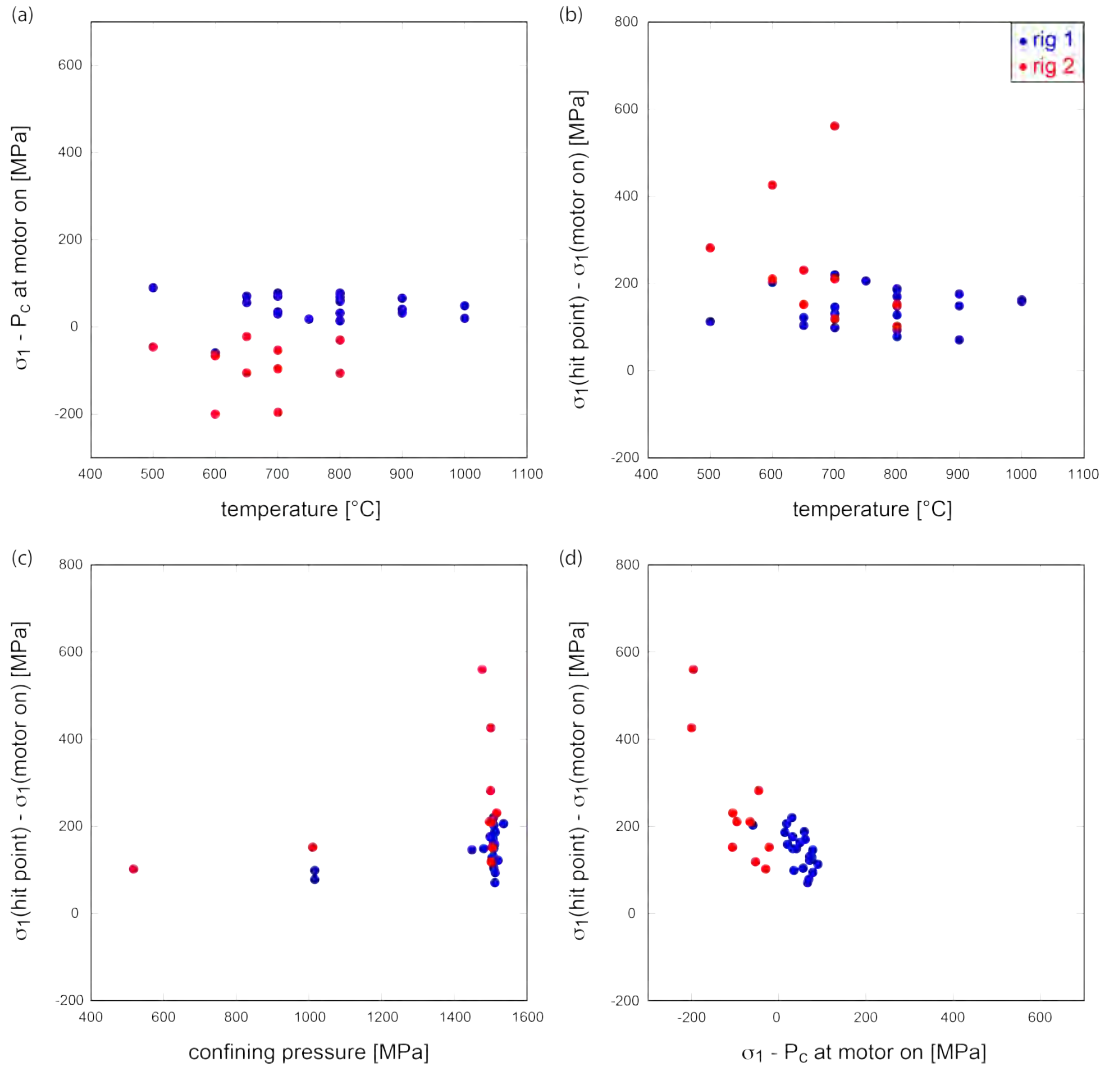

Fig. 2.25: Same plots as in figure 2.24 but only high quality data are used (without pressure vessel failure, leaks or the use of two Pt discs).

Since confining pressure and σ_1 differ at the hit point, the confining pressure at the hit point is considered to be the minimum principal stress (σ_3) at the start of the experiment ($t = 0$) and σ_1 is set to the same level, $\sigma_3(0) = \sigma_1(0)$. The differential stress ($\Delta\sigma$) at $t = 0$ is set to 0. During the experiment, $\Delta\sigma(t)$ is calculated as the change of force $\Delta F = F(t) - F(0)$ divided by the constant cross sectional area of the Al_2O_3 forcing blocks and σ_1 is the sum of the differential stress and the minimum principal stress. The constant area approach only applies to the stresses in the forcing blocks assuming no deformation of the forcing blocks at the *PT* conditions. The stresses in the sample have to account for the changing area overlap of the forcing blocks in consequence of the 45° pre-cut (Fig. 2.26a). Therefore, the differential stress is corrected for the decreasing area by a cosine function to the 1.5 as approximation to the auto correlation function with a smooth transition at zero. As a result, $\Delta\sigma$ increases with increasing displacement of the forcing blocks. Simultaneously, the advancement of the force piston reduces the volume in the pressure vessel (Fig. 2.26b) and increases the confining pressure (i.e. σ_3). Hence, a displacement-dependent correction of the confining pressure is applied, which considers the compression of the confining medium (e.g. sodium chloride) and the temperature gradient in the sample assembly [Heilbronner et al., 2015].

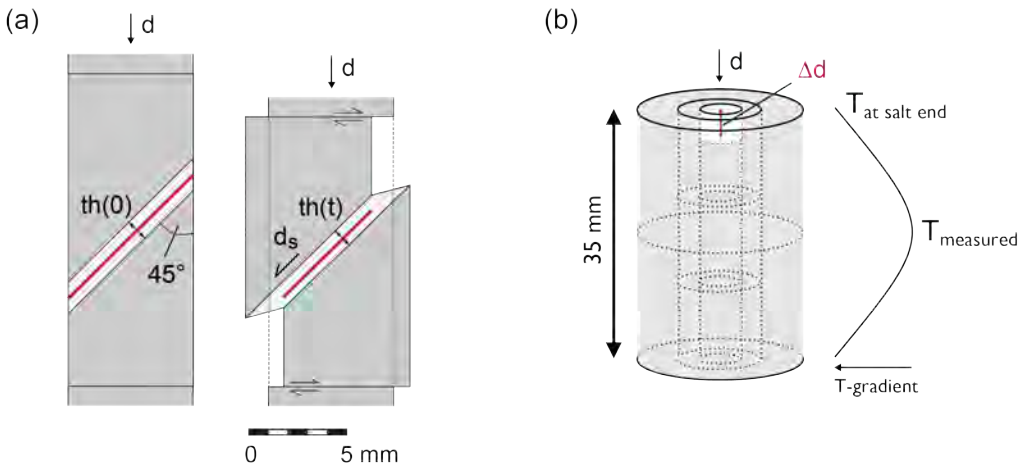

Fig. 2.26: Sketch for data corrections [after Heilbronner et al., 2015]. (a) Sample chamber at start with initial thickness, $th(0)$, and during the experiment with decreasing thickness, $th(t)$. The red line indicates the area of overlap of the forcing blocks. (b) Sketch showing the piston advancement of the forcing piston (Δd). The grey volume marks the compressed confining medium in the pressure vessel.

Assuming a 2D Mohr circle construction, the shear stress is $\tau(t) = \Delta\sigma(t)/2$ and normal stress is $\sigma N(t) = (\sigma_1(t) + 2\Delta\sigma_3(t))/3$ for a sample orientated at 45° with respect to the applied force. For $\sigma_2 = \sigma_3$, the 3D mean stress equals the normal stress.

A so-called friction correction (a constant increase of σ_1 extrapolated from the slope of the run-in curve, see Pec [2014]) of about 1.3 kN/mm is not used. The shear stress of weak samples becomes negative if this correction is applied (Fig. 2.27). Hence, the calculation would contradict the observation. Also, the correction of the differential stress proposed by

Holyoke and Kronenberg [2010] is not applied, which is based on comparisons between axial shortening experiments in gas apparatus and Griggs apparatus. It reduces the differential stress measured in the Griggs apparatus by about ∼25 % (2.10):

$$\Delta\sigma = 0.73 \cdot \Delta\sigma_{Griggs} - 48\,\text{MPa}(\pm 30\,\text{MPa}) \tag{2.3}$$

This correction is based on experiments at low confining pressures (< 400 MPa) and the applicability to shear experiments at high confining pressures is arguable. Furthermore, there is evidence from fluid inclusions analysis that stresses measured with the Griggs apparatus are accurate [Tarantola et al., 2012]. Furthermore, microstructural observations in combination with mechanical data from experiments in the study presented here indicate an accurate stress record without this correction.

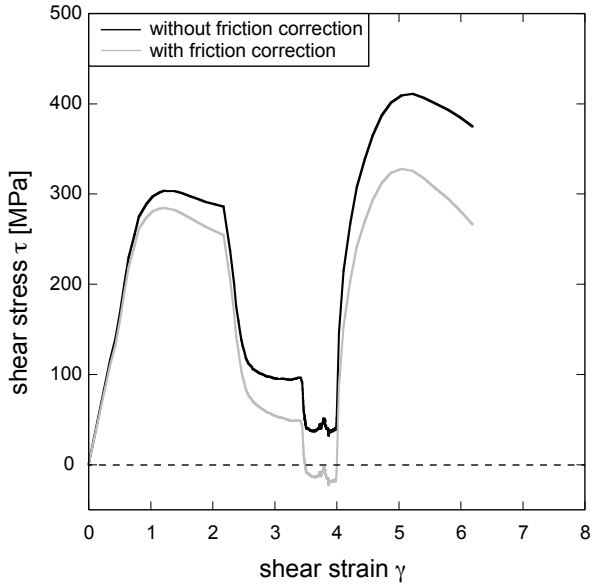

Fig. 2.27: Stress-strain curve of 485br, one of the weakest samples. The shear stress becomes negative for high strain if a friction correction is used (grey line).

Samples are thinned during the experimental run and the finite thickness can be measured in thin sections. Displacement of the force piston compared to thickness of the sample show a linear trend for all samples (Fig. 2.28). It suggests a starting thickness of 0.8 mm. The temperature-dependent thinning indicates linear trends for all temperatures, too. The slope is similar for the analysed temperatures except for 500 °C and 700 °C (shallower slope) and the suggested starting thickness is 0.8 ± 0.04 mm except for 700 °C (0.72 mm). Low temperatures indicate slightly larger starting thicknesses compared to high temperatures. Hence, a continuous linear thinning is assumed for all experiments and it is used for calculating the shear strain ($\gamma = ds/th$).

The shear strain is calculated by summing the incremental shear strains between the recorded data points. It is noticeable that the calculated shear strain differs from the measured shear strain independently of the used rig (Fig. 2.29a). Although the overall trend of all samples indicate similar calculated and measured shear strains, the calculated strain is underestimated compared to the measured strain at high temperatures ($\geq$ 700 °C) and it is

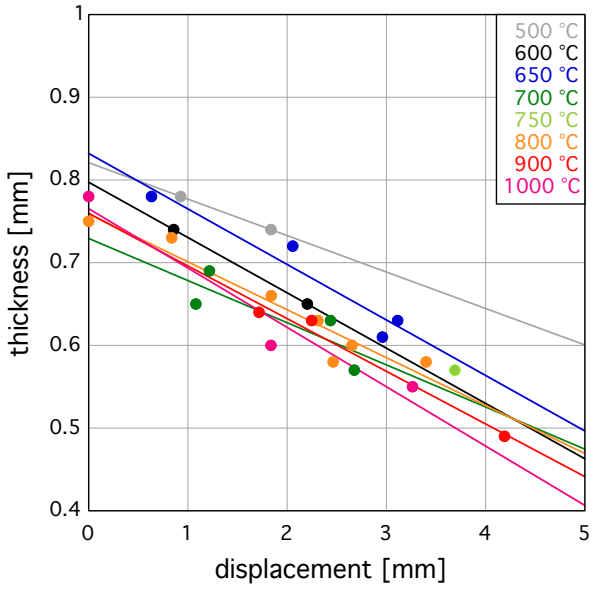

Fig. 2.28: Thickness versus displacement. Independently of temperature, all samples show a decreasing linear trend

overestimated at low temperatures (< 700 °C). At 1.5 GPa and $2.5 \cdot 10^{-5}\, s^{-1}$, this trend becomes very clear in stress-strain curves including the measured shear strain as final value (shear stress = 0 MPa), (Fig. 2.29b). For various strain rates, confining pressures or pretreatment (hot pressing), this temperature effect is less obvious (Fig. 2.30, appendix B for experimental conditions). Yet, a correlation between maximum strength and relation between measured and calculated strain occurs. Apart from four experiments, in which measured and calculated strain are similar, high shear stresses (> 1 GPa) indicate overestimated calculated shear strains, and low shear stresses (< 1 GPa) indicate underestimated calculated shear strains compared to the measured shear strain. It can be a residue of the apparatus distortion. Hence, the calculated shear strain is overestimated for high stress experiments because more displacement of the force piston than assumed is absorbed by extension of the rig resulting in less displacement that affects the sample. In contrast, the calculated shear strain is underestimated for low stress experiments since more displacement than assumed affects the sample.

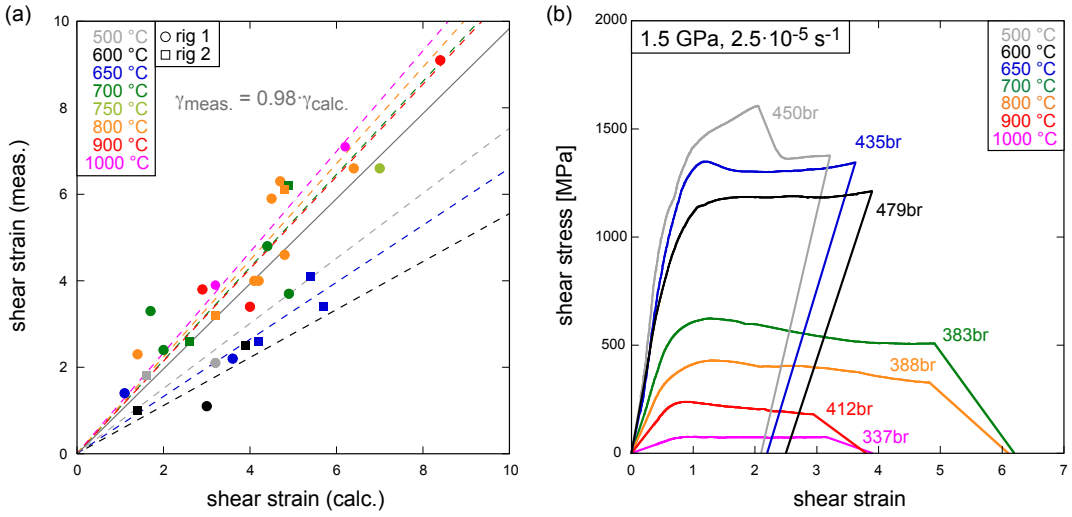

Fig. 2.29: Comparison between calculated and measured shear strain. (a) Measured versus calculated shear strain. The trend of all samples has a slope close to one (solid grey line). $T \geq 700\,^{\circ}\mathrm{C}$ indicate a steeper slope while $T < 700\,^{\circ}\mathrm{C}$ indicate a more gently inclined slope (dashed lines). (b) Stress-strain curves with measured shear strain added as final value to the calculated shear stress (shear stress = 0 MPa).

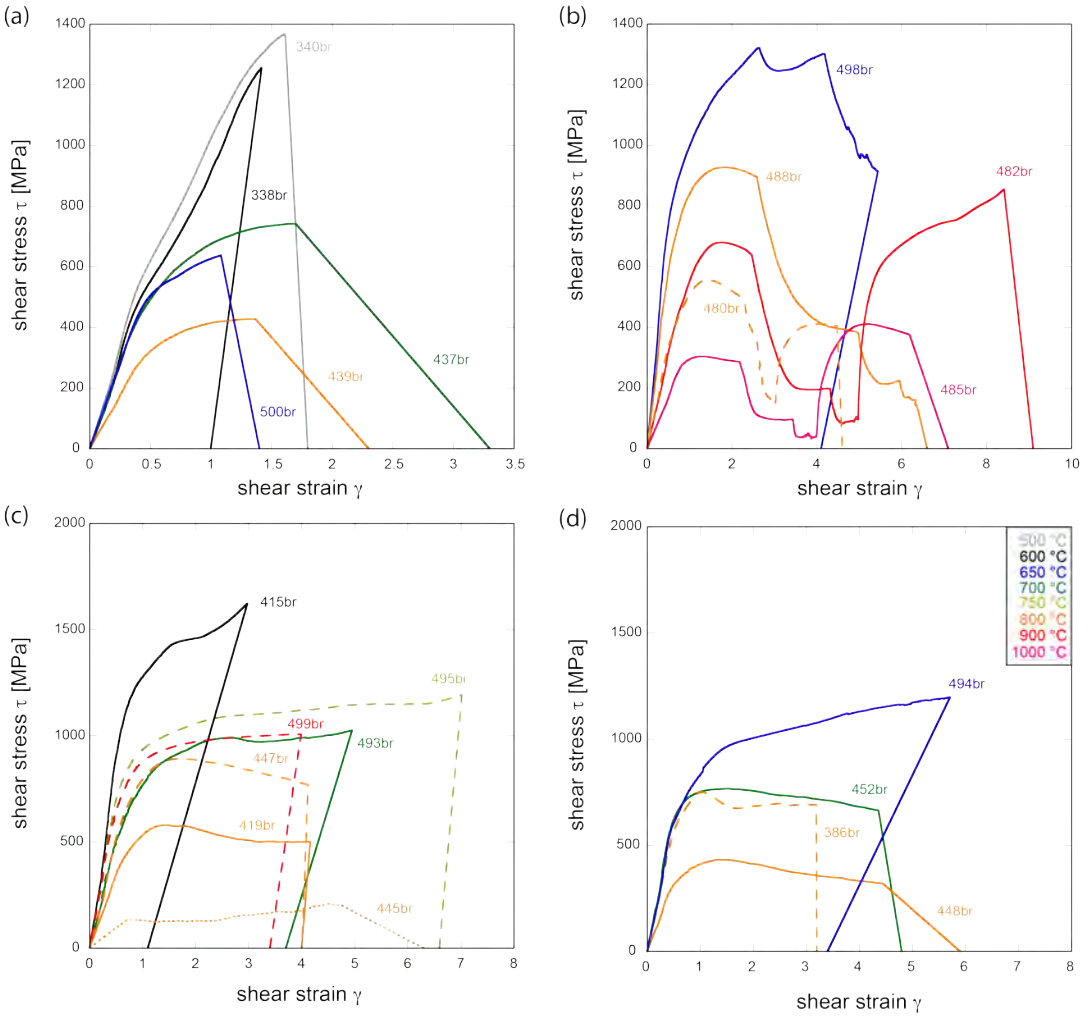

Fig. 2.30: Stress-strain curves with measured shear strain as final strain value for (a) peak stress experiments, (b) strain rate stepping experiments, (c) hot pressing and strain rates $\neq 10^{-5}s^{-1}$ and (d) low confining pressures.

3 | Analytical methods

For microstructural analysis, all samples are cut parallel to the displacement direction (Fig. 3.1) and impregnated under vacuum with epoxy to prepare double-polished thin sections (20-25 µm). The thin section of 417br (hydrostatic at 1000 °C and 1.5 GPa) is prepared without epoxy to avoid any external carbon compounds in the section. At these *PT* conditions the chance of breaking apart during the preparation process is relatively small.

In the next sections, the analysis of texture, grain size distribution and fabric as well as Raman spectroscopy will be described. The software for computer-integrated polarisation microscopy (CIP) and shape analysis can be found on www.earth.unibas.ch/micro. Detailed descriptions of these methods, the mathematical background and applications can be found in Heilbronner and Barrett [2014]. The MTEX toolbox is available on mtex-toolbox.github.io.

Fig. 3.1: Sample 412br is cut into halves parallel to the displacement direction. The oblique dark zone in the middle is quartz. The forcing blocks are white to transparent. The thin section was made from the right half (slightly smaller than the left one).

3.1 Texture analysis

The crystallographic preferred orientation (CPO) is analysed with CIP [Panozzo Heilbronner and Pauli, 1993; Heilbronner and Barrett, 2014] and electron backscatter diffraction (EBSD) [e.g. Prior et al., 1999]. The former enables the calculation of *c*-axis orientations. This method is fast and only requires a monochromatic camera mounted on a light microscope and a polished thin section. Large areas can be analysed at once depending on the magnification. Unfortunately, the CPO of small grains cannot be determined since the superposition of refraction on grain boundaries suppresses the signal of small grains. Hence, EBSD is used for fine-grained areas and reveals the orientation of all crystallographic axes. For EBSD thin sections are polished additionally with colloidal silica suspension "OP-U non

dry" and carbon coated with a very thin layer. Data is acquired on a field emission Zeiss Merlin scanning electron microscope (SEM) with a Nordlys nano camera using AZtech software at the electron microscopy department of the university of Tromsø (overview of acquired maps in table B-3). Acceleration voltages vary between 10 and 15 kV and step sizes are between 0.1-1.0 µm depending on the grain size. An initial noise reduction of the EBSD data is performed with CHANNEL 5 by removing isolated, misindexed points. Furthermore, non-indexed patterns are replaced with respect to their neighbours (iteratively filled starting with eight similar neigbours down to six or five similar neigbours).The detailed evaluation of the EBSD data is carried out with the MATLAB based MTEX toolbox [Hielscher and Schaeben, 2008].

High quality EBSD data is collected for high temperature samples ($\geq 700\,^{\circ}$C) with hit rates above 65 %. Unfortunately, low temperature samples cannot be analysed due to poor pattern qualities and, consequently, low hit rates (<40 %). These samples have large contrasts in grain size with very fine-grained crushed material (diameter <1 µm) next to large clasts (diameter >30 µm), which could be hard to polish without any relief. Furthermore, high dislocation densities can impede the measurement of diffraction pattern causing low quality EBSD maps [Humphreys, 1999; Trepmann et al., 2007; Schwartz et al., 2009].

3.2 Determination of grain size

Grain maps are obtained with MTEX from EBSD maps with a step size of 0.2 µm. Individual grains are separated by a misorientation of 10 °. Dauphine twins are excluded from grain boundaries (misorientation of $60 \pm 5\,^{\circ}$) and grains have to contain at least five pixels to be recognised as grains. The equivalent diameter ($d_{equ} = 2 \cdot \sqrt{(\text{area}/\pi)}$) is calculated based on the derived grain map.

Number weighted histograms of the calculated equivalent diameter are used as input for a StripStar programme based on Heilbronner and Barrett [2014] to calculate the number and volume weighted diameter of volume equivalent spheres. The modal value of the grain size distribution is used as representative value for the grain size. It is estimated with a kernel density function.

3.3 Microstructural analysis

Thin sections are analysed with light microscopy and scanning electron microscopy. Light microscopy uses polarised and reflected light. The Philips XL 30 field emission SEM at the Nano Imaging Lab of the university of Basel (former ZMB) is used for backscatter electron (BSE) imaging at acceleration voltages of 10, 15 and 20 kV. The thin sections are coated with a thin carbon film and conducting silver is used to prevent charging.

Based on these BSE images and MTEX derived grain maps (see section 3.2) the shape preferred orientation (SPO) is analysed. Therefore, bitmaps of segmented microphotographs have to be prepared or grain maps and grain boundary maps can be used. The particle orientation is determined with PAROR [Panozzo, 1983] by means of best-fit ellipses calculated for the two-dimensional cross sections of grains. The axial ratio of the longest and shortest axis defines the shape of the grain while the orientation of the long axis defines the orientation of the grains. In this way, the bulk fabric as well as the orientation of the individual grains are calculated. Surface orientations or rather line orientations (e.g. grain boundaries) are analysed with a MATLAB programme by Rüdiger Kilian equal to the SURFOR method [Panozzo, 1984]. A distribution function of grain boundary segments (TDF) is determined to evaluate the orientation.

In samples that are difficult to segment, especially in low temperature samples, the SPO is estimated with the help of the autocorrelation function [ACF; Panozzo Heilbronner, 1992; Heilbronner, 2002]. Grain maps of these samples cannot be obtained by EBSD (see section 3.1) and ACF does not need segmentation of particles. In general, ACF reveals information about the bulk orientation and bulk shape. But by varying the size of the area to which the ACF is applied information about individual shapes can be obtained.

3.4 Raman spectroscopy

Raman spectroscopy is a non-destructive method that uses the material-dependent inelastic scattering of light. Raman spectrograms are conducted on a Bruker SENTERRA spectrometer at the university of Basel with a 532 nm laser. It is used to identify infiltrated carbon, which could not be measured by energy-dispersive X-ray spectroscopy (EDS) or wavelength-dispersive X-ray spectroscopy (WDS). The possibility to measure light elements like carbon is an advantage since these elements are hard to detect in common SEM. Furthermore, samples are carbon coated for SEM analysis to prevent charging. Moreover, fluid inclusions can be analysed with Raman spectroscopy because this method is not limited to the surface and inclusions or grains below the surface can be analysed. But the spectrogram will include the signal of the material above. Amorphous carbon included in fluid inclusions as well as pure carbon are measured. In addition SiO_2 polymorphs can be distinguished by Raman spectroscopy (see chapter 4).

4 | Stresses and pressures at the quartz-to-coesite phase transformation in shear-deformation experiments[1]

Abstract

Coesite was found in quartz aggregates, experimentally deformed at confining pressures of 1.0 - 1.5 GPa and temperatures between 600 °C and 900 °C. The confining pressure (P_c) and, in most cases, the mean stress (σ_m) of the experiments were below those of the quartz-to-coesite phase transformation. Yet, coesite formed when the maximum principal stress (σ_1) was within the *PT* range of the coesite stability field. In one sample, the euhedral coesite grains were corroded indicating that coesite had started to transform back to quartz. It is inferred that this sample started to deform with σ_1 above the quartz-to-coesite phase transformation and, with on-going deformation, σ_1 decreased to values in the quartz stability field due to strain weakening. In all cases, σ_1 triggered the quartz-to-coesite reaction as well as the reverse reaction, suggesting that σ_1 is the critical parameter for the quartz-to-coesite transformation – not P_c or σ_m. With progressive deformation, the coesite laths rotated towards the shear plane as more rigid particles with the sense of shear. In case of back reaction, new quartz grains exhibit no systematic crystallographic relationship with respect to old coesite. The experiments cover different degrees of pressure 'overstepping', different temperatures, and different experimental duration at *P* and *T* and deformation always enhances the reaction kinetics. The observation that σ_1 is critical for a pressure-dependent phase transformation (also for reversals) poses questions for the thermodynamic treatment of such phase transformations.

[1] published as Richter, B., Stünitz, H., Heilbronner, R. (2016) in *Journal of Geophysical Research: Solid Earth*, 121:8015-8033 (doi:10.1002/2016JB013084)

4.1 Introduction

Since its discovery in natural rocks [Chopin, 1984; Smith, 1984], coesite, a high-pressure polymorph of silica, has been widely used as an indicator of high-pressure conditions in metamorphic rocks, because the phase transformation is only subordinately temperature-dependent. Using piston cylinder apparatus, a number of studies have been carried out to establish the pressure and temperature conditions of the phase transformation [e.g. Boyd and England, 1960; Kitahara and Kennedy, 1964; Mirwald and Massonne, 1980; Bohlen and Boettcher, 1982; Akella 1979; Bose and Ganguly, 1995]. A selection of transformation relations is shown in figure 4.1. Several studies were dedicated to the kinetics of the phase transformation [e.g. Mosenfelder and Bohlen, 1997; Perrillat et al., 2003; Schönbohm, 2003].

Using the experimental data by Bohlen and Boettcher [1982] and Mirwald and Massonne [1980] which are in good agreement at 800 °C, Akaogi et al. [1995] were able to construct a consistent thermochemical database. Earlier, Berman [1988] also used the data of Bohlen and Boettcher [1982] to calculate the pressure, P, at the quartz-to-coesite phase transformation as a function of temperature. Following these two studies, we used $P(T) = 21.6 + 0.0079 \cdot T \pm 0.2$ (with pressure in kb and temperature in °C), the equation given by Bohlen and Boettcher [1982], as the most reliable one (see Fig. 4.1). In the following, we will refer to P calculated from this PT relation as the transformation pressure (see below).

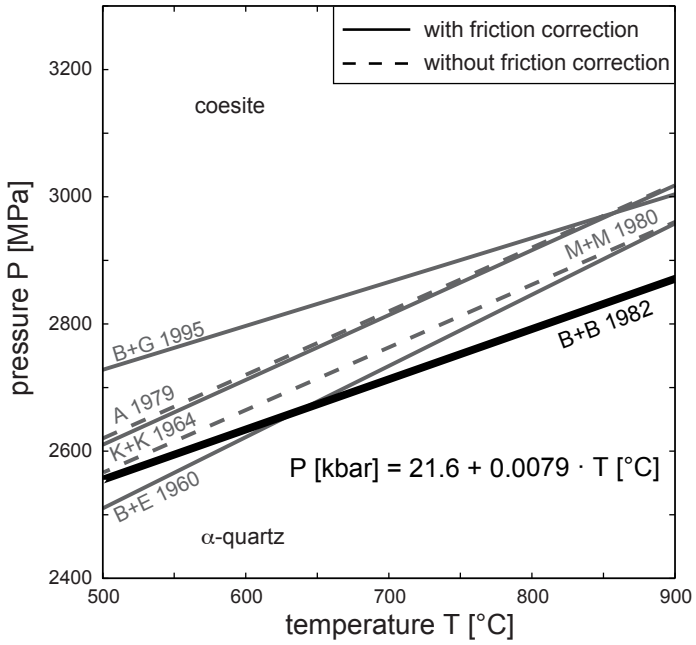

Fig. 4.1: Selection of published PT relations at the quartz-to-coesite phase transformation. Bold line - B+B 1982 - Bohlen and Boettcher [1982] (used in this study), K+K 1964 - Kitahara and Kennedy [1964], B+E 1960 - Boyd and England [1960], A 1979 - Akella [1979], M+M 1980 - Mirwald and Massonne [1980] (using α-quartz), B+G - Bose and Ganguly [1995].

In several deformation studies on quartz, performed in solid medium deformation apparatus, coesite was detected as a reaction product [e.g. Hobbs, 1968; Green et al., 1970; Hirth and Tullis, 1994; Zhou et al., 2005. The reported applied confining pressures (P_c) were always considerably below the transformation pressure of the quartz-to-coesite phase transformation. Green [1972] explained the coesite formation by metastable growth from flint (partly amorphous SiO_2) according to the Ostwald step rule, while Hirth and Tullis [1994] attributed the formation of coesite to the effect of the maximum principal stress (σ_1) instead of the confining pressure.

The concept of (equilibrium) pressure, as used in thermodynamics, is based on the assumption of a (lithostatic) stress state, where all principal stresses are equal: $P = \sigma_1 = \sigma_2 = \sigma_3$. In absence of an equilibrium stress state, the mean stress σ_m (average principal stress, average P) is usually considered the equivalent of the pressure P [e.g. Fitts, 1962; Stüwe and Sandiford, 1994]. Under non-lithostatic stress conditions, the principal stresses are different and may have different effects on the metamorphic transformations depending on the specific processes that are involved, as discussed in several studies [e.g. Kamb, 1959; Paterson, 1973; Shimizu, 1992; Wheeler, 2014].

In polycrystalline rocks, stress raisers may exist, giving rise to local differential stresses, such that the normal stress acting on the grain boundaries could control reactions, e.g. pressure solution [e.g. Shimizu, 1992; Wheeler, 2014]. The interaction of stresses on grain boundaries and the consequences for pressure estimates were analysed in recent studies [e.g. Moulas et al., 2013; Wheeler, 2014; Tajčmanová et al., 2015; Petrini and Podladchikov, 2000]. Wheeler [2014] calculated the effect of differential stresses on the chemical potential along grain boundaries and showed that differential stress could significantly shift the pressure-threshold for metamorphic reactions. Moulas et al. [2013] evoked a "pressure variation" (i.e. a differential stress) to which the rock as a whole is exposed. Their theory predicted that for equilibrium to exist after a phase transformation, the pressure of the new phase had to be close to the minimum or the maximum principal stress (σ_1 or σ_3). When considering observations made on experiments [e.g. Hirth and Tullis, 1994], they concluded that it should be σ_1.

Research on mineral equilibria under non-lithostatic stress is in its infancy and may require the application of non-hydrostatic thermodynamics. Such a treatment is beyond the scope of the study presented here. For the presentation and discussion of our experimental results, we will distinguish the following terms; in particular, we will refer to the (temperature-dependent) pressure at the quartz-to-coesite transformation as the transformation pressure P_{trans}.

- Principal stresses: σ_1, σ_2, σ_3, where σ_1 is the maximum compressive stress
- Confining pressure: P_c, in experiments $P_c = \sigma_3 = \sigma_2 < \sigma_1$

- Mean stress: $\sigma_m = (\sigma_1 + \sigma_2 + \sigma_3)/3$, in experiments $\sigma_m = (\sigma_1 + 2P_c)/3$
- Transformation pressure: P_{trans}, the pressure at the quartz-to-coesite transformation, as determined for a given temperature T
- σ_1-flow stress: the constant level of σ_1 during steady state deformation
- σ_1-overstepping: the amount by which σ_1 exceeds P_{trans} for the quartz-to-coesite transformation, or the amount by which σ_1 falls below P_{trans} for the coesite-to-quartz transformation

The kinetics of the coesite-to-quartz transformation has been studied to understand the preservation potential of coesite in high-pressure metamorphic rocks. The first order reconstructive phase transformation between trigonal quartz and monoclinic coesite requires nucleation of a new phase and thus activation energy. Therefore, overstepping of the phase boundary has a strong effect on the kinetics of the phase transformation. As the quartz-to-coesite transformation is primarily pressure dependent, usually only pressure overstepping is considered, and overstepping of ~200 to 600 MPa has been applied in kinetic studies by Mosenfelder and Bohlen [1997] and Perrillat et al. [2003]. Mosenfelder and Bohlen [1997] found a strong dependence of the transformation on nucleation rate while Perrillat et al. [2003] observed that nucleation rate was always fast, so that the growth rate was the controlling factor for the kinetics of the transformation. In addition, the growth rates of the coesite-to-quartz transformation reported by these studies differed by one order of magnitude or more.

Studies on the coesite-to-quartz transformation published so far are difficult to compare because the experimental procedures, the degree of overstepping, the grain size of the material, the water content, and the duration of the experiments vary considerably [Mosenfelder and Bohlen, 1997; Perrillat et al., 2003; Schönbohm, 2003]. Mosenfelder and Bohlen [1997] used single runs of loading and tried to minimize cracking during the preparation, whereas Perrillat et al. [2003] applied several cycles of prograde and retrograde transformations to one sample which may have increased the defect density in the material. This in turn could have caused higher nucleation rates as were indeed observed in the study by Perrillat et al. [2003].

All kinetic studies found that, once a sufficient pressure overstepping was achieved, increasing the temperature had an additional enhancing effect on the rate of the phase transformation [Mosenfelder and Bohlen, 1997; Perrillat et al., 2003; Schönbohm, 2003]. Perrillat et al. [2003] observed lower transformation rates for the coesite-to-quartz transformation than the quartz-to-coesite transformation (by one order of magnitude). Schönbohm [2003] found significantly faster transformation rates for the coesite-to-quartz transformation than Perrillat et al. [2003], but the water content of the starting material in the study by Perril-

lat et al. [2003] was very small, while Schönbohm [2003] did not measure the exact water content (but high water contents were assumed).

In the study presented here coesite was formed in shear experiments performed on quartz aggregates in a modified Griggs apparatus at confining pressures below those of the phase transformation. In experiments where σ_1 exceeded the transformation pressure, coesite was found in the samples. Where σ_1 dropped below the transformation pressure again, the back reaction to quartz was observed. We will discuss both, the level of the principal stresses necessary to trigger the reaction as well as the influence of deformation and other parameters on the kinetics of the quartz-to-coesite phase transformation.

4.2 Experiments

Fifteen shear-deformation experiments were carried out using two modified Griggs type solid-medium deformation apparatus. The following sections address the preparation of the sample assembly, the experimental procedure, the description of the data processing, with special emphasis on the stress conditions, and the microstructural analysis methods.

4.2.1 Sample preparation

The starting material was crushed quartz from a single crystal derived from a cleft in the Aar Massif (Planggenstock, Switzerland). Parts with few fluid inclusions were used. The inclusions were composed of H_2O-rich fluids with minor CO_2 and NaCl [Tarantola et al., 2012], but most of them decrepitated during the crushing procedure. All samples were prepared in the same way. A grain size fraction below 100 µm obtained by sieving was used. This powder, with 0.2 wt% H_2O added, was placed between 45° pre-cut Al_2O_3 forcing blocks, where it formed a zone of ∼1 mm thickness (Fig. 4.2). This assembly was wrapped with a Ni foil and inserted into a Pt jacket, which was then weld-sealed. The confining medium was solid NaCl. The temperature was controlled by S-type (Pt/Pt-Rh) or K-type (Cr-Al) thermocouples (depending on the deformation temperature). Maximum temperature fluctuations of ±3 °C were recorded during experiments. The vertical temperature gradient inside the jacket was ∼10 °C mm^{-1} for experiments deformed at 700 °C. A more detailed description of the sample assembly can be found in Pec et al. [2012a].

4.2.2 Experimental procedure

The samples were pressurized and heated to the required deformation conditions within 5 - 9 h. The pressure was slowly increased to ∼150 MPa, before heating the furnace to 100 °C (heating rate 20 °C min^{-1}), to prevent the added water from evaporating. Temperature and confining pressure were increased in alternating steps of 100 °C and 100 - 200 MPa respectively, such that the conditions always remained in the α-quartz stability field (Fig. 4.3,

inset). During pressurization the confining pressure (P_c) was nominally hydrostatic. A non-hydrostatic stress component on the samples (resulting from a difference between the load applied through the force piston and the confining pressure piston) could not be entirely avoided but rarely exceeded 100 MPa.

At the end of the pressurization, when the desired *PT* conditions were reached (end of stage (1), Fig. 4.3), the external pistons were in a piston-out position. The experiment was started by moving the force piston through the top lead piece to bring it into contact with the upper forcing block [see Renner, 1996 for more details]. At the beginning of this so-called run-in (stage (2) in Fig. 4.3) the load on the piston increased sharply by approx. 50 - 100 MPa (occasionally even more). After this, the force record curved over and increased gently throughout the run-in until it got close to the hit point where it started increasing again until it was as steep as the loading part of the force record (stage (3) in Fig. 4.3). The hit point is therefore not well defined, rather it has to be constructed. The 'classical' hit point (point B, Fig. 4.3) is obtained by intersecting the tangent lines to the run-in and the loading curve (stippled lines, Fig. 4.3) as described, e.g. by Pec [2014]. In this study, we used point A (Fig. 4.3) on the same tangent to the loading curve, however, at a load level that corresponds to the beginning of the run-in (obtained by intersecting the tangent lines to the initial steep part and the subsequent flatter part of the run-in stage).

After an initial steep increase of the load, the sample continued to deform at increasing, decreasing or constant load levels. The experiment was stopped by quenching the sample to 200 °C within 2 or 3 minutes (cooling rates 150 - 300 °C min^{-1}) and retreating the force piston in such a way that σ_1 was at a slightly higher level ($\sim$200 MPa) than the confining pressure. The sample was depressurized to $\sim$250 MPa followed by the decrease of pressure and temperature to room conditions.

4.2.3 Calculation of stress and strain in sample

An external load cell was used to measure the force applied to the force piston (Fig. 4.2a). A direct current displacement transducer (DC-DT, resolution $\sim$1 µm) was used to record the displacement of the force piston relative to the steel frame of the Griggs apparatus; one of the machines (rig 2) was additionally equipped with a digital linear-transformation measurement system (LTM, resolution = 0.1 µm). Measuring the pressure of the hydraulic ram, which actuates the confining pressure piston, continually monitored the confining pressure. All data were digitally recorded at a frequency of 1 Hz and analysed with a modified version of one of the programs that were used previously [e.g. in Pec, 2014]. The details of this correction are not the subject of this paper, however, the software can be downloaded from www.earth.unibas.ch/micro.

In a first step, the displacement, load, and pressure measurements were used to derive the principal stresses, σ_1 and σ_3, in the forcing blocks, which were assumed to remain unde-

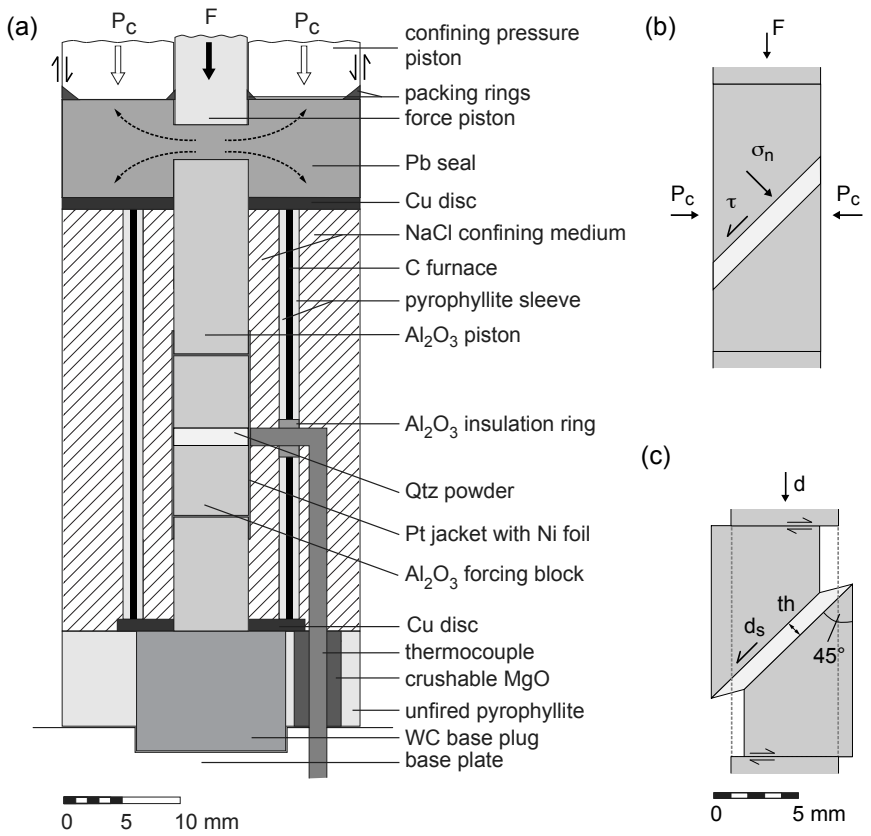

Fig. 4.2: Sample assembly. (a) Sample (quartz powder) is inserted on 45° pre-cut between forcing blocks, surrounded by the confining medium (NaCl) and a carbon furnace [modified after Pec et al., 2012a] (b) Stresses in the sample: F - load applied to upper forcing block, P_c - confining pressure (MPa), σ_n - normal stress, τ - shear stress. (c) Sample geometry: d - displacement of force piston, th - thickness of sample, ds = shear displacement parallel to sample-forcing block interfaces. Small shear couple arrows indicate sideways escape of forcing blocks.

formed under the applied P, T and loading conditions. The second step was the calculation of the stresses transmitted to the deforming sample along the 45° pre-cut.

Stresses in the forcing block: at the start of the experiment ($t = 0$), the minimum and the maximum principal stresses were both set to the value of the confining pressure measured at the hit point (A in Fig. 4.3) such that $\sigma_1(0) = \sigma_3(0) = P_c$ and $\Delta\sigma(0) = 0.00$. The maximum principal stress (σ_1) was calculated by adding the differential stress ($\Delta\sigma$) to σ_3. During the experiment, $\sigma_1(t)$ was calculated assuming a constant cross sectional area of the Al_2O_3 forcing blocks (Fig. 4.2b), and $\Delta\sigma(t)$ was calculated as the difference between $\sigma_1(t)$ and $\sigma_3(t)$. It is assumed that σ_3 is not constant but increases with time as the force piston gets pushed into the pressure vessel.

The shear and normal stresses acting on the sample (across the piston sample interface) were calculated using the Mohr circle construction. For a sample orientated at 45° with respect to the applied σ_1, the shear stress $\tau(t) = \Delta\sigma(t)/2$, and the normal stress $\sigma_n(t) = (\sigma_1(t) + \sigma_3(t))/2$. Normal and shear stresses inside the sample were calculated by balancing the normal and shear forces across the piston sample interface taking into consideration the ever decreasing area of piston overlap [Heilbronner and Tullis, 2006] and the increasing confining pressure [Heilbronner et al., 2015] resulting in a combined correction for piston overlap and confining pressure build-up.

As the principal stress (σ_1) at $t = 0$ was not determined from the 'classical' hit point but from the lower value of the new hit point (B in Fig. 4.3), the so-called friction correction (an increase of σ_1 extrapolated from the slope of the run-in curve, see Pec [2014]) was not necessary. Also, the correction proposed by Holyoke and Kronenberg [2010] was not applied, as will be discussed later.

All samples thinned during the experiments, as could be measured after deformation. For the calculation of the shear strain ($\gamma = ds/th$, see Fig. 4.2), it was assumed that thinning was continuous and linear throughout the experiment. At each point, the shear strain was obtained by summing the incremental shear strains (calculated for decreasing sample thickness) between the recorded data points.

4.2.4 Texture and microstructure analysis

To analyse the microstructure, samples were cut parallel to the displacement direction and impregnated under vacuum with epoxy to prepare doubly polished thin sections. Thin sections were analysed by means of light microscopy and scanning electron microscopy (Philips XL 30 ESEM). The acceleration voltage varied between 10 and 15 kV. Raman spectroscopy was conducted on a Bruker SENTERRA spectrometer using a 532 nm laser. For EBSD analysis, the thin sections were polished additionally with colloidal silica suspension "OP-U-non-dry" for 2 to 3 minutes. A field emission Zeiss Merlin SEM with a Nordlys nano camera was used and the samples were analysed in high vacuum. The data were acquired

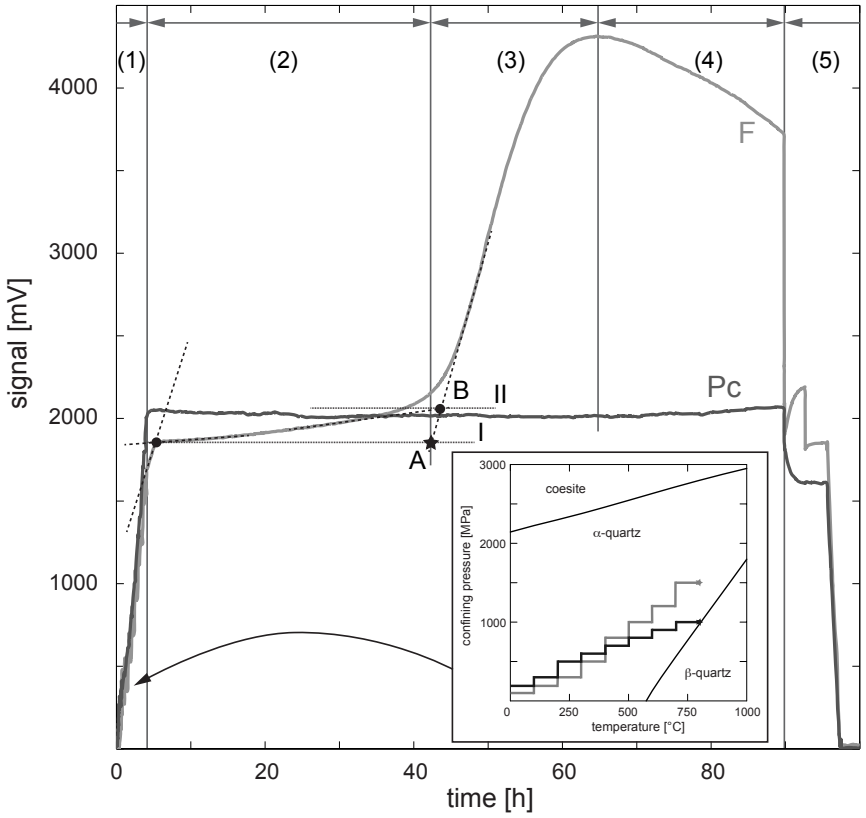

Fig. 4.3: Signal-time plot of a typical mechanical data record (452br). F - force on force piston, P_c - confining pressure measured as oil pressure applied through the hydraulic ram. Five stages are indicated: (1) pressurization (static) - attaining *PT* conditions, (2) run-in - advancing force piston through top lead piece, (3) loading of sample (4) deformation of sample, (5) quenching and subsequent slow depressurization. The inset shows a schematic *PT* path during pressurization for 800 °C at 1.0 and 1.5 GPa in a SiO_2 phase diagram (calculated with Theriak Domino based on the Berman database, 1988; tridymite not shown).

with Oxford AZtec software and processed with Channel 5 and MTEX. Grain sizes were calculated using the stripstar method [Heilbronner and Barrett, 2014].

4.3 Results

One suite of experiments was carried out at 1.5 GPa confining pressure and temperatures between 600 °C and 900 °C (Table 4.1). The shear-strain rates varied between $\sim 2.5 \cdot 10^{-5}\,s^{-1}$, $\sim 2.5 \cdot 10^{-4}\,s^{-1}$ and $\sim 2 \cdot 10^{-3}\,s^{-1}$. Additional experiments were conducted at 1.0 GPa confining pressure and temperatures of 650 °C, 700 °C and 800 °C.

4.3.1 Stresses, pressures, and the formation of coesite

All samples were loaded to peak stress conditions and some were stopped at this point. Some samples displayed steady state or weakening stress conditions with on-going deformation. Plotting the maximum principal stress (σ_1) - rather than the differential stress - against shear strain, the samples can be divided into three classes with respect to the quartz-to-coesite phase transformation (Fig. 4.4):

(1) The first class is characterized by the formation of coesite. In these experiments, σ_1 attained a level above the transformation pressure, P_{trans}, before reaching the peak stress and stayed above P_{trans} until quenching (Fig. 4.4). Some experiments were stopped at or shortly after the peak stress yielding only small amounts of coesite.

(2) In the second class, σ_1 never reached P_{trans} at any time during the entire experiment; no coesite could be detected.

(3) In the third class (one experiment), σ_1 also reached a level above P_{trans} before reaching peak stress, and coesite was formed. As a consequence of strain weakening during the subsequent deformation, σ_1 fell below P_{trans} again (Fig. 4.4a) triggering a reverse reaction of coesite to quartz.

This correlation between σ_1 and presence or absence of coesite is independent of confining pressure and shear-strain rate. Whenever σ_1 exceeded P_{trans}, coesite was found in the samples, with the sole exception of experiment 338br, which was stopped close to peak stress. In it, no coesite could be found despite σ_1 having exceeded P_{trans}, suggesting that the duration of the experiment, in other words, transformation kinetics plays an important role.

In all of our experiments the confining pressure P_c and the mean stress σ_m stayed far below P_{trans} (Fig. 4.5a and b). Data from published studies, also included in Fig. 4.5, show a few cases where $\sigma_m > P_{trans}$, due to the high values reached for σ_1 [e.g. Hirth and Tullis, 1994]. In contrast, coesite formed if σ_1 exceeded P_{trans}, with one exception (338br) at 600 °C (Fig. 4.5). If σ_1 stayed below P_{trans}, no coesite was found, even for values of σ_1 close to P_{trans}. The same correlation holds for the study by Hirth and Tullis [1994], with exceptions at low temperatures (500 °C) where no coesite was detected despite σ_1 having exceeded P_{trans}.

Tab. 4.1: Experimental conditions and results.

exp. #	T [C]	P_c [a] [MPa]	H_2O content	shear-strain rate [10^{-5} s^{-1}]	shear strain γ	max. σ_1 [b] [MPa]	max. $\Delta\sigma$ [c] [MPa]	max. σ_m [d] [MPa]	σ_1-over-stepping [MPa]	time at PT conditions [h]	deformation time [h]	time in coe field [h]	coe
338br	600	1522	0.2 µl	1.4	1.4	4042	2513	2367	1408	46.0	29.3	16.8	
479br	600	1538	0.2 µl	2.1	3.9	4005	2423	2390	1370	72.2	57.1	43.9	<0.1 %
435br[e]	650	1507	0.2 µl	2.1	3.6	4242	2698	2449	1568	76.7	48.4	38.3	3.2 %
481br[f]	650	1554	0.2 µl	3.7	4.2	4085	2538	2393	1411	46.5	33.0	26.0	<0.5 %
351br	700	1533	as-is	2.7	2.6	2817	1247	1985	105	62.8	27.8	6.7	<0.1 %
339br	700	1524	0.2 µl	2.1	2.0	2837	1298	1971	124	50.2	27.5	6.5	<0.1 %
437br	700	1529	0.2 µl	1.9	1.7	3028	1483	2039	315	32.1	26.4	11.6	<0.5 %
383br	700	1585	0.2 µl	2.8	4.9	2808	1246	1987	95	97.6	50.3	17.3	1.9 %[g]
388br	800	1527	0.2 µl	2.8	4.8	2383	858	1813	-	69.0	49.8		
494br	650	1088	0.2 µl	4.8	5.7	3547	2395	1950	913	49.8	34.7	23.9	<0.1 %
452br	700	1064	0.2 µl	2.7	4.4	2585	1535	1579	-	84.5	47.1		
448br	800	1067	0.2 µl	2.9	4.5	1918	863	1347	-	69.3	44.2		
495br	750	1612	0.2 µl	29	7.0	4098	2384	2509	1345	9.6	6.9	5.7	29.8 %
447br	800	1556	0.2 µl	27	4.1	3336	1783	2149	544	6.9	4.5	3.1	<0.5 %
499br	900	1535	0.2 µl	189	4.0	3597	2015	2255	726	1.1	0.6	0.4	<0.1 %

[a] mean confining pressure
[b] maximum principal stress $\sigma_1 = \sigma_3 + \Delta\sigma$
[c] differential stress $\Delta\sigma$
[d] mean stress $\sigma_m = 1/3 \cdot (\sigma_1 + \sigma_3 + \sigma_3)$
[e] upper alumina piston deformed
[f] stick slip at the end
[g] back reaction of coesite to quartz indicated

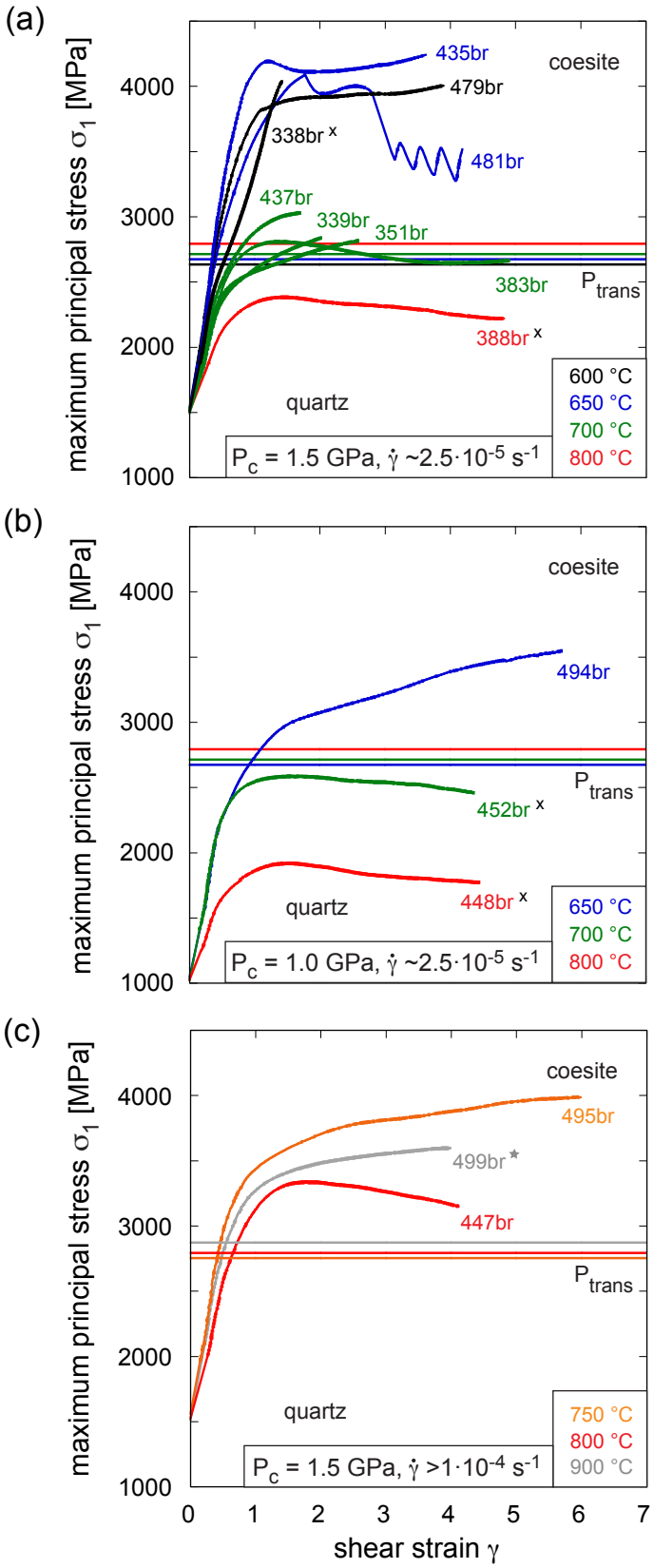

Fig. 4.4: Maximum principal stress as a function of shear strain. The transformation pressure, P_{trans}, of the quartz-to-coesite phase transformation [after Bohlen and Boettcher, 1982] is marked by a horizontal line, colour-coded for each temperature. All samples, except those marked with (x) contain coesite. (a) Samples deformed at 1.5 GPa confining pressure and shear-strain rates of $\sim 2.5 \cdot 10^{-5}$ s^{-1}. (b) Samples deformed at 1.0 GPa confining pressure and shear-strain rates of $\sim 2.5 \cdot 10^{-5}$ s^{-1}. (c) Samples deformed at 1.5 GPa confining pressure and shear strain rates of $\sim 1 \cdot 10^{-4}$ s^{-1}. The asterisk at 499br indicates an even faster strain rate of $\sim 1 \cdot 10^{-3}$ s^{-1}.

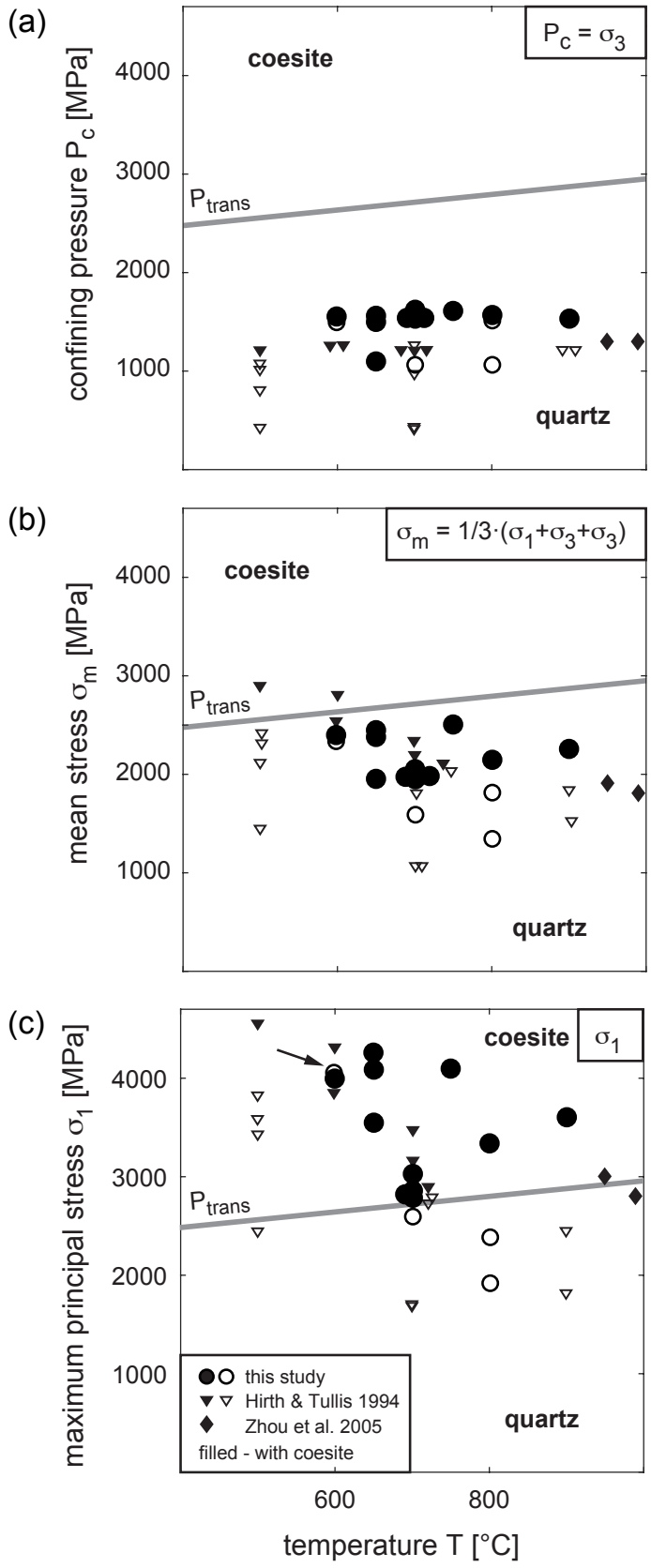

Fig. 4.5: Pressure-temperature plots for maximum stresses reached during experiments. Data from present study and published data are compiled. Filled markers indicate coesite occurrence. P_{trans} - transformation pressure after Bohlen and Boettcher [1982] (line width proportional to an error of ± 20 MPa. (a) Confining pressures ($P_c = \sigma_3$). (b) Mean stresses (σ_m). (c) Maximum principal stress (σ_1).

4.3.2 Microstructural observations of the quartz-to-coesite phase transformation

All samples start out as pure quartz powders and acquire, in the course of the experiments, typical dense quartz microstructures in response to compaction, temperature, flow stress and strain rate. Coesite forms in a small volume fraction (see Table 4.1) and it probably does not influence the microstructure development of quartz in a significant way. Rather, coesite grains seem to nucleate and grow, adjusting to the deformation of quartz as rigid particles without deforming internally. In the next paragraphs, we therefore start by describing the microstructures and textures of quartz, followed by a description of coesite as well as the interaction between coesite and quartz.

4.3.2.1 Microstructure and texture of quartz

Samples deformed at 1.5 GPa and temperatures below 700 °C are characterized by fracturing and probably frictional sliding, accompanied by dissolution-precipitation processes as well as the beginning of dynamic recrystallization. Riedel shears dominate the microstructure. At 700 °C and higher temperatures, recrystallization becomes pervasive, and viscous-deformation microstructures dominate. At low strain ($\gamma < 2$) or strain rates faster than 10^{-5} s^{-1}, shear bands develop. At high strains ($\gamma > 3$), samples are more homogeneously deformed with pervasive dynamic recrystallization (Fig. 4.6). The recrystallized grains of the sample deformed at 700 °C show a strong crystallographic preferred orientation (CPO) with one peripheral maximum of the *c*-axes subnormal to the shear plane, rotated slightly with the sense of shear (red colour-coding of Z direction) and a maximum of *a*-axes subparallel to the shearing direction (Fig. 4.6a). The CPO is consistent with dislocation creep as the dominant deformation mechanism for quartz. The typical equivalent diameters of recrystallized grains in samples deformed at 700 °C and 800 °C (measured as the mode of the 3D recalculated grain size distributions) are 2.5 µm and 5 µm, respectively. At lower temperatures or higher strain rates grains are smaller.

4.3.2.2 Microstructure and CPO of coesite

Coesite crystals can be distinguished from quartz on account of their higher birefringence in light microscopy and higher Z-contrast in SEM backscattered-electron (BSE) images (Fig. 4.7). Using Raman spectroscopy coesite is easily distinguished from quartz (Fig. 4.8) by distinct peaks, at 465 cm^{-1} (quartz) and at 522 m^{-1} (coesite). In measurements made in small grains both bands can appear. In this case, the signal is not considered as evidence for intergrowth between these two phases; rather the Raman spectrum is a mixed signal of the small coesite grain and the surrounding quartz.

An elongated tabular shape characterizes euhedral coesite crystals with the largest diameter (less than 10 µm up to a few 10's of micrometers) parallel to the *c*-axis and the shortest diameter parallel to the *b*-axis [Renner, 2001]. Coesite grains (< 20 µm largest diameter)

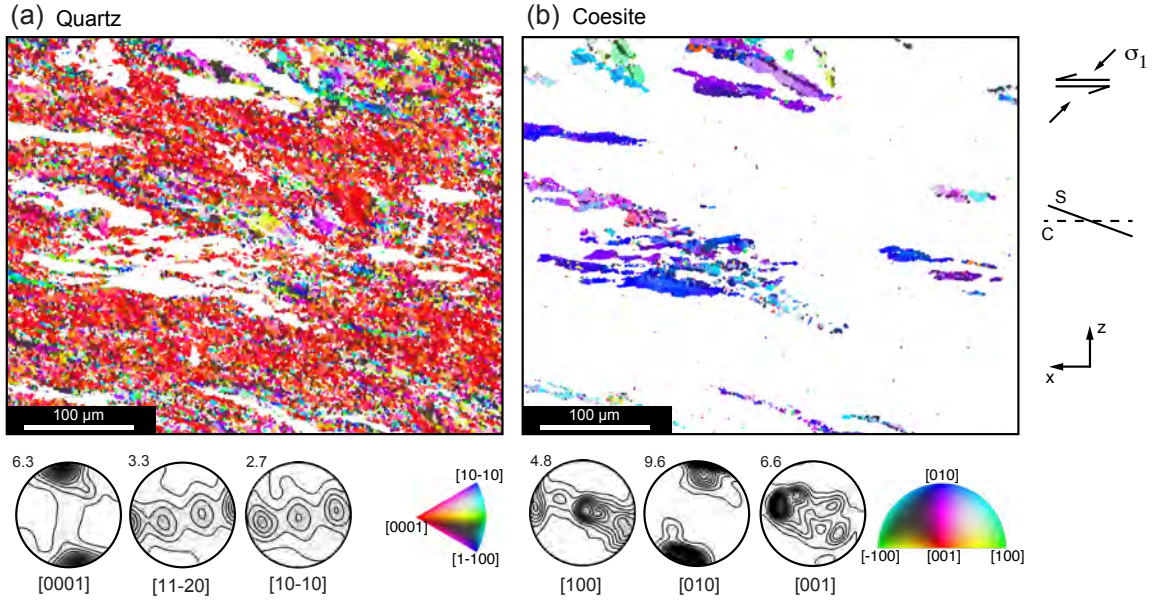

Fig. 4.6: EBSD orientation maps of quartz (a) and coesite (b). Sample 383br (step size 0.8 µm) with pole figures (maxima indicated, contour intervals 0.5 times uniform distribution), IPF colour-coding in z direction (normal to shear plane).

appear around and between quartz clasts (diameter 30 - 40 µm, see Fig.4.7c), as well as dispersed among recrystallized grains. In highly deformed samples, the coesite platelets (predominantly high aspect ratios > 2.5) are aligned at a small angle to the shear plane (Fig. 4.7a, 4.6). Occasionally, multiple coesite grains seem to grow from single nucleation sites, forming rare spherulitic structures (Fig. 4.7b). They may also grow from the surfaces of larger quartz grains (Fig. 4.7c). In 383br (700 °C, $\gamma \sim 5$), many coesite grains have partly lost their well-defined euhedral shape; instead, grain boundaries show a corroded appearance indicating the reverse transformation of coesite to quartz (Fig. 4.7e and f).

In general, coesite forms throughout the sample, most abundantly in the region where the forcing blocks overlap (Fig. 4.8). The less deformed end regions of the samples are always coesite-free. Moreover, coesite is usually absent near the 'heels' of the forcing blocks where stress concentrations are expected. In some cases, coesite may be related to local stress concentrations, for example, at contact surfaces of clasts (Fig. 4.7c).

The amount of coesite found in the samples varies considerably. Three samples (435br, 383br, 495br, Fig. 4.9) deformed at 650 °C, 700 °C and 750 °C, respectively, show a distinct pattern. At 650 °C, coesite crystals nucleate with random orientations at random sites within the quartz matrix as small volume fractions, often much less than 1 vol% (Table 4.1). At 700 °C and with increasing shear deformation, the coesite platelets are rotated as rigid particles towards the shear plane in the dynamically recrystallizing quartz matrix. Volume fractions of 2-3 vol% coesite are attained. Finally, at 750 °C, the volume fraction of coesite crystals keeps increasing (up to ~30 vol%) defining a wavy foliation (Fig. 4.7a).

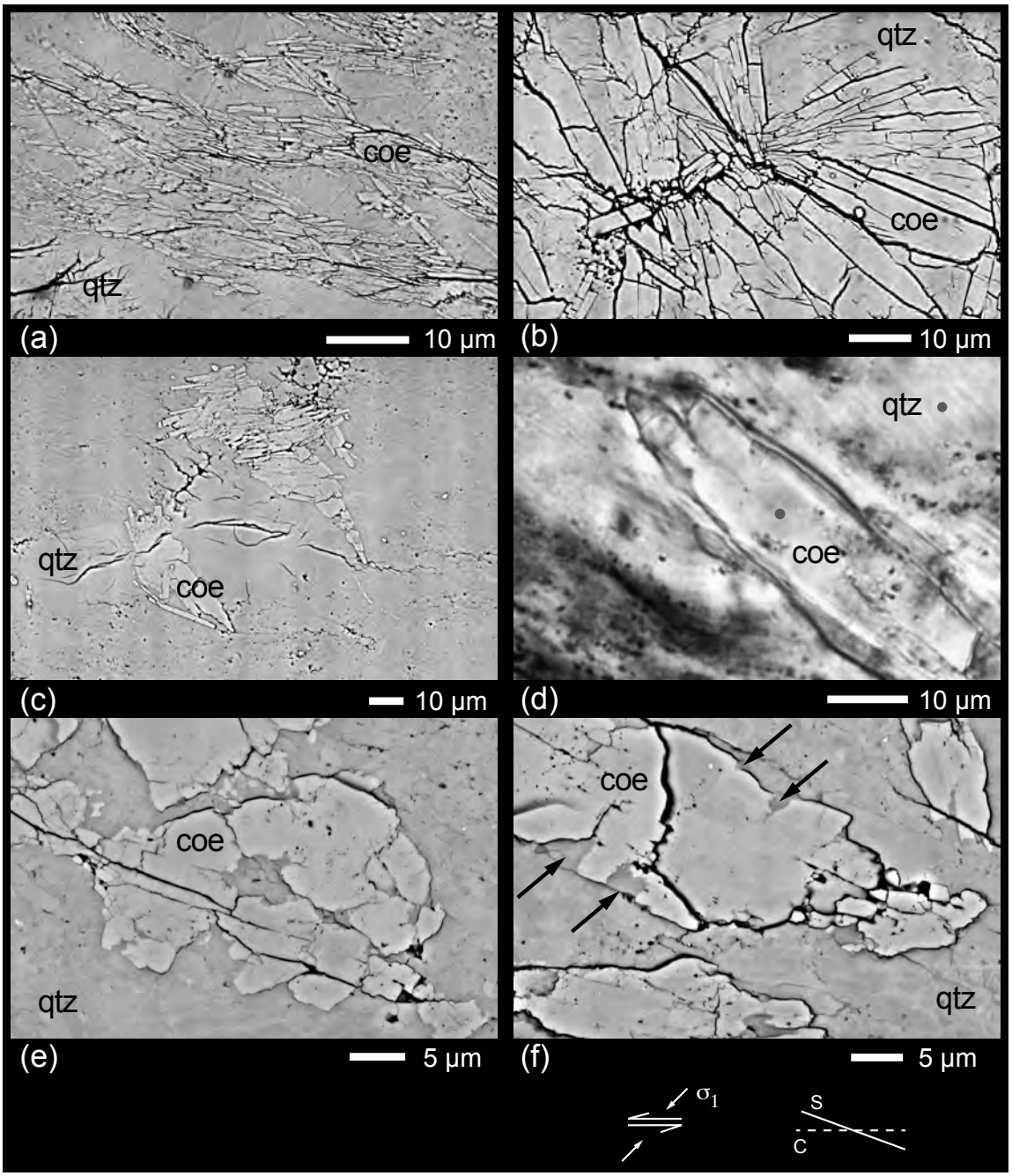

Fig. 4.7: Coesite in deformed samples. (a) Alignment of coesite grains (495br, SEM/BSE). (b) Radial aggregate of coesite grains (435br, SEM/BSE). (c) Coesite grains nucleated along surface of quartz clasts (447br, SEM/BSE). (d) Single coesite grain embedded in quartz (383br, reflected light) with measurement points for Raman spectra (Fig. 4.8). (e) Coesite grain with corroded appearance (383br, SEM/BSE). (f) Same as (e) with arrows pointing to locations of the reverse coesite-to-quartz transformation.

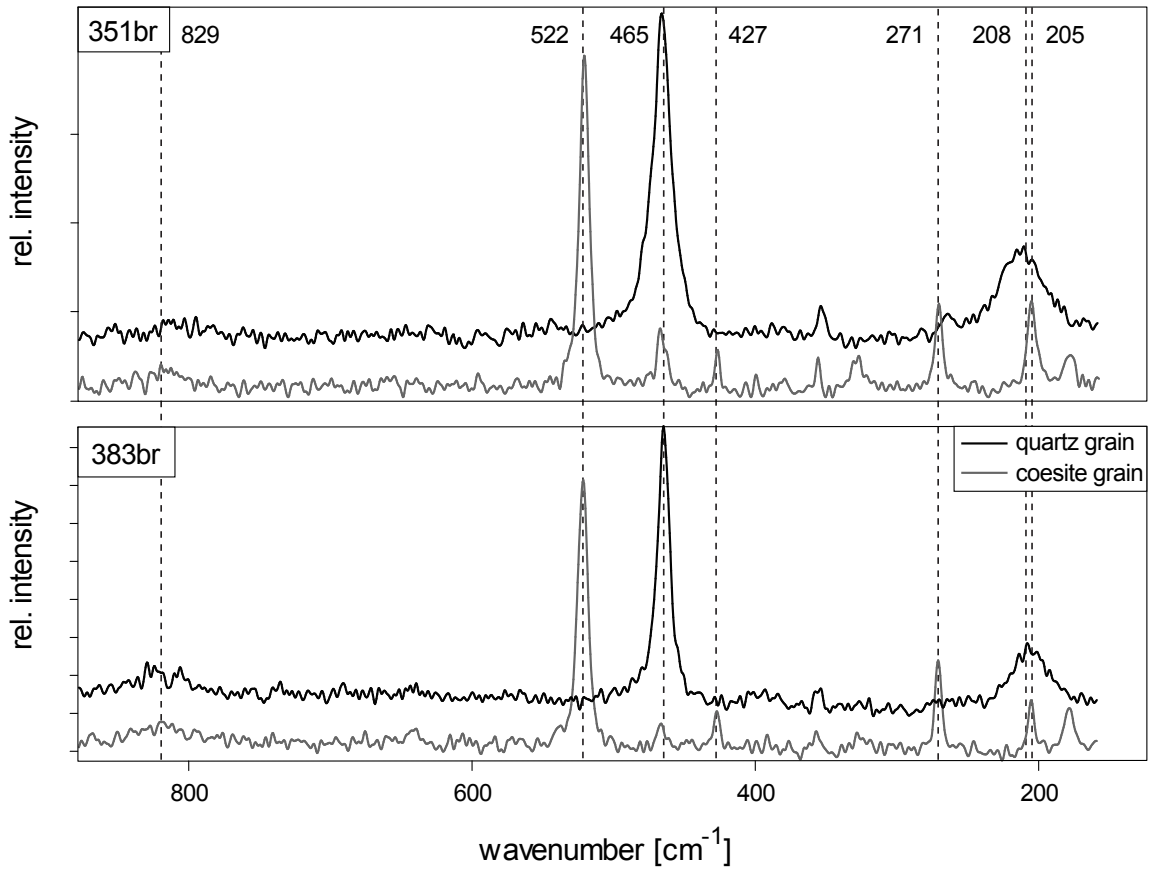

Fig. 4.8: Raman spectra of quartz and coesite grains from two different samples. The small peak at 465 nm in the spectrum of the coesite grain of sample 351br is a background signal of the surrounding or underlying quartz. For wavelengths below 200 cm^{-1} the mineral spectra are superposed by epoxy in the thin section and therefore neglected. Spots of Raman measurements of sample 383br are marked in Fig. 4.7d.

At high strain ($\gamma > 3$) and 700 °C, coesite shows a strong CPO with a strong alignment of the 010 planes subparallel to the shear plane and the 100 planes subnormal to the shear plane (Fig. 4.6b). The coesite grains do not display any dynamic recrystallization or bending of crystals (intra-crystalline plasticity), so that the CPO is interpreted to be the consequence of the shape anisotropy and rotation of rigid tabular coesite grains towards the shear plane in the weaker quartz matrix.

Earlier studies indicate a growth relationship between coesite and quartz ([130] || [10-11], Zinn, 1996). This correlation could not be observed, neither for the growth of coesite on quartz nor for the reverse reaction. Furthermore, no clear growth direction of quartz on coesite was found

4.3.2.3 Transformation kinetics

A suite of experiments (339br, 351br, 383br, 437br) performed at intermediate temperature of 700 °C, 1.5 GPa, 10^{-5} s^{-1} and different amounts of finite strains ($2.0 < \gamma < 4.9$) shows that the longer the duration at the condition where $\sigma_1 > P_{trans}$ the more coesite forms (Fig. 4.10). Samples 339br and 351br yield the same amount of coesite after 6.5 h and 6.7 h (< 0.1 vol%) demonstrating good reproducibility. Sample 437br yields ~0.5 vol% after 11.6 h, and sample 383br yields ~1.9 vol% after 17.3 h. Note that 383br also shows microstructures of the reverse reaction of coesite to quartz, hence the amount of coesite originally formed may have been slightly higher.

The lower the temperature, the more time is needed to obtain a given coesite fraction. For example, in sample 479br, deformed at 600 °C and 43.9 h at $\sigma_1 > P_{trans}$, only a few coesite grains (< 0.1 vol%) form. In contrast, sample 435br, deformed at 650 °C with 38.3 h at the same σ_1-overstepping and deformed at the same strain rate yields more than an order of magnitude more coesite (3.2 vol%; Fig. 4.10, Table 4.1).

The degree of σ_1-overstepping needs to be considered, too. High σ_1-overstepping during an experiment (~1350 to 1600 MPa, in 435br, 481br, 479br, 338br, 495br) does not yield systematically higher amounts of coesite compared to lower σ_1-overstepping values (< 500 MPa in 383br, 437br, 447br) - temperature and strain rate are more important factors (Fig. 4.10, Table 4.1).

Despite the fact that the stress difference between σ_1 and P_{trans} and the time in the respective stability field was the same, the amount of quartz produced during the back transformation was very small. The precise amount could not be determined because we did not find a reliable criterion (textural or microstructural) that could help us distinguish between the back reacted and the original quartz in every case.

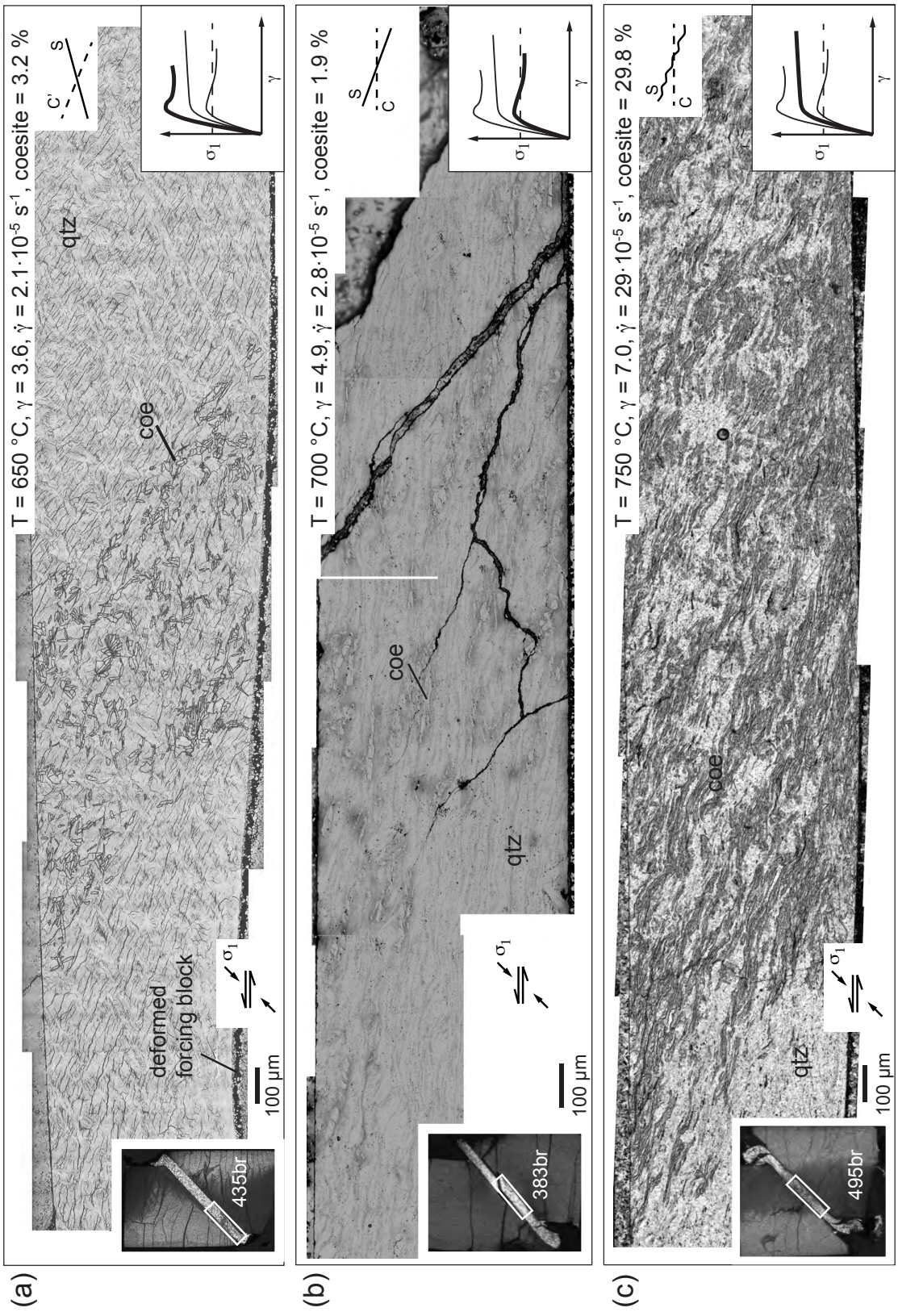

Fig. 4.9: Distribution of coesite in samples after deformation. (a) Sample 435br (SEM/BSE image). Note deformed forcing block at left. (b) Sample 383br (reflected light with polariser). (c) Sample 495br (transmitted light).

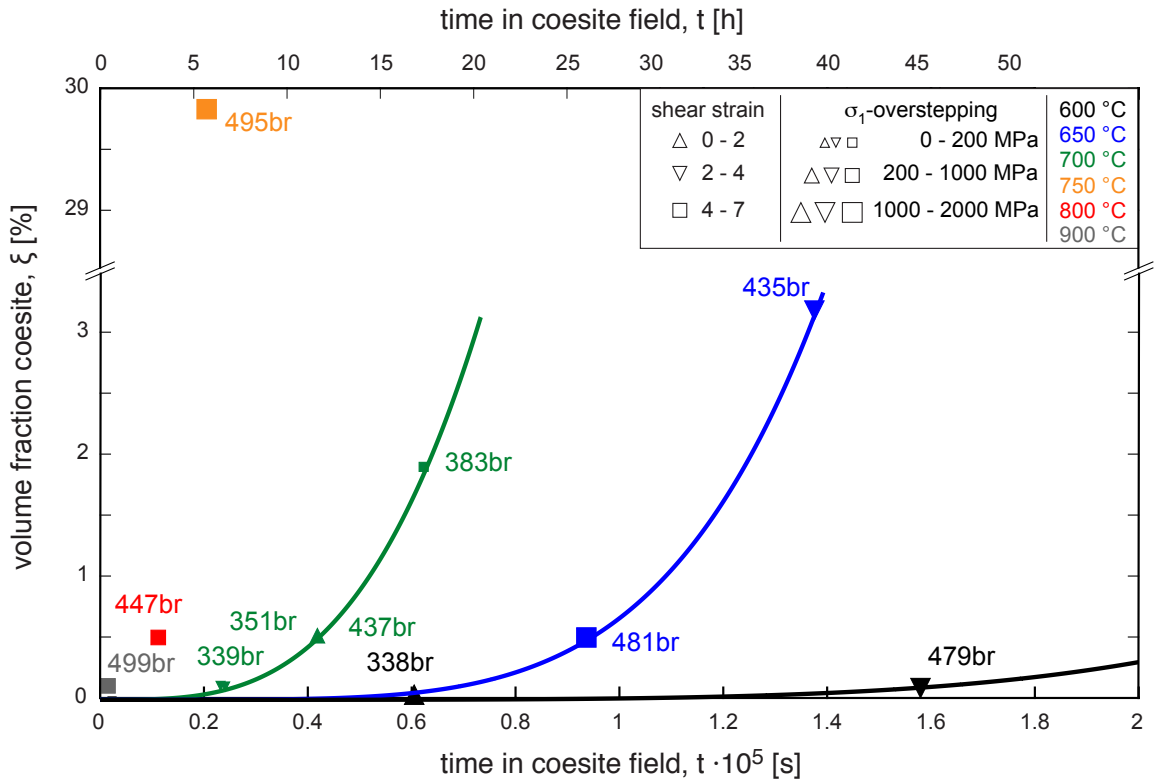

Fig. 4.10: Avrami plot for coesite at 1.5 GPa confining pressure. Temperature is colour-coded, symbols denote amount of shear strain, size of symbols denotes amount of σ_1-overstepping. Avrami equation is fitted to data at 700 °C ($n = 3.3$ and $k = 4.8 \cdot 10^{-6}$), 650 °C ($n = 4.9$ and $k = 3.6 \cdot 10^{-6}$) and 600 °C ($n = 4.8$ and $k = 1.5 \cdot 10^{-6}$).

4.4 Discussion

The following discussion focuses on microstructural characteristics of the quartz-to-coesite phase transformation at non-hydrostatic stresses and the kinetics of this transformation. In addition, metastable formation and geological implications will be discussed.

4.4.1 Maximum principal stress as critical parameter for the quartz-to-coesite phase transformation

All coesite-bearing samples of our experiments were subjected to σ_1 higher than P_{trans} derived from nominally hydrostatic experiments (Figs. 4.4, 4.5). Samples without coesite were subjected to σ_1 below P_{trans}. At 700°C and $\gamma \sim 5$, the transformation from coesite back to quartz is observed. It is assumed that the back-reaction starts when σ_1 decreases with progressive deformation and falls below P_{trans} (Fig. 4.4a, sample no. 383br). The mean stress, σ_m, in samples containing coesite remains below P_{trans} (Fig. 4.5b), even if the transformation pressures of Bohlen and Boettcher [1982] are used, the lowest value of all experimentally determined pressures (Fig. 4.1). The σ_m realized in our experiments cannot explain the coesite occurrence, because in most experiments, σ_m remains up to several

hundreds of MPa below P_{trans}. Thus, using the mean stress concept as the representative for P_{trans} fails and it is implied that $\sigma_1 > P_{trans}$ is a sufficient condition for coesite formation.

The data set by Hirth and Tullis [1994] shows similar results like ours. All coesite-bearing samples experienced σ_1 higher than P_{trans} but the mean stress of two coesite-bearing experiments by Hirth and Tullis [1994] reached P_{trans} for the given temperature (Fig. 4.5b). Three samples deformed at 500 °C had σ_1 values higher than P_{trans}, but no coesite was found (Fig. 4.5c), which is most likely related to sluggish transformation kinetics at low temperatures. The study by Zhou et al. [2005] contains two coesite-bearing experiments where σ_1-values are close to P_{trans}. One experiment reached the coesite stability field and the other one is in the quartz stability field, but in both of them coesite formed.

4.4.2 Metastable formation of coesite?

The σ_1-values in most samples of Green [1972] and one described in detail by Hobbs [1968] have remained below the P_{trans} of the quartz-to-coesite transformation, and only one of the two described samples of Zhou et al. [2005] has reached the P_{trans} without exceeding it (Fig. 4.5). These situations are different from the ones described by Hirth and Tullis [1994] and those of this study, in which σ_1 has been well above P_{trans} in all coesite-containing samples. Therefore, it is unlikely that in our samples coesite forms as a metastable phase as it is concluded by Hobbs [1968], Green [1972] and Zhou et al. [2005] for their experiments.

Furthermore, during deformation of all of our samples, a large part of the quartz recrystallizes dynamically. If coesite did form as a metastable phase, such coesite is expected to decompose (back-transform) during continuing reconstitution (recrystallization) of the material. However, the back-transformation of quartz to coesite is only observed in the sample, in which σ_1 values decrease below P_{trans}. In addition, we do not observe a systematic effect of the confining pressure on coesite formation as inferred by Zhou et al. [2005]. Coesite occurs if the σ_1 values are higher than P_{trans}, at 1.0 GPa or 1.5 GPa confining pressure, P_c (i.e. σ_3) (see Fig. 4.4a and 4.4b).

An extreme approach for the phase transformation in conjunction with deformation has been taken by Su et al. [2006], who ball-milled their quartz samples before subjecting them to high pressure and temperature. Similar to Kingma et al. [1993], they observed the formation of an amorphous phase during ball-milling, and during subsequent high-pressure treatment coesite grew after extremely short times (less than one minute). Their results appear to be similar to those of Green [1972], who explained the formation of coesite below the transformation pressure as the result of metastable crystallization from partly amorphous material according to the Ostwald step rule. This rule implies that a metastable phase (coesite) nucleates and grows more efficiently than a stable phase (quartz) because the activation energy for the formation of the metastable phase with respect to the original material (partly amorphous SiO_2) is smaller than the activation energy for the stable phase [Green, 1972]. The experiments of Green et al. [1970] and Green [1972] have been carried out using flint.

Flint contains large amounts of amorphous silica, so that the Ostwald step rule applies to the formation of a crystalline phase from amorphous material. Our starting material consists of fully crystalline quartz; and no signs of amorphous material, produced during loading or deformation, have been observed. Furthermore, Pec et al. [2012b] produced (partly) amorphous material in experimentally deformed granitoid rocks where the quartz remained always crystalline and the amorphous domains were depleted in SiO_2 relative to the starting material. Hence, amorphisation of quartz has never been observed. Given the reasons above, in our study, which considers the direct phase transformation from quartz to coesite, it is very unlikely that coesite should have formed as a metastable phase.

4.4.3 Effect of potential stress raisers

Only bulk measurements of force can be made with our experimental equipment and the stress states considered above refer to the entire sample. As the quartz powder is a polycrystalline material the stress state of individual grains is expected to be heterogeneous and will depend on the neighborhood relationships, elastic anisotropy, grain boundary orientations, etc. The analysis of the stress state of individual grains requires special equipment (see e.g. Bystricky et al. [2015] - not commonly employed for hydrostatic and deformation experiments). The stress state of a grain boundary depends on the orientation of that boundary with respect to the acting forces. Therefore, the normal stress acting on a grain boundary was introduced as a scalar term by Gibbs [1906]. This approach was further developed by using the chemical potential to describe the stress state at grain boundaries [e.g. Robin, 1978] in the theory of pressure solution: For stress states with σ_1 above and σ_3 below the equilibrium pressure of the phase transformation, the high-pressure phase is expected to grow in the compression direction and react back to the low-pressure phase on the extensional side of the grains [Shimizu, 1992]. We do not observe a specific growth direction of coesite with respect to σ_1, probably because the more rigid character of coesite grains with respect to quartz causes an alignment of the coesite grains at a small angle to the shear plane during subsequent deformation stages (see Fig. 4.6b, 4.7a, 4.9b and 4.9c), so that the overall preferred orientation of coesite and, locally, its orientation with respect to the neighboring quartz is the result of this alignment rather than the original stress state.

Stress concentrations have to be expected in a polycrystalline material, especially when deforming in the brittle field. But in most samples we observe coesite distributed throughout the shear zone and not only in specific locations. Moreover, if stress raisers did occur, they should only persist for short time spans in a continuously deforming sample. If the stress concentration provided a stress high enough to nucleate coesite, the stress would decrease instantaneously and coesite could not grow any further, because it is in a metastable state. Instead, the observed coesite of our samples indicates continued growth, and metastable growth has been excluded above. In samples that are dominated by brittle deformation processes (e.g. at low deformation temperatures, high strain rates) it is possible that stress raisers

could persist. However, viscous deformation processes and extensive recrystallization (e.g. at high deformation temperatures) as occurred in our experiments make stress raisers an unlikely candidate for stable coesite formation.

4.4.4 Stress estimates from recorded force data

The force-displacement record of each experiment is converted to a stress-strain plot using the new combined correction for confining pressure and piston overlap. Both are a function of the advancement of the force piston, and thus of the increasing shear strain. We did not use the stress correction proposed by Holyoke and Kronenberg [2010] because it was determined for coaxial experiments under low confining pressures (≤ 0.4 GPa), while the experiments discussed here were performed under shearing conditions on quartz at high confining pressures (up to 1.5 GPa). Furthermore, the stresses published by Hirth and Tullis [1994] and Zhou et al. [2005], to which we compare our results (Fig. 4.5), do not include this correction. Note that if the correction proposed by Holyoke and Kronenberg [2010] were used, the calculated maximum stresses of most of the coesite producing experiments shown in Fig. 4.5 would not reach the coesite stability field.

In addition, sample 452br (700 °C, 1.0 GPa confining pressure, $\gamma \sim 4.4$) remains below P_{trans} ($\sim$130 MPa) and does not contain any coesite while 383br (700 °C, 1.5 GPa confining pressure, $\gamma \sim 4.9$) exceeds P_{trans} by $\sim$100 MPa and contains coesite. If the correction by Holyoke and Kronenberg [2010] would be applied, both samples would not reach P_{trans} and the absence or presence of coesite at these similar conditions (same temperature, similar shear strain and shear-strain rate, difference in $\sigma_{1,max} < 230$ MPa) could not be explained.

4.4.5 Kinetics of the quartz-to-coesite transformation

Our experiments were not originally intended for systematic kinetic studies of the quartz-to-coesite transformation, and systematic overstepping criteria are lacking. They were carried out with the aim of finding steady state flow stresses for quartz. Yet, we can analyse semi-quantitatively the transformation progress (expressed by the amount of coesite produced) that varies considerably with pressure overstepping, temperature, and strain [Rubie and Thompson, 1985], and fit an Avrami-type curve ($\xi = 1 - exp(-(k \cdot t)^n$ with ξ [%] - volume fraction) to the amount of coesite formed (as vol%) against time spent in the coesite stability field (in s), (Fig. 4.10). For $T = 700$ °C our curve fit yields $n = 3.3$ and $k = 4.8 \cdot 10^{-6}$; for $T = 650$ °C the curve yields $n = 4.9$ and $k = 3.6 \cdot 10^{-6}$; and for $T = 600$ °C the curve yields $n = 4.8$ and $k = 1.5 \cdot 10^{-6}$. The increase of k with increasing temperature illustrates the temperature dependence of nucleation and growth rate, which are included in the k-value [Porter and Easterling, 1992]. At 700 °C, n is between 3 and 4, indicating the dominance of the nucleation rate. The high n-values ($n > 4$) for lower temperatures can suggest an inhomogeneous distribution of nuclei or very high nucleation rates [Sun et al., 1996]. However,

n-values above 4 correlate with high overpressure (> 1 GPa at 600 °C and 650 °C), see Table 4.1). Unfortunately, low volume fractions of coesite at 600 °C make it difficult to fit the data.

For 700 °C, 14.6 h are needed for the growth of 1 vol% coesite. In contrast after less than one second 1 vol% coesite has grown in Perrillat et al. [2003] experiments, which is faster than in our experiments. Perrillat et al. [2003] calculated n-values below 1 ($n = 0.73 \pm 0.1$ for 700 °C) indicating diffusion as controlling factor. The k-values ($k = 2.3 \pm 0.5 \cdot 10^{-3}$ for 700 °C) are higher by three orders of magnitude compared to our k-values illustrating the earlier onset of the transformation. The H_2O content in our experiments is approximately one to two orders of magnitude higher than those of Perrillat et al. [2003]. A catalytic effect of H_2O on reaction kinetics is generally assumed, although its physical nature is not well understood. However, it should be noted that there are several parameters (e.g. grain size) that vary between our study and Perrillat et al. [2003]. The most important difference is the fact that we deformed our samples and therefore, only σ_1 but not σ_m exceeds P_{trans} (i.e. in the coesite stability field). In contrast, static kinetic studies [e.g. Perrillat et al., 2003] have applied a constant pressure overstepping of σ_m.

The observations of different duration and extents of σ_1-overstepping, different finite strains, and different ξ-values in samples deformed at 700 °C (Figs. 4.4, 4.10) suggest that deformation and time spent in the coesite stability field have a greater kinetic effect on the transformation than the σ_1-overstepping alone. Furthermore, the back-reaction has occurred to a small extent in 383br (Fig. 4.7) even though the time is equal to the time in the coesite stability field, supporting the conclusion by Perrillat et al. [2003] that the coesite-to-quartz transformation is slower than the quartz-to-coesite one.

The slow reaction rates at low temperatures (≤ 600 °C) appear to be the reason why coesite is not present in our sample 338br, although σ_1 exceeded P_{trans} by ~1400 MPa during ~17 h. In sample 479br (same temperature, confining pressure, σ_1-overstepping, and strain rate), which was in the coesite field for ~44 h, coesite is present (Fig. 4.10), probably because the reaction rate is not fast enough at low temperatures of 600 °C to form coesite at duration shorter than ~30-40 h. At 600 °C and 650 °C, σ_1-overstepping is similar (Fig. 4.4), but the volume fraction of coesite is considerably higher after shorter duration (Fig.4.10). Probably the absence of coesite in the samples of Hirth and Tullis [1994], deformed at 500 °C with high σ_1-overstepping values (Fig. 4.5c), can be explained by the same kinetic barrier of low-temperature.

In deformation experiments it is difficult to separate the quantitative contribution of individual factors to kinetics, such as temperature, strain rate, duration, and σ_1- or P_{trans}-overstepping. It has been inferred for solid-solid metamorphic reactions between plagioclase and olivine that deformation may increase the reaction kinetics by approximately one order of magnitude [de Ronde and Stünitz, 2007]. As a consequence, it can be concluded that, in addition to temperature and pressure overstepping, deformation adds a third variable to the kinetics of the phase transformation.

The term 'deformation' refers to the process and includes the effect of finite strain and strain rate. For example, samples deformed at high strain rates (Fig. 4.4c) show the fastest reaction kinetics, i.e. the highest reaction rates of our samples in the Avrami plot (Fig. 4.10, Table 4.1). The deformation process will increase the Gibbs free energy (G) of the deforming phases, providing a driving potential for the transformation similar to overstepping [Stünitz, 1998; de Ronde and Stünitz, 2007]. It probably is not the dislocation density alone, which provides the additional ΔG, because the dislocation density is proportional to the differential stress [Kohlstedt, 2007], and the differential stress in the high strain rate samples (495br, 499br, 447br) has been similar to or lower than that of the lower strain rate samples (479br, 481br, 338br), which show slower reaction kinetics (Fig. 4.10, Table 4.1). As the kinetics is strain-rate dependent, it may be the energy dissipation rate during deformation [Austin and Evans, 2007], which plays an important role for the driving potential in reaction kinetics.

4.4.6 Geological implication

The growth of coesite in these experiments illustrates that the high-pressure phase can nucleate and grow if σ_1 reaches values above P_{trans}, even if σ_3 or σ_m are below this pressure. Under low differential stresses, where the difference between σ_1 and σ_m is small, it is difficult to identify whether σ_1, σ_3, or σ_m is responsible for the phase transformation. Our results support the view expressed in the literature [e.g. Schmalholz and Podladchikov, 2014] that the presence of high-pressure phases in deformed rocks is not necessarily an indicator for high lithostatic pressure. Numerical models indicate the possibility of high differential stresses in parts of the lithosphere [Schmalholz and Podladchikov, 2013, Reuber et al., 2016]. The critical question is: how high can differential stresses be in nature?

Typically, flow laws for wet quartz [Paterson, 1990, Hirth et al., 2001] indicate 'normal' geological strain rates of 10^{-12} to 10^{-14} s^{-1} for differential stresses of 10's to 100's of MPa, so that these are typical estimates for natural conditions (e.g.Wheeler, 2014 and references therein). Values of 300 ± 100 MPa have been independently determined for quartz, jadeite, and calcite at 300 - 350 °C in Küster and Stöckhert [1999], and 50 - 100 MPa for dry quartz at ~800 °C in Menegon et al. [2011]. In general, high σ_1-values are expected to occur in mechanically strong lithologies. Dry quartz has been proposed as an example for strong lithologies [e.g, FitzGerald et al., 2006, Menegon et al., 2011]. Therefore, dry quartz and a strong lithology at higher temperatures may be candidates for the occurrence of elevated differential stresses and thus phase transformation with σ_1 above P_{trans} and σ_m below P_{trans}.

Stress data are often 'bulk' measurements on the km-scale. But there is evidence for local variations in the stress state (e.g. creeping fault segments; Rowe and Griffith, 2015) if stresses localize over several decimeters to meters producing temporary stress raisers. In addition, the introduction of mechanically strong heterogenities in numerical models [Reuber et al., 2016] produces local high-stress regions in subduction zones, so that apparently, high σ_1 could be temporarily realized on a local scale. It should be noted that the stress raiser

at the grain scale are transient in space and time. The mesoscopic stress raisers, mentioned above, could possibly be more persistent. Consequently, under high σ_1 new phases could grow, which normally are associated with higher depth. Therefore, depth estimates made from high-pressure phases in such situations could overestimate the actual depth.

Coesite is predominantly found as inclusions in mechanically strong phases, e.g. garnet, where the back reaction of coesite-to-quartz is suppressed [e.g. Chopin, 1984, Chopin, 2003; Tajčmanová et al., 2015]. One of the main reasons given for the preservation is that the strong minerals may act as a 'pressure vessel' and thus maintain a high pressure for the coesite [e.g. Moulas et al., 2013]. This study demonstrates that deformation enhances the reaction kinetics so that the back-transformation of coesite to quartz is very likely to occur in a deforming matrix. So, the back reaction to quartz may be likely - as in the case of a slowly deforming matrix (deformation active over a long time) - or impossible - as in the case where coesite may remain locked inside a non-deforming mineral.

4.5 Conclusions

(1) In shear experiments, quartz can transform to coesite as soon as the maximum principal stress (σ_1) exceeds the (temperature-dependent) pressure for transformation (P_{trans}) determined from hydrostatic experiments. The reverse transformation of coesite to quartz is triggered only when σ_1 drops below P_{trans} during strain weakening deformation. The formation of (stable) coesite can take place, even when P_c and σ_m are below P_{trans}; the formation of metastable coesite is excluded in our experiments.

(2) The positive effect of the deformation process, namely strain and strain rate, on the kinetics of the phase transformation can be separated qualitatively from the effects of temperature, time and σ_1-overstepping. Enhancing effects of temperature, time, and σ_1-overstepping on kinetics are confirmed, too.

(3) High maximum principal stresses (σ_1) associated with high differential stresses may induce phase transformations, such as quartz to coesite, at a shallower depth than equating lithostatic pressure and transformation pressure determined from isostatic experiments.

5 | Interplay of deformation mechanisms in experimentally deformed quartz gouge

Abstract

Shear experiments on quartz gouge were performed at elevated confining pressures (predominantly 1.5 GPa) and temperatures (500 °C - 1000 °C) at intermediate to fast shear-strain rates ($3.5 \cdot 10^{-6}$ s^{-1} to $2 \cdot 10^{-3}$ s^{-1}) to study the semi-brittle-to-viscous transition. Ambiguous temperature dependence at low temperatures changes into a pronounced inverse temperature dependence above 650 °C. The transition from positive to negative pressure dependence takes place continuously between 650 °C and 800 °C. Strain rate stepping experiments reveal power law breakdown at low temperatures ($\sim$650 °C). At high temperatures (800 °C - 1000 °C), a stress exponent of $n = 1.9 \pm 0.7$ and an activation energy of $Q = 170 \pm 72$ kJ/mol indicate a combination of diffusion creep and dislocation creep. Localised deformation in Riedel shear orientation at low temperatures merges into homogeneous deformation with pervasive foliation accompanied by a continuous texture evolution between 600 °C and 1000 °C. Fracturing dominates at low temperatures accompanied by increasing amounts of dissolution-precipitation in fine-grained zones with increasing temperature. Above 650 °C, dislocation creep is the dominating deformation mechanism favouring larger grains while dissolution-precipitation is still active in the fine-grained fraction.

5.1 Introduction

The transition from fully brittle to fully viscous deformation occurs over a broad range of conditions in pressure, temperature, strain rate, and water content with several changes in deformation mechanisms [e.g. Kohlstedt et al., 1995; Scholz, 2007; Hirth and Tullis, 1994]. This transition commonly takes place within the middle crust [Schmocker et al., 2003; Sibson, 1989] but it may extend into the upper mantle for some rocks. It is characterised by reaching the maximum strength of rocks, and many earthquakes nucleate in this zone [Pec et al., 2016].

Under brittle conditions (e.g. low crustal levels), the strength of rocks depends strongly on normal stress and pore pressure [Byerlee, 1978]. Friction controls the rock deformation and cataclastic processes (e.g. fracturing, frictional sliding) characterise the microstructure. The degradation of the relationship between shear stress and normal stress (Byerlees rule) marks the onset of semi-brittle deformation [e.g. Kohlstedt et al., 1995]. In contrast, the Goetze criterion ($\Delta\sigma = P_c$) indicates the transition from semi-brittle to viscous deformation [e.g. Kohlstedt et al., 1995]. Viscous deformation (e.g. deep crustal levels) depends on strain rates that are linked to dislocation density and velocity [Orowan, 1940]. Recovery processes like dynamic recrystallisation accompanies deformation mechanisms (e.g. dislocation creep) lowering the flow stress.

In the transitional semi-brittle zone, stress required to create new fractures is lower than stress for sliding on pre-existing faults [e.g. Kohlstedt et al., 1995], causing pervasive fracturing and grain size reduction. Crack propagation is inhibited while more dislocations are generated. But the mobility of dislocations and the generated strain are limited. Grain size reduction may play an important role for the onset of viscous deformation by increasing the surface leading to accelerated mass-transfer processes [e.g. Pec et al., 2012a; Trepmann and Stöckhert, 2003; Menegon et al., 2008; van Daalen et al., 1999]. At the same time, tangled dislocations due to increasing dislocation densities produce strain hardening leading to high stresses [e.g. Barber et al., 2010]. Towards viscous deformation, dislocation climb and recrystallisation are more pronounced due to higher temperatures and increased dislocation velocity.

Quartz as one of the most abundant silicates in the Earth's crust is often used to model the behaviour of the continental crust in experiments. In addition, deformation mechanisms in quartz can be studied independently of chemical variations due to its simple chemistry. Laboratory conditions (e.g. high strain rates: $10^{-3}\,s^{-1}$ - $10^{-7}\,s^{-1}$, high temperatures) of viscous deformation can be extrapolated to natural conditions (e.g. low strain rates: $10^{-10}\,s^{-1}$ - $10^{-14}\,s^{-1}$, low temperatures) via flow laws [e.g. Kronenberg and Tullis, 1984; Paterson, 1989; Hirth et al., 2001; Stipp et al., 2002; Rutter and Brodie, 2004]. Unfortunately, there is a large spread in determined stress exponents and activation energies for e.g. dislocation

creep in deformation experiments [e.g. Gleason and Tullis, 1995; Luan and Paterson, 1992; Kronenberg and Tullis, 1984; Jaoul et al., 1984].

We present a series of deformation experiments on quartz gouge in a modified Griggs apparatus that simulate the rheological behaviour of reactivated fault rock gouge at elevated pressure and temperature. A large grain size range (< 100 µm) promotes the early onset of diffusion processes at semi-brittle condition. Subsequent dislocation creep is accompanied by diffusion processes over a broad range of pressure and temperature conditions influencing stress exponents and activation energies.

5.2 Methods

5.2.1 Experimental method

The experiments were carried out on a crushed quartz single crystal in a Griggs-type solid medium deformation apparatus (Fig. 5.1). The gouge derives from a hydrothermally grown single crystal originating from an alpine cleft (Aar Massif, Switzerland). Parts of the crystal were broken into small fragments, repeatedly pestled and screened. A grain size fraction below 100 µm was used for the experiments except for one sample that uses a grain size fraction of 7-11 µm. The single crystal contained several fluid inclusions (5-200 µm) that incorporate most of the water [Tarantola et al., 2010]. The quartz itself was almost dry and the water amount was close to the detection limit of FTIR measurements [Thust, 2014]. Parts of the crystal with fewer inclusions were used and most of these inclusions, especially large ones, cracked during the crushing procedure.

Quartz powder (0.1 g) with 0.2 wt% water added was introduced in 45° pre-cut alumina (Al_2O_3) forcing blocks forming a $\sim$ 1 mm thick zone. The assembly was weld-sealed in a platinum jacket with a nickel foil insert. Sodium chloride was used as confining medium because of its stability over the wide range of the experimental conditions. The temperature was controlled by S-type (Pt/Pt-Rh) or K-type (Cr-Al) thermocouples. More details on the sample assembly can be found in Pec [2014]. Samples were pressurised to confining pressure while the temperature was continuously increased in 100 °C steps (20 °C per minute) to experimental conditions. The deformation experiment started by applying a directional compressive force on the sample by moving the σ_1 piston [Richter et al., 2016]. Due to the experimental set up, the σ_1 piston had to push through a lead piece (so-called run-in) before it got in contact with the alumina piston on top of the sample. At this point deformation of the sample started. The experiment was stopped by quenching the sample to 200 °C within 2 or 3 minutes (cooling rates between 150 °C and 300 °C per minute). Four experiments included a hot pressing stage prior to deformation. Therefore, temperature was set to 1000 °C. At these hydrostatic conditions (1.5 - 1.6 GPa confining pressure) the sample was left for 20 hours before decreasing the temperature to deformation conditions (2.5 °C per minute).

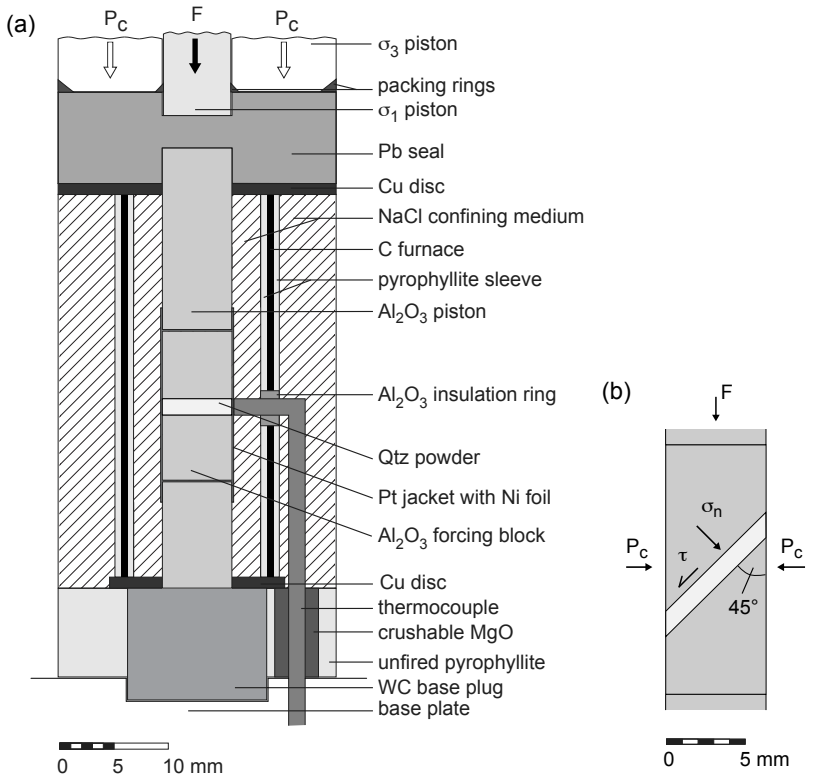

Fig. 5.1: Sample assembly. (a) Sample material is inserted on 45° pre-cut between forcing blocks, surrounded by confining medium (NaCl) and a carbon furnace [after Richter et al., 2016] (b) Stresses in the sample: F - load applied to upper forcing block, P_c - confining pressure (MPa), σ_N - normal stress, τ - shear stress.

Two types of experiments were conducted. Experiments of type 1 were conducted at constant displacement rates. The constant displacement rate of the σ_1 piston could be translated to an approximately constant shear-strain rate. For type 2, the displacement rate was decreased about one half or one order of magnitude after reaching peak strength. When steady state was achieved for this rate the displacement rate was further decreased. At the end, the displacement rate was increased to the initial value for two experiments.

5.2.2 Data acquisition

During the experiment the applied force on the σ_1 piston, the displacement of the σ_1 piston and the oil pressure of the hydraulic ram were recorded with a frequency of 1 Hz. These signals (measured in mV) were translated into maximum principal stress (σ_1 in MPa) and minimum principal stress (σ_3 in MPa) as well as axial displacement (d in mm). Data processing was performed according to Richter et al. [2016].

For determining the stress exponents (n) and the activation energies (Q), the differential stresses ($\Delta\sigma$) at a shear strain (γ) of 3 of constant displacement rate experiments were used. The mean steady state stresses of strain-rate stepping steps were used as well as the mean shear-strain rates of each displacement rate.

The equivalent friction coefficient (μ) was calculated for the 45° pre-cut of the forcing blocks. The friction coefficient on the shear-zone surface equalled the shear stress (τ) divided by the normal stress (σ_N). For peak-strength experiments, the maximum friction coefficient was calculated. Steady state stress at $\gamma = 3$ was used for high strain experiments. The difference between peak stress and steady state stress was relatively small as a result of minor weakening after peak strength. The stress value before decreasing the displacement rate was used for the first step of the strain-rate-stepping experiments. For the following strain-rate steps the mean values at steady state conditions were used.

5.2.3 Analytical methods

Jackets were cut parallel to the displacement direction and impregnated with epoxy for preparing double-polished thin sections. For all subsequent analyses, samples were orientated with a sinistral shear sense (shear zone boundary is horizontal). All samples were analysed with light microscopy and scanning electron microscopy (for imaging: a field emission Philips XL 30 ESEM, for electron backscatter diffraction: a field emission Zeiss Merlin SEM with a Nordlys nano camera).

Computer-integrated polarisation microscopy (CIP) [Panozzo Heilbronner and Pauli, 1993] and electron backscatter diffraction (EBSD) were used to obtain crystal orientations. Polishing and lapping for EBSD analysis was carried out with colloidal silica suspension Struers OP-U non dry for 3-6 minutes. Samples were coated with a thin carbon layer to prevent charging under high vacuum conditions. Acceleration voltages between 10 and 15 kV were used with step sizes of 0.2 μm. EBSD data were measured with AZtec software and analysed with the MTEX toolbox [Hielscher and Schaeben, 2008]. Initial noise reduction was performed with CHANNEL 5 software by removing isolated, misindexed points and replacing non-indexed pattern with respect to their neighbours (iteratively filled starting with eight similar neighbours down to six or five similar neigbours). Grain maps obtained with MTEX separated individual grains by a misorientation of 10 °. Dauphine twins ($60 \pm 5°$ misorientation) were excluded from defining grain boundaries. Grains had to contain at least five pixels to be recognised as grains. The calculated equivalent diameters ($d_{equ} = 2 \cdot \sqrt{area/\pi}$) were used as input for a StripStar programme based on Heilbronner and Barrett [2014] to get equivalent volume weighted diameters. The modal value of the volumetric diameters was estimated with a density function and it was used as a representative value for grain sizes.

5.3 Mechanical results

27 constant shear-strain rate experiments (Table 5.1) between 500 °C - 1000 °C were performed and five strain-rate-stepping experiments (Table 5.2) at shear-strain rates between $\sim 2.5 \cdot 10^{-6}\,s^{-1}$ and $\sim 2.5 \cdot 10^{-3}\,s^{-1}$ for ~ 650 °C, 800 °C, 900 °C and 1000 °C were conducted. The influence of temperature, confining pressure, initial grain size and shear-strain

rate as well as the resulting friction coefficients, stress exponents and activation energies will be presented.

Tab. 5.1: Experimental conditions for constant shear-strain rate experiments.

exp. #	T [°C]	P_c[1] [MPa]	hot pressed for 20 h	shear strain rate [10^{-5} s^{-1}]	shear strain	max. $\Delta\sigma$[2] [MPa]	$\Delta\sigma$ at $\gamma = 3$ [MPa]	μ at $\gamma = 3$[3]
340br*[4]	500	1510		1.4	1.6	2738	-	0.47
450br	500	1540		2.1	3.2	3212	2747	0.46
338br*	600	1522		1.4	1.4	2513	-	0.45
479br	600	1538		2.1	3.9	2423	2368	0.43
415br	600	1512	1000 °C/ 1.5 GPa	1.9	3.0	3246	3246	0.51
435br	650	1507		2.1	3.6	2698	2627	0.46
481br	650	1554		3.0	4.2	2538	2364	0.43
380br	700	1500		-	-	-	-	-
339br*	700	1524		2.1	2.0	1298	-	0.30
437br*	700	1529		1.9	1.7	1483	-	0.32
383br	700	1585		2.8	4.9	1246	1085	0.25
493br	700	1512	1000 °C/ 1.5 GPa	2.7	4.9	2051	1951	0.39
487br	800	1511		-	-	-	-	-
439br*	800	1526		2.1	1.4	856	-	0.22
388br	800	1527		2.8	4.8	858	791	0.21
445br[5]	800	1578		3.0	4.7	415	309	0.09
419br	800	1556	1000 °C/ 1.5 GPa	2.8	4.2	1159	1016	0.25
412br	900	1530		2.8	2.9	475	360	0.10
417br	1000	1576		-	-	-	-	-
337br	1000	1506		3.0	3.2	152	147	0.05
494br	650	1088		4.8	5.7	2396	2126	0.49
452br	700	1064		2.7	4.4	1536	1452	0.40
386br	800	574		2.3	3.2	1500	1384	0.53
448br	800	1067		2.9	4.5	864	728	0.25
500br	650	1502		0.35	1.1	1276	-	0.30
447br	800	1556		27	4.1	1783	1677	0.35
499br	900	1535		189	4.0	2015	1992	0.39

[1] average of the confining pressure P_c
[2] differential stress $\Delta\sigma$
[3] friction coefficient $\mu = \tau/\sigma_N$
[4] friction coefficient at peak conditions
[5] initial grain size of powder 7-11 μm

Tab. 5.2: Experimental conditions for shear-strain rate stepping experiments. Sample 480br was hot pressed for 20 h at 1000 °C and 1.5-1.6 GPa before deformation.

exp. #	T [°C]	P_c[1] [MPa]	shear strain	stress exponent	shear strain rate [10^{-5} s^{-1}]	flow stress $\Delta\sigma$[2] [MPa]	μ[3]
498br[4]	~650	1589	5.4	6.4	2.6	2608	0.46
					1.2	2517	0.44
					0.30	1842	0.36
488br	800	1623	6.4	1.8	28	1811	0.37
					5.1	783	0.20
					1.2	422	0.11
					0.48[5]	250	0.07
480br	800	1601	4.5		2.3	1040	0.25
					0.63	293	0.09
					2.7	820	0.20
482br	900	1583	8.4	2.0	28	1272	0.29
					3.6	389	0.11
					0.49	178	0.05
					41[6]	1494	0.32
485br	1000	1588	6.2	1.8	27	578	0.16
					4.0	189	0.06
					0.37	75	0.02
					34	794	0.20

5.3.1 Temperature dependence

With increasing temperature a decrease in strength is observed (Fig. 5.2a). Samples deformed at temperatures below 700 °C show steady state to slight strain hardening. At 700 °C or higher, samples show steady state or minor strain weakening at high strain. Thereby, peak stress is achieved at lower shear strain with increasing temperature. The gap in strength between 600 °C and 700 °C is significant (difference ~ 700 MPa). At low temperatures, no significant stress drop or strain weakening occurs after yield strength, except for 450br and 481br. These samples show stress drops as a result of slip along the shear zone-forcing block interface caused by high shear stresses. In addition, the alumina forcing blocks start to deform, due to the high stresses, affecting the finite stress (e.g. 415br).

The slope of the loading curve decreases with decreasing strength independent of confining pressure or shear-strain rate. At constant confining pressure and shear-strain rate, a

[1] average of the confining pressure P_c
[2] differential stress $\Delta\sigma$
[3] friction coefficient $\mu = \tau/\sigma_N$
[4] imprecise temperature (furnace output very low)
[5] power failure
[6] forcing block-piston contact at the end causing hardening

temperature dependence is well established with a decreasing slope towards high temperatures (Fig. 5.2a).

5.3.2 Pressure effect

The temperature-dependent decrease in shear stress corresponds to a systematic difference in pressure dependence of shear stress (Fig. 5.3): at 650 °C, shear stress increases with increasing confining pressure. At 700 °C, the pressure dependence is ambiguous. At 800 °C the pressure dependence is not visible between 1.0 GPa and 1.5 GPa, but between 0.5 GPa and 1.0 GPa an inverse pressure dependence is pronounced (Fig. 5.3c).

5.3.3 Influence of grain size

Samples with hot pressing reach higher stresses compared to samples without hot pressing prior to deformation (Fig. 5.2b). The difference in differential stress is at least 500 MPa at 600 °C, whereby the forcing blocks start to deform in the hot pressed sample. At 700 °C, the hot pressed sample is about 900 MPa stronger and shows strain hardening in contrast to strain weakening without hot pressing. At 800 °C, the difference is $\sim$ 200 MPa and both samples show strain weakening.

A small initial grain size fraction (7-11 µm) is deformed at 1.5 GPa, 800 °C and $2.5 \cdot 10^{-5}$ s^{-1} (445br, Fig. 5.2b). It is significantly weaker than experiments performed at the same conditions but with a larger initial grain size fraction (< 100 µm). At a shear strain of three the differential stress of 445br is $\sim$ 500 MPa below the differential stress of 388br. Steady state conditions exist between a shear strain of $\sim$ 0.5 - 2.5. Afterwards, a low but continuous increase in strength occurs ($\sim$ 100 MPa) until the end of the experiment.

5.3.4 Influence of strain-rate

Strain rate stepping experiments (Fig. 5.4) in combination with constant displacement experiments at various strain rates show a distinct positive strain rate dependence of strength for all temperatures. It is less pronounced at 650 °C. A negative temperature dependence occurs at all strain rates. One strain rate stepping experiment included a hot pressing stage prior to deformation. The initial strength is similar to the hot pressed constant displacement experiment. At the next strain rate steps, stresses are similar to the experiments without hot pressing and significantly lower than the hot pressed sample ($\sim$ 200 MPa).

A good reproducibility and high precision of the mechanical data can be noted. At 900 °C and 1000 °C, the last step has slightly higher shear-strain rates than the first step and the differential stress is slightly higher. The experiment at 900 °C shows abrupt strain hardening at the end of the last strain-rate step. This is a consequence of the sample geometry: the lower forcing block collides with the upper alumina piston. Therefore hardening records the deformation of the alumina, which is stronger than quartz.

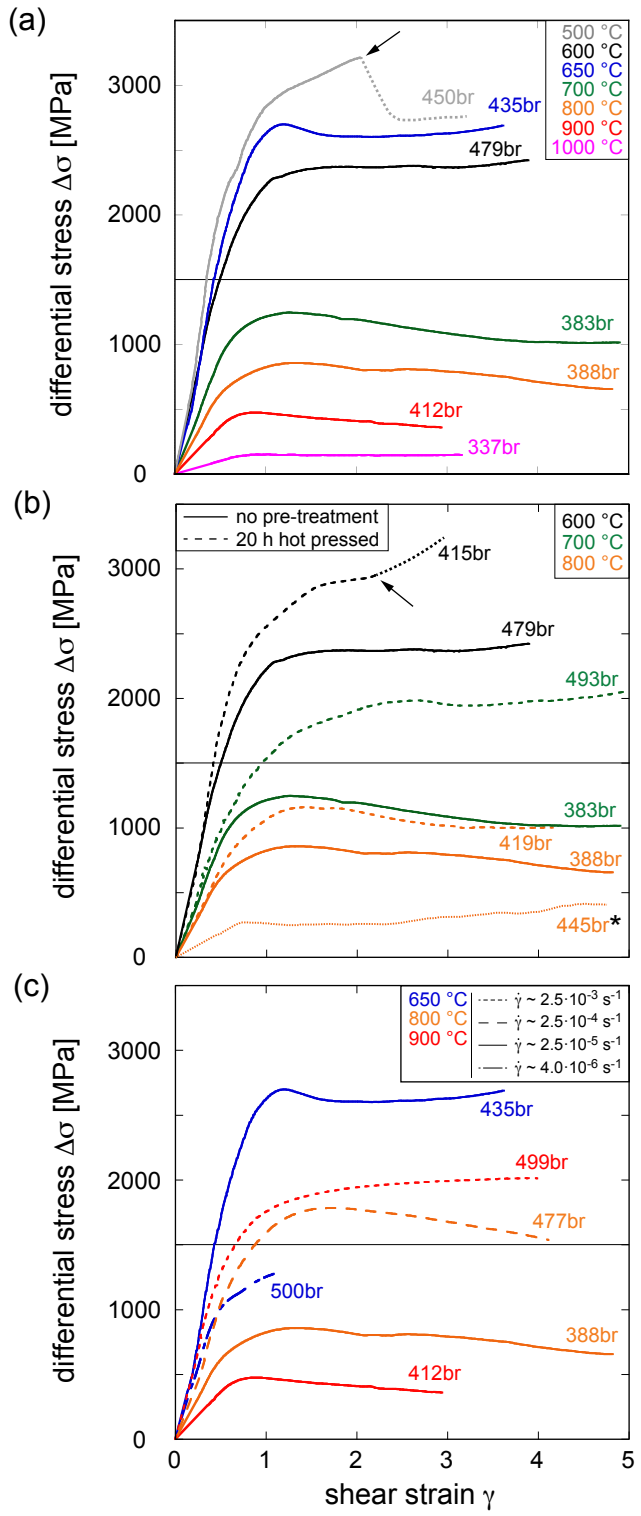

Fig. 5.2: Differential stress vs. shear strain for constant shear-strain rate experiments at 1.5 GPa confining pressure. (horizontal lines mark the Goetze criterion) (a) Temperature dependence at $2.5 \cdot 10^{-5}$ s^{-1}. Low strain experiments are not shown. An inverse temperature dependence occurs above 650 °C. At lower temperatures, it is ambiguous. Arrow indicates slip at sample-piston interface. (b) Hot pressed experiments (dashed lines) compared to experiments without pre-treatment at $2.5 \cdot 10^{-5}$ s^{-1}. Hot pressed samples have significantly higher strength than samples without pre-treatment. Sample with a smaller grain size range (dotted line) of the initial powder (7-11 µm, indicated with an asterisk) is weaker than the normal sample. Arrow indicates the onset of forcing block deformation. The subsequent stresses include stress build up due to deforming alumina. (c) Various shear-strain rates at 650 °C, 800 °C and 900 °C illustrate increasing stresses with increasing shear strain rates.

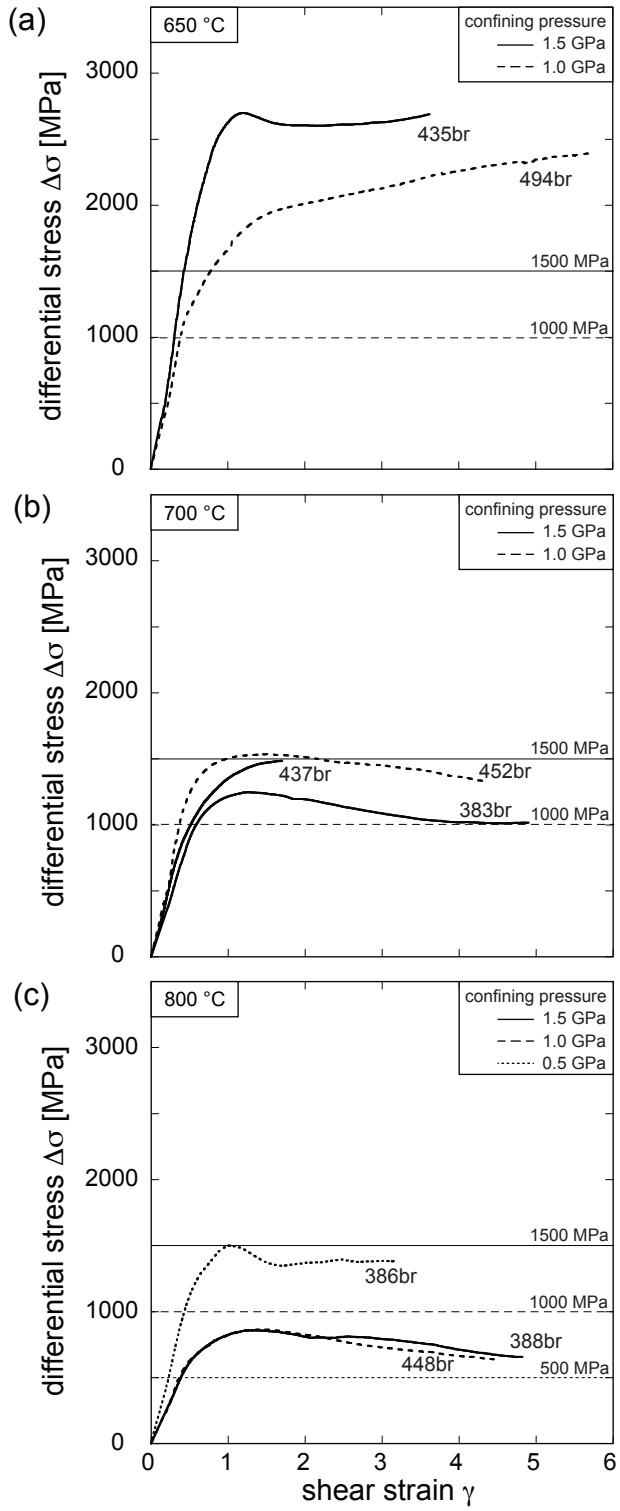

Fig. 5.3: Pressure dependence (horizontal lines mark the Goetze criterion for different confining pressures). (a) A positive pressure dependence occurs at 650 °C. (b) At 700 °C the pressure dependence is ambiguous. (c) At 800 °C, no pressure dependence occurs between 1.0 GPa and 1.5 GPa. Towards lower confining pressures, an inverse pressure dependence is observed.

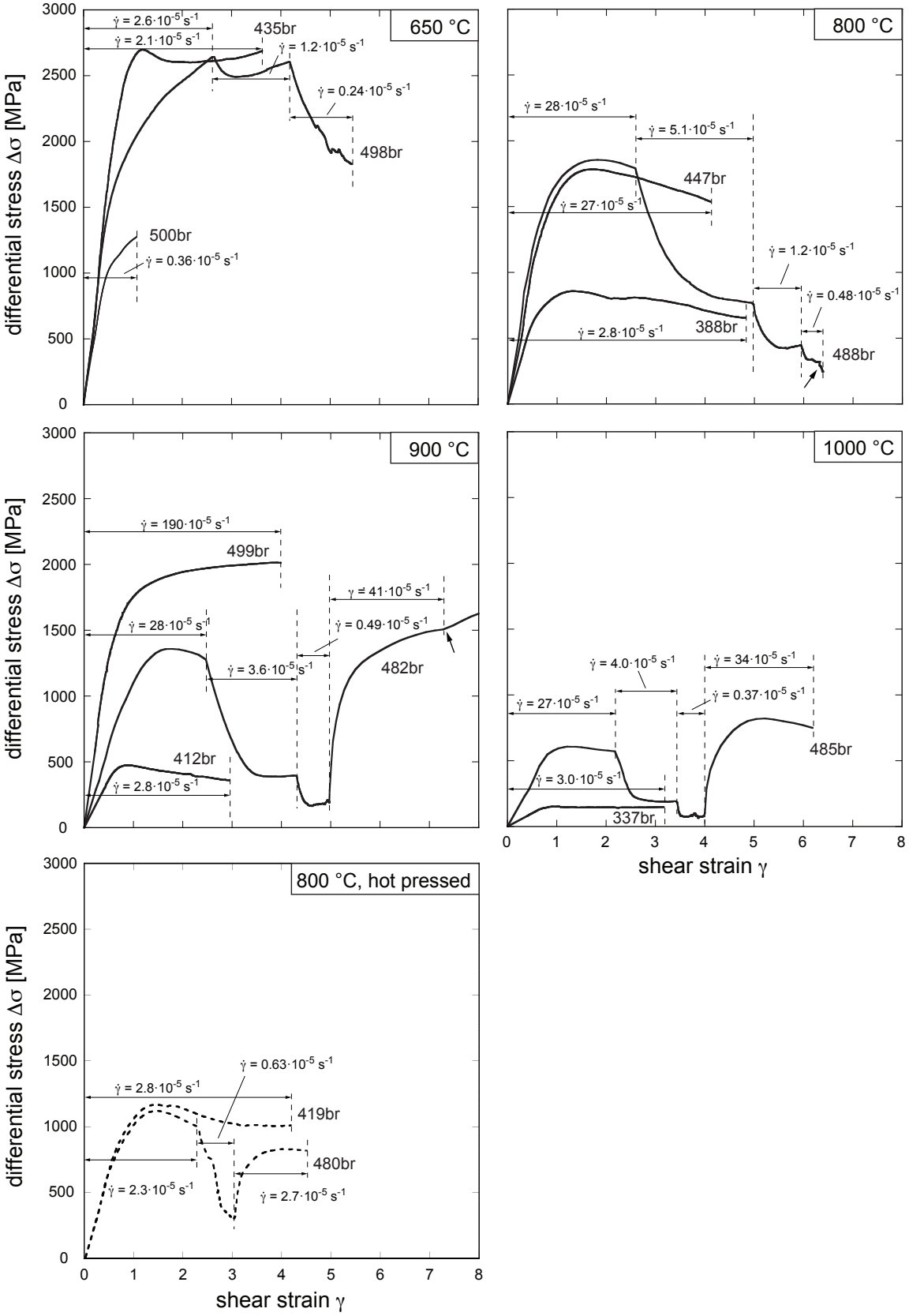

Fig. 5.4: Stress-strain curves for strain rate stepping experiments at ∼650 °C, 800 °C, 900 °C, 1000 °C and 800 °C (hot pressed) in comparison with constant displacement experiments at similar conditions (all at 1.5 GPa confining pressure). Note the good reproducibility of mechanical data. The arrow at 488br (800 °C) points out a power blackout. The arrow at 482br (900 °C) marks a change of sample geometry due to colliding forcing blocks.

5.3.5 Coefficient of friction

At 1.5 GPa, the friction coefficient ($\mu = \tau/\sigma_N$) below 700 °C is high (μ 0.45; Fig. 5.5) and a minimal negative temperature dependence is visible. From 700 °C - 1000 °C, the friction coefficient shows a strong temperature dependence at 1.5 GPa confining pressure for $2.5 \cdot 10^{-5}$ s^{-1} ($\mu \sim 0.3$ to 0.05) and $2.5 \cdot 10^{-4}$ s^{-1} ($\mu \sim 0.35$ to 1.6). At slow strain rates, the low friction coefficient ($\mu < 0.1$) still decreases with increasing temperature.

Low confining pressures cause a higher friction coefficient. The increase is small ($\Delta\mu < 0.1$) at 1.0 GPa. At 0.5 GPa and 800 °C, the highest friction coefficient occurs ($\mu = 0.53$) and it doubles with regard to the value at 1.0 GPa.

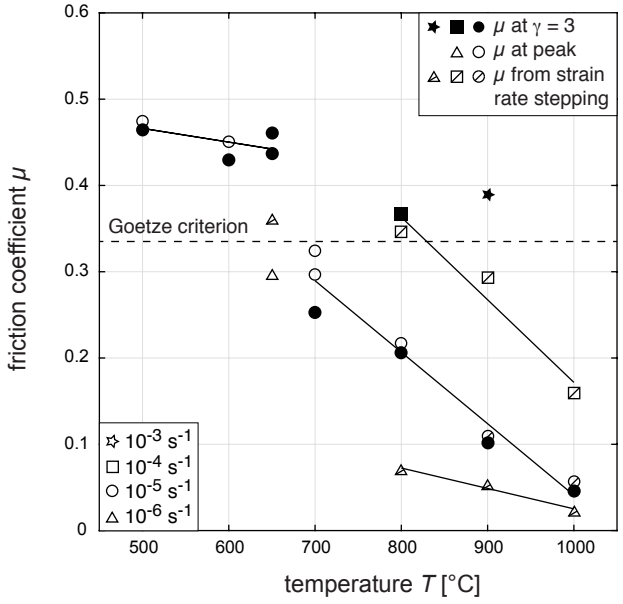

Fig. 5.5: Friction coefficient at 1.5 GPa for different shear-strain rates. At low temperatures, the friction coefficient is almost independent of temperature. At high temperatures ($\geq$ 700 °C), the friction coefficient significantly decreases with increasing temperature for strain rates of $10^{-5}s^{-1}$ to $10^{-4}s^{-1}$.

5.3.6 Stress exponent and activation energy

The mechanical data can be fitted to a flow law of a power law type (Eq. 5.1). Thereby, stress exponent (n) and activation energy (Q) can be determined.

$$\dot{\gamma} = A \cdot \Delta\sigma^n \cdot exp(-\frac{Q}{R \cdot T}) \tag{5.1}$$

Here, $\dot{\gamma}$ [s^{-1}] is the shear-strain rate, A [MPa$^n \cdot s^{-1}$] is a material-dependent factor, $\Delta\sigma$ [MPa] is the differential stress, R [J·mol^{-1}·K^{-1}] is the ideal gas constant and T [K] is the absolute temperature. The stress exponent of high-temperature experiments (800 °C - 1000 °C) is $n = 1.9 \pm 0.6$ (Fig. 5.6a). No trend is visible towards a higher stress exponent at higher temperatures. At low temperatures ($\sim$ 650 °C) the n-value is significantly higher ($n = 6.4 \pm 1.3$).

For high temperature experiments, the activation energy is $\sim 170 \pm 72$ kJ/mol for $n = 1.9 \pm 0.6$ (Fig. 5.6b). The values for 900 °C at $\sim 10^{-3}s^{-1}$ and 800 °C at $\sim 10^{-4}s^{-1}$ are not

included in the calculation of the stress exponent and activation energy because steady state is not indicated in the mechanical data. The microstructure reveals no pervasive foliation and recrystallisation, which supports the exclusion. Furthermore, the data of 800 °C at $\sim 10^{-4} s^{-1}$ indicate a smaller activation energy compared to the data at 900 °C and 1000 °C.

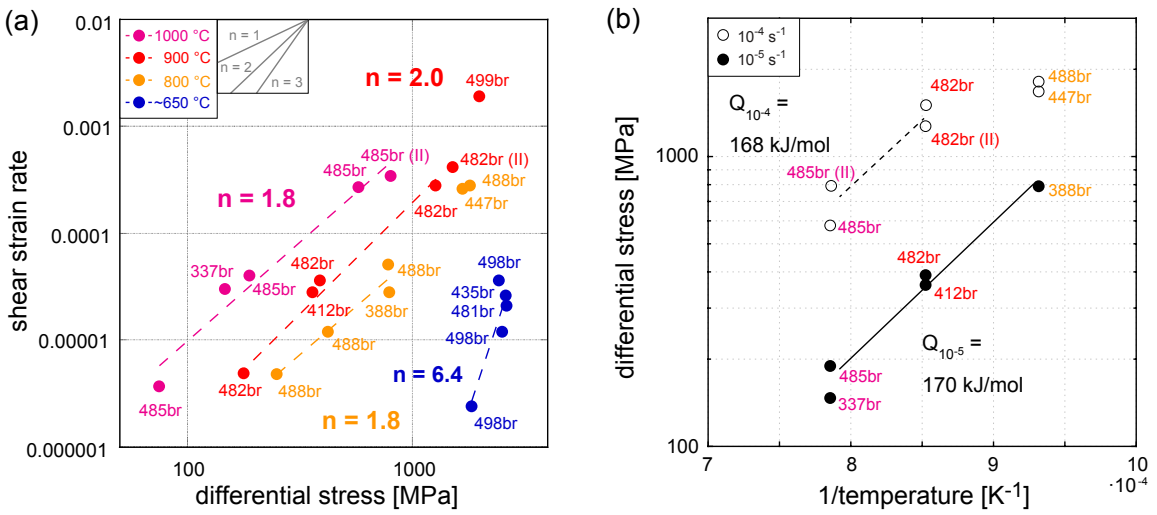

Fig. 5.6: (a) Stress exponent (n). For 800 °C - 1000 °C $n \sim 1.9$. It changes to $n \sim 6.4$ around 650 °C. (b) The activation energy is relatively high ($Q \sim 170$ kJ/mol).

5.4 Microstructural observations

The starting material has a broad grain size distribution (< 100 µm). Large grains are fractured early in the pressurisation and loading process while more fine-grained material is produced by comminution. The effect of temperature and grain size on the microstructural evolution at high confining pressures will be discussed. Then, the influence of pressure and strain rate will be described. Resulting recrystallised grain sizes and crystallographic preferred orientations (CPO) are compared.

5.4.1 Deformation microstructures of high confining pressure (1.5 GPa)

Between 500 °C and 1000 °C at a constant shear-strain rate of $2.5 \cdot 10^{-5}$ s^{-1}, the microstructure evolves from heterogeneously towards homogeneously deformed on thin-section scale. In this process, the initial grain size distribution before deformation (Fig. 5.7) influences the microstructural evolution (Fig. 5.8).

5.4.1.1 Low-temperature samples ($\leq$ 650 °C)

Low-temperature samples are dominated by complex Riedel band geometry developed with synthetic R bands and partially antithetic P and R' bands (Fig. 5.8). The R bands are subparallel to the direction of σ_1. Riedel bands are not connected and do not cross the whole

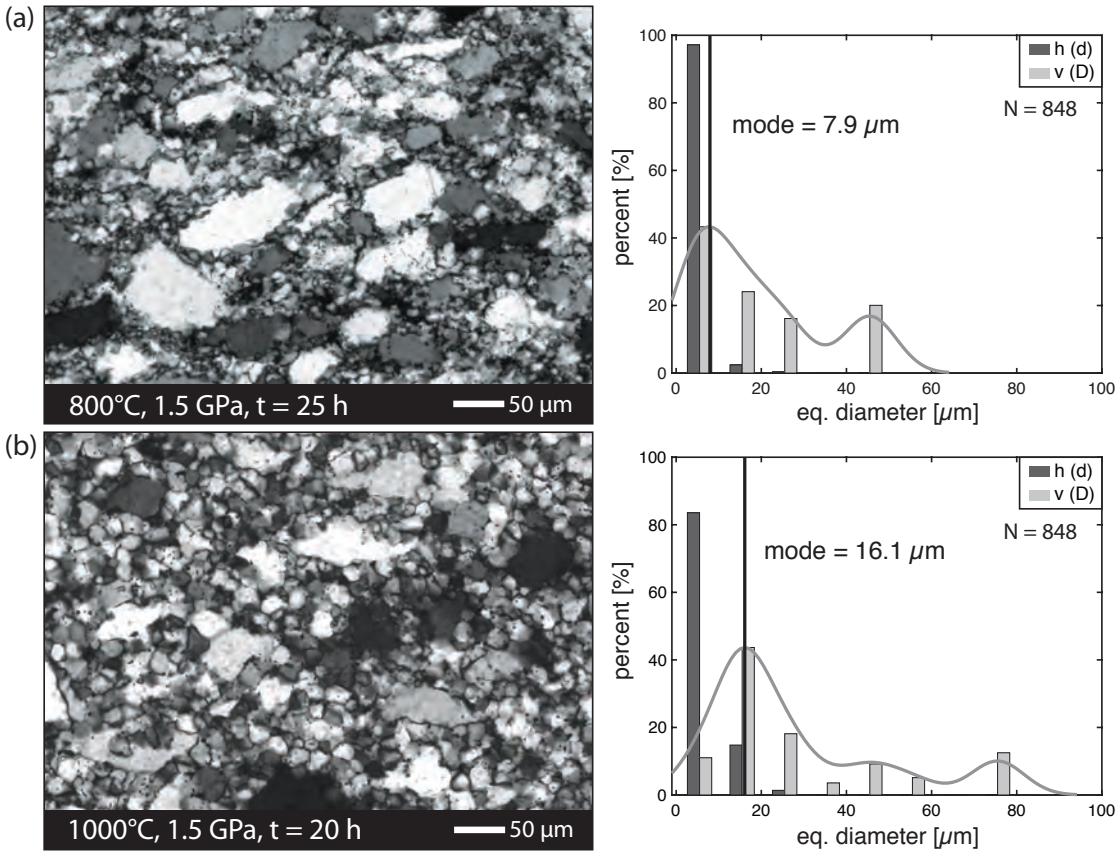

Fig. 5.7: Quartz powder after run-in at (a) 800 °C and (b) 1000 °C. More large clasts remain at 800 °C. The mode of v(D)(D = diameter of volume equivalent spheres and v = volume weighted frequency distribution) is larger at 1000 °C indicating more intensive grain growth (reduction of fine-grained fraction). The h(d) distribution describes frequency distribution (h) of the diameter of area equivalent circles (d).

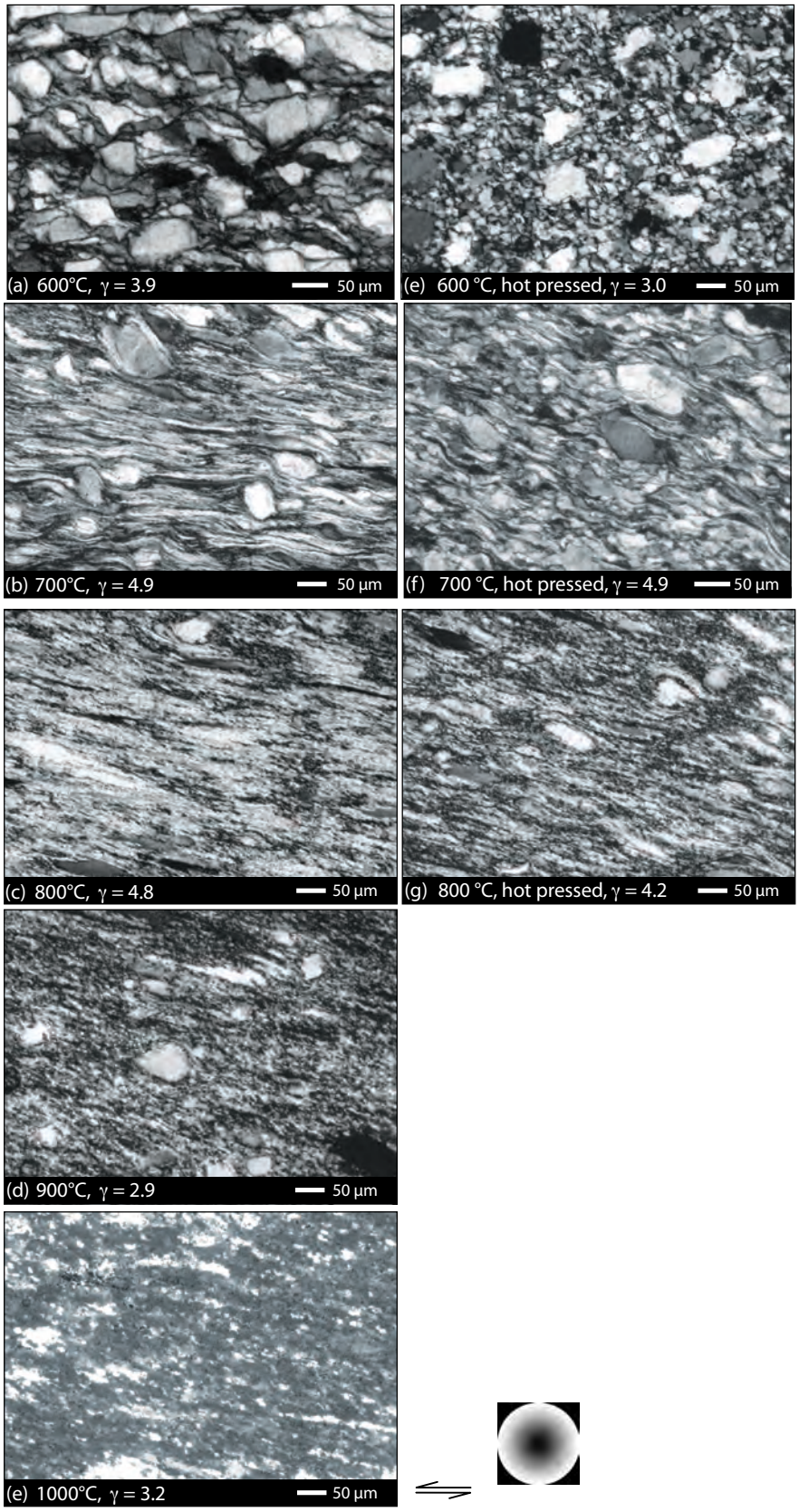

Fig. 5.8: Microstructural evolution with increasing temperature (circular polarised images). (a) - (e) Riedel shear geometry evolves into a pervasive foliation with increasing temperature (f) - (h) By annealing before deformation, more clasts remain at high strain and an S-C' fabric is still present at 700 °C.

sample, which is in accord with the mechanical data that show no stress drop or failure. Most of the original clasts are visible with rounded edges. Undulatory extinction and deformation bands with a high angle towards the shear zone boundary exist in several clasts. At 600 °C, tails at clasts are partly developed and deformation lamellae start to develop in clasts at 600 °C. An S-C' fabric is developed at 650 °C besides the Riedel geometry with S planes in P band orientation and C' bands subparallel to R bands. At 600 °C, zones with small, equiaxed grains evolve in R band direction. These zones become more pronounced with increasing temperatures.

5.4.1.2 High-temperature samples ($\geq$ 700 °C)

At high temperatures, viscous processes define the microstructure (Fig. 5.8). At low shear strain (700 °C and 800 °C with $\gamma \sim 1.5$), an S-C' fabric is developed. Tails develop at more rounded clasts. With increasing shear strain, the S-C' fabric evolves into a single penetrative foliation of elongated and recrystallised grains. Large clasts show more penetrative recrystallisation with increasing temperature of deformation and with increasing strain. At $\gamma \sim 5$ about 10 % of clasts remain at 700 °C and 5 % of clasts can be distinguished at 800 °C. Rounded clasts are predominant at 700 °C. At 800 °C, highly elongated clasts dominate. Deformation lamellae are distinct in clasts at 700 °C and 800 °C. They diminish at 900 °C.

5.4.1.3 Pre-deformational annealing

Hot pressing causes annealing of the starting material (Fig. 5.7). Cracks anneal and are barely visible. Small grains grow at the expense of larger grains. Hence, the smallest grain size fraction is reduced. Grain growth is more efficient at 1000 °C than e.g. at 800 °C. The average grain size of 8 µm after 25 h at 800 °C and hydrostatic conditions increases to 16 µm after 20 h at 1000 °C and hydrostatic conditions (hot pressing, Fig. 5.7).

Subsequent deformation at 600 °C causes little transformation of the fabric (Fig. 5.8e). No Riedel geometry develops and minor grain boundary alignment occurs. At 700 °C, an S-C' fabric persists at high shear strain with several remaining rounded clasts that develop tails (Fig. 5.8f). Recrystallisation occurs along shear bands in C' orientation. At 800 °C, a pervasive foliation dominates the fabric similar to the fabric of the sample without hot pressing (Fig. 5.8g). Yet, more elongated clasts are present compared to the sample without hot pressing.

5.4.2 Effect of confining pressure on the microstructural development

Samples deformed at 1.0 GPa confining pressure and 650 °C show Riedel bands and an S-C' fabric, similar to 1.5 GPa confining pressure (Fig. 5.9). Yet, clasts have less rounded corners. At 700 °C, the sample is characterised by an S-C' fabric at high strain, something

which is absent at 1.5 GPa confining pressure (Fig. 5.9b). Several rounded clasts with in part long tails remain at 700 °C. At 800 °C, a penetrative foliation is established but more remaining clasts exist and recrystallisation is less completed than at 1.5 GPa. Clasts are predominantly elongated.

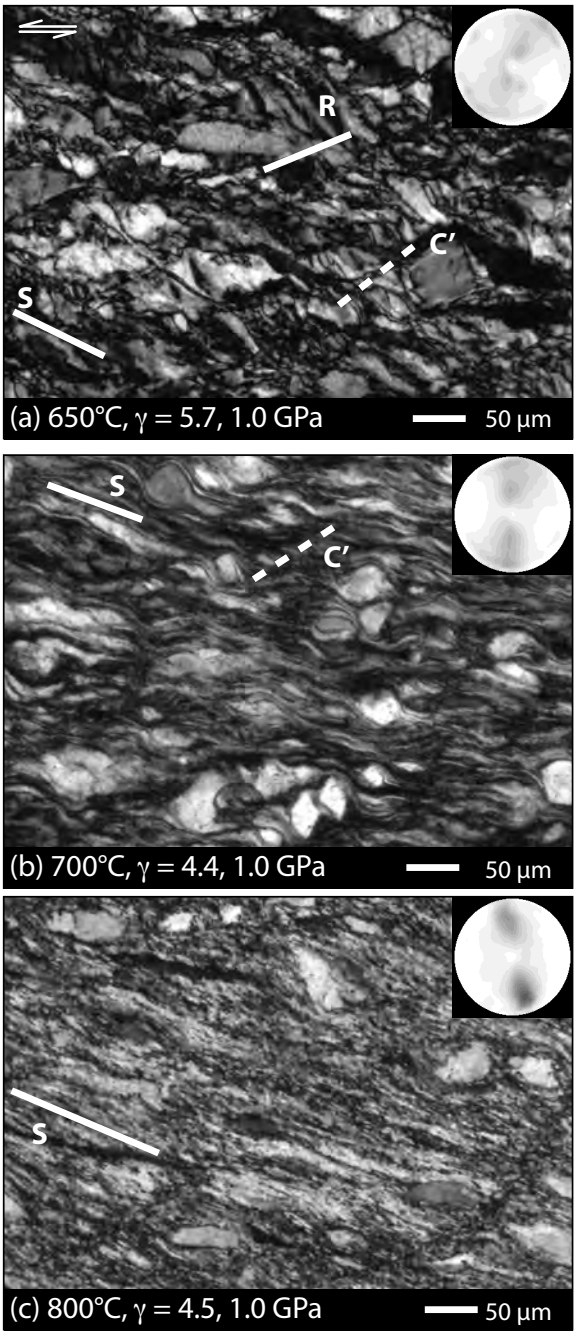

Fig. 5.9: Microstructure and CIP derived *c*-axis pole figures (contouring interval 0.5) at 1.0 GPa confining pressure. (a) At 650 °C synthetic Riedel bands are accompanied by a beginning S-C' fabric (crossed polarised image). (b) At 700 °C, S-C' fabric is developed and the *c*-axis orientation indicates a maximum that is slightly rotated anticlockwise with the sense of shear (circular polarised image). (c) At 800 °C, one pervasive foliation is visible (circular polarised image).

At 0.5 GPa confining pressure and 800 °C, deformation localises along through-going, close synthetic Riedel bands accompanied by several intergranular fractures (Fig. 5.10). Most of the displacement is accumulated along R bands, along which the gouge material is highly pulverised (submicron-scale). Large clasts are rounded at the edges.

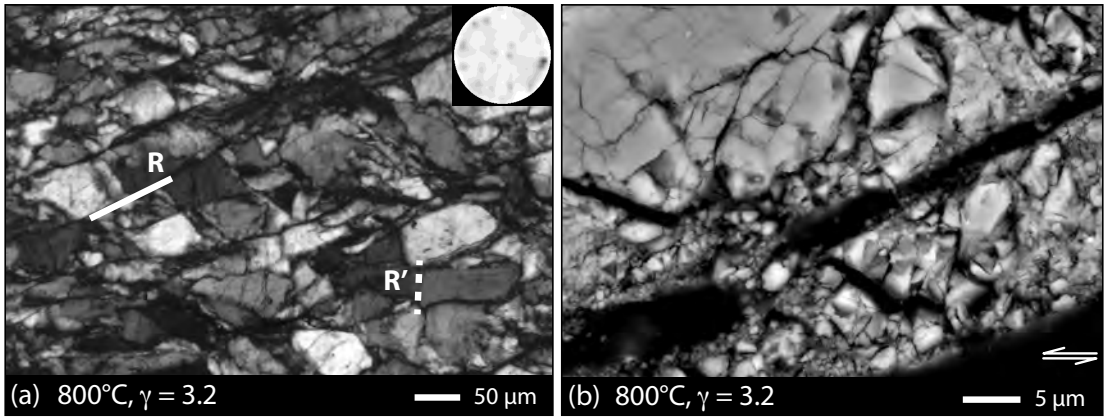

Fig. 5.10: Brittle-dominated sample at 800 °C and 0.5 GPa. (a) The shear zone is cross cut by several closely spaced Riedel fractures (crossed polarised image). Some of them cut through the whole shear zone. The *c*-axis orientation is random (contouring interval 0.5). (b) Very fine-grained material is generated by comminution along Riedel bands (BSE image).

5.4.3 Influence of strain rate on microstructure

Three constant shear-strain rate experiments are conducted at different shear-strain rates than $\sim 2.5 \cdot 10^{-5}\,s^{-1}$ (Fig. 5.11). At 650 °C and a shear-strain rate of $3.5 \cdot 10^{-6}\,s^{-1}$ several grains already have rounded grain boundaries at low shear strain ($\gamma = 1.1$). An S-C' fabric is developed as well as Riedel shear. At 800 °C and 900 °C, faster shear-strain rates ($2.7 \cdot 10^{-4}\,s^{-1}$ and $1.9 \cdot 10^{-3}\,s^{-1}$, respectively) cause a more heterogeneous deformation and an S-C' fabrics is preserved at high shear strain. Recrystallisation along shear bands is accompanied by grain growth of the smallest fraction especially at 900 °C.

5.4.4 Crystallographic preferred orientation

The CPO of *c*-axes progressively changes with increasing temperature at 1.5 GPa confining pressure (Fig. 5.12, Fig. 5.13). Below 650 °C, the CPO is dominated by large clasts and it shows a random distribution. At 650 °C the *c*-axes develop a slightly preferred orientation. At 700 °C and 800 °C, a strong CPO with one peripheral maximum of the *c*-axes that are slightly rotated with the sense of shear is revealed. At 900 °C, a peripheral and a central *c*-axes maximum are established. Towards 1000 °C the CPO evolves to a single central maximum. The recrystallised matrix dominates the CPO at temperatures above 700 °C. At slower strain rates and 650 °C, a weak peripheral CPO of *c*-axes is already developed at low shear strain (Fig. 5.11a). Faster strain rates cause less pronounced preferred orientation compared to $\sim 2.5 \cdot 10^{-5}\,s^{-1}$ (Fig. 5.11).

If the smallest grain size fraction is reduced by hot pressing a less pronounced CPO at 700 °C is developed (Fig. 5.12). Especially, the *a*- and *m*-axes show a weak texture while both show girdles subparallel to the shearing direction in the sample without hot pressing. At 800 °C, the CPO of the hot pressed sample is well pronounced with a peripheral *c*-axes maximum rotated with the sense of shear and girdles of *m*- and *a*-axes. It is similar to the

sample without hot pressing. In contrast, small initial grain sizes (7-11 µm) cause a CPO with a peripheral maximum that is rotated anticlockwise with respect to the sense of shear. The girdles of the *m*- and *a*-axes are indicated.

At 1.0 GPa confining pressure, the less pronounced CPO is developed and shows a peripheral maximum at 700 °C and 800 °C. A clast-dominated random texture occurs at 800 °C and 0.5 GPa confining pressure (Fig. 5.9).

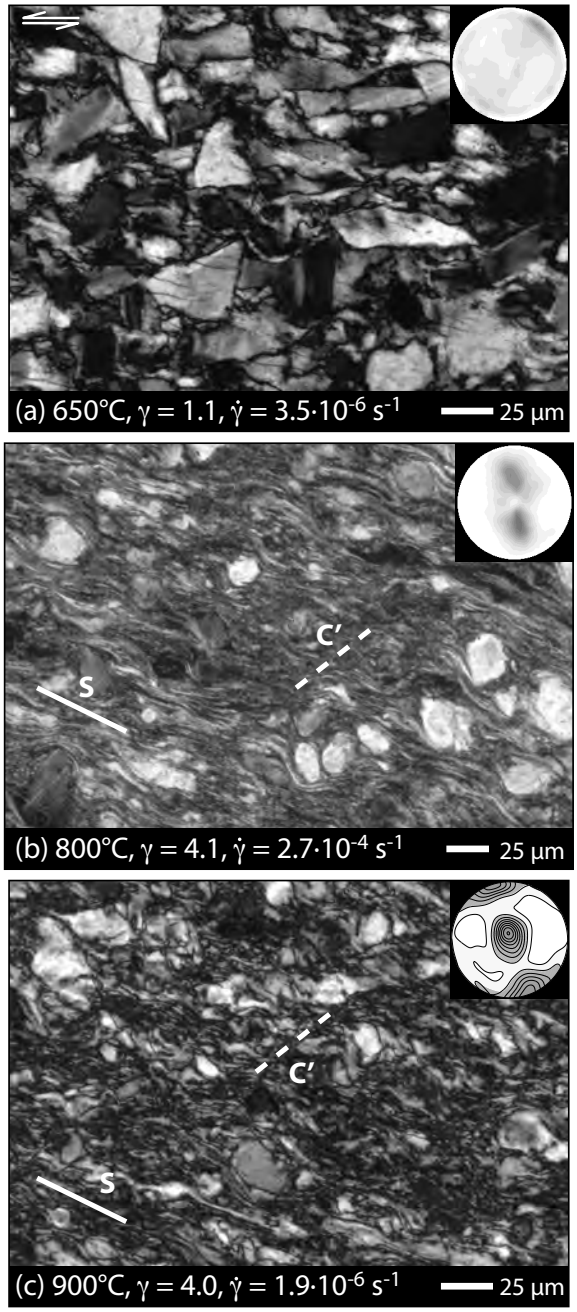

Fig. 5.11: Microstructures and CIP derived *c*-axis pole figures (contouring interval 0.5) at different shear-strain rates. (a) R Riedel bands and C' planes are developed at low shear strain for a slow shear-strain rate at 650 °C (crossed polarised image). (b) and (c) Fast shear-strain rates create an S-C' fabric at high shear strain. (b) 800 °C (circular polarised image) (c) 900 °C (crossed polarised image, EBSD derived pole, maximum 3.3)

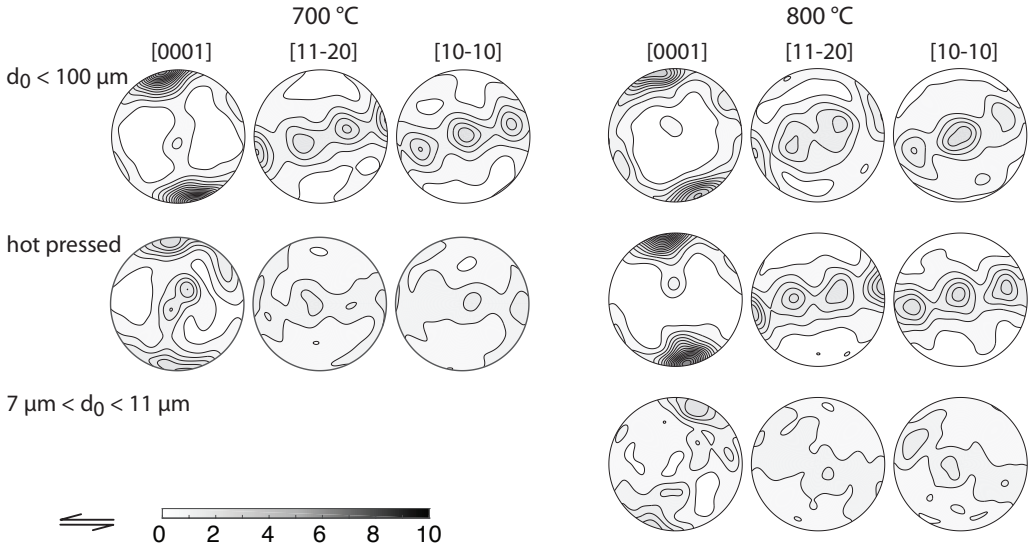

Fig. 5.12: Influence of initial grain size distribution on texture evolution at 700 °C and 800 °C. Hot pressing subordinately affects the CPO. An initially small grain size fraction of 7-11 µm results in a weak CPO that is rotated anticlockwise with the sense of shear.

5.4.5 Recrystallised grain sizes

The grain size of the smallest fraction increases continuously from 700 °C to 1000 °C at 1.5 GPa and $\sim 2.5 \cdot 10^{-5}\,s^{-1}$ (Fig. 5.13; 700 °C - 1.8 µm, 800 °C - 3.8 µm, 900 °C - 5.6 µm, 1000 °C - 10.1 µm). At 1.0 GPa confining pressure, the recrystallised grain size is slightly smaller (700 °C - 1.4 µm, 800 °C - 3.0 µm). At 0.5 GPa and 800 °C, no recrystallised grains occur. Faster shear-strain rates (higher differential stresses) cause smaller recrystallised grain sizes at 800 °C (2.0 µm) and 900 °C (2.5 µm).

Comparing small initial grain sizes (445br) to a broad initial grain size distribution (388br) at 800 °C and 1.5 GPa confining pressure (Fig. 5.14), the grain size distributions are similar, especially for small grains (< 3 µm) at a final shear strain of $\gamma \sim 5$. The average grain size is slightly smaller in the originally fine-grained sample (3.5 µm compared to 3.8 µm).

With hot pressing at 700 °C, the average grain size is slightly smaller (1.5 µm compared to 1.8 µm) and the smallest fraction is more strongly (Fig. 5.14). At 800 °C deformation temperature, annealing results in slightly larger grain sizes (4.1 µm compared to 3.8 µm). The grain size distribution reveals an underrepresented smallest fraction compared to the sample without hot pressing.

It should be noted that the differentiation between recrystallised grains, newly grown grains and remaining grains is problematic in the small grain size fraction. The internal misorientation of grains can be used as indicator for recrystallisation. Low intragranular misorientations are related to a slightly bent crystal lattice while high misorientations indicate a strongly bent lattice. Remaining clasts show high intragranular misorientations (Fig. 5.14: 700 °C, hot pressed). Small, elongated grains are more intensely bent than grains with low aspect ratios (Fig. 5.13, 5.14) indicating that the latter are recrystallised. Elongated grains

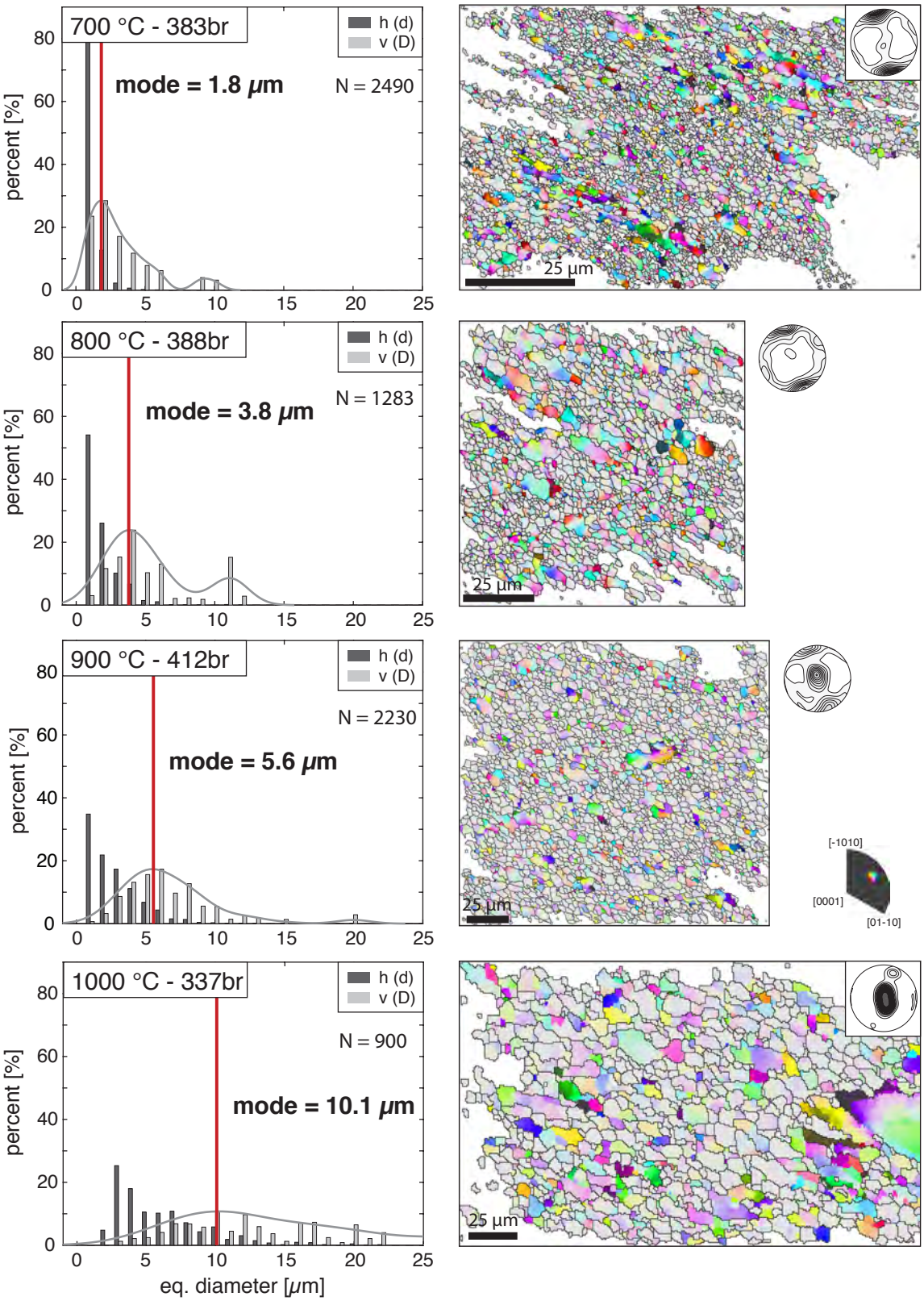

Fig. 5.13: Grain size distribution between 700 °C and 1000 °C. Histograms show the frequency distribution of the equivalent diameter of circles (h(d)) and the volume weighted frequency distribution of the equivalent diameter of spheres (v(D), mode indicated). Associated *c*-axis pole figures and intragranular misorientation maps are shown (step size 0.2 µm; colour range of 20 °). Light grey indicates small misorientations. The mode of the volumetric equivalent diameter continuously increases with increasing temperature.

occur at 700 °C and 800 °C. At higher temperatures, they are diminished. Some grains with low aspect ratios and high internal misorientations are scattered in all samples. They could be related to originally small grains that are not recrystallised. But the grain size analysis is based on regions that are dominated by grains with low intragranular misorientation and represent the recrystallised grain size. In 445br (800 °C, small initial grain size), grains with low aspect ratios and large misorientations are more abundantly.

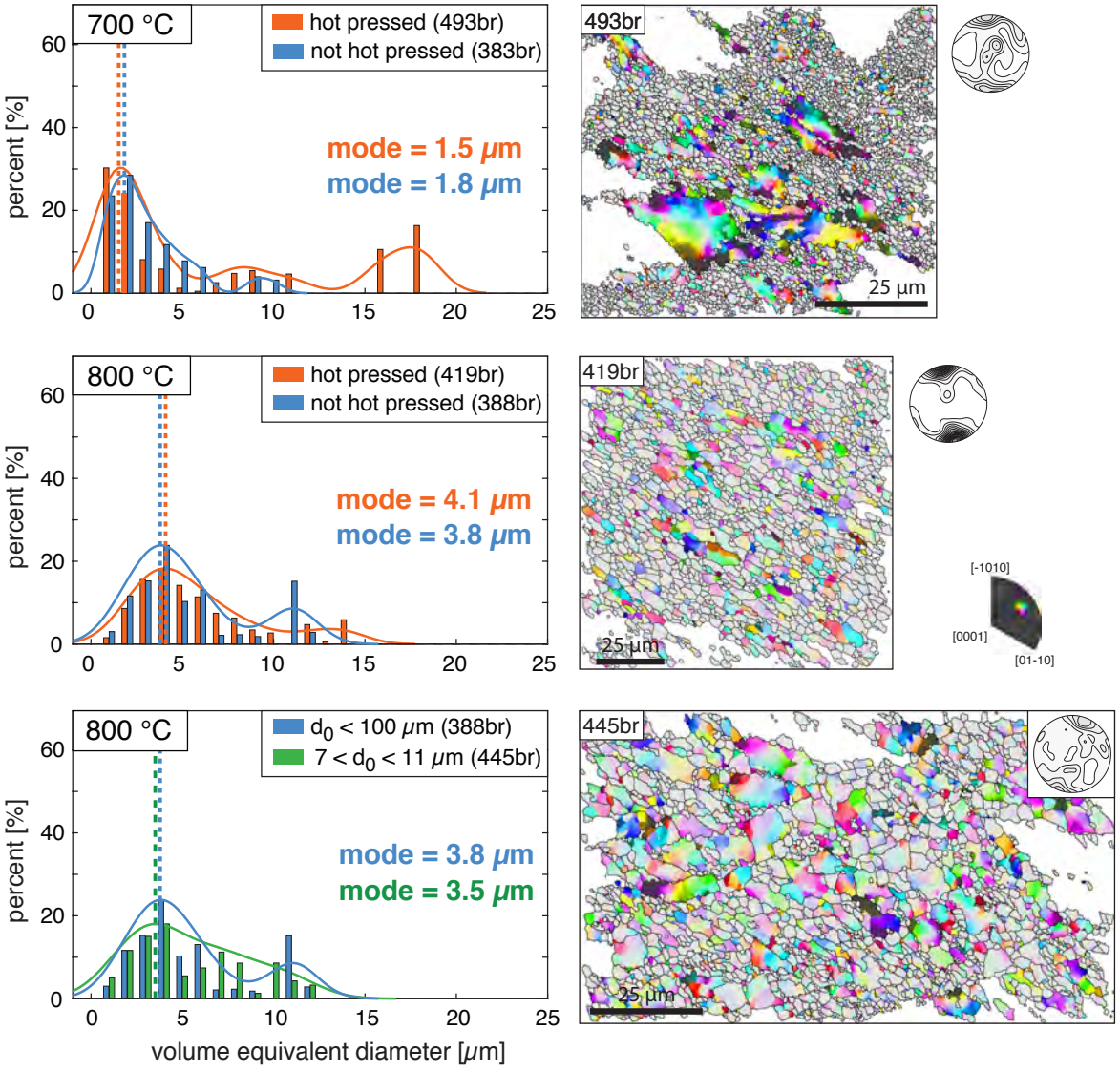

Fig. 5.14: Influence of initial grain size distribution. Histograms show the equivalent diameter of spheres (mode indicated). Associated *c*-axis pole figures and intragranular misorientation maps are shown (step size 0.2 µm; colour range of 20 °). (a) Comparison of samples with and without hot pressing at 700 °C. (b) Comparison of samples with and without hot pressing at 800 °C. (c) Comparison of initial grain size fraction of the quartz powder (> 100 µm versus 7-11 µm). Details in the text.

5.5 Discussion

Differences in the mechanical behaviour are related to dominating deformation processes supported by microstructural evidence. Afterwards, the inferred stress exponents are verified with respect to the experimental set up, followed by an extrapolation of the experiments to natural conditions.

5.5.1 Characteristics of the brittle-to-viscous transition

The large decrease in strength between 650 °C and 700 °C (Fig. 5.2a) coincides with flow stresses decreasing to values below the Goetze criterion and marks the transition from semi-brittle deformation ($\Delta\sigma > P_c$) to viscous dominated deformation ($\Delta\sigma < P_c$) [Kohlstedt et al., 1995]. For low temperatures (≤ 650 °C) differential stress exceeds the confining pressure. The brittle character of these samples is emphasised by an ambiguous temperature dependence of stress and minimal developed temperature dependence of the high friction coefficient ($\mu \sim 0.45$, Fig. 5.5). However, the friction coefficient is lower than the typically quoted values ($\mu \sim 0.6$; Byerlee, 1968) for frictional sliding.

At high temperatures (≥ 700 °C), differential stress is below the Goetze criterion and a pronounced inverse temperature dependence of strength and friction coefficients occur. The initial slope of the stress strain curves decreases with decreasing peak stress for stresses below the Goetze criterion (Fig. 5.2, Fig. 5.3, Fig. 5.4). The decreasing slope can be linked to increasing viscous deformation processes. Above the Goetze criterion, the slope is similar for all samples indicating subordinate viscous deformation processes.

The Orowan equation [e.g. Orowan, 1940; Kohlstedt and Hansen, 2015] implies a stress dependence of the strain rate. Brittle deformation is characterised by a behaviour that is independent from strain-rate, empirically described by Byerlees rule [Byerlee, 1978; Kohlstedt et al., 1995]. Our observed positive shear-strain rate dependence between 650 °C and 900 °C (Fig. 5.2c, Fig. 5.4) emphasises a semi-brittle character at low temperatures.

High confining pressure enables the build up of high strength by preventing crack propagation across grain boundaries due to compaction and limited dislocation mobility [Tullis et al., 1979; Kronenberg and Tullis, 1984]. The positive pressure dependence of flow stress at low temperatures (650 °C, Fig. 5.3a) is consistent with brittle behaviour. Towards higher temperature, an inverse flow-stress-pressure dependence is developed (Fig. 5.3b, c). It is less distinct between 1.0 GPa and 1.5 GPa at 700 °C and 800 °C but clearly established between 0.5 GPa and 1.0 GPa. Kronenberg and Tullis [1984] observed a similar trend in Heavitree quartzite and novaculite with stresses independent of confining pressure ≥ 1.0 GPa and distinct inverse pressure dependence at lower confining pressures. They relate the decreasing peak stress with increasing pressure to increased water fugacity [Tullis et al., 1979; Kronenberg and Tullis, 1984] enhancing recovery processes.

Semi-brittle conditions are associated with strain hardening [e.g. Barber et al., 2010]. The initial crushing of the single crystal, pressurisation to experimental conditions, and later on loading, initiates dislocations. Resulting high dislocation densities cause tangling of dislocations [Hirth and Tullis, 1994], which causes strain hardening. Thereby, high stresses can be achieved due to high confining pressures that prevent failure. Strain weakening occurs due to strain localisation along faults and stable sliding [semi-brittle faulting; Hirth and Tullis, 1994]. Low dislocation velocities and limited thermally active dislocation climb inhibit recovery processes [e.g. Kohlstedt and Hansen, 2015]. We only observe weakening related to slip at the piston-sample interface in two samples. Apart from that, samples with semi-brittle microstructures show mechanical steady state with minor strain hardening at high shear strain (Fig. 5.2). Steady state is related to intragranular microcracking [semi-brittle flow; Hirth and Tullis, 1994], which is less pronounced in our samples. But dissolution-precipitation is observed favouring the smallest grain size fraction (≤ 1 µm). Small resulting grains are strain-free and weaker than the surrounding larger grains. The occurrence of these grains is not sufficient to cause intense strain weakening but stress build up can be compensated. Hence, mechanical steady state is achieved without microstructural steady state.

Close to the Goetze criterion, typical regime 1 curves after Hirth and Tullis [1992] are only observed at 800 °C and $\sim 2.7 \cdot 10^{-4}\,\mathrm{s}^{-1}$. Here, intense work-hardening is followed by distinct weakening (Fig. 5.2c). Small dislocation free grains are produced along shear bands. After sufficient recrystallisation, strain partitioning and weakening occur while mechanical and microstructural steady state is not achieved.

Below the Goetze criterion, generally at higher temperatures and low strain rates, mechanical steady state with minor strain weakening is developed. The associated microstructure is dominated by a pervasive foliation of recrystallised grains. Hence, almost mechanical steady state correlates with a steady state microstructure. Due to higher temperatures, dislocation velocity is increased and dislocation climb produces strain more effectively. Low dislocation densities are achieved by intense recrystallisation (bulging and subgrain rotation).

The transition from semi-brittle to viscous deformation lacks distinct changes in stress strain curves. In fact, approximately steady state is developed for most samples but the level of flow stress is significantly reduced for viscous-dominated conditions. The broad initial grain size distribution promotes this development because diffusion creep processes are active in the small fraction early on. Thereby, a pronounced peak stress is inhibited and a smooth transition from loading to steady state is generated.

5.5.2 Influence of initial grain size distribution

Significant low strength of initially fine-grained material (7-11 µm, 800 °C; Fig. 5.2b) cannot be related to dislocation creep that is insensitive to grain size. Instead, grain size sensitive deformation mechanisms dominate (e.g. diffusion creep accommodated by grain boundary sliding). With increasing shear strain accompanied by grain growth, diffusion is

less effective [Kohlstedt and Hansen, 2015] and dislocation creep becomes more important. The different orientation of the *c*-axis maximum and the weaker texture of the fine-grained sample support a subsequent dominance of dislocation creep.

Hot pressing, and thus annealing of the initial gouge material, reduces the dislocation density and causes growth of the fine-grained fraction. Thereby, more dislocations have to be produced during the loading before dislocation creep can be active. Thereby, higher stresses are achieved at the same deformation conditions (Fig. 5.2b). Dynamic recrystallisation is marginally influenced by this. Stress-induced dissolution-precipitation, favouring small grains, is reduced. A small fine-grained fraction could be produced during loading again causing diffusion processes to a small extent (800 °C, Fig. 5.14). At 700 °C and hot pressing, the increase in flow stress changes the microstructure from pervasive foliation and recrystallisation to an S-C' fabric with the formation of strain free grains along shear bands. Hence, the differences cannot merely be related to the dislocation density as it is at 800 °C. Furthermore, the hot pressed sample has flow stresses above the Goetze criterion. According to 5.5.1, different deformation processes dominate in the samples. Dislocation glide is less effective in the hot pressed sample and comminution by fracturing produces fine-grained material. The grain size distribution is a mixture of both processes and the small grains are predominantly related to brittle processes instead of recrystallisation. At 600 °C, there is no evidence for stress-induced dissolution-precipitation of fine grains after hot pressing. But mass transfer by grain boundary sliding [e.g. Kohlstedt and Hansen, 2015] is indicated by minor grain boundary alignment of equiaxed grains with ~ 15 µm diameter (Fig. 5.8e).

5.5.3 Deformation mechanisms inferred from stress exponents

The calculated stress exponents confirm the transition from brittle-dominated to viscous-dominated deformation estimated from microstructure and stress evaluation (see 5.5.1). The high stress exponent for low temperatures of ~ 6.4 indicates the beginning of the breakdown of power law behaviour, which cannot be assumed for brittle deformation processes, e.g. cataclasis.

The low stress exponent ($n = 1.9$) for high temperatures suggests mixed deformation processes. Grain size insensitive dislocation creep is related to $n = 3$-5 and creates pronounced CPO [e.g. Kohlstedt and Hansen, 2015]. Grain size sensitive diffusion creep is associated with low stress exponents ($n \sim 1$) while grain boundary sliding is related to $n = 2$ and less pronounced textures [e.g. Kohlstedt and Hansen, 2015]. The microstructure does not reveal indications for dominating grain boundary sliding and all samples have pronounced CPO. Hence, grain boundary sliding can be excluded as dominating deformation process. The stress exponent is apparently a result of combined dislocation creep and diffusion creep processes: diffusion creep is more efficient in small grains while dislocation creep is grain size insensitive and limited by dislocation velocities [Tullis, 2002].

5.5.3.1 Evaluation of stress exponents derived from solid medium deformation apparatus

Stress exponents of $n \sim 4$ are consistent with dislocation creep [Gleason and Tullis, 1995; Luan and Paterson, 1992]. Lower estimates ($n \sim$ 2-3) for similar pressure and temperature conditions [e.g. Jaoul et al., 1984; Kronenberg and Tullis, 1984] are often related to imprecise stress measurements in solid medium deformation apparatuses, which are often criticised e.g. for the lack of accuracy of measured stresses [e.g. Gleason and Tullis, 1995]. The strength is assumed to be overestimated due to e.g. the strength of the confining medium and friction in the assembly. NaCl, which is often used as confining medium, is relatively weak [Pec et al., 2012a] and friction correction and hit point determination have been improved. A recent study indicates a good accuracy of mechanical data derived from Griggs apparatus [Richter et al., 2016]. Furthermore, there is no evidence for partial melting in the samples that could lead to low values for stress exponents [Luan and Paterson, 1992].

Stress exponents can only be related to deformation processes if the underlying stress values reflect steady state conditions, especially for regime 1 conditions after Hirth and Tullis [1994]. Required high strain was hard to achieve in compression experiments. Our shear experiments are deformed to high shear strain (up to $\gamma \sim 5$) where mechanical and microstructural steady state is achieved for high temperatures. Hence, the low stress exponents cannot be related to incomplete steady state conditions as suggested by Gleason and Tullis [1995]. In addition, Gleason and Tullis [1995] associate low stress exponents with the transition from regime 2 to regime 1 after Hirth and Tullis [1992]. A similar temperature-dependent microstructural change is not observed in our samples used for calculating stress exponents. However, the microstructure indicates dislocation creep and diffusion creep between 800 °C and 1000 °C. In contrast, only dislocation creep was inferred in earlier studies [e.g. Gleason and Tullis, 1995; Jaoul et al., 1984]. These studies used quartzites with narrow grain size distribution and high average grain sizes whereby grain size sensitive deformation mechanisms are unlikely. The broad grain size range of our starting material with a pronounced fine-grained fraction enables grain size sensitive diffusion creep beside grain size insensitive dislocation creep. Hence, mixed stress exponents are determined.

5.5.4 Extrapolation to natural conditions

With the help of flow laws, laboratory conditions can be extrapolated to natural condition (in general lower strain rates and temperatures). Here, we use a power law flow law (Eq. 1) with the determined stress exponent and activation energy (see 5.5.2) for calculating the material-dependent constant A at 900 °C, 1.5 GPa confining pressure and a shear-strain rate of $1.8 \cdot 10^{-5}\,s^{-1}$.

Several studies [Paterson, 1989; Gleason and Tullis, 1995] indicate the importance of water fugacity to account for the chemical environment and Kohlstedt et al. [1995] intro-

duced a water fugacity term $f_{H_2O}^m$, where m is the exponent of water fugacity. The determination of the water fugacity exponent is crucial and experiments reveal a spread between ~ 0.4 [Chernak et al., 2009] up to 2.8 [Post et al., 1996]. However, it is often assumed to be $m = 1$ for water saturated dislocation creep [Kohlstedt et al., 1995; Hirth et al., 2001]. Hirth et al. [2001] attribute high exponents of $m = 2$ to changing deformation mechanisms (e.g. regime 2 to regime 1) and estimate $m = 1$ by extrapolating flow law parameters to the natural conditions of the Ruby Gap complex. Kidder et al. [2016] simplified the flow law by Hirth et al. [2001] by replacing the water fugacity with a direct relationship of confining pressure and temperature:

$$\dot{\gamma} = 7.6 \cdot 10^{-8} \cdot \Delta\sigma^4 \cdot exp(-\frac{170000 - 18 \cdot 10^{-6} \cdot P_c}{R \cdot T}) \tag{5.2}$$

Applying our flow law parameter to this relation (Eq. 5.2) reveals higher stresses, which is in accord with underestimated stresses at high confining pressures indicated by Gleason and Tullis [1995]. The dominating difference between Kidder et al. [2016] and our study is the low stress exponent, whereby stresses accumulate faster with increasing strain rate (Fig. 5.15b).

The flow law can be tested for natural conditions of the eastern Tonale fault zone, which provides the possibility to analyse quartz microstructures across the brittle-to-viscous transition over a broad temperature range [Stipp et al., 2002]. For subgrain rotation recrystallisation associated with dislocation creep Stipp et al. [2002] calculated strain rates after Hirth et al. [2001] between $10^{-14}\,s^{-1}$ and $10^{-12}\,s^{-1}$. Similar strain rates are extrapolated with our flow law parameters considering water fugacity (Fig. 5.15b). Strain rates two orders of magnitude higher are calculated without accounting for water fugacity.

The calculations of water fugacity are based on the assumption of pure dislocation creep. The influence of mixed deformation mechanisms is unclear. Since our low stress exponent is related to a combination of dislocation creep and diffusion processes (see 5.5.2) the water saturation of dislocation creep processes is not guaranteed and the effect of water fugacity on diffusion is unclear. Hence, the extrapolation to lower strain rates is uncertain and the absolute value of the extrapolated strain rates is probably overestimated. But lower stress exponents indicate higher differential stress at intermediate strain rates ($10^{-10}\,s^{-1}$ - $10^{-8}\,s^{-1}$).

Tab. 5.3: Selection of flow law parameters from literature.

source	Pc [GPa]	n	Q [kJ/mol]	comments	label in Fig. 5.15
Jaoul et al. (1984)	1.5	2.3	171	water 'as-is'	J et al. '84
Kronenberg and Tullis (1984)	0.9-1.6	2.6	134		K & T '84

source	Pc [GPa]	n	Q [kJ/mol]	comments	label in Fig. 5.15
Paterson and Luan (1990)	0.3	2.3	148	silica gel	P & L '90
Luan and Paterson (1992)	0.3	4	152	silica acid	L & P '92
Gleason and Tullis (1995)	1.5-1.7	4	223	no melt	G & T '95
Hirth et al. (2001)		4	135	water fugacity term included	H et al. 01
Kidder et al. (2016)	1.3	4	135	simplified water fugacity	K '16
this study	1.5	1.9	170		

Correlating microstructure and mechanical data with natural conditions without flow law extrapolation avoids the uncertainties of water fugacity and portions of mixed deformation mechanisms. Samples with overall viscous deformation structures have differential flow stresses below confining pressure values (Goetze criterion). All other samples have differential flow stresses that exceed the confining pressure (Fig. 5.16a). A lower boundary for transitional samples cannot be determined. Based on the microstructure an empirical transition zone is indicated in figure 5.16b and 5.16c for 1.5 GPa confining pressure. This transition is not isostatic. Apparently, the shear-strain rate is overestimated without data correction for lower confining pressures.

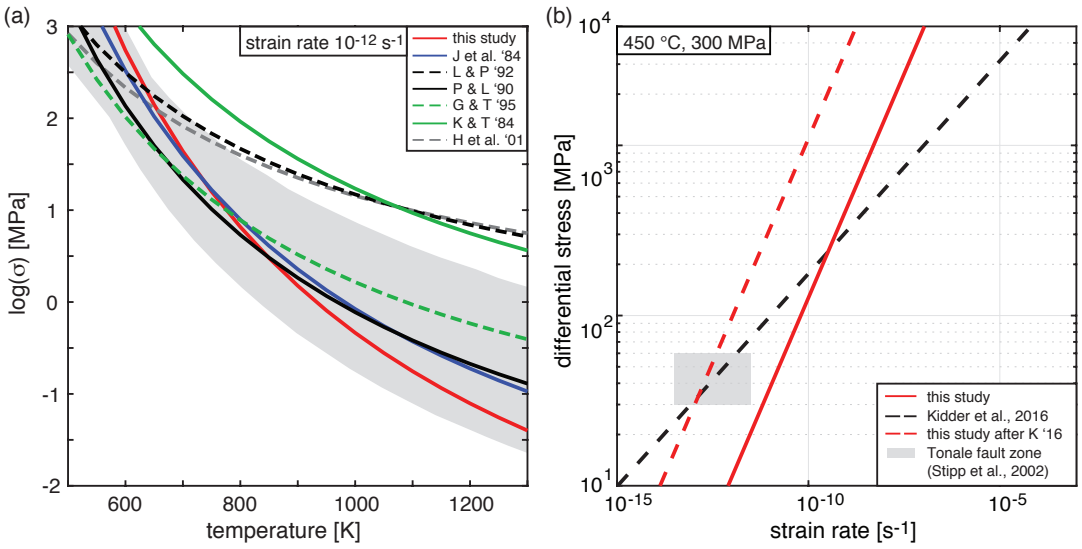

Fig. 5.15: Extrapolation of calculated flow law parameters. (a) Differential stress - temperature plot for a strain rate of $10^{-12}\,s^{-1}$. Grey area marks the experimental range for stress exponent, activation energy and flow stress analysed in Paterson and Luan [1990]. Calculated lines of some, mostly more recent studies are included (dashed lines - $n = 4$, solid line - $n < 3$). Studies with low activation energies lie outside the grey area towards higher temperatures. Labels relate to table 5.3. (b) Differential stress - shear-strain rate plot at 450 °C and 300 MPa. Applying the water fugacity term after Kidder et al. [2016] to this study shifts the differential stress to higher values at the same strain rate. The grey area marks the conditions of the Tonale fault zone [Stipp et al., 2002].

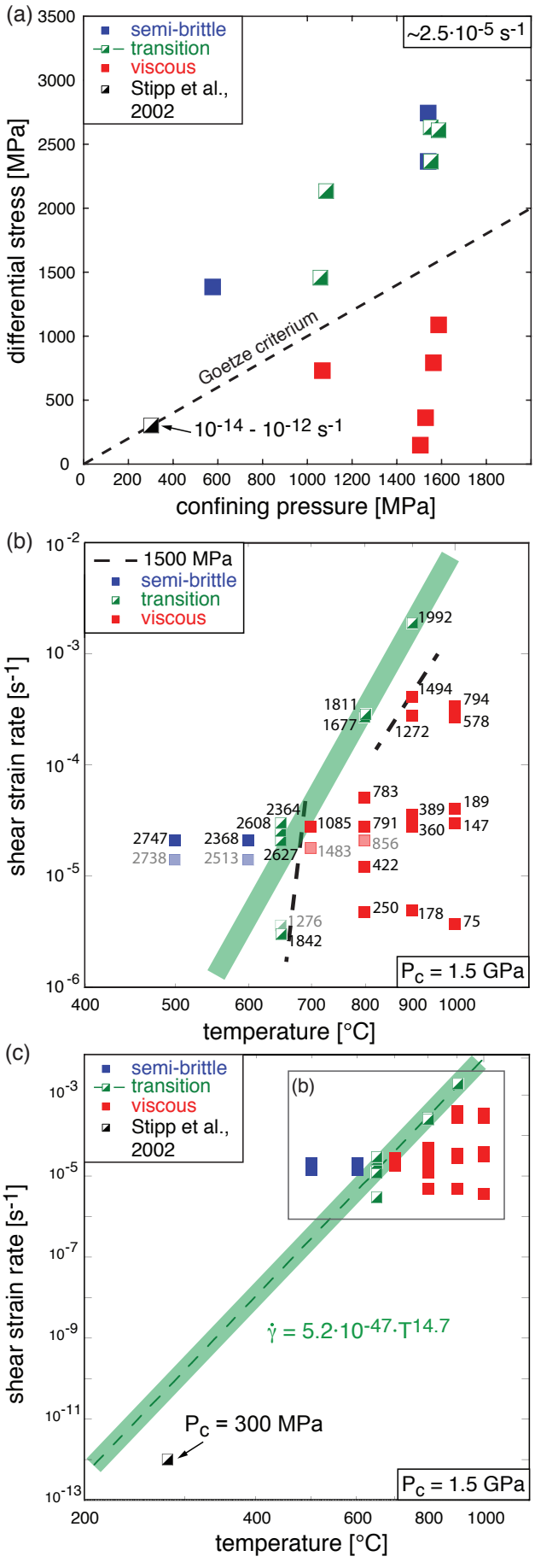

Fig. 5.16: Extrapolation based on differential stresses or microstructure. (a) Differential stress versus confining pressure at $2.5 \cdot 10^{-5}\,s^{-1}$. Viscous dominated samples are below the Goetze criterion (dashed line) while all other samples are above it. Semi-brittle samples cannot be separated from transitional samples. (b) Shear-strain rate versus temperature showing a microstructurally determined transition between semi-brittle and viscous dominated samples at 1.5 GPa confining pressure. Flow stresses are shown (grey values - peak stresses of peak stress samples). Dashed black lines indicate interpolations of 1500 MPa differential stresses. (c) Expansion of (b) to natural conditions. The green line marks the extrapolation of the approximated transition to slow shear-strain rates. The transition in natural sample from Stipp et al. [2002] is indicated (note the lower confining pressure).

5.6 Conclusions

A set of shear experiments performed on quartz gouge under elevated confining pressures (predominantly 1.5 GPa) and temperatures (500 °C - 1000 °C) at intermediate to fast shear-strain rates ($3.5 \cdot 10^{-6}\,s^{-1}$ to $\sim 2 \cdot 10^{-3}\,s^{-1}$) illustrates the transition from semi-brittle to viscous deformation. The Goetze criterion is reinforced as marker for this transition. Samples above ($\Delta\sigma > P_c$) are characterised by Riedel geometry or S-C' fabric at high shear strain and high friction coefficients. At low temperatures, a positive pressure-dependence is observed as well as an ambiguous temperature-dependence of stress. Cataclastic flow partly accompanied by stress-induced dissolution-precipitation is suggested as dominating deformation process supported by a power law breakdown indicated in the stress exponent ($n = 6.4 \pm 1.3$). For $\Delta\sigma < P_c$, viscous dominated deformation is supported by an inverse pressure and temperature dependence and low friction coefficients. The microstructure is dominated by a pervasive foliation at high shear strain accompanied by pronounced CPO and increasing recrystallised grain sizes with increasing temperature. The low stress exponent ($n = 1.9 \pm 0.6$) indicates a combination of diffusive mass transfer processes and dislocation creep. Thereby, diffusive mass transfer is favoured in the small grain size fraction while grain size insensitive dislocation creep dominates in large grains. The constant stress exponent between 800 °C and 1000 °C suggests no change in the limiting factor.

6 | Diffusion creep processes promoted by extensional shear bands in experimentally deformed quartz gouge

Abstract

Shear experiments on crushed quartz fragments are performed at high confining pressures (predominantly 1.5 GPa) and high temperatures (500 °C - 1000 °C) at intermediate to fast shear-strain rates ($3.5 \cdot 10^{-6}\,s^{-1}$ to $2 \cdot 10^{-3}\,s^{-1}$). The transition from semi-brittle flow to dominating crystal plasticity is characterised by an inverse temperature-dependence, a more pronounced shear-strain rate dependence with increasing temperature, and a shift in pressure dependence with increasing temperature. Localised deformation with Riedel geometry merges into a single penetrative foliation with a pronounced S-C' fabric as an intermediate state. In this process, mass transfer processes in highly fragmented, fine-grained zones are promoted. Deformation lamellae can occur in brittle dominated samples while relicts of high dislocation densities can remain in highly recrystallised samples with dominating viscous processes.

6.1 Introduction

In the transition zone from brittle-dominated to viscous-dominated deformation cataclasis (e.g. fracturing, frictional sliding) and intracrystalline processes (e.g. dislocation creep, dissolution-precipitation) are active next to each other. The interaction of these processes and the persistence of brittle features in crystal plastic regimes and vice versa are significant for stress build-up and stress distribution influencing e.g. the potential for earthquakes.

The importance of brittle precursors for the onset of crystal plasticity has been highlighted by previous studies [e.g. Mancktelow and Pennacchioni, 2005; van Daalen et al., 1999; Vernooij et al., 2006; Stünitz et al., 2003]. For example, comminution increases the fine-grained fraction and produces more surfaces in these regions promoting mass transfer processes (e.g. Pec et al., 2012a; Trepmann and Stöckhert, 2003; van Daalen et al., 1999; Keulen et al., 2008). In addition, high stress sites at crack tips are preferred spots for the generation of dislocations [e.g. Barber et al., 2010].

At the same time, dislocation pile-ups can be nucleation sites for microcracks [Wong, 1990]. Microstructures associated with the onset of crystal plasticity occur early in the semi-brittle field and are consumed by recrystallisation at low dislocation creep conditions, e.g. deformation lamellae (parallel sets of thin, closely spaced, optically distinct features) and misoriented bands (often referred to as deformation bands - bands in single grains with different crystallographic orientation from the host grain) [e.g. Carter et al., 1964; Tullis et al., 1973; Groshong Jr., 1988].

S-C' fabrics seem to be related to the transition from semi-brittle-flow to dominating crystal plasticity: At semi-brittle conditions, an S-C' fabric is developed at high strain [e.g. Pec et al., 2012a] while an S-C' fabric at low shear strain is indicated at viscous-dominated deformation [Dell'Angelo and Tullis, 1989].

We performed a set of deformation experiments at elevated pressures on quartz illustrating the brittle-to-viscous transition with focus on the development of mass transfer processes along extensional shear bands and misoriented zones in grains.

6.2 Methods

6.2.1 Experimental procedure

Experiments were performed on a crushed quartz single crystal that had been used in previous studies [e.g. Tarantola et al., 2012; Richter et al., 2016; Stünitz et al., 2017]. A sieved grain size fraction below 100 µm was used. This quartz powder (0.1 g) with 0.2 wt% water added was placed between alumina (Al_2O_3) forcing blocks (pre-cut at 45 °), wrapped in Ni foil and weld-sealed in a platinum jacket. The confining medium was NaCl. The tem-

perature was controlled by S-type (> 800 °C) or K-type (≤ 800 °C) thermocouples depending on the temperature of the experiment.

All samples were pressurised and heated to deformation conditions by increasing pressure and temperature in alternating steps. Care was taken to ensure that the water could not evaporate. The actual experiment started by applying a directional compressive force on the sample by moving the σ_1 piston. The displacement rate of the σ_1 piston was constant throughout the whole experiment and could be translated to an approximately constant shear-strain rate. The experiment was stopped by quenching the sample to 200 °C with cooling rates about 150-300 °C min^{-1} and slowly depressurising the sample to ∼ 250 MPa. Afterwards, pressure and temperature were decreased to room conditions.

The recorded applied force on the σ_1 piston, the displacement of the σ_1 piston and the oil pressure of the hydraulic ram (all measured in mV) were translated into maximum principal stress (σ_1 in MPa) and minimum principal stress (σ_3 in MPa) as well as displacement (d in mm). Data processing was performed according to Richter et al. [2016] including a correction of the apparatus distortion, an area correction for changing overlapping forcing blocks and a displacement-dependent correction of the confining pressure.

6.2.2 Microstructural analysis

Doubly polished thin sections (approximately 20-25 µm thickness) were prepared for microstructural analysis by cutting the samples parallel to the displacement direction. The thin sections were analysed with light microscopy and scanning electron microscopy. Backscatter images (BSE) were taken with a Philips XL 30 field emission environmental scanning electron microscope (SEM) operating at acceleration voltages between 10 kV and 20 kV. Computer-integrated polarisation microscopy (CIP) [Panozzo Heilbronner and Pauli, 1993] and electron backscatter diffraction (EBSD) were used to obtain orientation contrasts. CIP analysis was performed on a polarisation microscope using lambda plates. For EBSD analysis, thin sections were polished additionally with colloidal silica suspension Struers OP-U non dry for three to six minutes. The analysis was carried out under high vacuum on a Zeiss Merlin field emission SEM with a Nordlys nano camera using AZtec software for data acquisition of diffraction patterns. The acceleration voltages varied between 10 kV and 15 kV and step sizes between 0.15-0.4 µm were used. The EBSD data were analysed with the MTEX toolbox [Hielscher and Schaeben, 2008]. Volumetric grain sizes were calculated using the StripStar method [Heilbronner and Barrett, 2014] based on grain size maps derived from EBSD data. The modal value of volumetric equivalent diameters was used as representative value. The shape fabric is analysed with tessellations of autocorrelation functions (ACF) of greyscale micrographs [Panozzo Heilbronner, 1992; Heilbronner, 2002]. The average of 16-24 individual ACF (100 µm by 100 µm) was calculated.

All images of the microstructure are orientated with a sinistral sense of shear and horizontal shear zone boundaries.

6.3 Results

6.3.1 Mechanical data

Experiments are performed at temperatures between 500 °C and 1000 °C at confining pressures of 1.0 GPa or 1.5 GPa. Most of the experiments are conducted at a constant shear-strain rate of $\sim 2.5 \cdot 10^{-5}\,s^{-1}$ (Table 6.1). In general, samples with shear stresses (τ) above 750 MPa show steady state to minor strain hardening while low-stress samples ($\tau < 750$ MPa) show steady state or minor strain weakening (Fig. 6.1).

Tab. 6.1: Experimental conditions of experiments.

exp. #	T [°C]	P_c[1] [MPa]	shear strain rate [$10^{-5}\,s^{-1}$]	shear strain	max. τ [MPa]	τ at $\gamma = 3$ [MPa]
340br	500	1510	1.4	1.6	1369	-
450br	500	1540	2.1	3.2	1606	1374
338br	600	1522	1.4	1.4	1257	-
479br	600	1538	2.1	3.9	1212	1184
435br[2]	650	1507	2.1	3.6	1349	1314
481br	650	1554	3.0	4.2	1269	1182
380br	700	1500	-	-	-	-
437br	700	1529	1.9	1.7	742	-
383br	700	1585	2.8	4.9	623	543
487br	800	1511	-	-	-	-
439br	800	1526	2.1	1.4	428	-
388br	800	1527	2.8	4.8	429	396
412br	900	1530	2.8	2.9	238	180
417br	1000	1576	-	-	-	-
337br	1000	1506	3.0	3.2	76	74
494br	650	1088	4.8	5.7	1198	1063
452br	700	1064	2.7	4.4	768	726
448br	800	1067	2.9	4.5	432	364
500br	650	1502	0.35	1.1	638	-
447br	800	1556	27	4.1	892	839
499br	900	1535	189	4.0	1008	996

At 1.5 GPa confining pressure, shear-strain rates of $2.5 \cdot 10^{-5}\,s^{-1}$ and low temperatures (500 °C to 650 °C), peak and steady state shear stresses are high (~1200 to 1600 MPa) and vary unsystematically with temperature: at 600 °C, samples can be weaker than 650 °C samples or similar in strength, whereas samples at 500 °C are the strongest ones. At higher deformation temperatures (700 °C to 1000 °C), there is a systematic temperature depend-

[1] average of the confining pressure P_c
[2] upper alumina piston deformed

ence: shear stresses decrease with increasing temperature. The largest decrease occurs between 650 °C and 700 °C ($\Delta\tau \sim 600$ MPa). At higher temperatures, the decrease is not as pronounced as between 650 °C and 700 °C but systematic (700 °C: flow stress ~600 MPa, 1000 °C: ~75 MPa). High stress drops in 481br and 450br (Fig. 6.1a) are related to slip at the forcing-block-sample interface.

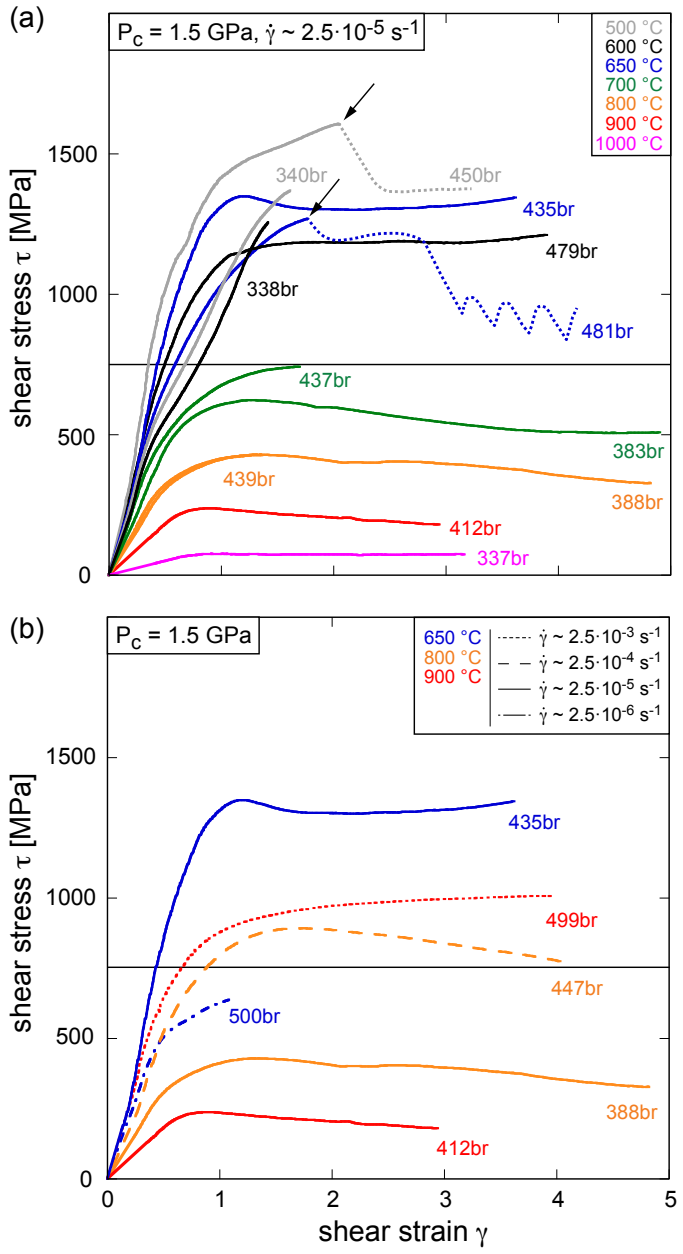

Fig. 6.1: Shear stress vs. shear strain (horizontal line marks the Goetze criterion). (a) Shear-strain rates of $\sim 2.5 \cdot 10^{-5}$ s^{-1} at 1.5 GPa confining pressure. At high temperatures an inverse temperature dependence is obvious whereas below 700 °C, there is no obvious temperature dependence. A significant decrease (~ 600 MPa) in strength occurs between 650 °C and 700 °C. In 450br and 481br, slip occurs along the shear zone-piston interface resulting in stress drops (arrows). The peak strength of sample 439br is almost identical with 388br. (b) Various shear-strain rates at 650 °C, 800 °C and 900 °C illustrating the positive shear-strain rate dependence.

The transition from loading to steady state occurs around a shear strain of 1 to 1.5 for temperatures > 650-700 °C. For higher temperatures the transition is earlier, around $\gamma = 0.7$.

A strong and positive strain-rate dependence of flow stress is observed at 650 °C, 800 °C and 900 °C (Fig. 6.1b): flow stresses decrease for slower strain rates (650 °C: $\Delta\tau \sim 700$ MPa; 800 °C: $\Delta\tau \sim 500$ MPa; 900 °C: $\Delta\tau \sim 800$ MPa).

At 1.0 GPa confining pressure, the shear stress at 650 °C is lower than the shear stress at 1.5 GPa confining pressure. At higher temperatures (700 °C and 800 °C), shear stresses are similar for 1.0 GPa and 1.5 GPa confining pressure (Table 6.1).

6.3.2 Microstructural observations

6.3.2.1 Starting material

The crushed starting material consists of sharp-edged splinters (Fig. 6.2a) many of which are highly elongated. The smallest grain size fraction is below 1 µm. Several highly elongated grains with long axis larger than 100 µm exist although a 100-µm sieve was used for grain size separation.

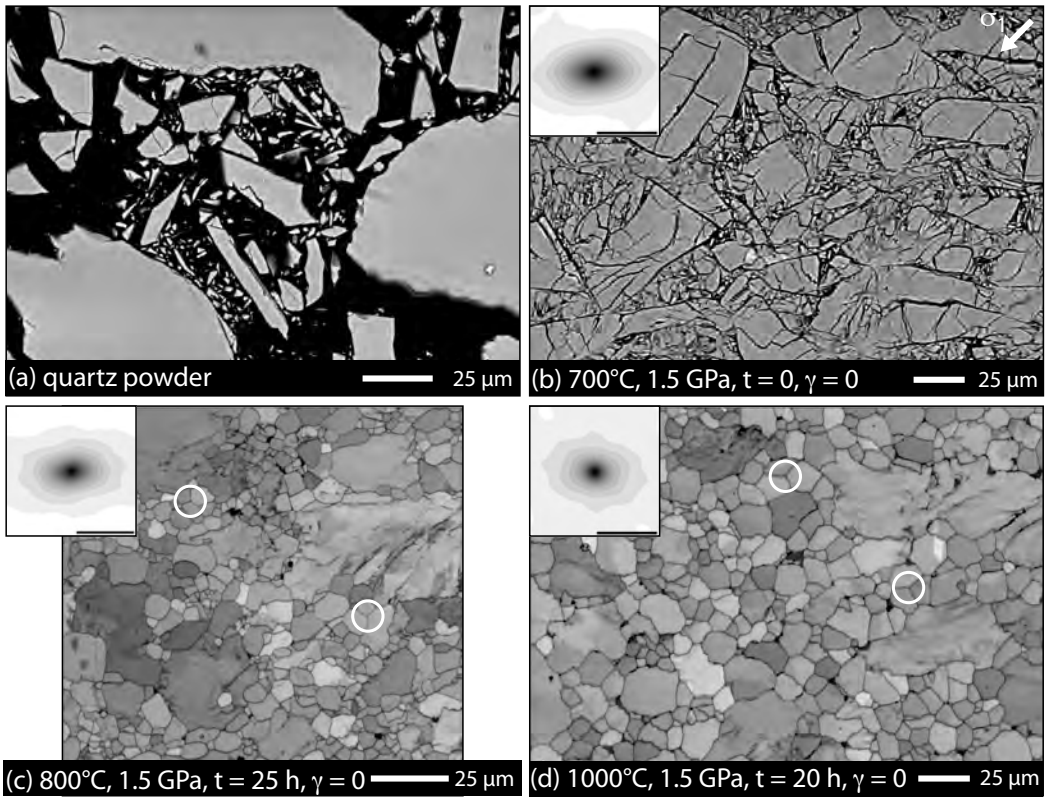

Fig. 6.2: Evolution of the starting material before actual deformation ($\gamma = 0$). Bulk autocorrelation functions (ACF) of pressurised samples are included (scale bar 50 µm). (a) Crushed quartz powder contains several elongated splinters and a lot of very fine-grained material (BSE image). (b) After pressurisation, the powder is highly compacted (380br, BSE image). The elongated grains are aligned and all grains are pervaded by fractures. (c) and (d) Hydrostatic conditions. During the simulated run-in the grains, especially the small ones, grow and cracks heal. Therefore, the amount of fine-grained material is reduced. In addition, porosity is reduced. Circles mark 120° triple points. (c) 800 °C (487br, band contrast image). (d) Hydrostatic conditions at 1000 °C (417br, band contrast image). Grain growth is more effective than at 800 °C.

At 1.5 GPa confining pressure the starting material is compacted by fragmentation and rearrangement of grains, resulting in ~ 8 % porosity. The sample thickness is ~ 0.8 mm after pressurisation. At 700 °C and 1.5 GPa confining pressure, the material shows a slight shape preferred orientation (SPO) of elongated grains subparallel to the piston-sample interface, inclined to the compaction direction (Fig. 6.2b). The grains are re-crushed and fractured on grain-to-grain contacts. Most of the large grains are fragmented or cut by several fractures.

Before deformation, the amount of small grains is reduced by grain growth depending on the applied temperature (Fig. 6.2c - 800 °C, Fig. 6.2d - 1000 °C). Small grains grow at the expense of large ones. At high temperatures, grains become equiaxial, straight grain boundaries develop and 120° angles at triple junctions are common. SPO still indicates a subparallel orientation to the shear zone boundaries but the elongation in this direction is less pronounced.

6.3.2.2 Temperature-dependent evolution at 1.5 GPa confining pressure

At a shear-strain rate of $2.5 \cdot 10^{-5}$ s^{-1}, the evolution of microstructure between 500 °C and 1000 °C is described. Samples deformed at temperatures below 700 °C appear heterogeneous on thin-section scale while samples deformed at temperatures above 700 °C are homogeneously deformed (Fig. 6.3) at high shear strain.

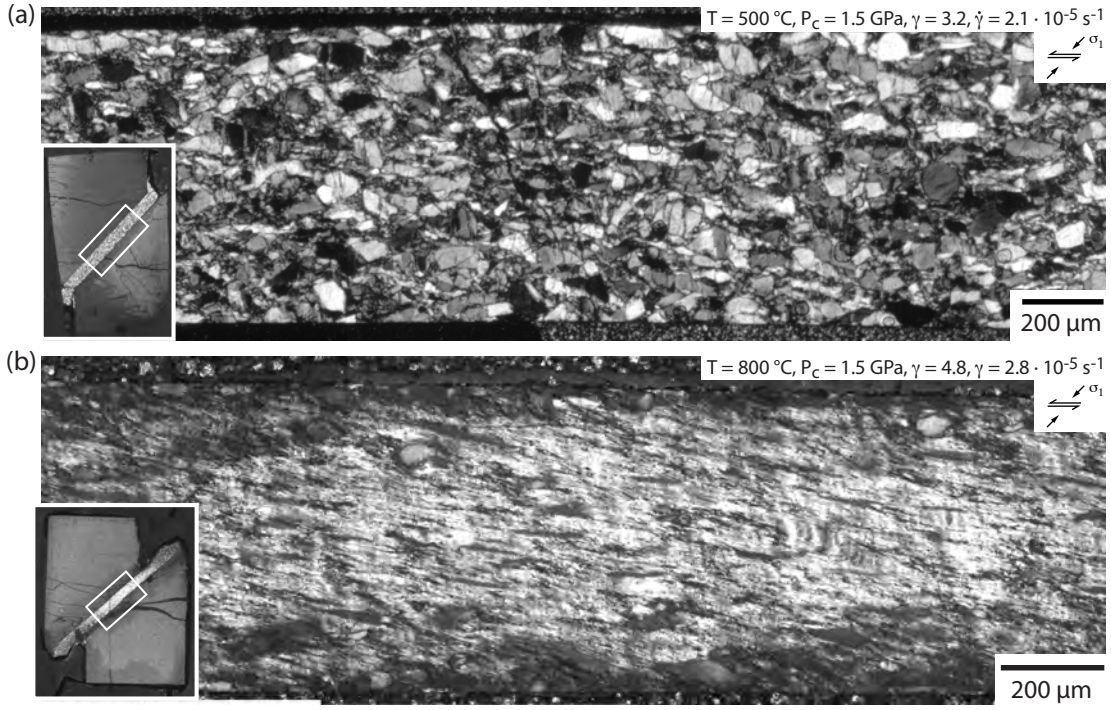

Fig. 6.3: Overview of samples. (a) At 500,°C, brittle deformation processes dominate the sample and deformation localises. (b) At 800,°C the sample is pervasively deformed by viscous deformation processes.

Low-grade conditions($\leq$ 650 °C)

Complex Riedel bands develop at low temperatures and high shear strain ($\gamma > 2.5$) with synthetic R bands and antithetic P and R' bands (Fig. 6.4: 500 °C - 650 °C). The R bands

are at $\sim$ 20-25° to the direction of external loading and grain size comminution occurs along these bands. Riedel bands are not connected and do not cross the whole sample, which is in accord with mechanical data that show no stress drop related to failure.

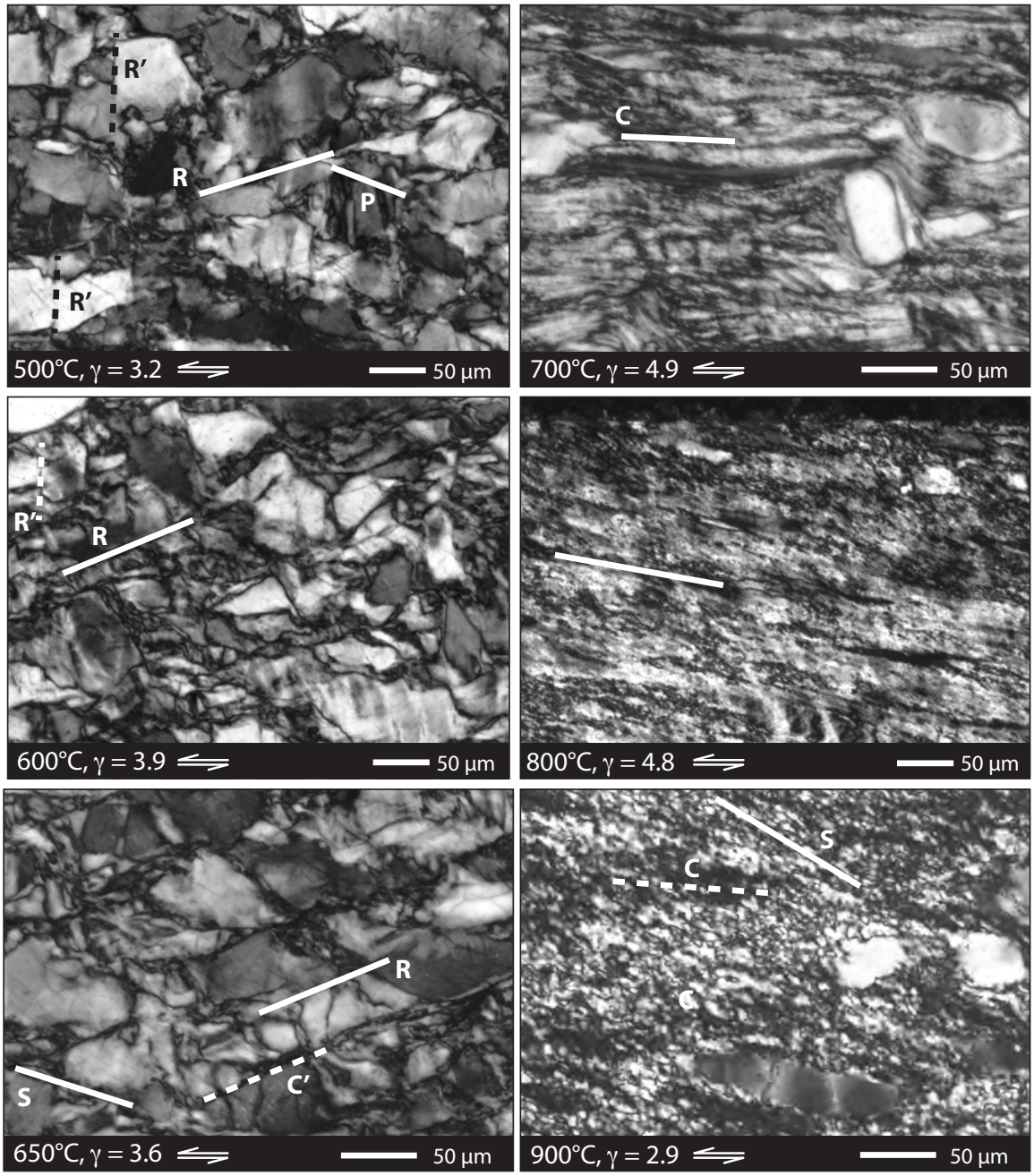

Fig. 6.4: Microstructural development with increasing temperature at 1.5 GPa (crossed polarised images). Fabrics with Riedel bands dominate at low temperatures ($\leq$ 650 °C) and evolve to penetrative foliations at high temperatures (> 700 °C). See text for more details.

Riedel geometry is not yet developed at low shear strain and grains are barely rounded (Fig. 6.5). The sharp edges of original fragments are dismantled. Grains are intensively cracked but no intergranular cracks occur. At high shear strain, the SPO indicates more elongated and flattened grains (Fig. 6.6). Grain boundaries become more irregular.

At high shear strain, several clasts show undulatory extinction that occurs in band-like zones (misoriented bands) at a high angle towards the shear zone boundary. The bands are narrow compared to the grain size and the transition to the host grain is sharp. These bands often appear in pairs or couple of pairs in a single grain (Fig. 6.4). Partly, the bands can be traced across grain boundaries (Fig. 6.5b) and some bands show small cracks in the centre (600 °C in Fig. 6.14a). The occurrence increases towards 650 °C. The crystallographic preferred orientation (CPO) of the bands rotates anticlockwise to the shear sense with respect to the host grain, which is commonly closer to the direction of external load.

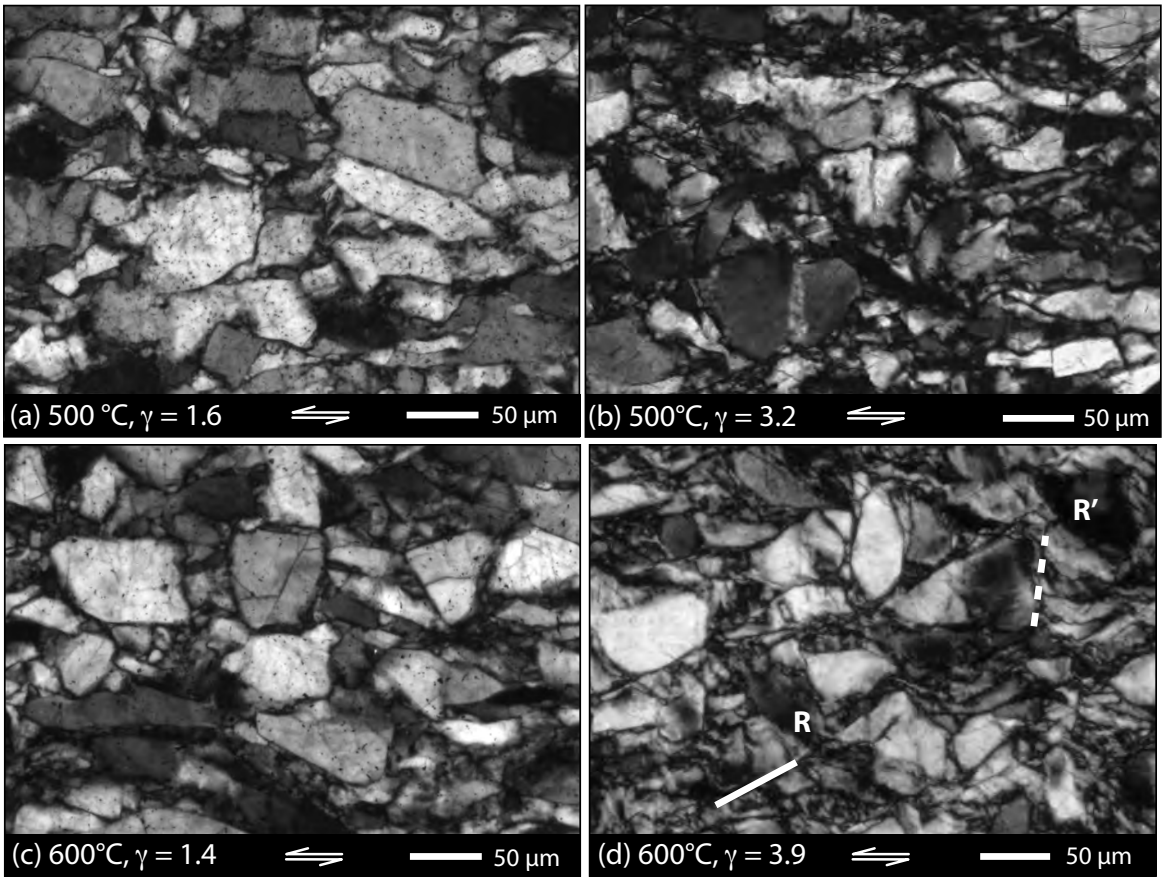

Fig. 6.5: Microstructural evolution with increasing shear strain at low temperatures. (a) and (c) Barely rounded grains at low shear strain (circular polarised images). (b) and (d) Riedel geometry at high shear strain (crossed polarised images). Misoriented bands are developed in several clasts.

Deformation lamellae start to form in some large clasts at 600 °C and become more pronounced with increasing temperature. The spacing between the lamellae is about 1-3 µm (in BSE images). Furthermore, zones with small, equiaxed grains evolve in R-band direction at 600 °C (Fig. 6.10a). The porosity is increased in between these grains. These zones widen towards higher temperatures (Fig. 6.10b).

Unloading cracks that originated during quenching and depressurisation are frequently generated subparallel to P bands. Some of them are 10's of micrometers long but most of them expand a few micrometers. The width is related to the elongation: long unloading cracks can open up to 1 µm while the width of short cracks is generally less than 200 nm.

They are often developed adjacent to zones with equiaxed grains. Larger cracks cross these zones while small cracks are restricted to the boundary.

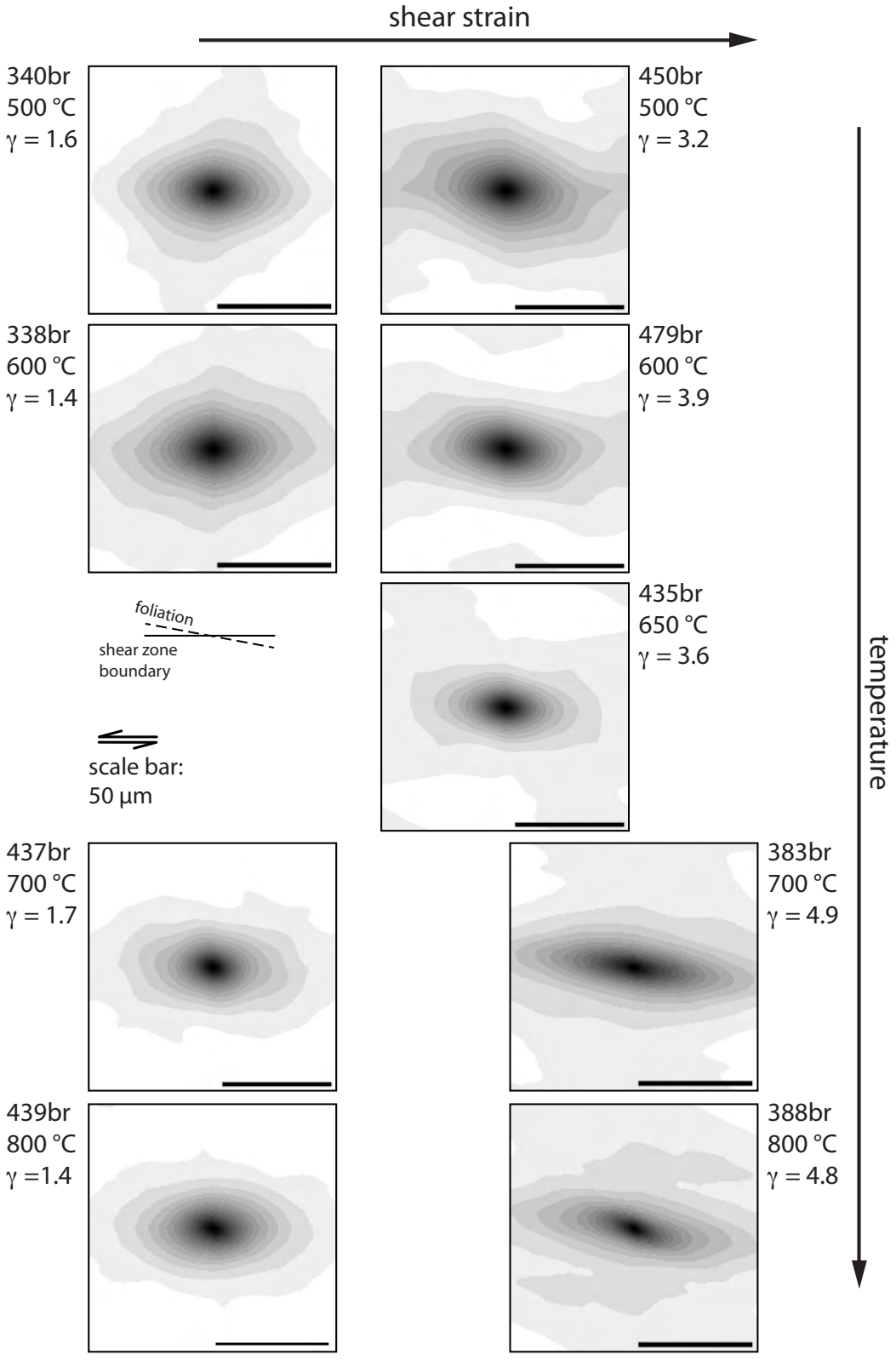

Fig. 6.6: Grain shape evolution with increasing temperature and increasing shear strain (ACF, scale bar 50 µm). Flattening and elongation increase with increasing temperature. With increasing shear strain, the shape becomes more elongated, especially at temperature above 650 °C.

At 650 °C, an S-C' fabric is developed besides Riedel geometry with S planes in P-band orientation and C' planes subparallel to R-bands. Several clasts with misoriented grains develop tails and grains with core-mantle structures (see section 6.3.2.6) start to develop.

High-grade conditions ($\geq$ 700 °C)

At high temperatures, viscous processes define the microstructure (Fig. 6.4: 700 °C - 900 °C) and a single penetrative foliation defined by elongated recrystallised grains and highly elongated remaining clasts is developed at high shear strain. At peak strength ($\gamma \sim$ 1-1.5), an S-C' fabric is developed at 700 °C and 800 °C (Fig. 6.7). The SPO indicates more flattening compared to lower temperatures for low shear strain (Fig. 6.6). With increasing shear strain, the shape becomes highly elongated.

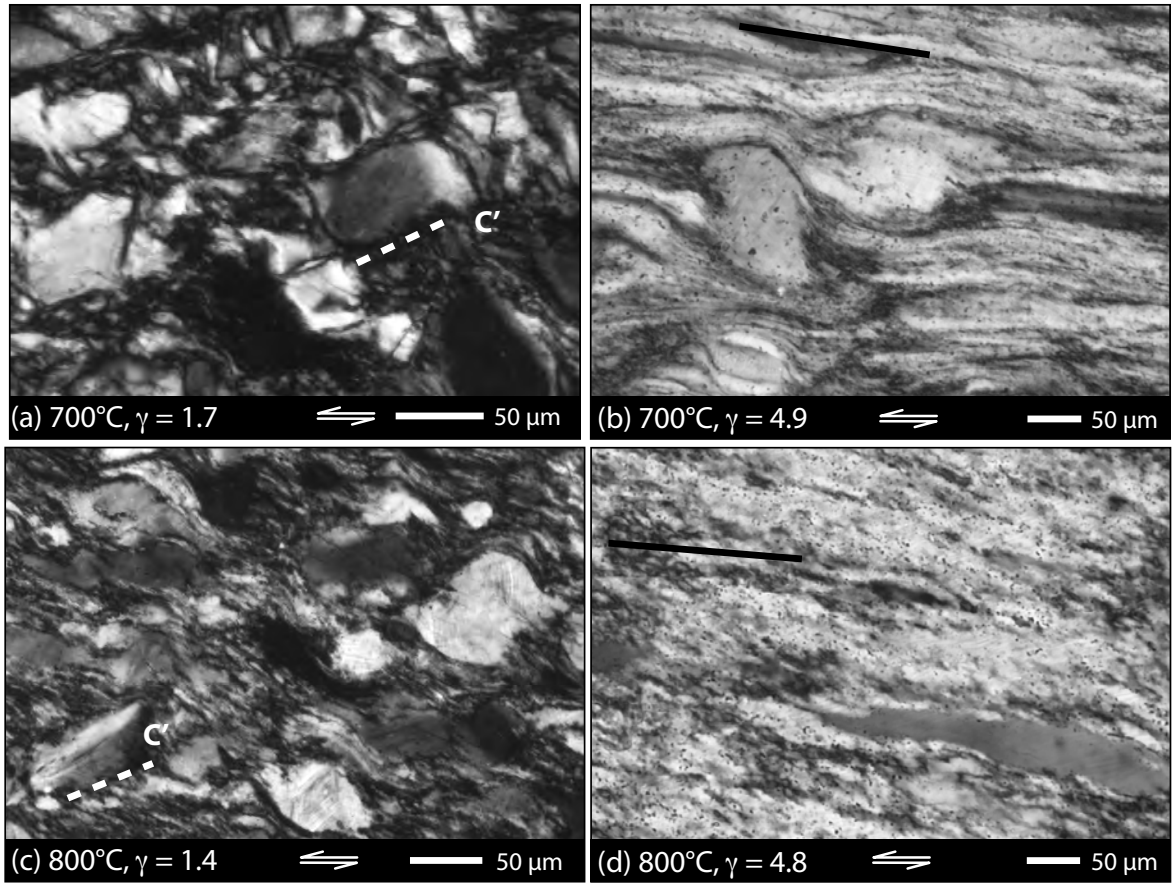

Fig. 6.7: Microstructural evolution with increasing shear strain at intermediate temperatures (circular polarised images). (a) and (b) S-C' fabric at low shear strains. (b) and (d) One pervasive foliation by recrystallised grains at high shear strains.

Larger clasts show more penetrative recrystallisation with increasing temperature of deformation and with increasing strain (Fig. 6.7). At $\gamma \sim 5$ about 10 % of clasts remain at 700 °C and 5 % of clasts can be distinguished at 800 °C. The recrystallised grain size increases continuously from 700 °C to 1000 °C (700 °C - 1.8 µm, 800 °C - 3.8 µm, 900 °C -

5.6 μm, 1000 °C - 10.1 μm). At 1000 °C, recrystallisation is almost complete at a shear strain of $\gamma \sim 3$.

At low shear strain, equiaxed grains exist along C' planes (Fig. 6.10c, 6.10d). Such zones of euhedral grains are not visible at high shear strain. Large clasts have tails and core-mantle structures frequently occur. Misoriented bands are less common. Remaining clasts at high shear strain are roundish (700 °C) with partly extensive tails and core-mantle structures, or are highly elongated (800 °C). Bands with different extinction occur in highly elongated clasts (Fig. 6.4: 800 °C, 900 °C).

Deformation lamellae (1-3 μm spacing) are well-established at low and high shear strain. They occur in elongated clasts as well as in roundish clasts. The lamellae are often subparallel to the basal plane. In highly elongated clasts, deformation lamellae are often wavy. At 700 °C and 800 °C, deformation lamellae are frequent. With increasing temperature, they become less common and they are no longer present at 1000 °C. But deformation lamellae cannot be identified with EBSD. No variations in diffraction patterns occur across lamellae (step size: 0.15 - 0.2 μm) although they are clearly visible in BSE images and light microscopy.

At low shear strain, unloading cracks are common in S plane orientation. With increasing shear strain, unloading cracks become less pronounced in the recrystallised matrix. But they are established in between deformation lamellae inside remaining clasts.

6.3.2.3 Texture evolution with temperature and strain

The starting material before deformation has a random CPO. Only *z*- and *r*-axes show a preferred orientation to some extent (Fig. 6.8: 1000 °C, hydrostatic). The CPO of deformed samples progressively changes with increasing temperature (Fig. 6.8, Fig. 6.9). Below 650 °C, the CPO of the *c*-axes, which is dominated by large clasts, shows a random distribution. At 650 °C, a slightly preferred orientation is developed by peripheral *c*-axes. At 700 °C, a strong CPO is developed with one peripheral maximum of *c*-axes that are slightly rotated with the sense of shear. The *a*-axes show a girdle inclined to the shear zone boundary ($\sim$ 10-15 °). At 900 °C, a central *c*-axis maximum is developed next to the peripheral *c*-axis maximum. Towards 1000 °C, the *c*-axes evolve to a single central maximum and the *a*-axis maxima become peripheral. The recrystallised matrix dominates the CPO of high strain samples above 700 °C.

At 700 °C and 800 °C, low-strain samples with pronounced S-C' fabrics also show a peripheral maximum of *c*-axes for small grains. But the maximum is less pronounced than at high strain and it is rotated anticlockwise with the sense of shear.

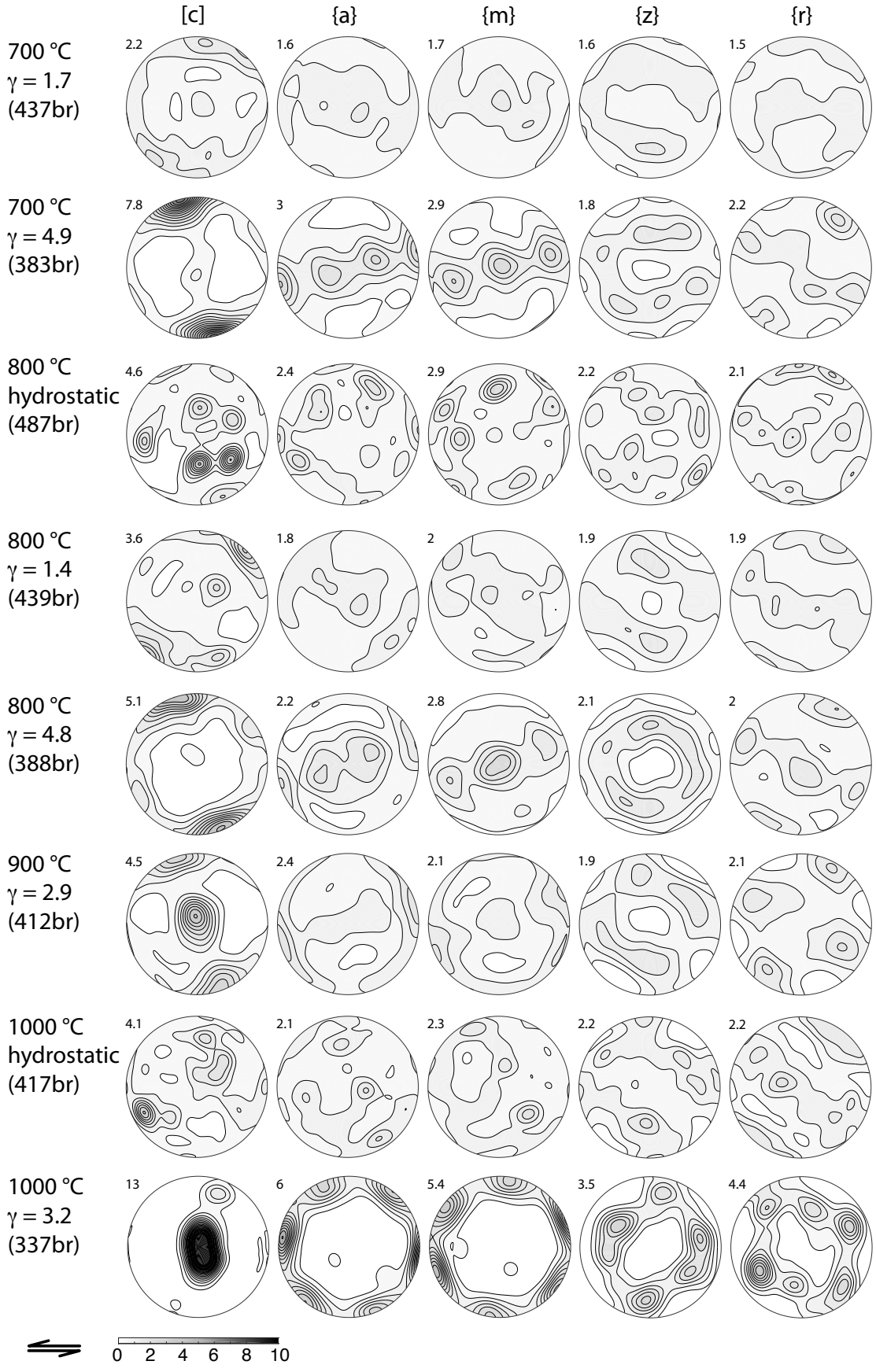

Fig. 6.8: Texture evolution at high temperatures (1.5 GPa confining pressure and $2.5 \cdot 10^{-5}\,\mathrm{s}^{-1}$). Pole figure maximum is indicated.

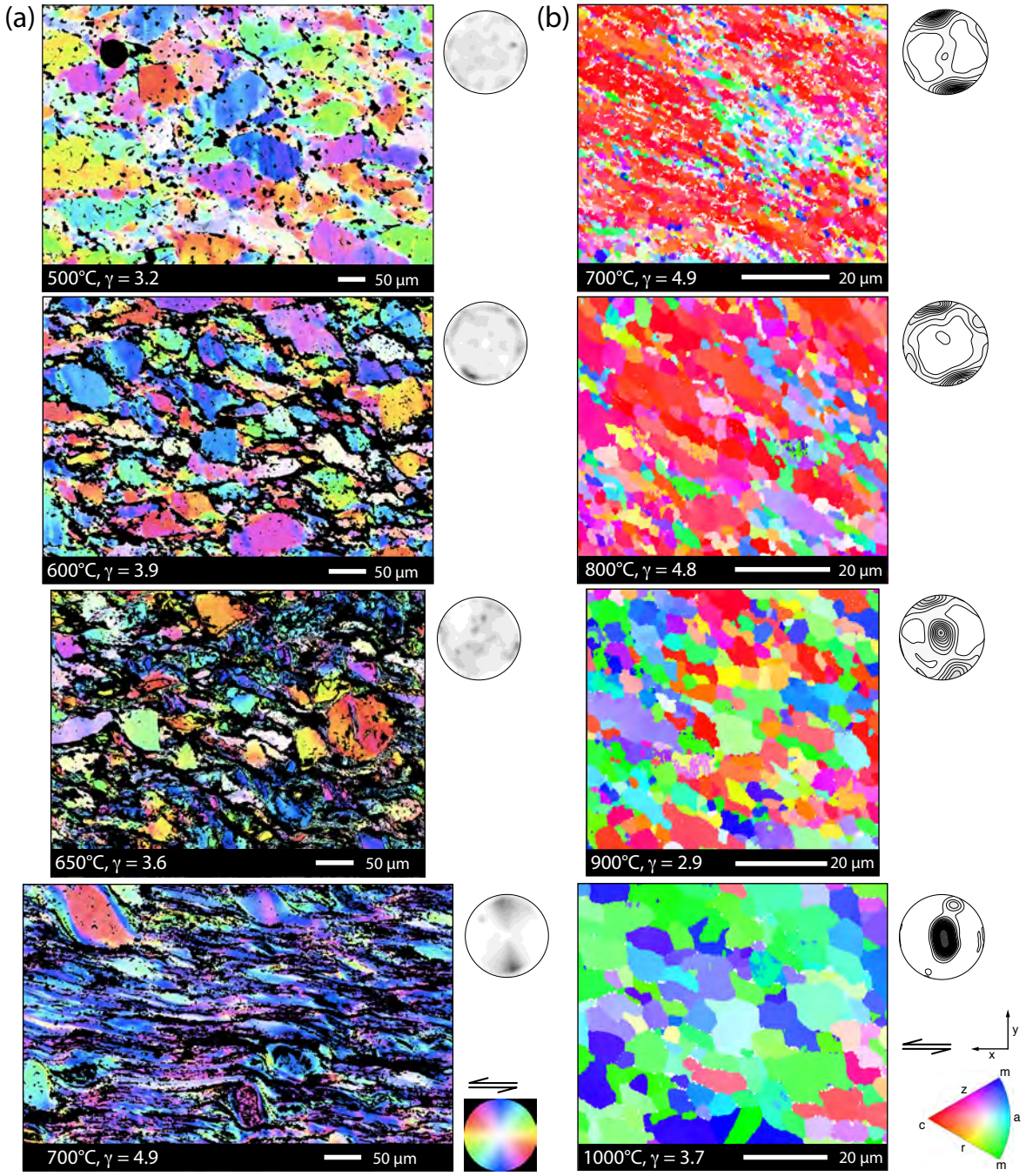

Fig. 6.9: Crystallographic preferred orientation (CPO) of *c*-axes with increasing temperature. (a) CIP-derived *c*-axes orientation images (COI) of samples between 500 °C and 700 °C. The CPO of the clasts evolves from a random texture towards a peripheral maximum slightly orientated with the sense of shear. (b) EBSD maps (IPF colouring in y direction) and pole figures of samples at high temperatures (step size 0.2 µm). The CPO of the *c*-axes evolves from a peripheral maximum (700 °C and 800 °C) towards a single central maximum (1000 °C).

6.3.2.4 Strain rate effect on microstructure

At 650 °C and a shear-strain rate of $3.5 \cdot 10^{-6}\,s^{-1}$, several grains already have roundish edges and irregular grain boundaries at low shear strain ($\gamma \sim 1.1$). An S-C' fabric is visible as well as Riedel bands. Several grains show core-mantle structures and the CPO of *c*-axes shows a slightly preferred orientation with an anticlockwise-rotated sense of shear.

At 800 °C and 900 °C, faster shear-strain rates ($2.7 \cdot 10^{-4}\,s^{-1}$ and $1.9 \cdot 10^{-3}\,s^{-1}$, respectively) cause a more heterogeneous deformation and an S-C' fabric is preserved at high strain. Several remaining clasts exist in the recrystallised matrix and many of these clasts show core-mantle structures. Equiaxed grains occur along C' planes (Fig. 6.10f). An anticlockwise-rotated peripheral maximum of *c*-axes is developed at 800 °C. At 900 °C, the CPO is similar to the CPO at $2.5 \cdot 10^{-5}\,s^{-1}$ with a peripheral and a central maximum.

6.3.2.5 Confining pressure of 1.0 GPa

For 650 °C and 800 °C, microstructure and CPO at 1.0 GPa confining pressure are similar to microstructure and texture at 1.5 GPa. An S-C' fabric is developed next to Riedel bands at 650 °C. Clasts with core-mantle structure and tails are common. At 800 °C, a penetrative foliation is developed with some remaining elongated clasts, that show deformation lamellae. The recrystallised grain size (3.0 µm) is smaller compared to 1.5 GPa (3.8 µm).

At 700 °C, an S-C' fabric is still present at high shear strain with several remaining clasts. These roundish clasts have pronounced tails and show core-mantle structures. The *c*-axis orientation shows a peripheral maximum almost perpendicular to the shear zone boundary. Equiaxed, euhedral grains are developed along C' planes with a grain size of ~ 2 µm (Fig. 6.11). Porosity is increased in between these equiaxed grains (Fig. 6.10, Fig. 6.11). The *c*-axes show a weak peripheral maximum at an angle of 15° - 45° to the shear zone boundary. This angle approximately correlates with the opening direction along C' planes. Next to the zone of equiaxed grains, several highly elongated grains (aspect ratios >2) are visible. Inside the zone, aspect ratio and internal misorientation are low.

6.3.2.6 Core-mantle structures

In S-C' fabrics, several roundish grains have a mantle (Fig. 6.7a, 6.7c) independently of confining pressure, temperature or shear-strain rate. In addition, these structures are still present in some remaining clasts at high shear strain at 700 °C. The mantle is not surrounding the grain continuously, in fact it occurs on two opposite sides (Fig. 6.12). The angle between the direction of external load and the boundary between core and mantle varies but predominantly it is above >45 °. High porosity zones are developed at sides without mantle structures (Fig. 6.12a). Here, grains are slightly elongated.

At 700 °C and high shear strain, the mantle is characterised by a different CPO than the core and the transition is marked by high misorientation angles (>20 °, Fig. 6.13). The

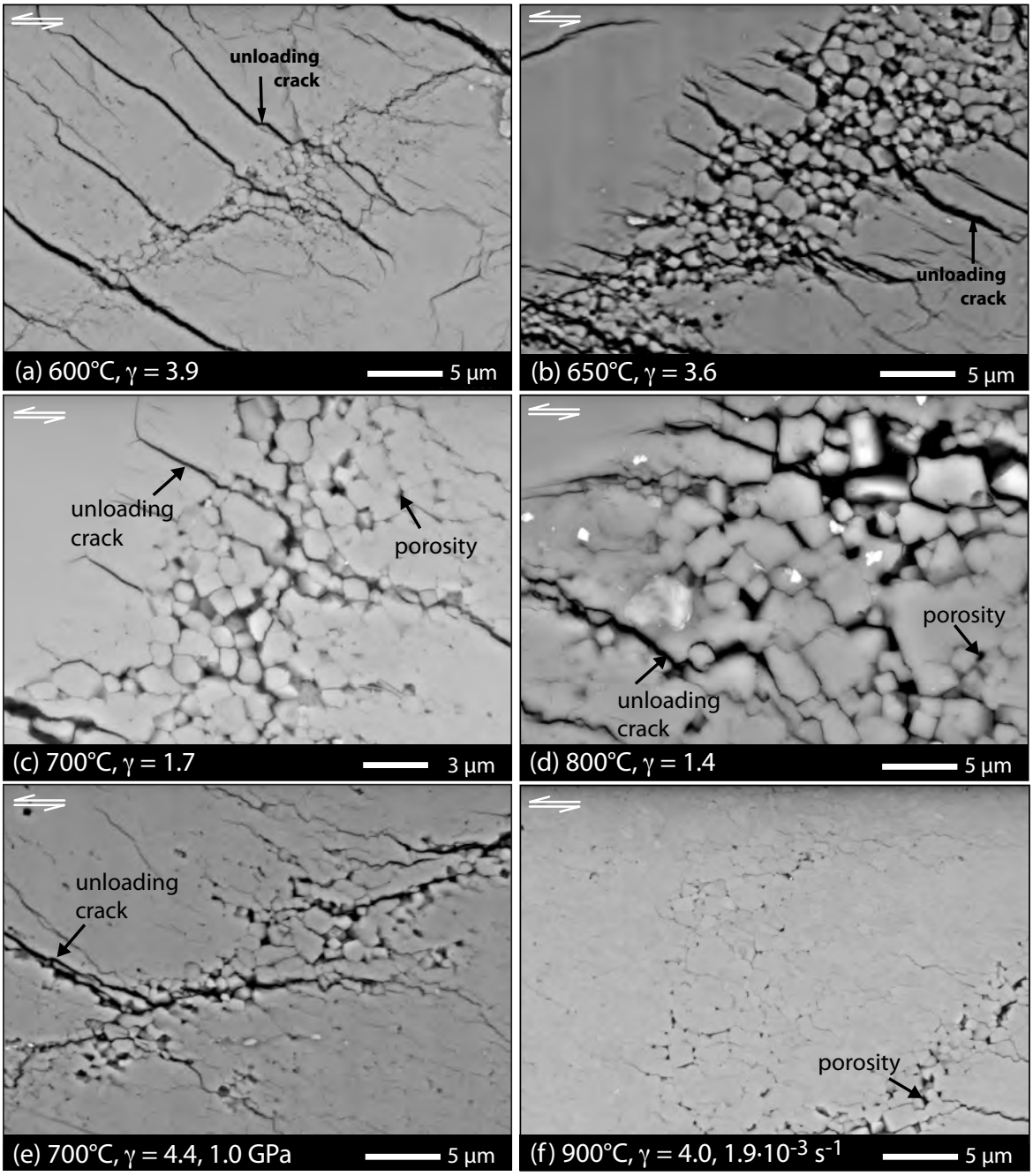

Fig. 6.10: Evolution of equiaxed, euhedral grains along R Riedel bands and C' planes, respectively. (BSE images) (a) to (d) at 1.5 GPa confining pressure and $\sim 2.5 \cdot 10^{-5}\,s^{-1}$. Zones widen with increasing temperature. (c) At low shear strain and 700 °C, the extension of the zone is visible (right site). (d) At peak strength and 800 °C, some of these zones are developed with relatively large grains (diameter of a few micrometer). (e) C' plane at 700 °C and 1.0 GPa confining pressure. (f) Equiaxed grains evolve at 900 °C and high shear strain ($\gamma = 4$) if fast shear-strain rates act on the sample ($\sim 2 \cdot 10^{-3}\,s^{-1}$).

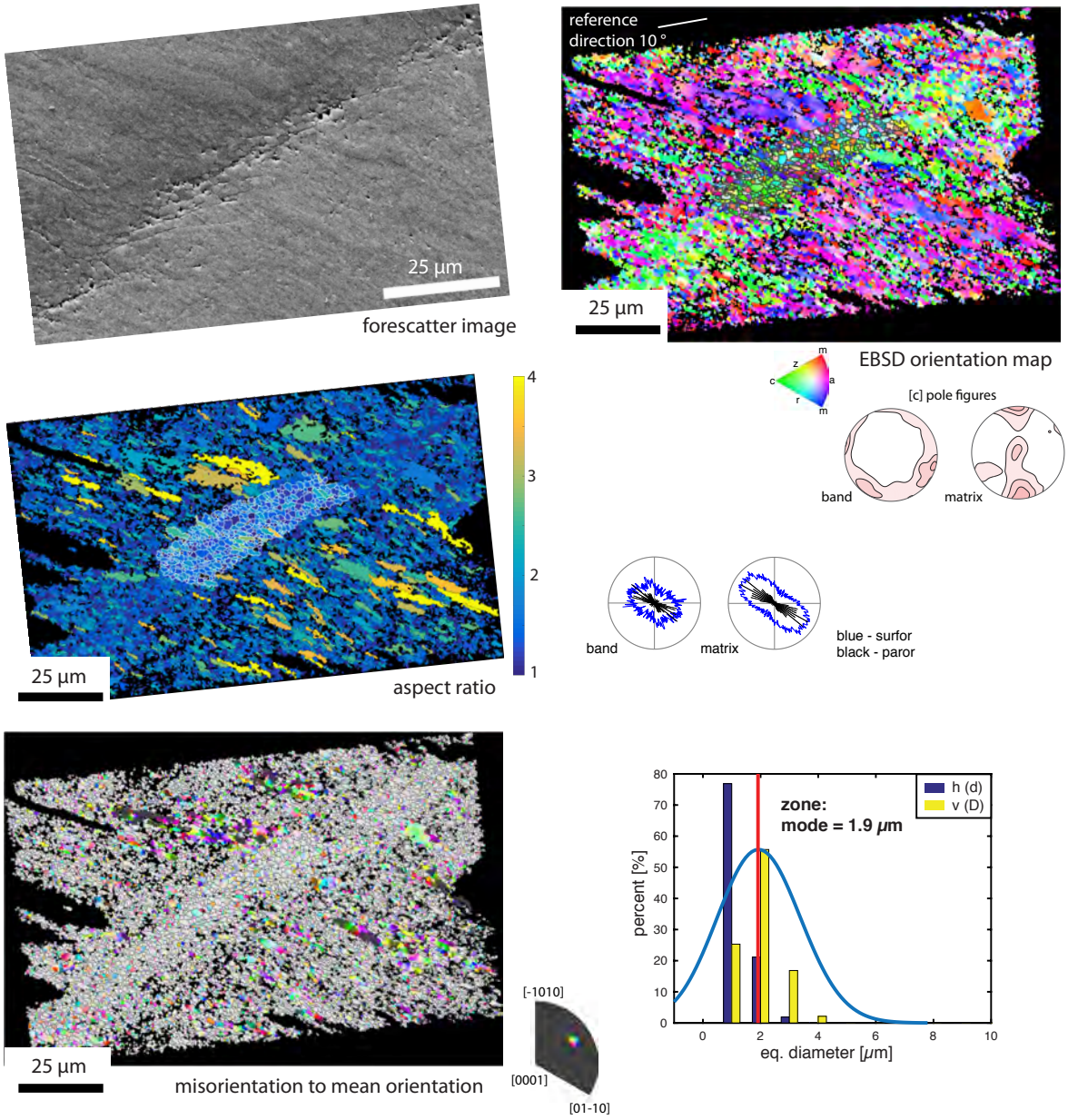

Fig. 6.11: EBSD analysis (step size 0.2 µm) of equiaxed grains along C' plane at 700 °C, 1.0 GPa confining pressure, $\sim 2.7 \cdot 10^{-5}\,\mathrm{s}^{-1}$ and $\gamma = 4.4$. Shear zone boundary is horizontal. Along the C' plane, grains have *c*-axis orientations with a peripheral maximum in opening direction of this extensional band. In contrast, the adjacent matrix shows a peripheral maximum perpendicular to the shear direction. Grains along the C' plane are less elongated and more equiaxial. Next to this zone, some highly elongated grains remain and the particle (PAROR - black) and the surface (SURFOR - blue) orientation are more elongated than inside the zone. The volumetric equivalent diameter in the zone is about ~ 2 µm.

orientation of the *c*-axes in the mantle rotates away from the orientation of the core in an anticlockwise sense and towards more peripheral orientations of *c*-axes. Both sides of the mantle show the same direction of rotation. The CPO of the mantle is independent of the CPO of the surrounding matrix. The basal planes of the cores are predominantly parallel to the direction of external load.

Deformation lamellae are commonly present in these grains and they cross the boundary between core and mantle. The orientation of the lamellae changes at the boundary so that they are subparallel to the basal plane in core and mantle. Furthermore, microcracks occur in the cores and unloading cracks are developed in between the deformation lamellae (Fig. 6.12b).

6.4 Discussion

6.4.1 Transition from semi-brittle flow to crystal plastic dominated deformation

The Goetze criterion ($P_c = \Delta\sigma = 2 \cdot \tau$; Kohlstedt et al., 1995; Evans and Kohlstedt, 1995) marks the transition from semi-brittle flow to dominating crystal plastic flow. This transition correlates with an ambiguous temperature dependence below 700 °C indicating less influence of viscous deformation processes while an inverse temperature dependence of strength is well pronounced at temperatures $\geq$ 700 °C revealing viscous deformation processes (1.5 GPa confining pressure, $2.5 \cdot 10^{-5}$ s^{-1}). In addition, a positive shear-strain rate dependence reinforces the increasing portion of viscous deformation processes [Evans and Kohlstedt, 1995] between 650 °C and 900 °C.

During subsequent loading, more fine-grained material is produced by fracturing. High confining pressures and ongoing pore-space collapse accompanied by rearrangement of small grains in between larger grains prevent crack propagation. The fine fraction shields large clasts and prevents through-going fractures. Hence, deformation is stabilized. Minor strain weakening is established for conditions below the Goetze criterion (high temperature / low shear-strain rates). Temperatures are high enough to promote dislocation glide and the S-C' fabric, which is developed at low shear strain, evolves with increasing recrystallisation into a penetrative foliation at high shear strain.

6.4.2 Extensional shear bands

In samples with semi-brittle flow, porosity reduction is not finished until peak strength is achieved ($\gamma \sim$ 1-1.5) [Pec et al., 2012a]. With increasing shear strain and more pronounced Riedel bands, comminution along R Riedel bands increases the fine-grained material [Kanagawa et al., 2000; Giger et al., 2008]. Thereby, the surface is increased in zones with fine-grained material. Accompanying dilatancy causes a pressure gradient towards R Riedel bands enhancing fluid flow along these zones. As a result of intensified fluid flow, mass

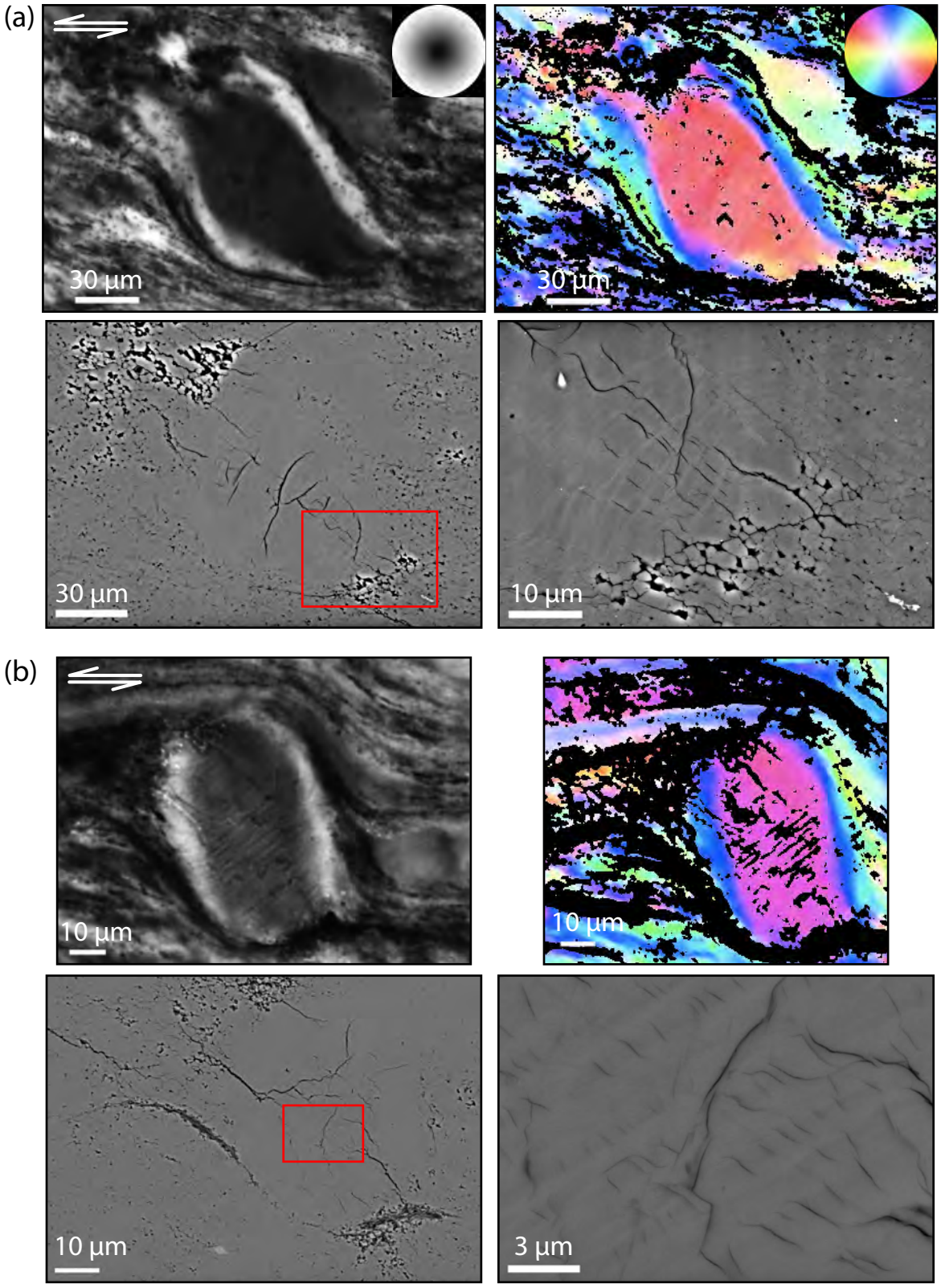

Fig. 6.12: Core-mantle structures at 700 °C and 1.5 GPa confining pressure. (a) Clast in circular polarised light, *c*-axis orientation image (COI) and BSE images. The mantle is clearly visible in crossed polarised light and COI. In BSE images, the mantle is hardly visible but high porosity is present in strain shadow zones. A close-up (red rectangle) of the clast reveals deformation lamellae that change their orientation abruptly towards the mantle. (b) A different clast in circular polarised light, COI and BSE images (same look up tables as in figure 6.12a). Unloading cracks between deformation lamellae are well established.

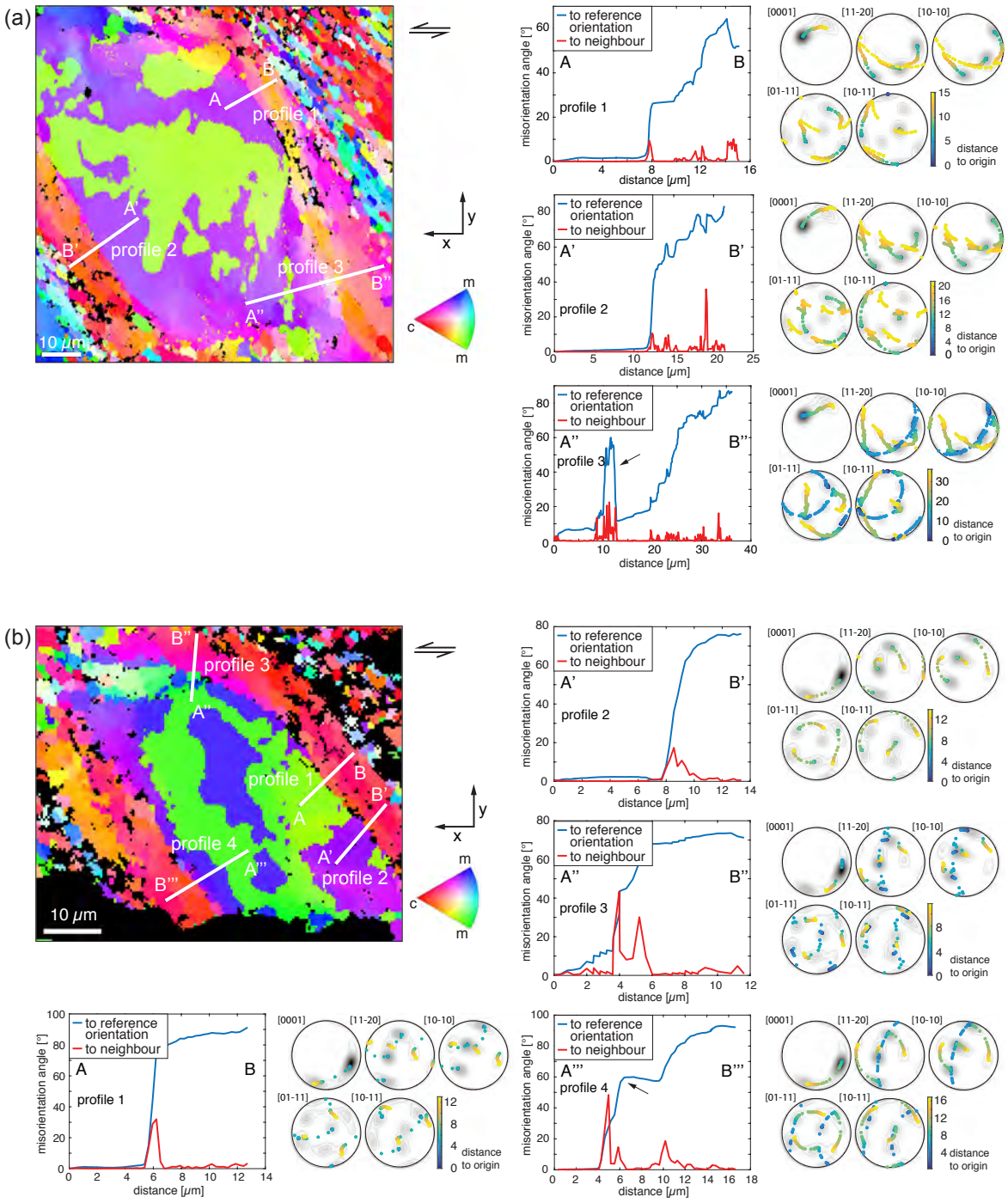

Fig. 6.13: Misorientation profiles along core-mantle structures at 700 °C and 1.5 GPa (383br). The cores are characterised by large Dauphiné twins (a) EBSD map (non-index = black) of the same clast as in figure 12a (0.15 µm step size). Misorientation profiles indicate large angles at the core-mantle boundary and the associated textures show anticlockwise rotation with the sense of shear. (arrow in profile 3 indicates misorientation angles related to twin boundaries) (b) The same observation can be made in another clast (0.4 µm step size). Arrow in profile 4 indicates misorientation angles related to twin boundaries.

transfer processes, e.g. dissolution-precipitation, are accelerated. Porosity is increased in between small, equiaxed grains, indicating euhedral growth [Kohlstedt and Hansen, 2015; den Brok and Spiers, 1991.]. At 500 °C, such grains are not visible. Probably, mass transfer processes are not fast enough to produce microstructural evidence. Pec et al. [2012a] study granitoid rocks and do not find microstructural evidence for mass transfer in fine-grained material at temperature ≤ 600 °C but chemical variations indicate dissolution-precipitation at 600 °C and short deformation time (less than 3 h). The duration of most of our experiments is longer (at least 24 h) and most of them are performed at temperatures above 600 °C whereby mass transfer is accelerated due to increased solubility of SiO_2. The widening of the zones can be attributed to increasing amounts of dissolution-precipitation with increasing temperature. Dissolution-precipitation processes are frequently accompanied by grain boundary sliding [e.g. Kohlstedt and Hansen, 2015]. Porosity is increased in these regions (Fig. 6.10).

At 700 °C and high shear strain, the CPO of these grains is slightly related to the extensional direction of the C' planes supporting growth [Trepmann et al., 2007]. Similar to our observations, Trepmann et al. [2007] find small, isometrically shaped grains in high stressed quartz ($\sim$ 400 °C / 2 GPa confining pressure). The grains are dislocation-free and occur along former fractures that evolve to 'deformation bands'. Originally, these zones are characterised by high dislocation densities. They conclude that recrystallisation is triggered by nucleation and growth [Trepmann et al., 2007].

S-C' fabrics are often related to high strain [e.g. White et al., 1980; Pec et al., 2012a]. Thereby, C' planes are interpreted as overprint of previous C planes (crenulation). In addition to 650 °C, 1.5 GPa confining pressure and $2.5 \cdot 10^{-5}$ s^{-1}, we observed this fabric at 1.0 GPa confining pressure (700 °C) or high shear-strain rates (800 °C and 900 °C). At higher temperatures ($\geq$700 °C) and 1.5 GPa confining pressure, extensional C' planes are already established at peak strength ($\gamma \sim$ 1-1.5). Hence, they cannot overprint a previous fabric, which is similar to the observations by Dell'Angelo and Tullis [1989]. With increasing shear strain at high temperatures, recrystallisation advances in the matrix. As a result, the fluid is redistributed in the whole sample and it is no longer enhanced along C' planes. Hence, the S-C' fabric evolves into a penetrative foliation formed by elongated recrystallised grains.

6.4.2.1 Unloading cracks associated with shear bands

Unloading cracks form in permanent plastically deformed material adjacent to more elastically deformed material since the material becomes extended by the release of elastic energy [FitzGerald et al., 1991; Stünitz et al., 2003; Pec et al., 2012a]. This elastic response triggers the opening along grain boundaries of equiaxed grains. Unloading cracks extent into the area around the grains, where mass transfer is still active but less pronounced, and vanish further away except for some large cracks.

Unloading cracks diminish with diminishing S-C' fabrics, e.g. towards higher shear strain or higher temperature. The difference in elastically and plastically deformed material is reduced, and deformation is more homogeneously and accompanied by recrystallisation. Only large remaining clasts can store elastic energy in the core and unloading cracks can be generated inside.

6.4.3 Core-mantle structure and brittle precursors

Misoriented bands parallel to *c*-axis orientation are common in experiments [e.g. Carter et al., 1964; Hirth and Tullis, 1992; Trepmann et al., 2007] and nature [e.g. White, 1973a; Bouchez, 1977]. They are often related to kinks that form perpendicular to the basal plane and hence, they indicate basal slip [e.g. Carter et al., 1964]. But we already observe such bands at 500 °C and 600 °C where high shear stresses are achieved and dislocation glide is less likely [see chapter 5]. Dislocations can easily be induced in the basal plane in <a> direction and accumulate since they can barely move. TEM studies show highly entangled dislocations in the basal plane while dislocations related to slip are predominantly oriented for slip [e.g. McLaren et al., 1970]. In addition, recent studies suggest, that <11-20> (0001) glide is of minor importance for producing strain in quartz [Rüdiger Kilian, personal communication].

Core-mantle structures developing next to misoriented bands in S-C' fabrics might be related to a similar origin as the misoriented bands (Fig. 6.14). Mantle and misoriented grains show the same sense of rotation of misorientation, anticlockwise to the shear sense. They are common in experiments [e.g. Tullis et al., 1973; Dell'Angelo and Tullis, 1989; Gleason and Tullis, 1995] but have not been observed in natural samples. The misorientation between core and mantle is significantly higher (at least 15 °) than progressive misorientation in the mantle itself (Fig. 6.13). Hence, continuous rotation from the core to the outer mantle boundary is not likely. Tails developed on sides without mantles indicate progressive misorientation by subgrain rotation.

Tullis et al. [1973] observe misoriented bands and similar core-mantle structure ("augen") at low strain. They infer that subsequent recrystallisation along the misoriented bands can separate an original grain in individual grains with the same crystallographic orientation. We observed such separation in S-C' fabric at 700 °C and 1.0 GPa confining pressure (Fig. 6.14c).

Core-mantle structure could originate from misoriented bands that are produced at an early experimental stage (before peak strength). In grains with couple of misoriented bands; these bands shield the internal part. The bands have a more suitable orientation for recrystallisation. In addition, boundaries of the grain are prone to recrystallisation as well due to more defects compared to the internal part of the grain [Tullis et al., 1973]. Hence, most of the grain is recrystallised if viscous deformation processes are increased (e.g. by increasing temperature). But the mantle can shield the core to a certain extent.

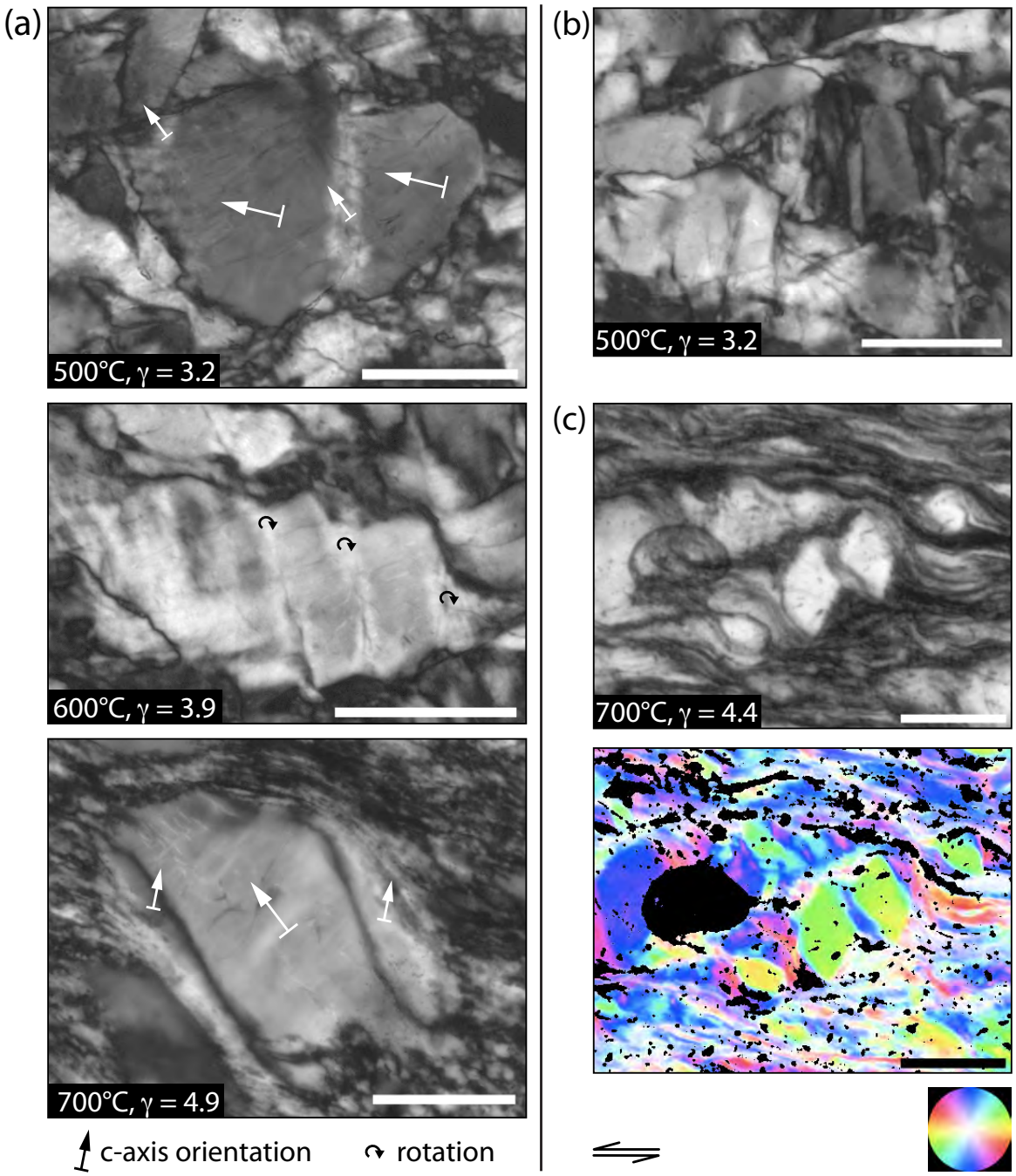

Fig. 6.14: Misoriented bands at various stages (scale bar 50 µm). (a) Evolution of clasts with increasing temperature at 1.5 GPa and $\sim 2.5 \cdot 10^{-5}$ s^{-1} (crossed polarised image). Distinct bands of different extinction at low temperatures are almost perpendicular to the shear zone boundary and several misoriented bands can occur in a single grain. At intermediate temperatures, core-mantle structures are pronounced and distinct misoriented bands are less frequent. The CPO of misoriented bands and mantle structures rotate anticlockwise to the sense of shear with respect to the core. (b) Separation of grain along boundary between misoriented band and host grain. (c) Two grains (700 °C, 1.0 GPa confining pressure) are separated by a band with less variations in CPO. The CPO of both grains is almost identical.

6.4.4 Deformation lamellae

Misoriented bands at intermediate temperatures are often related to subbasel deformation lamellae [e.g. Carter et al., 1964]. We observe lamellae in clasts in S-C' fabric and they are still present in remaining clasts at high shear strain at 700 °C and 800 °C (pronounced foliation). While the lamellae occur frequently at 800 °C, they disappear at higher temperatures. The absence of deformation lamellae in samples with dominating viscous deformation indicates that recovery keeps pace with deformation [Tullis et al., 1973].

Lamellae are caused by high dislocation densities characterised by several entangled dislocations [e.g McLaren et al., 1970; White, 1973b; Trepmann and Stöckhert, 2013]. They are often interpreted as highly elongated subgrains [e.g Carter et al., 1964; McLaren and Hobbs, 1972; White, 1973b; Vernooij and Langenhorst, 2005]. As deformation lamellae do not cause a change in diffraction patterns, they cannot be related to changing crystallographic misorientations without any reservation. Hence, it is less likely that deformation lamellae are necessarily attributed to a specific slip system [e.g. McLaren et al., 1970].

6.5 Conclusions

Shear experiments performed on quartz under high confining pressure (predominantly 1.5 GPa) and temperatures between 500 °C - 1000 °C with intermediate to fast shear-strain rates ($3.5 \cdot 10^{-6}\,s^{-1}$ to $\sim 2 \cdot 10^{-3}\,s^{-1}$) illustrate the transitions from semi-brittle flow to dislocation creep. Riedel band geometry is developed at dominating brittle deformation while a penetrative foliation is developed at dominating viscous deformation. An S-C' fabric is closely linked to the onset of dominating viscous processes independent of confining pressure, temperature, shear-strain rate or shear strain. Highly fragmented, fine-grained material along zones with R Riedel band orientation promotes the onset of dissolution-precipitation processes. In S-C' fabrics, localised dissolution-precipitation processes promote the formation of C' planes.

Pronounced misoriented bands and deformation lamellae, indication for crystal plasticity, frequently occur in S-C' fabrics and misoriented bands are already present in samples dominated by Riedel bands.

Grains with misoriented bands are consumed by recrystallisation leaving behind core-mantle structure that can remain at intense recrystallisation. These misoriented bands disappear with dominating crystal plasticity.

7 | Concluding remarks

Rheological and microstructural developments at the semi-brittle-to-viscous transition in polycrystalline quartz were the main focus of this study. Deformation mechanisms causing this behaviour were inferred and the interaction of different processes was evaluated. Furthermore, the correlation between thermodynamic pressure and stress state was analysed based on coesite formation during deformation. In this chapter, the major results are summarised and ideas for future research are presented.

"Evolution" of mechanical behaviour

Peak shear strength is achieved around a shear strain of γ= 1-1.5, except for the weakest samples ($\tau < 250$ MPa). Here, it is already achieved at $\gamma \sim 0.7$. The shear stress is highly temperature dependent and varies between a few 10's of MPa at 1000 °C up to $\sim$ 1.5 GPa at 500 °C. This inverse temperature dependence is well pronounced above 650 °C. Below this temperature, the temperature dependence is ambiguous but the highest strength occurs at 500 °C. The slope of the loading curve depends on the strength: high stress samples have a similar slope while the slope decreases for lower stresses. The Goetze criterion ($\Delta\sigma = 2 \cdot \tau = P_c$) marks these changes in behaviour. Samples with shear stresses exceeding the criterion have an ambiguous temperature dependence, a similarly steep slope and a weakly pronounced strain rate dependence. Samples that have stresses below the criterion show a pronounced temperature and strain rate dependence, and the slope decreases continuously with decreasing strength. Similar to shear stress, the calculated friction coefficient (μ) slightly depends on temperature below 700 °C and it is approximately 0.45. A strong inverse temperature dependence is indicated above 700 °C at $2.5 \cdot 10^{-5}$ s^{-1} and $2.5 \cdot 10^{-4}$ s^{-1}. Lower shear-strain rates ($4 \cdot 10^{-6}$ s^{-1}) are characterised by low friction coefficients ($\mu < 0.1$) and a small temperature dependence.

Between 1.0 GPa and 1.5 GPa confining pressure, a positive pressure dependence is observed for shear stress at 650 °C but at 700 °C the pressure dependence is ambiguous. At 800 °C, no pressure dependence occurs between 1.0 GPa and 1.5 GPa whereas a negative dependence is visible for decreasing confining pressures to 0.5 GPa.

Quartz powder with grains below 100 µm is used except for one case (445br). An initial powder with grains between 7-11 µm causes a weaker peak strength at 800 °C ($\Delta\sigma$ = 300 MPa). Annealing (by hot pressing at 1000 °C and 1.5-1.6 GPa for 20 h) of the initial powder causes

grain growth of the smallest fraction at the expense of the large grains. Hence, the grain size range is reduced. The resulting shear stresses are higher compared to samples without hot pressing ($\Delta\sigma \sim 100$ MPa at 800 °C; $\Delta\sigma \sim 450$ MPa at 700 °C; $\Delta\sigma \sim 250$ MPa at 600 °C).

Pronounced strain weakening is not observed with increasing shear strain, and stress drops only exist at high stresses if slip occurs on the forcing block-sample interface. In general, samples with shear stresses above the Goetze criterion show steady state or slight strain hardening. Minor strain weakening is observed for samples with stresses below the Goetze criterion.

Transitional microstructure and inferred deformation mechanisms

Similar to the mechanical data, microstructure changes significantly between 650 °C and 700 °C at $2.5 \cdot 10^{-5}$ s^{-1} and 1.5 GPa confining pressure. Low temperatures are characterised by Riedel geometry and heterogeneous deformation. Cataclastic flow dominates. Viscous processes control the microstructure at high temperatures and a penetrative foliation by slightly elongated recrystallised grains is developed.

An S-C' fabric is developed at high shear strain($\gamma > 3$) for high temperatures and stresses above the Goetze criterion due to e.g. faster shear strain rates. In contrast, an S-C' fabric is already present at low shear strain ($\gamma =$ 1-1.5) for high temperatures and stresses below the Goetze criterion. But the Goetze criterion cannot be correlated with S-C' fabrics at high strain. At 650 °C Riedel geometry and an S-C' fabric are developed next to each other at high shear strain. Hence, extensional C' planes are not necessarily related to high strain and overprinting of earlier foliations. In fact, C' planes are initiated by dissolution-precipitation processes. These processes are triggered in fine-grained material in zone with enhanced fluid flow (e.g. R Riedel band orientation or C' plane orientation) and progressively evolve. Hence, microstructural steady state is not achieved in S-C' fabrics, and mechanical steady state not necessarily indicates microstructural steady state, especially at high stresses, above the Goetze criterion. Early S-C' fabrics at high temperatures are overprinted by dislocation creep and recrystallised grains with increasing strain. In this process, water is homogeneously distributed along the grain boundaries and dissolution-precipitation is no longer enhanced by increased fluid flow along C' planes. Thereby, a steady state microstructure is achieved.

The grain size dependence of strength can be related to grain size sensitivity of deformation mechanisms: grain size sensitive dissolution-precipitation processes are pronounced in the fine-grained material of the 7-11-µm powder. Hot pressing and associated grain growth of the fine-grained fraction cause less pronounced dissolution-precipitation processes.

Due to the starting material fine-grained material in the range of recrystallised grains is already present at the onset of recrystallisation. Therefore, it is crucial to differentiate between recrystallised grains and relicts of crushing. A low internal misorientation in grains is a good indicator for recrystallisation since it suggests a low dislocation density. Neverthe-

less, the recrystallised grain size increases with increasing temperature but it does not fit in with the piezometer by Stipp and Tullis [2003].

The CPO progressively evolves with increasing temperature and cannot solely be related to increasing viscous deformation processes. Random CPO exists in the undeformed starting material and at low temperatures. A S-C' fabric is characterised by a peripheral *c*-axis maximum that is not rotated with the sense of shear. In fact, it is often rotated anticlockwise with respect to the shear sense. At 700 °C and 800 °C, the formation of a penetrative foliation causes a peripheral *c*-axis maximum that is rotated with the sense of shear. Meanwhile, the *a*-axes are slightly inclined with respect to the shear zone boundary. With increasing temperature, a central *c*-axis maximum develops next to the peripheral maximum. At 1000 °C, only the central maximum remains.

In contrast to deformed quartzite [e.g. Black Hills quartzite in Hirth and Tullis, 1992; Heilbronner and Tullis, 2002], intense weakening after peak strength is less pronounced at the transition from semi-brittle to viscous conditions. The early onset of dissolution-precipitation in fine-grained material causes a continuous evolution. The transition from stress accumulation to the onset of dislocation creep and recrystallisation is less abrupt. But high stresses can accumulate in this crushed material and annealing prior to deformation increases the potential for stress accumulation. Hence, reactivated fault gouge has a high potential for stress accumulation whereby the broad grain size range promotes mechanical steady state.

Extrapolation of experimental data to natural conditions

By fitting the data to a power law flow law, high stress exponents (n = 6.4±1.3) are calculated for temperatures below 700 °C. These values indicate a break down of power law behaviour. Between 800 °C and 1000 °C, a stress exponent of n =1.9±0.6 and an associated activation energy of $Q \sim 170$ kJ/mol are obtained. These low values are in contrast to previously determined and well-established values of $n \sim 4$ assuming pure dislocation creep [Gleason and Tullis, 1995; Hirth et al., 2001; Luan and Paterson, 1992]. But earlier studies already indicated lower values of $n \sim$ 2-3 for similar conditions [e.g. Jaoul et al., 1984; Kronenberg and Tullis, 1984; Paterson and Luan, 1990]. Hence, mixed deformation mechanisms are inferred in combination with microstructural observations. Dislocation creep is accompanied by dissolution-precipitation processes, which are linked to low stress exponents ($n \sim 1$). If these parameters are used for extrapolation to nature, faster strain rates are indicated for similar stresses. But water fugacity is an element of uncertainty. Calculations of water fugacity and the exponent of water fugacity are already uncertain for pure dislocation creep. The influence of diffusion creep processes on water affecting dislocation creep is unknown. Hence, extrapolations based on microstructural observations are considered and the Goetze criterion as boundary between semi-brittle and viscous deformation is independent of the shear strain rate.

Coesite formation by non-hydrostatic stress states

The occurrence of coesite is used to review the relationship between thermodynamic pressure and the stress state under non-hydrostatic conditions. The formation of coesite cannot be related to the confining pressure or the mean stress ($\sigma_m = (\sigma_1 + 2 \cdot P_c)/3$). These values do not systematically exceed the thermodynamic pressure of the quartz-to-coesite phase transformation (P_{trans}). But the magnitude of the maximum principal stress (σ_1) correlates with the presence of coesite: If σ_1 exceeds the quartz-to-coesite phase transformation, coesite exists. No coesite is present if σ_1 does not exceed the phase transformation. Furthermore, the formation of coesite and the back reaction of coesite to quartz is indicated in a single sample that exceeds the phase transformation with the σ_1 magnitude around peak strength and σ_1 progressively falls below the phase transformation with increasing shear strain due to strain weakening.

Hence, P_{trans} should be related to σ_1 whereby high-pressure phases like coesite are not necessarily an indicator for high lithostatic pressures. But low differential stresses are common in nature and the difference between σ_1 and σ_m is small. However, indication for high differential stresses exists in nature and recent studies indicate the potential for locally high differential stress in nature [e.g. Schmalholz and Podladchikov, 2013; Reuber et al., 2016].

Ideas for further research

(1) We extrapolated our microstructural observations to lower shear strain rates and lower temperature. Additional experiments in the close range of the transition would be interesting. We would expect dominating brittle deformation for fast shear strain rates (e.g. $10^{-3}\,s^{-1}$) at 800 °C and 1.5 GPa confining pressure as well as a shear strain rate of $10^{-6}\,s^{-1}$ at 500 °C and 1.5 GPa confining pressure. Dominating viscous deformation should occur for slow shear strain rates (e.g. $10^{-7}\,s^{-1}$) at 600 °C and 1.5 GPa confining pressure.

(2) The persistence of S-C' fabrics at low shear strain could be determined at high temperatures. An S-C' fabric is well pronounced at 800 °C and peak strength ($\gamma \sim$ 1-1.5). The peak strength is achieved at lower shear strain ($\gamma \sim 0.7$) at 900 °C and 1000 °C. Therefore, it would be interesting to see wether an S-C' fabric is already developed or a penetrative foliation is directly developed. In this process, TEM studies of the zones with equiaxed grains along C' planes could provide insights into dissolution-precipitation process and the effect on dislocation densities.

(3) The pressure dependence was investigated in a narrow *PT* range. Experiments at higher temperatures and lower confining pressure could provide more information on the extent of pressure independence or an inverse pressure dependence at viscous conditions.

(4) More data on water fugacity could improve extrapolations by flow laws. The difference of the fugacity of intracrystalline or intercrystalline water and water on larger scales should be investigated since water fugacity values are based on the latter. In addition, a theoretical basis for the interaction of deformation processes would be helpful to generate constitutive equations in this transitional regime. The water effect on different mechanisms (e.g. dislocation creep, diffusion creep) should be taken into account.

(5) Natural examples of high-pressure phases in rocks with indication of high differential stresses could be analysed regarding possible overestimations of the lithostatic pressure. Moreover, the effect of non-hydrostatic conditions on phase transformations could be studied on grain-scale, investigating the effect of different orientations of grain boundaries with respect to the stress field.

(6) Our observation of σ_1 as driving force for phase transformations should be verified with similar deformation experiments on different monophase material and polyphase aggregates.

(7) The determination of the confining pressure could be improved by measuring the oil pressure as close as possible to the pressure vessel. Additionally, simulations of the stress state inside the sample chamber could improve the translation of the confining pressure to minimum principal stress.

References

Akaogi, M., Yusa, H., Shiraishi, K., and Suzuki, T. (1995). Thermodynamic properties of α-quartz, and stishovite at equilibrium phase relations at high pressures and temperatures. *Journal of Geophysical Research*, 100:22337–22347.

Akella, J. (1979). Quartz $\leftrightarrows$ coesite transition and the comparative friction measurements in piston-cylinder apparatus using talc-alsimag-glass (TAG) and NaCl high-pressure cells. *Neues Jahrbuch für Mineralogie*, 5:217–224.

Austin, N. J. and Evans, B. (2007). Paleowattmeters: a scaling relation for dynamically recrystallized grain size. *Geology*, 35:343–346.

Barber, D. J., Wenk, H.-R., Hirth, G., and Kohlstedt, D. L. (2010). *Dislocations in minerals*, pages 171–232. Elsevier.

Berman, R. G. (1988). Internally-consistent thermodynamic data for minerals in the system $Na_2O-K_2O-CaO-MgO-FeO-Fe_2O_3-Al_2O_3-SiO_2-TiO_2-H_2O-CO_2$. *Journal of Petrology*, 87:445–522.

Bohlen, S. R. and Boettcher, A. L. (1982). The quartz $\leftrightarrows$ coesite transformation: A precise determination and the effects of other components. *Journal of Geophysical Research*, 87:7073–7078.

Bons, P. D. and den Brok, B. (2000). Crystallographic preferred orientation development by dissolution-precupitation creep. *Journal of Structural Geology*, 22:1713–1722.

Bose, K. and Ganguly, J. (1995). Quartz-coesite transition revisited: reversed experimental determination at 500-1200 °C and retrieved thermochemical properties. *American Mineralogist*, 80(3-4):231–238.

Bouchez, J.-L. (1977). Plastic deformation of quartzites at low temperature in an area of natural strain gradient. *Tectonophysics*, 39:25–50.

Boyd, F. R. and England, J. L. (1960). The quartz-coesite transition. *Journal of Geophysical Research*, 65(2):749–756.

Brace, W. F. and Kohlstedt, D. L. (1980). Limits on lithospheric stress imposed by laboratory experiments. *Journal of Geophysical Research: Solid Earth*, 85:6248–6252.

Byerlee, J. D. (1968). Brittle-ductile transition in rocks. *Journal of Geophysical Research*, 73:4741–4750.

Byerlee, J. D. (1978). Friction of rocks. *Pure and Applied Geophysics*, 116(4):615–626.

Bystricky, M., Béjina, F., and Baticle, J. (2015). Effect of pressure on the deformation of forsterite and of iron-free enstatite. *Geotectonic Research*, 97:126.

Carter, N. I., Christie, J. M., and Griggs, D. T. (1964). Experimental deformation and recrystallisation of quartz. *Journal of Geology*, 72:687–733.

Chernak, L. J., Hirth, G., Selverstone, J., and Tullis, J. (2009). Effect of aqueous and carbonic fluids on the dislocation creep strength of quartz. *Journal of Geophysical Research: Solid Earth*, 114(B4):B04201. B04201.

Chester, F. M. (1995). A rheological model for wet crust applied to strike-slip faults. *Journal of Geophysical Research*, 100:13033–13044.

Chester, F. M. and Higgs, N. G. (1992). Multimechanism friction constitutive model for ultrafine quartz gouge at hypocentral conditions. *Journal of Geophysical Research*, 97:1859–1870.

Chopin, C. (1984). Coesite and pure pyrope in high-grade blueschists of the Western Alps: a first record and some consequences. *Contributions to Mineralogy and Petrology*, 86(2):107–118.

Chopin, C. (2003). Ultrahigh-pressure metamorphism: tracing continental crust into the mantle. *Earth and Planetary Science Letters*, 212(1-2):1 – 14.

de Ronde, A. A. and Stünitz, H. (2007). Deformation-enhanced reaction in experimentally deformed plagioclase-olivine aggregates. *Contributions to Mineralogy and Petrology*, 153(6):699–717.

Dell'Angelo, L. N. and Tullis, J. (1989). Fabric development in experimentally sheared quartzites. *Tectonophysics*, 169:1–21.

den Brok, B. (1992). *An experimental investigation into the effect of water on the flow of quartzite*. PhD thesis, Rijksuniversiteit Utrecht.

den Brok, S. W. J. and Spiers, C. J. (1991). Experimental evidence for water weakening of quartzite by microcracking plus solution-precipitation creep. *Journal of the Geological Society London*, 148:541–548.

Di Toro, G. and Pennacchioni, G. (2005). Fault plane processes and mesoscopic structure of a strong-type seismogenic fault in tonalites (Adamello batholith, Southern Alps). *Tectonophysics*, 402:55–80.

Evans, B., Fredrich, J. T., and Wong, T.-F. (1990). The brittle-ductile transition in rocks: recent experimental and theoretical progress. In Duba, A. G., Durham, W. B., Handin, J. W., and Wang, H. F., editors, *The brittle-ductile transition in rocks*, pages 1–20. Geophysical Monographs Series.

Evans, B. and Kohlstedt, D. L. (1995). Rheology of rocks. In Ahrens, T. J., editor, *Rock Physics and Phase Relations*, pages 148–165. AGU reference shelf.

Fitts, D. (1962). *Nonequilibrium thermodynamics*. McGraw-Hill, New York.

FitzGerald, J. D., Boland, J. N., McLaren, A. C., Ord, A., and Hobbs, B. E. (1991). Microstructures in water-weakened single crystals of quartz. *Journal of Geophysical Research*, 96:2139–2155.

FitzGerald, J. D., Mancktelow, N. S., Pennacchioni, G., and Kunze, K. (2006). Ultrafine-grained quartz mylonites from high-grade shear zones: evidence for strong dry middle to lower crust. *Geology*, 34(5):369–372.

Fliervoet, T. F., White, S. H., and Drury, M. R. (1997). Evidence for dominant grain-boundary sliding deformation in greenshist- and amphibolite-grade polymineralic ultramilonites from the Redbank deformed zone, Central Australia. *Journal of Structural Geology*, 19:1495–1520.

Gibbs, J. W. (1906). On the equilibrium of heterogeneous substances. In *The Scientific Papers of J. W. Gibbs*, volume 1. Longmans, Green, and co., London.

Giger, S. B., Cox, S. F., and Tenthorey, E. (2008). Slip localisation and fault weakening as a consequence of fault gouge strengthening - insights from laboratory experiments. *Earth and Planetary Science Letters*, 276:73–84.

Gleason, G. C. and Tullis, J. (1995). A flow law for dislocation creep of quartz aggregates determined with the molten salt cell. *Tectonophysics*, 247:1–23.

Green, H. W. (1972). Metastable growth of coesite in highly strained quartz. *Journal of Geophysical Research*, 77(14):2478–2482.

Green, H. W., Griggs, D. T., and Christie, J. M. (1970). Syntectonic and annealing recrystallisation of fine-grained quartz aggregates. In Paulitsch, P., editor, *Experimental and natural rock deformation*, pages 272–335. Springer, Berlin Heidelberg New York.

Griggs, D. (1967). Hydrolytic weakening of quartz and other silicates. *Geophysical Journal of the Royal Astronomical Society*, 14:19–31.

Groshong Jr., R. H. (1988). Low-temperature deformation mechanisms and their interpretation. *Geological Society of America Bulletin*, 100:1329–1360.

Heilbronner, R. (2002). Analysis of bulk fabrics and microstructure variations using tesselations of autocorrelation functions. *Computer and Geosciences*, 28:447–455.

Heilbronner, R. and Barrett, S. (2014). *Image analysis in earth sciences*. Springer, Berlin Heidelberg.

Heilbronner, R., Stunitz, H., and Richter, B. (2015). Calibrating the Grigg's apparatus using experiments performed at the quartz-coesite transition. In *AGU fall meeting, San Francisco*.

Heilbronner, R. and Tullis, J. (2002). The effect of static annealing on microstructures and crystallographic preferred orientation of quartz experimentally deformed in axial compression and shear. *Geological Society, London, Special Publications*, 200:191–218.

Heilbronner, R. and Tullis, J. (2006). Evolution of *c* axis pole figures and grain size during dynamic recrystallization: results from experimentally sheared quartzite. *Journal of Geophysical Research: Solid Earth*, 111(B10). B10202.

Hielscher, R. and Schaeben, H. (2008). A novel pole figure inversion method: specification of the *MTEX* algorithm. *Journal of Applied Crystallography*, 41(6):1024–1037.

Hirth, G., Teyssier, C., and Dunlap, J. W. (2001). An evaluation of quartzite flow laws based on comparisons between experimentally and naturally deformed rocks. *International Journal of Earth Sciences*, 90(1):77–87.

Hirth, G. and Tullis, J. (1989). The effect of pressure and porosity on the micromechanics of the brittle-ductile transition in quartz. *Journal of Geophysical Research*, 94:17825–17838.

Hirth, G. and Tullis, J. (1992). Dislocation creep regimes in quartz aggregates. *Journal of Structural Geology*, 14(2):145–159.

Hirth, G. and Tullis, J. (1994). The brittle-plastic transition in experimentally deformed quartz aggregates. *Journal of Geophysical Research: Solid Earth*, 99(B6):11731–11747.

Hobbs, B. E. (1968). Recrystallization of single crystals of quartz. *Tectonophysics*, 6:353–401.

Holyoke, C. W. and Kronenberg, A. K. (2010). Accurate differential stress measurement using the molten salt cell and solid salt assemblies in the Griggs apparatus with applications to strength, piezometers and rheology. *Tectonophysics*, 494:17–31.

Hull, D. and Bacon, D. J. (2011). *Introduction to dislocations*. Butterworth-Heinemann, Elsevier, 5. edition.

Humphreys, F. J. (1999). Quantitative metallography by electron backscattered diffraction. *Journal of Microscopy*, 195(3):170–185.

Jaoul, O., Tullis, J., and Kronenberg, A. (1984). The effect of varying water contents on the creep behaviour of Heavitree quartzite. *Journal of Geophysical Research*, 89:4298–4312.

Ji, S. and Xia, B. (2002). *Rheology of polyphase earth materials*. Polytechnic International Press.

Kamb, W. B. (1959). Theory of preferred crystal orientation developed by crystallization under stress. *The Journal of Geology*, 67:153–170.

Kanagawa, K., Cox, S. F., and Zhang, S. (2000). Effects of dissolution-precipitation processes on the strength and mechanical behaviour of quartz gouge at high-temperature hydrothermal conditions. *Journal of Geophysical Research*, 105:11115–11126.

Keulen, N., Stünitz, H., and Heilbronner, R. (2008). Healing microstructures of experimental and natural fault gouge. *Journal of Geophysical Research: Solid Earth*, 113(6):B06205.

Keulen, N. T. (2006). *Grain scale processes in fault rock - a comparison between experimental and natural deformation*. PhD thesis, Universität Basel.

Kidder, S., Hirth, G., Avouac, J.-P., and Behr, W. (2016). The influence of stress history on the grain size and microstructure of experimentally deformed quartzite. *Journal of Structural Geology*, 83:194–206.

Kilian, R., Heilbronner, R., and Stünitz, H. (2011). Quartz grain size reduction in a granitoid rock and the transition from dislocation to diffusion creep. *Journal of Structural Geology*, 33:1265–1284.

Kingma, K. J., Meade, C., Hemley, R. J., Mao, H., and Veblen, D. R. (1993). Microstructural observations of α-quartz amorphization. *Science*, 259:666–669.

Kitahara, S. and Kennedy, G. C. (1964). The quartz-coesite transition. *Journal of Geophysical Research*, 69(24):5395–5400.

Kohlstedt, D. L. (2007). Properties of rocks and minerals - constitutive equations, rheological behavior, and viscosity of rocks. In Schubert, G., editor, *Treatise on Geophysics*, pages 389–417. Oxford: Elsevier Ltd.

Kohlstedt, D. L., Evans, B., and Mackwell, S. J. (1995). Strength of the lithosphere: constraints imposed by laboratory experiments. *Journal of Geophysical Research: Solid Earth*, 100(B9):17587–17602.

Kohlstedt, D. L. and Hansen, L. N. (2015). Constitutive equations, rheological behaviour, and viscosity of rocks. In Schubert, G., editor, *Treatise on Geophysics*, pages 441–472. Oxford: Elsevier, 2 edition.

Krabbendam, M., Urai, J. L., and van Vliet, L. J. (2003). Grain size stabilization by dispersed graphite in a high-grade quartz mylonite: an example from Naxos (Greece). *Journal of Structural Geology*, 25:855–866.

Kronenberg, A. K. and Tullis, J. (1984). Flow strengths of quartz aggregates: grain size and pressure effects due to hydrolytic weakening. *Journal of Geophysical Research: Solid Earth*, 89(B6):4281–4297.

Küster, M. and Stöckhert, B. (1999). High differential stress and sublithostatic pore fluid pressure in the ductile regime - microstructural evidence for short-term post-seismic creep in the Sesia Zone (Western Alps). *Tectonophysics*, 303(1-4):263 – 277.

Linde, A. T., Gladwin, M. T., Johnston, M. J. S., Gwyther, R. L., and Bilham, R. G. (1996). A slow earthquake sequence on the San Andreas fault. *Nature*, 383:65–68.

Lockner, D. A. (1995). Rock failure. In Ahrend, T. J., editor, *Rock Physics and Phase Relations*, pages 127–147. AGU reference shelf.

Luan, F. C. and Paterson, M. S. (1992). Preparation and deformation of synthetic aggregates of quartz. *Journal of Geophysical Research*, 97:301–320.

Mancktelow, N. S. and Pennacchioni, G. (2005). The control of precursor brittle fracture and fluid-rock interaction on the development of single and paired ductile shear zones. *Journal of Structural Geology*, 27:645–661.

McLaren, A. C. and Hobbs, B. E. (1972). Transmission electron microscope investigation of some naturally deformed quartzites. In Heard, H. C., Borg, I. Y., Carter, N. L., and Raleigh, C. B., editors, *Flow and fracture of rocks*, pages 55–66. AGU Geophysical Monograph.

McLaren, A. C., Turner, R. G., Boland, J. N., and Hobbs, B. E. (1970). Dislocation structure of the deformation lamellae in synthetic quartz; a study by electron and optical microscopy. *Contribution to Mineralogy and Petrology*, 29:104–115.

Menegon, L., Nasipuri, P., Stünitz, H., Behrens, H., and Ravna, E. (2011). Dry and strong quartz during deformation of the lower crust in the presence of melt. *Journal of Geophysical Research: Solid Earth*, 116(B10). B10410.

Menegon, L., Pennachioni, G., Heilbronner, R., and Pittarello, L. (2008). Evolution of quartz microstructure and *c*-axis crystallographic preferred orientation within ductilely deformed granitoids (Arolla unit, Western Alps). *Journal of Structural Geology*, 30:1332–1347.

Mirwald, P. W. and Massonne, H.-J. (1980). The low-high quartz and quartz-coesite transition to 40 kbar between 600 ° and 1600 °C and some reconnaissance data on the effect of $NaAlO_2$ component on the low quartz-coesite transition. *Journal of Geophysical Research: Solid Earth*, 85(B12):6983–6990.

Mosenfelder, J. L. and Bohlen, S. R. (1997). Kinetics of the coesite to quartz transformation. *Earth and Planetary Science Letters*, 153:133 – 147.

Moulas, E., Podladchikov, Y. Y., Aranovich, L. Y., and Kostopoulos, D. (2013). The problem of depth in geology: when pressure does not translate into depth. *Petrology*, 21(6):527–538.

Muto, J., Hirth, G., Heilbronner, R., and Tullis, J. (2011). Plastic anisotropy and fabric evolution in shear and recrystallised quartz single crystals. *Journal of Geophysical Research*, 116:B02206.

Orowan, E. (1940). Problems of plastic gliding. *Proceedings of the Physical Society*, 52:8–22.

Panozzo, R. (1983). Two-dimensional analysis of shape-fabric using projections of digitized lines in a plane. *Tectonophysics*, 95:279–294.

Panozzo, R. (1984). Two-dimensional strain from the orientation of lines in a plane. *Journal of Structural Geology*, 6:215–221.

Panozzo Heilbronner, R. (1992). The autocorrelation function: an image processing tool for fabric analysis. *Tectonophysics*, 212:351–370.

Panozzo Heilbronner, R. and Pauli, C. (1993). Integrated spatial and orientation analysis of quartz *c*-axes by computer-aided microscopy. *Journal of Structural Geology*, 15:369–382.

Paterson, M. S. (1973). Nonhydrostatic thermodynamics and its geologic applications. *Reviews of Geophysics*, 11(2):355–389.

Paterson, M. S. (1989). The interaction of water with quartz and its influence in dislocation flow - an overview. In Karato, S.-I. and Toriumi, M., editors, *Rheology of solids and of the earth*, pages 107–142. Oxford University Press.

Paterson, M. S. (1990). Rock deformation experimentation. In Duba, A. G., Durham, W. B., Handin, J. W., and Wang, H. F., editors, *The brittle-ductile transition in rocks*, pages 187–194. Geophysical Monographs Series.

Paterson, M. S. and Luan, F. C. (1990). Quartzite rheology under geological conditions. *Geological Society, London, Special Publications*, 54:299–307.

Paterson, M. S. and Wong, T. (2005). *Experimental rock deformation - the brittle field*. Springer.

Pec, M. (2014). *Experimental investigation on the rheology of fault rocks*. PhD thesis, Universität Basel.

Pec, M., Stünitz, H., and Heilbronner, R. (2012a). Semi-brittle deformation of granitoid gouges in shear experiments at elevated pressures and temperatures. *Journal of Structural Geology*, 33:200–221.

Pec, M., Stünitz, H., Heilbronner, R., and Drury, M. (2016). Semi-brittle flow of granitoid fault rocks in experiments. *Journal of Geophysical Research: Solid Earth*, 121(3):1677–1705.

Pec, M., Stünitz, H., Heilbronner, R., Drury, M., and de Capitani, C. (2012b). Origin of pseudotachylites in slow creep experiments. *Earth and Planetary Science Letters*, 355-356:299 – 310.

Perrillat, J. P., Daniel, I., Lardaux, J. M., and Cardon, H. (2003). Kinetics of the coesite-quartz transition: application to the exhumation of ultrahigh-pressure rocks. *Journal of Petrology*, 44(4):773–788.

Petit, J. P. (1987). Criteria for the sense of movement on fault surfaces in brittle rocks. *Journal of Structural Geology*, 9:597–608.

Petrini, K. and Podladchikov, Y. (2000). Lithospheric pressure-depth relationship in compressive regions of thickened crust. *Journal of Metamorphic Geology*, 18(1):67–77.

Porter, D. A. and Easterling, K. E. (1992). *Phase transformation in metals and alloys*. Chapman and Hall, London.

Post, A. D., Tullis, J., and Yund, R. A. (1996). Effects of chemical environments on dislocation creep of quartzite. *Journal of Geophysical Research*, 101:22143–22155.

Prior, D. J., Boyle, A. P., Brenker, F., Cheadle, M. C., Day, A., Lopez, G., Peruzzo, L., Potts, G. J., Reddy, S., Spiess, R., Timms, N. E., Trimby, P., Wheeler, J., and Zetterström, L. (1999). The application of electron backscatter diffraction and orientation contrast imaging in the SEM to textural problems in rocks. *American Mineralogist*, 84:1741–1759.

Renner, J. (1996). *Experimentelle Untersuchungen zur Rheologie von Coesit*. PhD thesis, Ruhr-Universität Bochum.

Reuber, G., K., B. J., Schmalholz, S. M., and White, R. W. (2016). Nonlithostatic pressure during subduction and collision and the formation of (ultra)high-pressure rocks. *Geology*, 44(5):343–346.

Richter, B., Stünitz, H., and Heilbronner, R. (2016). Stresses and pressures at the quartz-to-coesite phase transformation in shear deformation experiments. *Journal of Geophysical Research: Solid Earth*, 121(11):8015–8033. 2016JB013084.

Robin, P. F. (1978). Pressure solution at grain-to-grain contacts. *Geochimica et Cosmochimica Acta*, 42:1383–1389.

Rowe, C. D. and Griffith, W. A. (2015). Do faults preserve a record of seismic slip: a second opinion. *Journal of Structural Geology*, 78:1 – 26.

Rubie, D. C. and Thompson, A. B. (1985). Kinetics of metamorphic reactions at elevated temperatures and pressures: an appraisal of available experimental data. In Thompson, A. B. and Rubie, D. C., editors, *Metamorphic reactions - Kinetics, textures, and deformation*, pages 27–79. Springer New York.

Rutter, E. H. (1986). Fault nomenclature of mode of failure transition in rocks. *Tectonophysics*, 122:381–387.

Rutter, E. H. and Brodie, K. H. (2004). Experimental grain size-sensitive flow of hot-pressed Brazilian quartz aggregates. *Journal of Structural Geology*, 26(11):2011–2023.

Schmalholz, S. M. and Podladchikov, Y. (2013). Tectonic overpressure in weak crustal-scale shear zones and implications for the exhumation of high-pressure rocks. *Geophysical Research Letters*, 40(10):1984–1988.

Schmalholz, S. M. and Podladchikov, Y. Y. (2014). Metamorphism under stress: the problem of relating minerals to depth. *Geology*, 42(8):733–734.

Schmocker, M., Bystricky, M., Kunze, K., Burlini, L., Stünitz, H., and Burg, J.-P. (2003). Granular flow and Riedel band formation in water-rich quartz aggregates experimentally deformed in torsion. *Journal of Geophysical Research*, 108:B52242.

Scholz, C. H. (2007). *The Mechanics of Earthquakes and Faulting*. Cambridge University Press, 2 edition.

Schönbohm, D. (2003). *Untersuchungen zur Kinetik der Coesit → Quarz Umwandlung unter in-situ Bedingungen mittels Synchrotronstrahlung sowie Analyse der Mikrostrukturen im Transformationsbereich mittels TEM*. PhD thesis, Rheinische Friedrich-Wilhelms-Universität.

Schwartz, A., Kumar, M., Adams, B. L., and Field, D. P., editors (2009). *Electron backscatter diffraction in material science*. Springer, 2 edition.

Shimizu, I. (1992). Kinetics of pressure solution creep in quartz: theoretical considerations. *Tectonophysics*, 245:121–134.

Sibson, R. H. (1989). Earthquake faulting as a structural process. *Journal of Structural Geology*, 11(1):1–14.

Smith, D. C. (1984). Coesite in clinopyroxene in the Caledonides and its implications for geodynamics. *Nature*, 310(5979):641–644.

Stipp, M., Stünitz, H., Heilbronner, R., and Schmid, S. M. (2002). Dynamic recrystallization of quartz: correlation between natural and experimental conditions. *Geological Society, London, Special Publications*, 200(1):171–190.

Stipp, M. and Tullis, J. (2003). The recrystallized grain size piezometer for quartz. *Geophysical Research Letters*, 30(21):n/a–n/a.

Stünitz, H. (1998). Syndeformational recrystallization - dynamic or compositionally induced? *Contributions to Mineralogy and Petrology*, 131(2):219–236.

Stünitz, H., FitzGerald, J., and Tullis, J. (2003). Dislocation generation, slip systems, and dynamic recrystallization in experimentally deformed plagioclase single crystals. *Tectonophysics*, 372(3-4):215 – 233.

Stünitz, H., Thust, A., Heilbronner, R., Behrens, H., Kilian, R., Tarantola, A., and FitzGerald, J. D. (2017). Water redistribution in experimentally deformed natural milky quartz single crystals - implications for H_2O-weakening processes. *Journal of Geophysical Research: Solid Earth*, 122(2):866–894.

Stüwe, K. and Sandiford, M. (1994). Contribution of deviatoric stresses to metamorphic P-T paths: an example appropriate to low-P, high-T metamorphism. *Journal of Metamorphic Geology*, 12(4):445–454.

Su, W.-H., Liu, S.-E., Xu, D.-P., Wang, W.-R., Yao, B., Liu, X.-M., Liu, Z.-G., and Zhong, Z. (2006). Effects of local mechanical collision with shear stress on the phase transformation from α-quartz to coesite induced by high static pressure. *Phys. Rev. B*, 73:144110.

Sun, N., Liu, X., and Lu, K. (1996). An explanation to the anomalous avrami exponent. *Scripta Materialia*, 34(8):1201 – 1207.

Tajčmanová, L., Vrijmoed, J., and Moulas, E. (2015). Grain-scale pressure variations in metamorphic rocks: implications for the interpretation of petrographic observations. *Lithos*, 216-217:338 – 351.

Tarantola, A., Diamond, L. W., and Stünitz, H. (2010). Modification of fluid inclusions in quartz by deviatoric stress I: experimentally induced changes in inclusion shapes and microstructures. *Contributions to Mineralogy and Petrology*, 160(6):825–843.

Tarantola, A., Diamond, L. W., Stünitz, H., Thust, A., and Pec, M. (2012). Modification of fluid inclusions in quartz by deviatoric stress III: influence of principal stresses on inclusion density and orientation. *Contributions to Mineralogy and Petrology*, 164(3):537–550.

Thust, A. (2014). *Experimentelle Verformung von natürlichen Quarzeinkristallen: Einfluss der Wasserneuverteilung auf die Deformation und mikrostrukturelle Untersuchungen*. PhD thesis, Universität Basel.

Trepmann, C. A. and Stöckhert, B. (2003). Quartz microstructures developed during non-steady state plastic flow at rapidly decaying stress and strain rate. *Journal of Structural Geology*, 25(12):2035 – 2051.

Trepmann, C. A. and Stöckhert, B. (2013). Short-wavelength undulatory extinction in quartz recording coseismic deformation in the middle crust - an experimental study. *Solid Earth*, 4(2):263–276.

Trepmann, C. A., Stöckhert, B., Dorner, D., Moghadam, R. H., Küster, M., and Röller, K. (2007). Simulating coseismic deformation of quartz in the middle crust and fabric evolution during postseismic stress relaxation - an experimental study. *Tectonophysics*, 442:83 – 104.

Tullis, J. (2002). Deformation of granitic rocks: experimental studies and natural examples. *Reviews in Mineralogy and Geochemistry*, 51(1):51–95.

Tullis, J., Christie, J. M., and Griggs, J. T. (1973). Microstructures and preferred orientations of experimentally deformed quartz. *Geological Society of America Bulletin*, 84:297–314.

Tullis, J., Shelton, G. L., and Yund, R. A. (1979). Pressure dependence of rock strength: implications for hydrolytic weakening. *Bulletin de Min'eralogie*, 102:110–114.

Tullis, J. and Yund, R. A. (1982). Grain growth kinetics of quartz and calcite aggregates. *Journal of Geology*, 90:301–318.

Tullis, T. E. and Tullis, J. (1986). *Experimental rock deformation techniques*, volume 36, pages 297–324. Geophysical Monographs.

van Daalen, M., Heilbronner, R., and Kunze, K. (1999). Orientation analysis of localized shear deformation in quartz fibres at the brittle-ductile transition. *Tectonophysics*, 303:83–107.

Vernooij, M. G. C., den Brok, B., and Kunze, K. (2006). Development of crystallographic preferred orientations by nucleation and growth of new grains in experimentally deformed quartz single crystals. *Tectonophysics*, 427(1):35–53.

Vernooij, M. G. C. and Langenhorst, F. (2005). Experimental reproduction of tectonic deformation lamellae in quartz and comparison to shock-induced planar deformation features. *Meteoritics and Planetary Science*, 40:1353–1361.

Wheeler, J. (2014). Dramatic effects of stress on metamorphic reactions. *Geology*, 42(8):647–650.

White, S. (1973a). Deformation lamellae in naturally deformed quartz. *Nature Physical Science*, 245:26–28.

White, S. (1973b). The dislocation structures responsible for the optical effects in some naturally-deformed quartzes. *Journal of Material Science*, 8:490–499.

White, S. H., Burrows, S. E., Carreras, J., Shaw, N. D., and Humphreys, F. J. (1980). On mylonites in ductile shear zones. *Journal of Structural Geology*, 2(1):175 – 187.

Wong, T.-F. (1990). A note on the propagation behavior of a crack nucleated by a dislocation pileup. *Journal of Geophysical Research*, 95:8639–8646.

Zhou, Y., He, C.and Song, J., Ma, S., and Ma, J. (2005). An experiment study of quartz-coesite transition at differential stress. *Chinese Science Bulletin*, 50:446–451.

Zinn, P. (1996). *Die Hochdrucksynthese von Coesit und die experimentelle Bestimmung seiner Stabilität als Funktion des Verzwilligungsgrades sowie Untersuchung zur Kinetik der Phasentransformation*. PhD thesis, Justus-Liebig-Universität Giessen.

Appendix

A List of abbreviations and symbols

A	material-dependent flow law factor
ACF	autocorrelation function
BSE	backscatter electron
CIP	computer-integrated polarisation microscopy
coe	coesite
COI	*c*-axis orientation image
CPO	crystallographic preferred orientation
d	displacement
$\mathbf{d}_s$	shear displacement
$\dot{\mathbf{d}}$	displacement rate
$\mathbf{d}_0$	initial diameter
$\mathbf{d}_{equ}$	equivalent diameter
EBSD	electron backscatter diffraction
EDX	energy-dispersive X-ray spectroscopy
f	fugacity
F	force
FTIR	fourier transform infrared spectroscopy
h (d)	distribution of equivalent sectional diameters
IPF	inverse pole figure colouring
m	fugacity exponent
n	stress exponent
N	number
P	pressure
$\mathbf{P}_c$	confining pressure
qtz	quartz
Q	activation energy
(E)SEM	(environmental) scanning electron microscope
SPO	shape preferred orientation
T	temperature
TC	thermocouple
TEM	transmission electron microscopy
TDF	trend distribution function
th	thickness
v (D)	distribution of volumetric equivalent spheres

γ	shear strain (unless stated otherwise, γ is the value calculated from digital record)
$\gamma_{calc.}$	shear strain calculated with digital data record
$\gamma_{meas.}$	shear strain calculated with displacement measured on thin section
$\dot{\gamma}$	shear strain rate
μ	friction coefficient
σ_1	maximum principal stress
σ_2	intermediate principal stress
σ_3	minimum principal stress
σ_m	mean stress
σ_n	normal stress
$\Delta\sigma$	differential stress
τ	shear stress

B Experimental data

Tab. B-1: Experimental conditions of all experiments. Difficulties occurred during the experimental procedure of grey-coloured samples (e.g. pressure vessel failure, tilted Pt discs, TC failure, slip at piston-sample interface). These samples are excluded from detailed microstructural investigations and the mechanical data are not used.

exp. #	T [°C]	P_c [GPa]	$\dot{d}$ [10^{-8} m^{-1}]	H_2O [μl]	salt	rig	$\gamma_{meas.}$	$\gamma_{calc.}$	notes
333BR	800	1.5	-	0.2	KI	1	-	-	failed after 14 h
334BR	700	1.45	-	0.2	NaCl	1	-	-	failed during pumping
335BR	800	1.0	0.8	0.2	NaCl	1	3.0	1.9	slip at psi[1]
336BR	600	1.5	1.3	0.2	NaCl	2	1.8	0.5	slip at psi
337BR	1000	1.5	1.7	0.2	NaCl	1	3.9	3.2	
338BR	600	1.5	0.82	0.2	NaCl	2	1.0	1.4	
339BR	700	1.5	1.3	0.2	NaCl	1	2.4	2.0	
340BR	500	1.5	0.79	0.2	NaCl	2	1.8	1.6	
345BR	900	1.5	-	0.2	NaCl + hem	1	4.4	-	failed after 2.5 h
346BR	800	1.5	1.2	0.2	NaCl	2	1.1	2.5	Pb leak
347BR	800	1.5	1.2	0.2	NaCl + hem	1	1.2	2.4	"too strong"[2]
348BR	700	1.5	1.6	0.2	NaCl	1	3.6	3.0	hot pressed[3]
349BR	700	0.5	1.5	0.2	NaCl	2	1.5	2.9	slip at psi
350BR	600	0.8	-	0.2	NaCl	1	0.4	-	failed during pumping
351BR	700	1.5	1.6	'as-is'	NaCl	2	2.6	2.6	
352BR	600	1.5	0.97	0.2	NaCl	1	0.6	1.0	hot pressed
353BR	500	0.7	-	0.2	NaCl	1	0.6	-	failed during pumping
354BR	900	1.5	0.93	0.2	NaCl + hem	2	1.0	1.4	"too strong"
355BR	900	1.5	-	0.2	NaCl	1	0.8	-	PV[4]broken
376BR	800	1.5	1.5	0.2	NaCl	2	1.1	4.3	slip along Pt discs
378BR	800	1.5	1.3	0.2	NaCl	2	2.1	3.1	"too strong"
380BR	700	1.5	-	dried[5]	NaCl	2	0.4	-	PV broken
381BR	800	0.5	1.5	0.2	NaCl	2	1.4	1.2	stick-slip before peak
383BR	700	1.5	1.5	0.2	NaCl	2	6.1	4.9	
384BR	800	0.5	-	0.2	NaCl	2	1.4	-	PV broken
386BR	800	0.5	1.5	0.2	NaCl	2	3.2	3.2	
388BR	800	1.5	1.5	0.2	NaCl	2	6.1	4.8	
412BR	900	1.5	1.6	0.2	NaCl	1	3.8	2.9	
415BR	600	1.5	1.1	0.2	NaCl	1	1.1	3.0	hot pressed
417BR	1000	1.5	hydro[6]	0.2	NaCl	1	0.8	-	
419BR	800	1.5	1.6	0.2	NaCl	1	4.0	4.2	hot pressed
422BR	900	0.6	-	0.2	NaCl	1	1.3	-	failed after 24 h
435BR	650	1.5	1.2	0.2	NaCl	1	2.2	3.6	
437BR	700	1.5	1.2	0.2	NaCl	1	3.3	1.7	

exp. #	T [°C]	P_c [GPa]	$\dot{d}$ [10^{-8} m^{-1}]	H_2O [μl]	salt	rig	$\gamma_{meas.}$	$\gamma_{calc.}$	notes
439BR	800	1.5	1.3	0.2	NaCl	1	2.3	1.4	
441BR	700	1.0	0.75	0.2	NaCl	1	2.5	0.8	PV broken
443BR	800	1.0	1.6	0.2	NaCl	1	6.2	4.6	slip at psi
445BR	800	1.5	1.6	0.2	NaCl	1	6.3	4.7	7-11 μm powder
447BR	800	1.5	15	0.2	NaCl	1	4.0	4.1	
448BR	800	1.0	1.6	0.2	NaCl	1	5.9	4.5	
450BR	500	1.5	1.2	0.2	NaCl	1	2.1	3.2	
452BR	700	1.0	1.4	0.2	NaCl	1	4.8	4.4	
479BR	600	1.5	1.2	0.2	NaCl	2	2.5	3.9	
480BR	800	1.5	1.4/ 0.36/ 1.3	0.2	NaCl	1	4.6	4.5	hot pressed, srs[7]
481BR	650	1.5	2.1	0.2	NaCl	2	2.6	4.2	
482BR	900	1.5	13/ 2.6/ 0.56/ 16	0.2	NaCl	1	9.1	8.4	srs
485BR	1000	1.5	16/ 2.1/ 0.19/ 17	0.2	NaCl	1	7.1	6.2	srs
487BR	800	1.5	hydro	0.2	NaCl	1	1.2	-	
488BR	800	1.5	13/ 3.3/ 0.74/ 0.22	0.2	NaCl	1	6.6	6.4	power failure at the end, srs
493BR	700	1.5	1.5	0.2	NaCl	1	3.7	4.9	hot pressed
494BR	650	1.0	2.6	0.2	NaCl	2	3.4	5.7	
495BR	750	1.5	15	0.2	NaCl	1	6.6	7.0	
496BR	700	1.5	-	0.2	NaCl	2	1.1	-	Pb leak, srs
497BR	700	1.0	1.1/ 1.1/ 0.27	0.2	NaCl	1	4.5	5.6	jacket leak, srs
498BR	700	1.5	1.3/ 0.66/ 0.13	0.2	NaCl	2	4.1	5.4	low output[8], srs
499BR	900	1.5	110	0.2	NaCl	1	3.4	4.0	
500BR	650	1.5	0.21	0.2	NaCl	1	1.4	1.1	

[1] psi = piston-sample interface
[2] unexpected high stress values, probably due to additional platinum disc
[3] hot pressed at 1000 °C and ∼1.6 GPa for 20 h
[4] PV = pressure vessel
[5] vacuum dried at 900 °C
[6] hydrostatic experiment
[7] different displacement rates (srs = strain-rate stepping)
[8] low output of the furnace (lower temperature as set to)

Tab. B-2: Use of platinum discs

exp. #	# of Pt discs	T [°C]	P_c [GPa]	PV	comment	shape of loading curve
333BR	1	800	1.5	new	-	
334BR	1	800	1.5	new	-	
335BR	1	800	1.0	new	slip	ok
336BR	1	600	1.5	old	failed	ok
337BR	1	1000	1.5	new	ok	ok
338BR	2	600	1.5	old	ok	wavy
339BR	2	700	1.5	new	ok	ok
340BR	2	500	1.5	old	ok	wavy
345BR	2	900	1.5	new	failed	-
346BR	2	800	1.5	old	too strong	wavy
347BR	2	800	1.5	new	too strong	wavy
348BR	2	700	1.5	new	ok?	ok
349BR	2	700	0.5	old	slip	(wavy)
350BR	2	600	0.8	new	failed (TC)	-
351BR	2	700	1.5	old	ok	ok
352BR	2	600	1.5	new	weak	ok
353BR	2	500	0.7	new	failed (TC)	-
354BR	2	900	1.5	old	too strong	wavy
355BR	2	900	1.5	new	failed (PV)	-
376BR	2	800	1.5	old	too strong	wavy
378BR	2	800	1.5	old	too strong	wavy
380BR	2	700	1.5	old	failed (PV)	-
381BR	1	800	0.5	old 2	stick slip	ok
383BR	1	700	1.5	strict	ok	ok
384BR	1	800	0.5	old 2	failed (PV)	-
386BR	1	800	0.5	combo	ok	ok
388BR	1	800	1.5	combo	ok	ok
412BR	1	900	1.5	strict	ok	ok
415BR	1	600	1.5	strict	ok	ok
417BR	1	1000	1.5	strict	-	-
419BR	1	800	1.5	strict	ok	ok
422BR	1	900	0.6	strict	failed (TC)	-
435BR	1	650	1.5	strict	ok	ok
437BR	1	700	1.5	combo	ok	ok
439BR	1	800	1.5	combo	ok	ok
441BR	1	700	1.0	combo	failed (PV)	ok
443BR	1	800	1.0	combo (new)	weak	ok
445BR	1	800	1.5	combo (new)	weak	ok
447BR	1	800	1.5	combo (new)	ok	ok
448BR	1	800	1.0	combo (new)	ok	ok
450BR	1	500	1.5	combo (new)	ok	ok
452BR	1	700	1.0	combo (new)	ok	ok

exp. #	# of Pt discs	T [°C]	P_c [GPa]	PV	comment	shape of loading curve
479BR	1	600	1.5	combo (new)	ok	ok
480BR	1	800	1.5	strict	ok	ok
481BR	1	650	1.5	combo (new)	ok	ok
482BR	1	900	1.5	strict	ok	ok
485BR	1	1000	1.5	strict	ok	ok
487BR	1	800	1.5	strict	-	-
488BR	1	800	1.5	strict	ok	ok
493BR	1	700	1.5	strict	ok	ok
494BR	1	650	1.0	combo (new)	ok	ok
495BR	1	750	1.5	strict	ok	ok
496BR	1	700	1.5	combo (new)	lead leak	ok
497BR	1	700	1.0	strict	salt leak	ok
498BR	1	700	1.5	combo (new)	bad T control	ok
499BR	1	900	1.5	strict	ok	ok
500BR	1	650	1.5	strict	ok	ok

Tab. B-3: List of EBSD measuring sites with good or high quality except for samples 435br and 495br.

exp. #	EBSD map	step size [μm]	x [μm]	y [μm]	hit rate [%]	# of site in D
337BR	ebsd02_map2	0.75	381	145.5	91.8	
	aug02_site1	0.2	250	200	94.9	site 1
	aug03_site3	0.2	165	165	96.8	site 2
383BR	ebsd03_site2_map2	0.8	450.4	360	69.5	site 1
	ebsd03_site3_map3	0.4	124	88	74.9	site 2
	RH_map5	0.15	130	110	81.2	site 3
	Feb2016_site2	0.2	75	50	77.3	site 4
	Feb2016_site3	0.2	105	65	72.8	site 5
388BR	newAug01_site3_m7	0.05	30	50	73.4	site 1
	newAug04_site13_m13	0.2	100	100	94.0	site 2
	newAug04_site14_m14	0.2	70	50	93.9	site 3
412BR	newAug02_site2_m2	0.1	100	40	80.5	site 1
	newAug02_site3_m3	0.1	70	70	89.0	site 2
	newAug02_site3_m4	0.1	50	50	84.7	site 3
	newAug02_site3_m5	0.1	50	50	89.1	site 4
	newAug04_site1	0.2	185	170	87.8	site 5
415BR	ebsd_site1_m1	0.5	530	430	81.4	
417BR	newAug01_site4_m5	0.2	100	100	87.7	site 1
	newAug01_site4_m6	0.2	150	75	89.5	site 2
	newAug01_site6_m8	0.2	330	250	93.0	site 3
419BR	newAug	0.15	120	135	91.5	
435BR	renee_site5	1.5	481.5	321	37.4	
	renee_site6	1.5	537	318	20.7	
	ebsd_site1_m4	0.4	193.6	149.6	43.8	
437BR	ebsd_site2_m5	0.3	201	99	71.1	
439BR	ebsd_site1	0.4	550	394	78.9	
445BR	newAug04_site1	0.1	95	70	83.5	site 1
	newAug04_site2	0.1	120	70	82.8	site 2
447BR	Feb2016_site1	0.2	200	150	79.8	site 1
	Feb2016_site2	0.2	200	150	80.8	site 2
	Feb2016_site3	0.2	250	190	82.5	site 3
448BR	Feb2016_site1	0.2	160	120	77.9	site 1
	Feb2016_site2_m2	0.1	160	90	82.6	site 2
452BR	Feb2016_site1	0.2	140	105	63.4	site 1
	Feb2016_03_site1	0.15	123	90	62.2	site 2
487BR	newAug04_site1_m1	0.2	125	140	95.4	site 1

exp. #	EBSD map	step size [μm]	x [μm]	y [μm]	hit rate [%]	
	newAug04_site2_m4	0.2	240	155	96.1	site 2
493BR	Feb2016_site3_m3	0.2	160	120	77.0	site 1
	Feb2016_site6_m11	0.2	80	70	75.6	site 2
	Feb2016_site6_m12	0.2	120	40	79.6	site 3
	Feb2016_site6_m13	0.2	60	70	76.3	site 4
495BR	Feb2016_site1_m3	0.2	40	25	51.3	
	Feb2016_site_m4	0.2	60	40	50.3	
499BR	Feb2016_site3_m4	0.2	141.6	102.4	65.4	
500BR	Feb2016_site1_m1	0.3	228	171	85.5	

C Additional observations

Different additional microstructural observations are made in experiments. The mechanical data or the bulk microstructural development are not influenced by these microstructures. However, they are prominent features and their formation could provide further insight for active processes. Partly, these microstructures could not be reproduced (section C.3), which makes the analysis more difficult. In the following, they will be described but more research is needed to fully understand the formation.

C.1 Carbon infiltration during experiments

Carbon particles infiltrate several samples during the experiment. No carbon traces occur in the original quartz powder. Hence, the carbon source has to be somewhere in the sample assembly, whereby only the furnace contains carbon (Chapter 2). It is clearly identified with Raman spectroscopy (Fig. C.1-1). Especially, sample 417br was not exposed to epoxy or other carbon-sources during the thin section preparation. Therefore, the carbon signal can only be related to particles that infiltrate the sample during the experiment.

The occurrence of carbon (Table C.1-1) does not correlate with the used apparatus or the season (humidity in the laboratory). But high temperatures and time spent at *PT* conditions are associated with high carbon content. A dependence of the confining pressure cannot be excluded and high water content seems to intensify the infiltration.

Tab. C.1-1: Occurrence of carbon particles in the samples. High quality samples are black. Different problems occur in grey-shaded samples (e.g. pressure vessel broken, salt or lead leak, tilting in sample assembly due to additional Pt disc).

exp. #	C content[1]	t in rig [h]	t at PT [h]	P_c [GPa]	T [°C]	note	rig	season
333BR	-	14.2	-	1.5	800	KI[2]	1	june/july
334BR	-	-	-	1.5	800		1	june/july
335BR	frequently	123.5	46.6	1.0	800		1	june/july
336BR	negligible	44.6	23.3	1.5	600		2	june/july
337BR	frequently	47.4	37.5	1.5	1000		1	june/july
338BR	negligible	75.1	48.3	1.5	600		2	june/july
339BR	frequently	100.4	51.3	1.5	700		1	june/july
340BR	negligible	71.1	43.3	1.5	500		2	june/july
345BR	frequently	66.3	2.5	1.5	900	hem[3]	1	oct/nov
346BR	negligible	153.2	98.7	1.5	800		2	oct/nov
347BR	negligible	68.8	40.8	1.5	800	hem	1	oct/nov
348BR	some	76.7	44.7	1.5	700	hp	1	oct/nov
349BR	negligible	97.1	73.7	0.5	700		2	oct/nov
350BR	negligible	6.6	-	0.8	600		1	oct/nov
351BR	negligible	114.1	67.1	1.5	700		1	oct/nov
352BR	some	95.3	49.0	1.5	600	hp	2	oct/nov

exp. #	C content	t in rig [h]	t at PT [h]	P_c [GPa]	T [°C]	note	rig	season
353BR	negligible	4.9	-	0.7	500		1	oct/nov
354BR	negligible	88.8	74.3	1.5	900	hem	2	oct/nov
355BR	negligible	25.2	2.0	1.5	900		1	oct/nov
376BR	some	97.4	68.4	1.5	800		2	june/july
378BR	negligible	120.3	78.6	1.5	800		2	june/july
380BR	negligible	11.0	1.1	1.5	700		2	june/july
381BR	negligible	71.5	54.0	0.5	800		2	june/july
383BR	frequently	120.9	98.7	1.5	700		2	june/july
384BR	negligible	20.8	13.1	0.5	800		2	june/july
386BR	some	96.1	75.0	0.5	800		2	june/july
388BR	some	97.4	70.5	1.5	800		2	june/july
412BR	frequently	98.1	71.3	1.5	900		1	oct/nov
415BR	frequently	125.4	77.0	1.5	600	hp	1	oct/nov
417BR	frequently	27.1	20.0	1.5	1000	hydro	1	oct/nov
419BR	frequently	118.3	76.5	1.5	800	hp	1	oct/nov
422BR	negligible	30.0	24.3	0.6	900		1	oct/nov
435BR	negligible	114.0	77.8	1.5	650		1	feb/mar
437BR	some	74.0	33.8	1.5	700		1	feb/mar
439BR	some	47.1	38.4	1.5	800		1	feb/mar
441BR	negligible	66.8	55.5	1.0	700		1	feb/mar
443BR	some	81.6	72.9	1.0	800		1	feb/mar
445BR	frequently	97.7	73.6	1.5	800		1	feb/mar
447BR	some	29.0	6.9	1.5	800		1	feb/mar
448BR	some	77.1	70.7	1.0	800		1	feb/mar
450BR	negligible	97.4	74.0	1.5	500		1	feb/mar
452BR	some	191.0	85.5	1.0	700		1	feb/mar
479BR	negligible	98.4	70.7	1.5	600		2	jan
480BR	frequently	145.3	92.5	1.5	800	hp	1	jan
481BR	negligible	72.3	46.7	1.5	650		2	jan
482BR	frequently	81.3	72.0	1.5	900	srs[4]	1	jan
485BR	frequently	74.0	64.9	1.5	1000	srs	1	jan
487BR	frequently	35.6	25.0	1.5	800	hydro	1	jan
488BR	frequently	98.0	76.0	1.5	800	srs	1	jan
493BR	negligible	103.0	71.6	1.5	700	hp	1	aug
494BR	negligible	55.8	50.5	1.0	650		2	aug
495BR	negligible	32.0	9.9	1.5	750		1	aug
496BR	negligible	47.0	39.1	1.5	700	srs	2	aug
497BR	some	190.3	186.2	1.0	700	srs	1	aug
498BR	negligible	201.8	193.4	1.5	700	srs	2	aug
499BR	negligible	11.8	1.1	1.5	900		1	aug
500BR	negligible	∼11 days	∼10 days	1.5	650		1	aug

[1] qualitative estimated
[2] potassium iodide used as confining medium
[3] hematite mixed with NaCl
[4] srs - strain rate stepping experiment

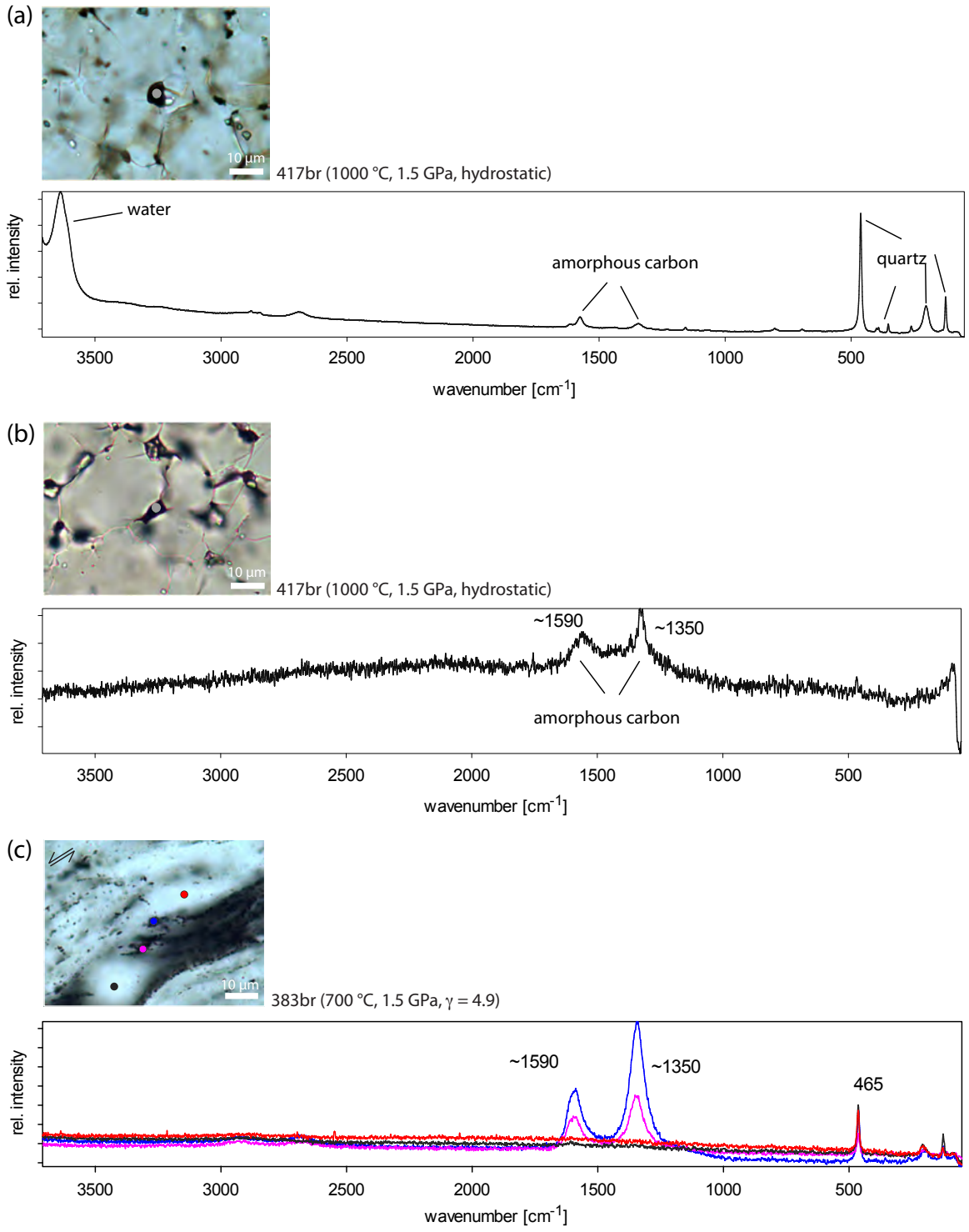

Fig. C.1-1: Raman spectrograms of carbon. (a) Single fluid inclusion (peak above 3500 cm^{-1} indicating water) below the surface containing carbon (peaks at ~1590 cm^{-1} and ~1350 cm^{-1}). A background signal of quartz (peak at ~465 cm^{-1}) is detected. (b) Carbon at the surface in 417br. (c) All spots show the 465cm^{-1}-quartz peak while two spots (blue and magenta) additionally indicate carbon (peaks at ~1590 cm^{-1} and ~1350 cm^{-1}).

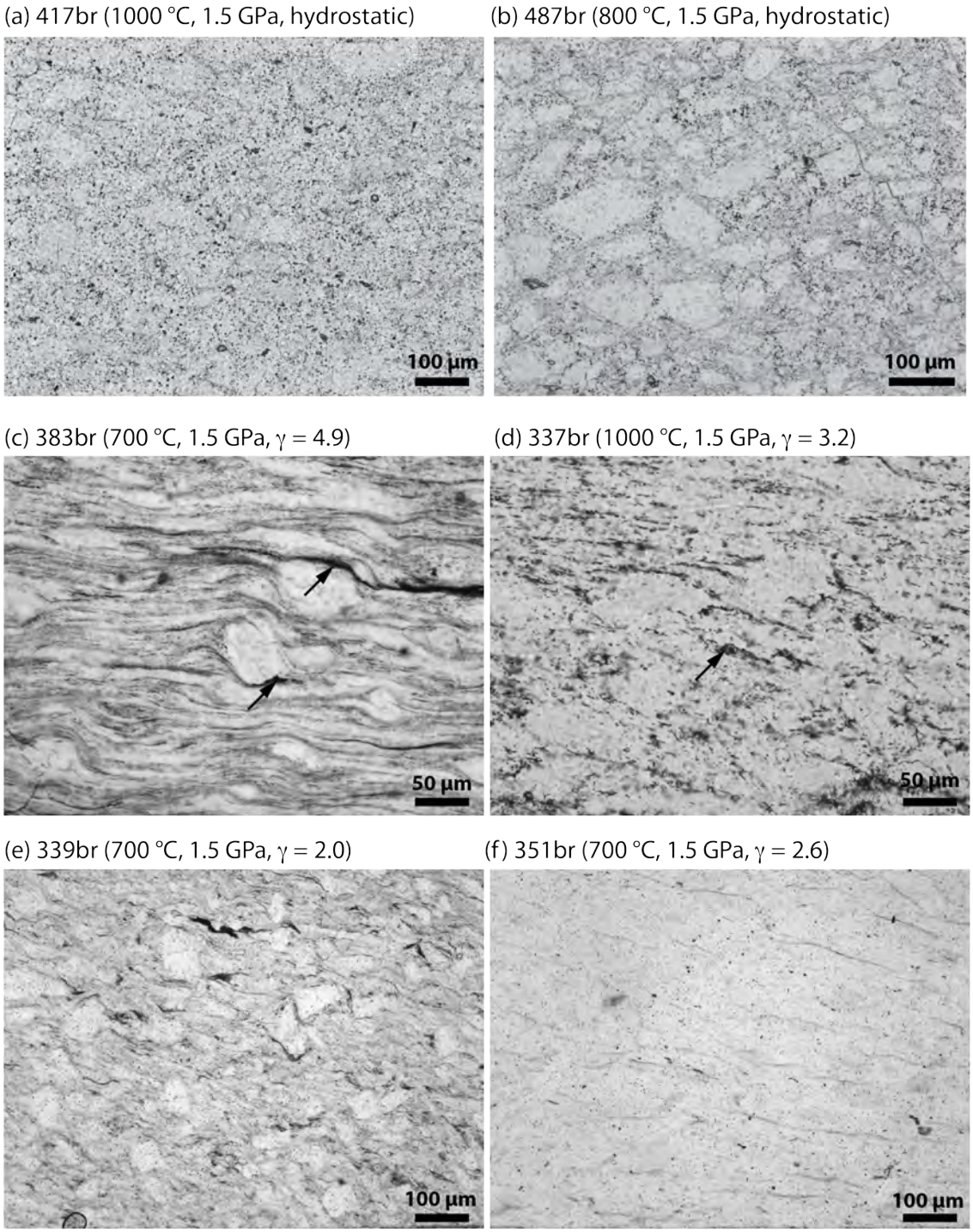

Fig. C.1-2: Carbon infiltration in different samples (all images in plane polarised light, c-f with sinistral shear sense). The opaque carbon often occurs along grain boundaries. (a) and (b) Carbon is evenly distributed in hydrostatic samples. (c) and (d) Conglomeration (arrow) occur with increasing strain. (e) and (f) Two samples at similar $PT\gamma$ conditions that differ in water content. (e) A lot of carbon is present in the sample with 0.2 wt % water added. (f) The 'as-is' sample with no additional water includes less carbon.

In hydrostatic experiments, carbon is evenly distributed in the sample along grain boundaries (Fig. C.1-2a and C.1-2b). In deformed samples, it is also spread in the whole sample but conglomerations can occur (Fig. C.1-2c and C.1-2d).

The effect of water can be observed in 339br (Fig C.1-2e) and 351br (Fig. C.1-2f). In the first one, 0.2 wt% water are added to the quartz powder. The second one is deformed without adding water ('as-is'). The deformation conditions of these two experiments are almost identical. 351br has a slightly higher displacement rate and spent a bit more time at *PT* conditions than 339br. However, the carbon content in 339br is significantly higher than in 351br. Hence, the transport of carbon through the sample appears to be enhanced by water, which is supported by Raman measurements of carbon that is incorporated in fluid inclusions.

Carbon can be seen as a second phase next to quartz that can affect the grain size of quartz by pinning [e.g. Krabbendam et al., 2003]. Krabbendam et al. [2003] analysed natural quartz mylonites containing dispersed graphite. They conclude that a minimum diameter of the graphite particles is necessary to affect the grain size of quartz by pinning (~ 5 µm). The microstructure and grain size distribution of 339br and 351br (same experimental conditions except for the water content) are similar indicating a minimal pinning effect. Nevertheless, this infiltration should be kept in mind, especially for grain size piezometers.

Furthermore, Chernak et al. [2009] performed experiments on Black Hills quartzite with CO_2 added. They conclude that the strength of the quartzite is secondarily affected by carbon particles present on grain boundaries between recrystallised grains [Chernak et al., 2009]. This conclusion is in accord with our observation of the strength of 339br and 351br. Despite the different carbon content in these two samples, the strength is similar.

C.2 Accumulations of fine-grained quartz

Accumulations of submicron-sized grains occur in the quartz powder (Fig. C.2-1). Similar features appear in several experiments with low shear strain and / or low deformation temperature (Table C.2-1). After deformation, they are elongated and deformed on the whole to some extent (Fig. C.2-2). No such accumulations are visible in high-strain experiments deformed at high temperatures. Possibly, the fine grains are consumed by grain growth or recrystallisation while deforming.

The accumulations are not related to the added water since they already occur in the dried powder. Furthermore, only some of them occur at the piston-sample interface and the position does not correlate with location of the added water on the upper forcing block. In addition, no effect on the mechanical data can be identified if comparing samples with and without agglutinations at the same *PT* conditions.

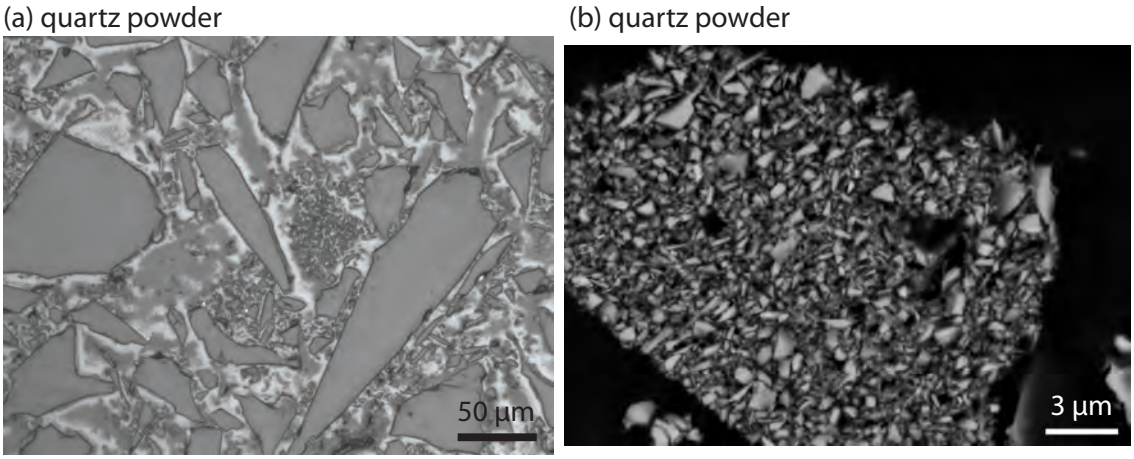

Fig. C.2-1: Accumulations of fine-grained quartz in the initial powder. (a) and (b) Submicron-sized splinters can agglutinate in the powder. (a) reflected light. (b) Close-up of a single accumulation of fine-grained quartz (BSE image).

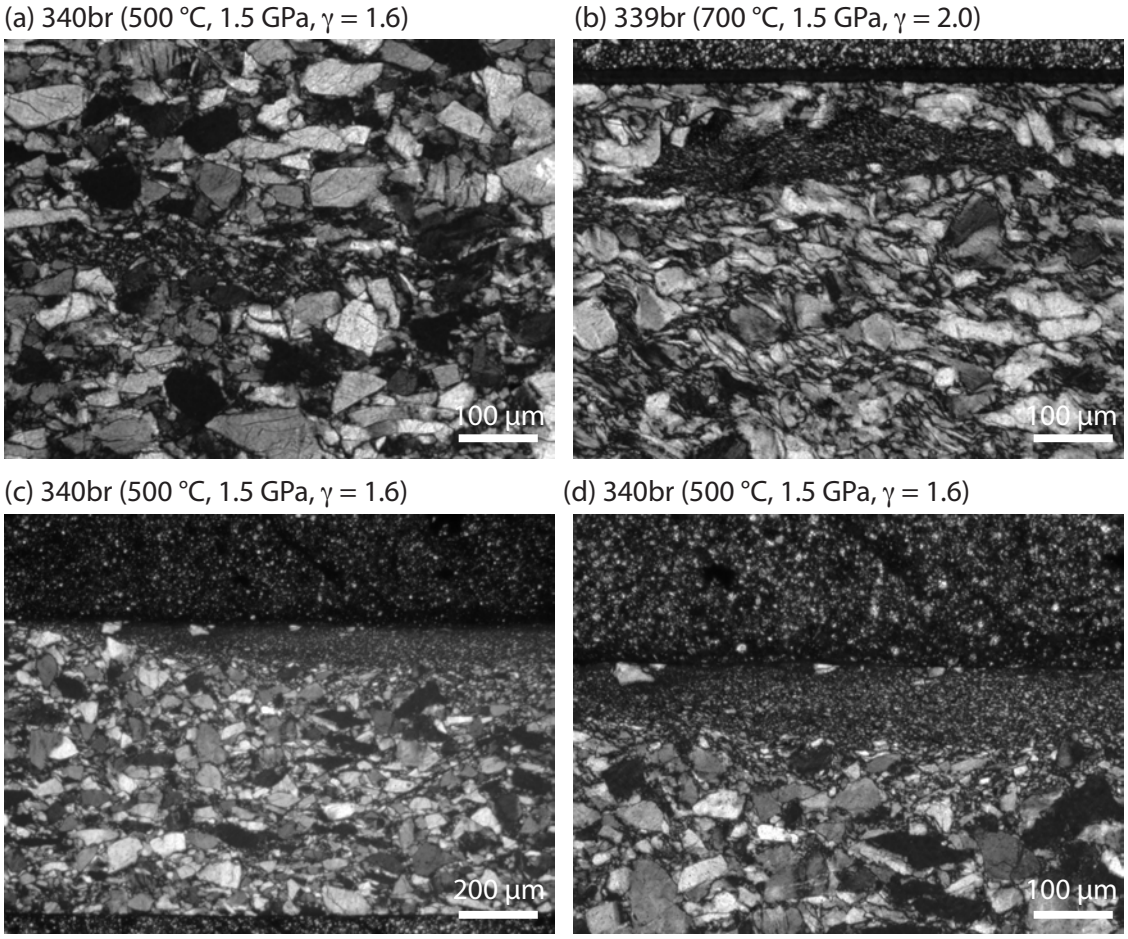

Fig. C.2-2: Accumulations of fine-grained quartz in deformed samples. Agglutinations can survive pressurisation and loading (sinistral shear sense, crossed polarised light). (a) Potential remains of a small agglutination. (b) Accumulation of small grains that is deformed on the whole. (c) and (d) A single large accumulation along the sample-piston interface.

Tab. C.2-1: Occurrence of fine-grained accumulations in the samples. High quality samples are black. Different problems occurred in grey-shaded samples (e.g. pressure vessel broken, salt or lead leak, tilting in sample assembly due to additional Pt disc).

exp. #	fine-grained agglutinations	t [h] at T	γ	T [°C]
powder	several	-	-	-
333BR		14.2	-	800
334BR		-	-	800
335BR	2 small[1](close to the forcing block)	46.6	3.0	800
336BR	2-3 small	23.3	1.8	600
337BR	-	37.5	3.9	1000
338BR	-	48.3	1.0	600
339BR	1 long[2]	51.3	2.4	700
340BR	1 normal[3], 1 very long	43.3	1.8	500
345BR	1 small, 1 large	2.5	4.4	900
346BR	1 very long, 1 long, 2 normal	98.7	1.1	800
347BR	1 long, 2-3 normal	40.8	1.2	800
348BR	-	44.7	3.6	700
349BR	1 normal	73.7	1.5	700
350BR	1-2 small to normal	-	0.4	600
351BR	-	67.1	2.6	700
352BR	-	49.0	0.6	600
353BR	1 normal, 2 small	-	0.6	500
354BR	1 normal	74.3	1.0	900
355BR	3 small, 1 normal, 1 large	2h	0.8	900
376BR	-	68.4	1.1	800
378BR	-	78.6	2.1	800
380BR	at least 1 normal	1.1	0.4	700
381BR	-	53.9	1.4	800
383BR	-	98.7	6.2	700
384BR	-	13.1	1.4	800
386BR	-	75.0	3.2	800
388BR	-	70.5	6.1	800
412BR	-	71.3	3.8	900
415BR	1 normal	77.0	1.1	600
417BR	-	-	0.8	1000
419BR	-	76.5	4.0	800
422BR	-	24.3	1.3	900
435BR	-	77.8	2.2	650
437BR	-	33.8	3.3	700
439BR	-	38.4	2.3	800
441BR	1 normal, 1-2 small	55.5	2.5	700
443BR	-	72.9	6.2	800
445BR	-	73.6	6.3	800
447BR	-	6.9	4.0	800
448BR	-	70.7	5.9	800

exp. #	fine-grained agglutinations	t [h] at T	γ	T [°C]
450BR	1 normal	74.0	2.1	500
452BR	1 small at the end of the shear zone	85.5	4.8	700
479BR	-	72.2	2.5	600
480BR	-	92.5	4.6	800
481BR	1 normal	46.7	2.6	650
482BR	-	72.0	9.1	900
485BR	-	64.9	7.1	1000
487BR	-	25.0	1.2	800
488BR	-	76.0	6.6	800
493BR	-	71.6	3.7	700
494BR	-	50.5	3.4	650
495BR	-	9.9	6.6	750
496BR	-	39.1	1.1	700
497BR	-	186.2	4.5	700
498BR	-	193.4	4.1	700
499BR	-	1.1	3.4	900
500BR	-	~10 days	1.4	650

C.3 'Bubble' structure

Sample 340br (500 °C, 1.5 GPa, $\gamma = 1.6$, $1.4{\cdot}10^{-5}$ s^{-1}) is crossed by several fractures that often merge into anastomosing networks towards the shear zone boundary (Fig. C.3-1a). A large fracture zone is developed in the middle of the central fracture. Along one boundary of this fracture a zone with slightly lower Z contrast in BSE images (less dense) is formed (Fig. C.3-1) and continues until the shear zone boundary. There, it proceeds along the interface between shear zone and forcing block (Fig. C.3-1b). Thickness varies between ~1 - 10 µm and several bubbles are developed inside ('bubble-zone'). Most bubbles have diameters of submicron size but a few are about 1-2 µm in diameter. Some small bubbles are elongated parallel to the boundary of the 'bubble-zone'. With energy-dispersive X-ray spectroscopy (EDX), only SiO_2 could be identified in the bubbles. Furthermore, rounded quartz fragments are still visible in the 'bubble-zone' whereas almost no fractures or unloading cracks are developed. The 'bubble-zone' is fractured and mixed with normal quartz fragments in the middle of the shear zone.

The mechanical data does not indicate failure and the sample is loaded to almost peak conditions ($\Delta\sigma \sim 2700$ MPa) at slow displacement rate ($0.79{\cdot}10^{-8}$ m^{-1}). The shear strain accumulated in the shear zone is small ($\gamma = 1.6$).

Unfortunately, the structure occurs in a single experiment and could not be reproduced in another experiment at the same conditions. Similar structures have been observed in

[1] small - <50 µm
[2] long - >200 µm
[3] normal - 50 - 200 µm

previous studies, e.g. Pec et al. [2012b]. They experimentally deformed granitoids at similar displacements rates and interpreted these structures as amorphous layers produced by intense comminution and amorphisation at high stresses and shear strains [Pec et al., 2012b].

C.4 Contaminations in samples

EDX measurements in some thin section reveal traces of aluminium, sodium, platinum and calcium (Fig. C.4-1). Platinum (jacket) and aluminium (forcing blocks) are close to the shear zone and can be transported to the surface of the shear zone during thin section preparation (polishing). Small pieces of quartz can break out while polishing and other particles can get stuck in these cavities. But some particles are strained whereby transportation during polishing is unlikely. Potential sources for sodium are sodium-bearing fluid inclusions in the starting material [Tarantola et al., 2010] but most of the inclusions, especially the large ones, are already cracked during the preparation of the quartz powder. Some traces of aluminium are close to the sample-piston interface and can be produced by interaction of the quartz with the alumina of the forcing block. However, contamination of the quartz powder cannot be excluded.

C.5 High density zones in low-temperature samples

Zones with slightly higher Z contrast than the overall quartz exist in low temperature samples (Fig. C.5-1). These clustered structures are several micrometers up to 10's of micrometers long while the width is predominantly on submicron scale. At 500 °C, these zones are at a high angle - almost perpendicular - to the shear zone boundary. Similar orientations are typical for antithetic R' and X Riedel shear (Fig. C.5-2) and have been observed e.g. by Schmocker et al. [2003]. The structures are less pronounced towards the shear zone boundary and sometimes merge into anastomosing networks. These zones are not visible at low shear strain and low temperatures. More of these zones develop in R shear or C' direction with increasing temperature, and therefore increasing viscous deformation, but in general, they become less pronounced.

Unloading cracks are not developed in the bright zones even though they are well pronounced close to these zones. Hence, these structures are real features and they are not related to charging effects. Higher Z contrast indicates more dense material. These zones could be related to high dislocation densities or parts that are intensively compressed (high elasticity). Further analysis, e.g. transmission electron microscopy (TEM), should be performed to understand the evolution of these structures.

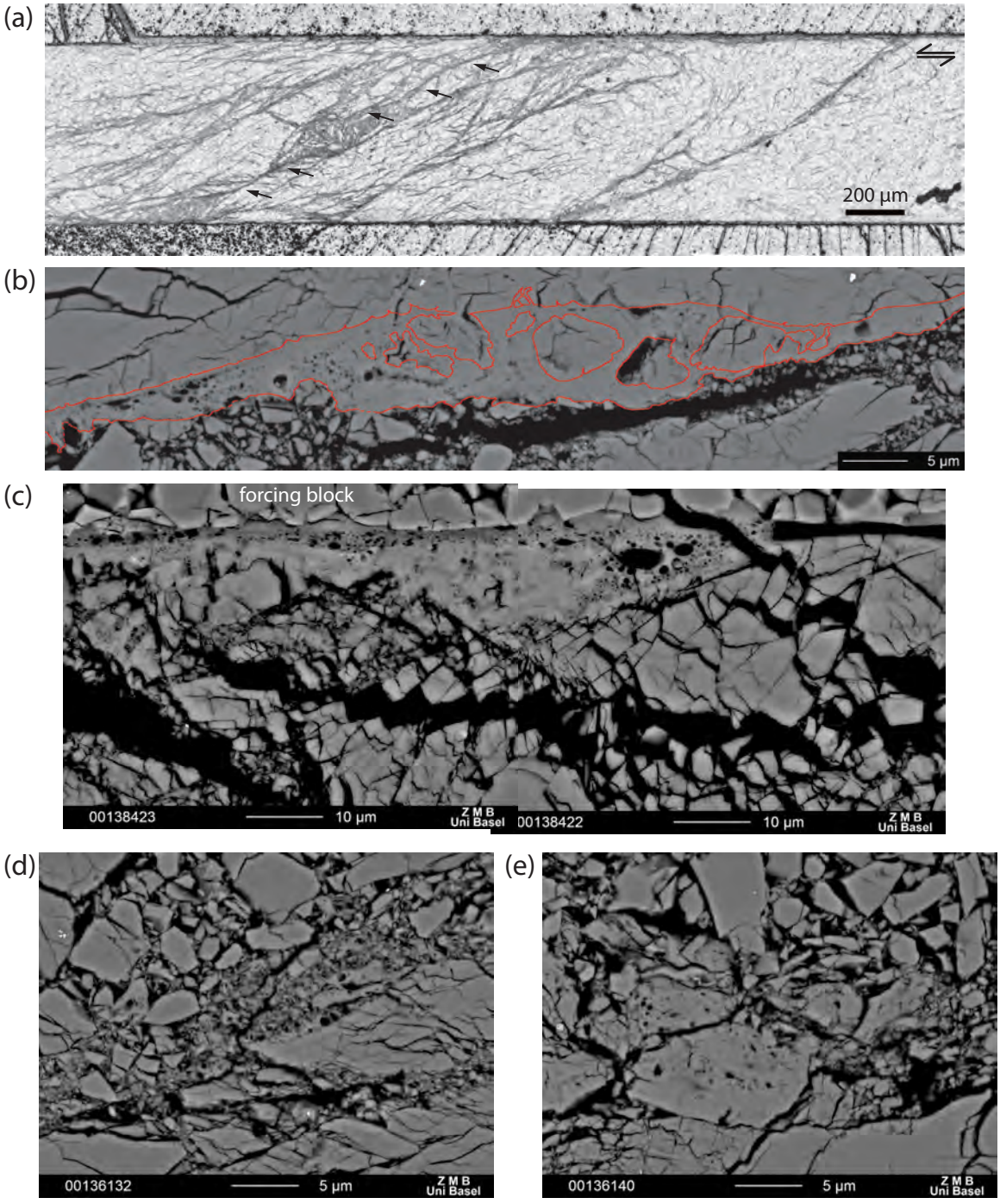

Fig. C.3-1: Sample 340br (500 °C, 1.5 GPa, $1.4 \cdot 10^{-5}$ s^{-1}, γ = 1.6). (a) The sample is crossed by several through-going fractures. Along the central fracture a zone with bubbles forms (arrows). (transmitted light) (b) Close-up of this 'bubble-zone' (red outline). The bubbles appear dark and some rounded fragments are incorporated. (BSE image) (c) Close-up of the zone at the piston-sample interface. The bubbles vary in size and some of the smaller ones are elongated. The zone itself shows slightly darker colour in BSE than the surrounding quartz. (BSE image) (d) and (f) In the middle of the sample the zone is fractured and fragments are mixed with quartz fragments. (BSE image)

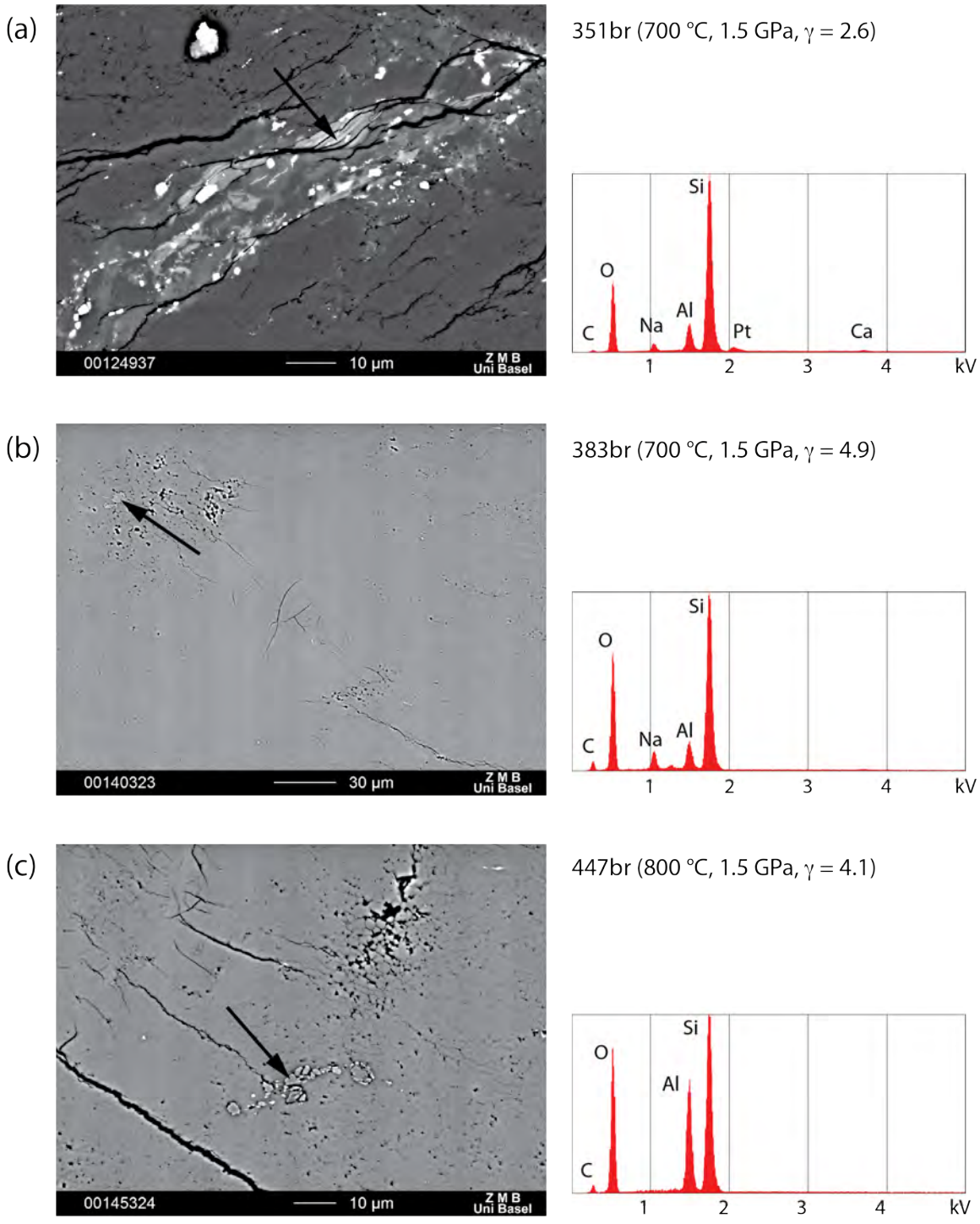

Fig. C.4-1: EDX analysis and BSE image of special features (arrows). (a) Traces of aluminium, platinum, calcium and sodium occur. The brightest particles have angular edges. The intermediate grey particles are strained. The particle in the upper left is dirt on top of the surface. (b) Aluminium and sodium. (c) Roundish particles include aluminium.

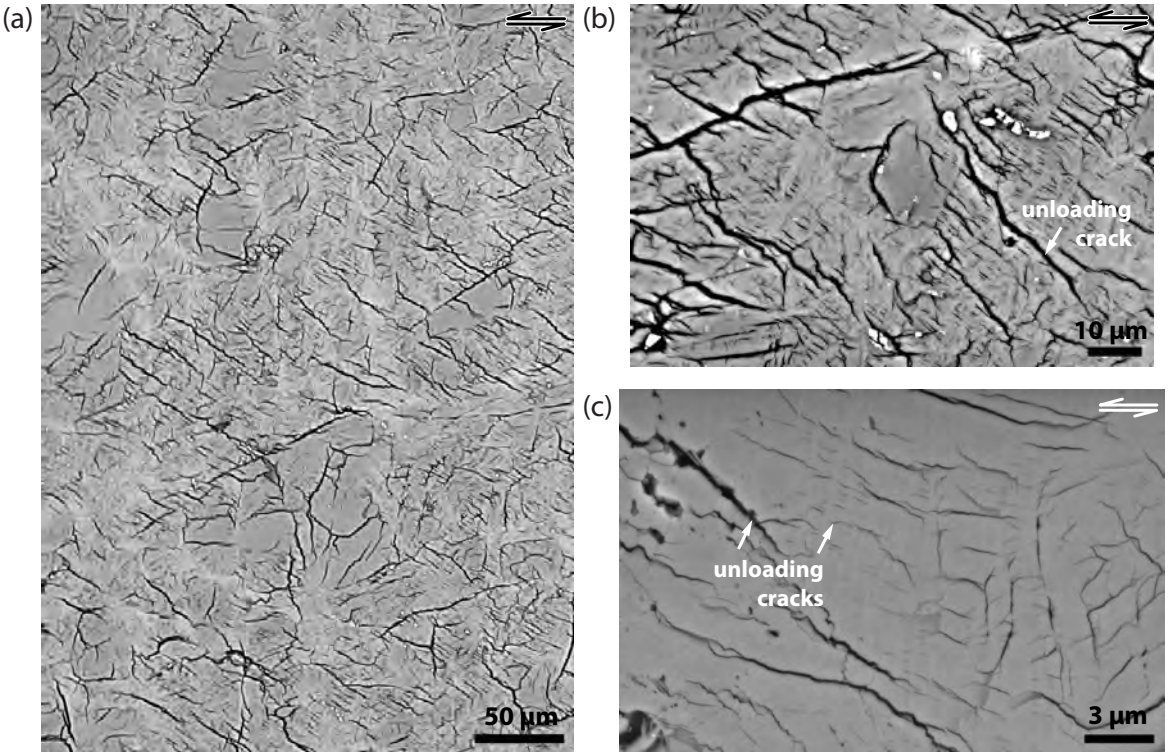

Fig. C.5-1: Bright, predominantly steep zones in low temperature samples. (BSE images) (a) 500 °C, 1.5 GPa confining pressure and $2.1 \cdot 10^{-5}$ s^{-1}. Most of the zones are almost perpendicular with regard to the shear zone boundary. Some are at a low angle to the shear zone boundary. (b) Detail of the sample in (a) illustrates anastomosing networks of the bright zones that are not pervaded by unloading cracks. (c) Several thin, subparallel, steep bright zones at 650 °C, 1.5 GPa confining pressure and $0.35 \cdot 10^{-5}$ s^{-1}.

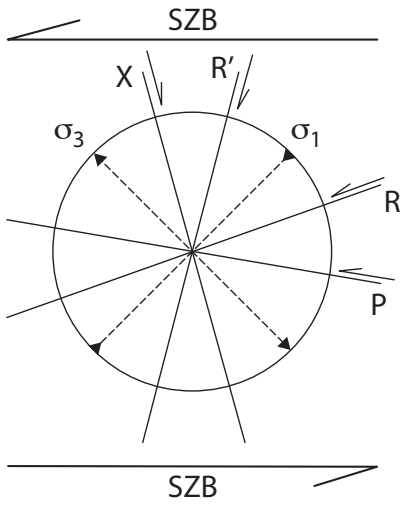

Fig. C.5-2: Schematic Riedel shear orientation modified after Schmocker et al. [2003] and Petit [1987].

D Microstructure, texture and mechanical data of selected samples

In the following section microstructural and textural details of 28 high quality samples will be presented. Stress-strain curves and an image of the jacket after deformation are shown. In an overview image of each sample, the position of CIP and EBSD sites are marked. The *c*-axis orientation image, a representative EBSD map and images of special features are presented.

The shear zone boundary is horizontal for all micrographs in all samples.

337BR:	1000 °C, 1.5 GPa	
338BR:	600 °C, 1.5 GPa	(peak strength)
339BR:	700 °C, 1.5 GPa	
340BR:	500 °C, 1.5 GPa	(peak strength)
351BR:	700 °C, 1.5 GPa	('as-is')
380BR:	700 °C, 1.5 GPa	(after pressurisation)
383BR:	700 °C, 1.5 GPa	
386BR:	800 °C, 0.5 GPa	
388BR:	800 °C, 1.5 GPa	
412BR:	900 °C, 1.5 GPa	
415BR:	600 °C, 1.5 GPa	(hot pressed)
417BR:	1000 °C, 1.5 GPa	(hydrostatic)
419BR:	800 °C, 1.5 GPa	(hot pressed)
435BR:	650 °C, 1.5 GPa	
437BR:	700 °C, 1.5 GPa	(peak strength)
439BR:	800 °C, 1.5 GPa	(peak strength)
445BR:	800 °C, 1.5 GPa	(7-11 μm initial size of powder)
447BR:	800 °C, 1.5 GPa	
448BR:	800 °C, 1.0 GPa	
450BR:	500 °C, 1.5 GPa	
452BR:	700 °C, 1.0 GPa	
479BR:	600 °C, 1.5 GPa	
487BR:	800 °C, 1.5 GPa	(hydrostatic)
493BR:	700 °C, 1.5 GPa	(hot pressed)
494BR:	650 °C, 1.0 GPa	
495BR:	750 °C, 1.5 GPa	
499BR:	900 °C, 1.5 GPa	
500BR:	650 °C, 1.5 GPa	

337BR

T = 1000 °C
P_c = 1.5 GPa
$\dot{d} = 1.7 \cdot 10^{-8}$ ms^{-1}

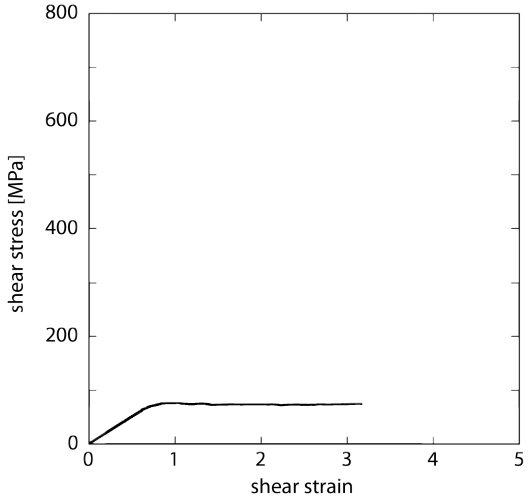

Overview of the sample (crossed polarised light):

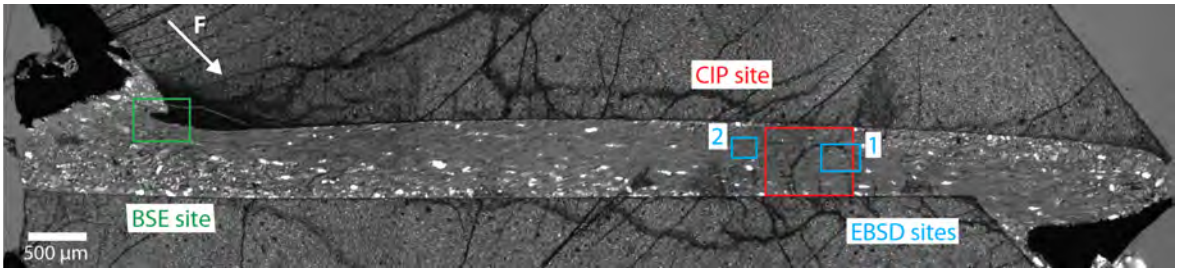

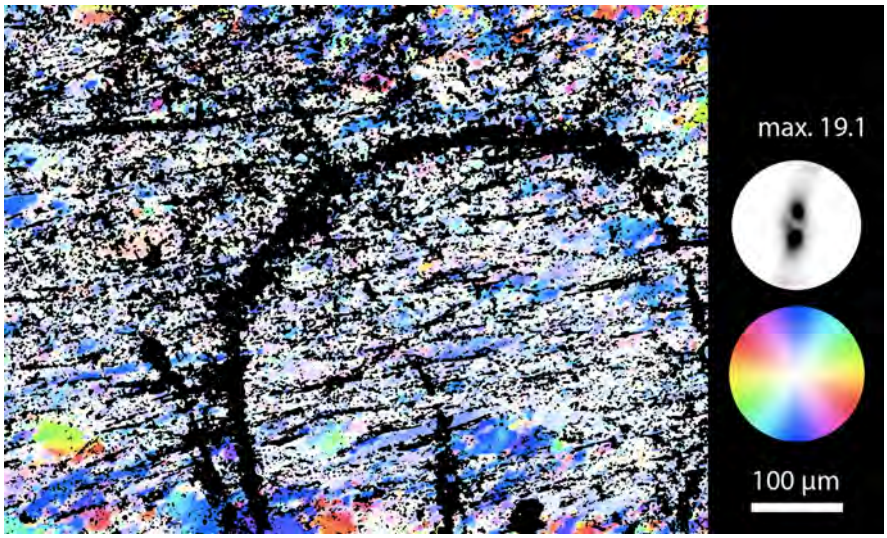

C-axis orientation image of CIP site

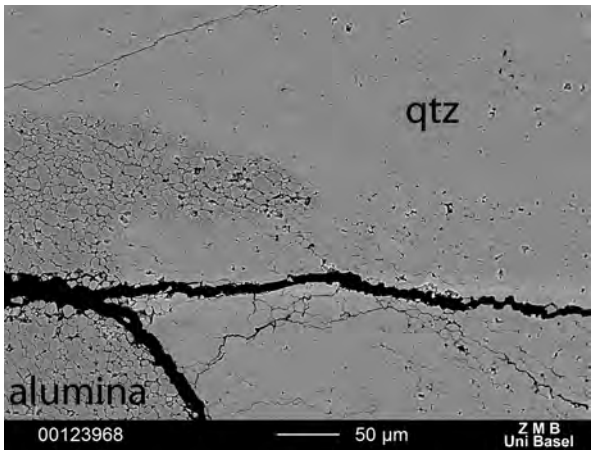

The alumina forcing block is highly influenced by high temperature (BSE image).

EBSD site 2:

IPF colouring in z direction, black colour indicates non-indexed pixels.

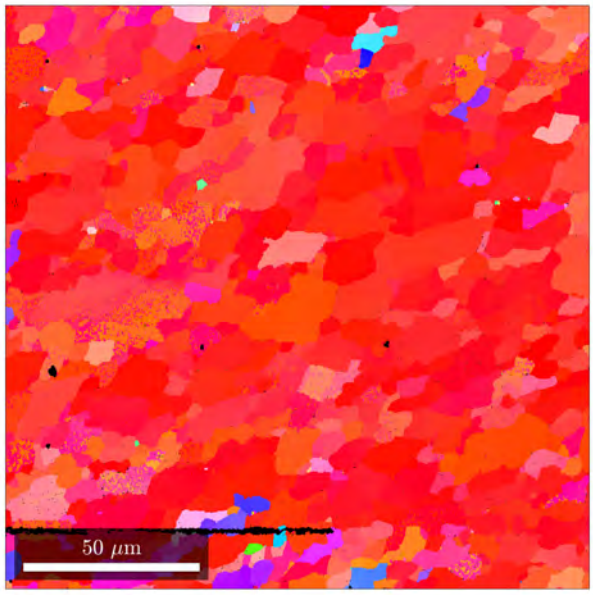

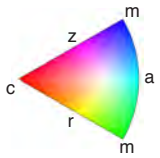

Associated pole figures.

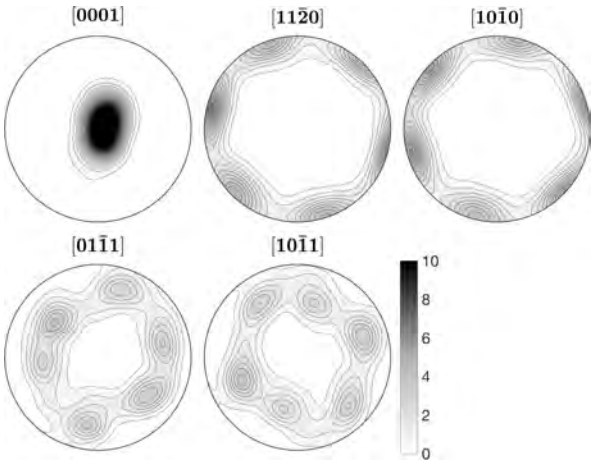

338BR

T = 600 °C
P_c = 1.5 GPa
$\dot{d} = 0.82 \cdot 10^{-8}$ ms^{-1}

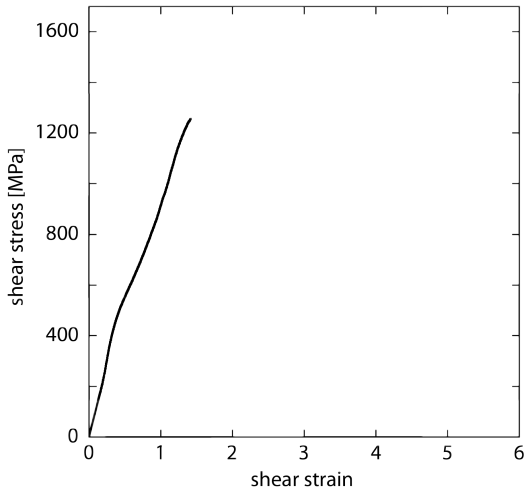

Overview of the sample (crossed polarised light):

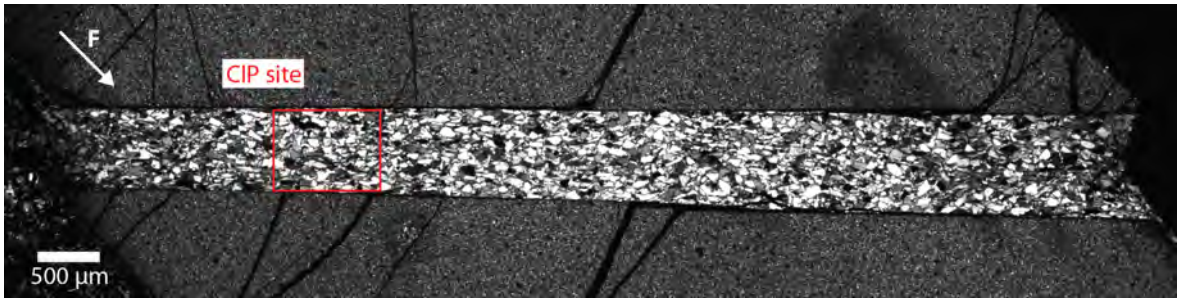

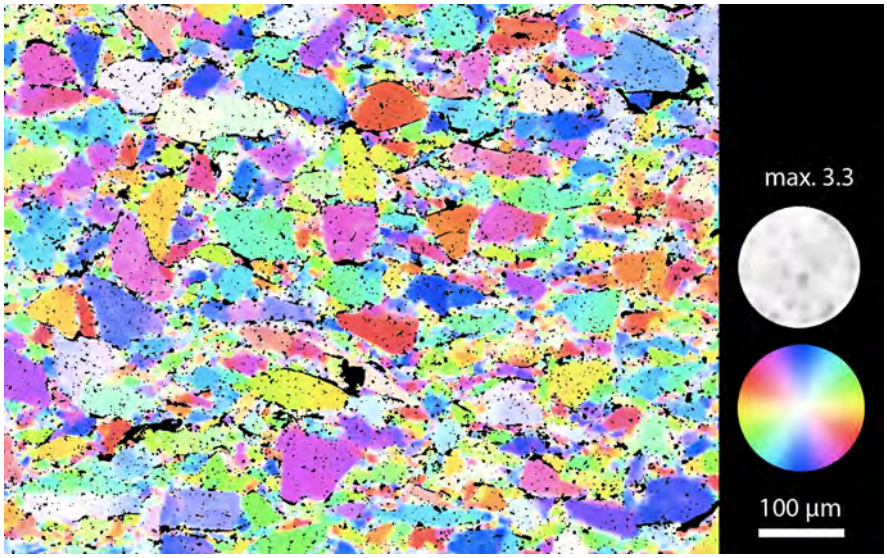

C-axis orientation image of CIP site

339BR

T = 700 °C
P_c = 1.5 GPa
$\dot{d} = 1.3 \cdot 10^{-8}$ ms^{-1}

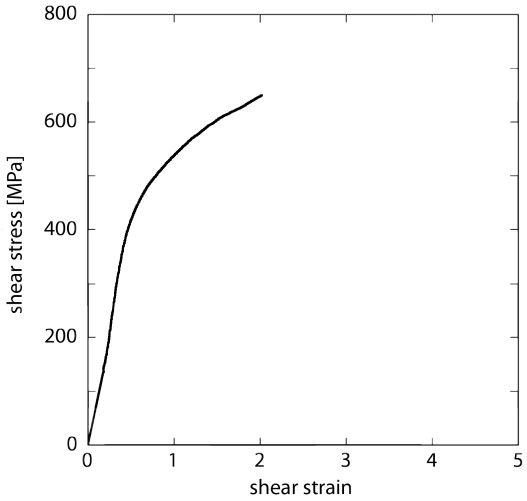

Overview of the sample (crossed polarised light):

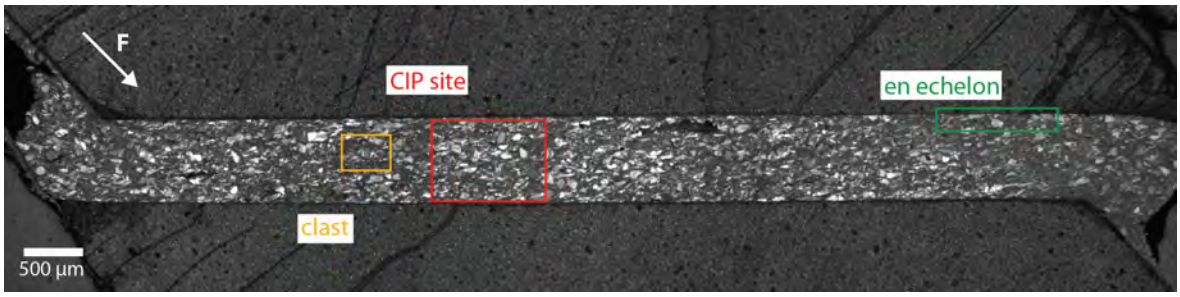

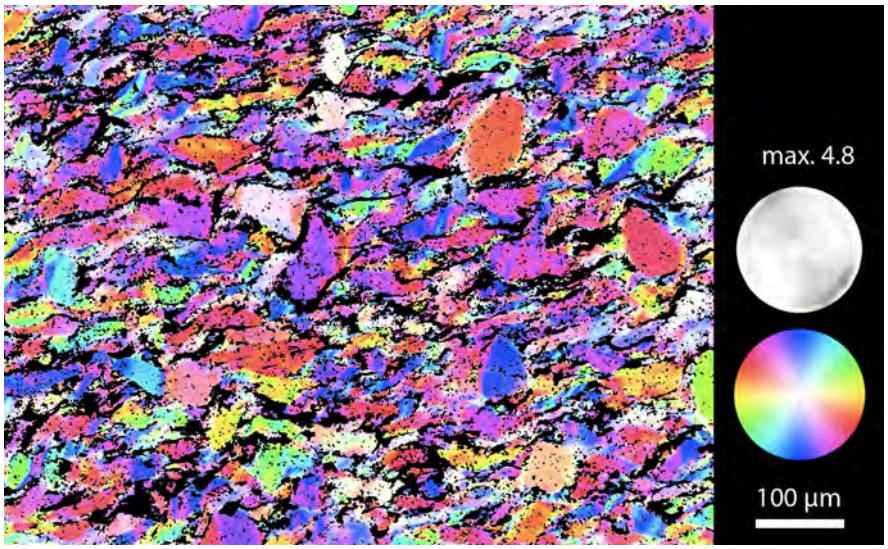

C-axis orientation image of CIP site

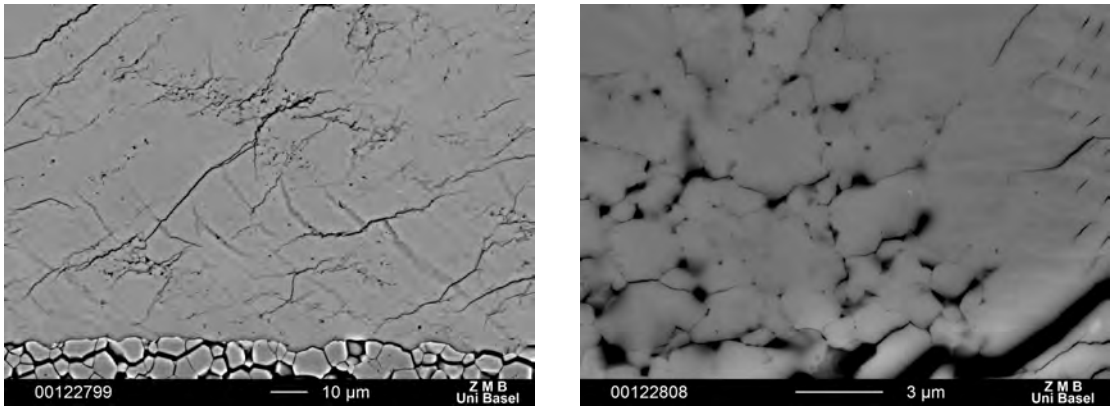

Left: En echelon structure. **Right:** Small grains with several pores at grain boundaries. (BSE images)

340BR

T = 700 °C
P_c = 1.5 GPa
$\dot{d} = 0.79 \cdot 10^{-8}$ ms^{-1}

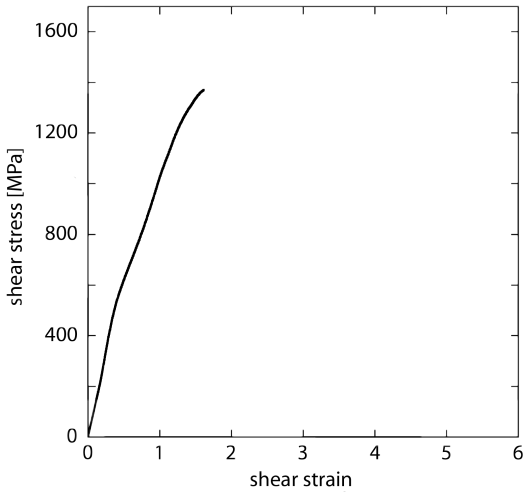

Overview of the sample in (a) crossed polarised light and (b) transmitted light:

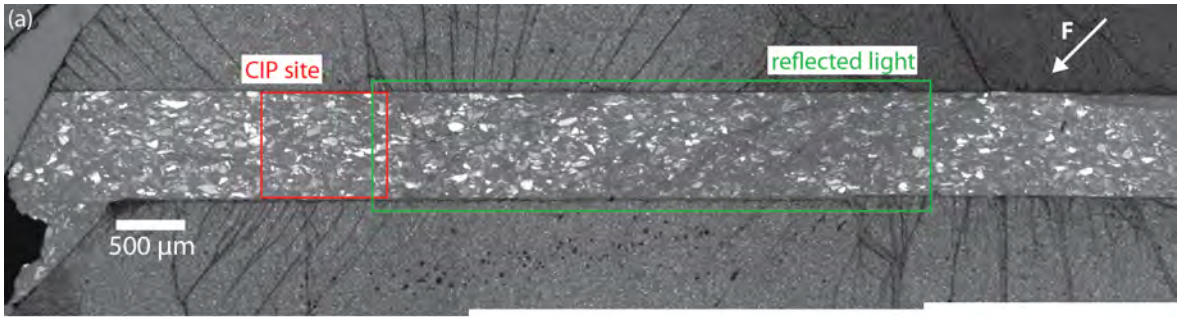

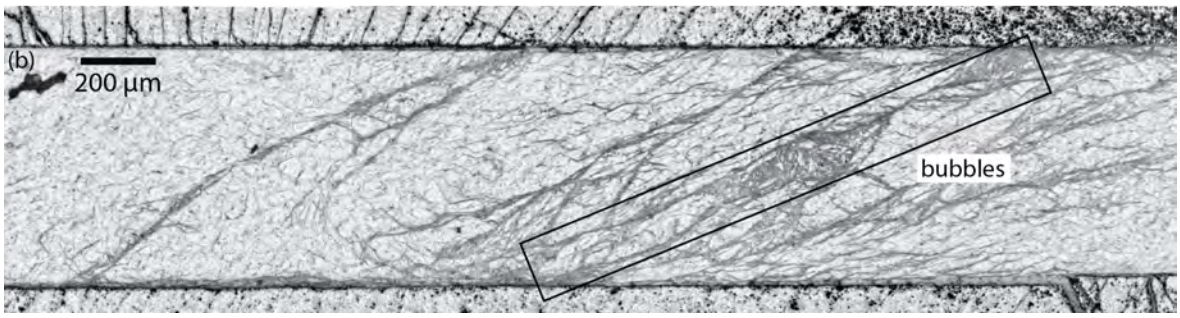

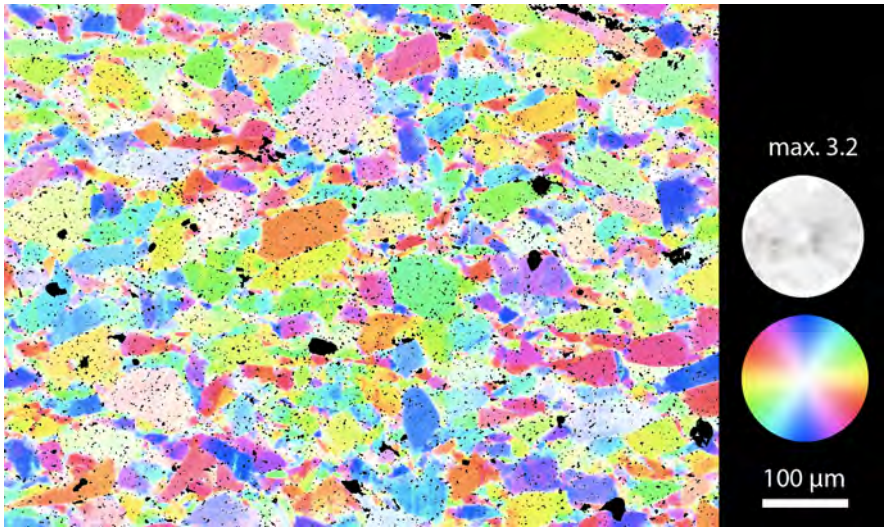

C-axis orientation image of CIP site

351BR

T = 700 °C
P_c = 1.5 GPa
$\dot{d} = 1.6 \cdot 10^{-8}$ ms^{-1}

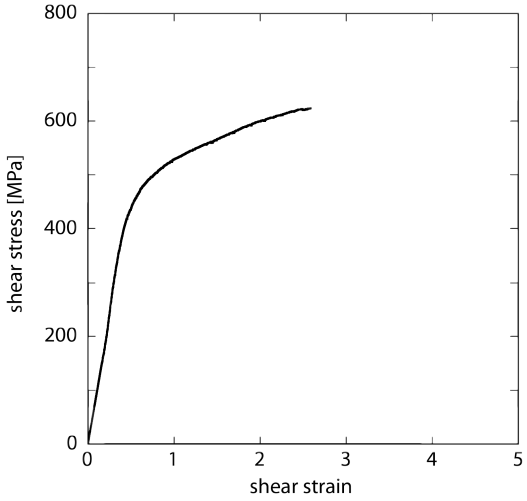

Overview of the sample (crossed polarised light):

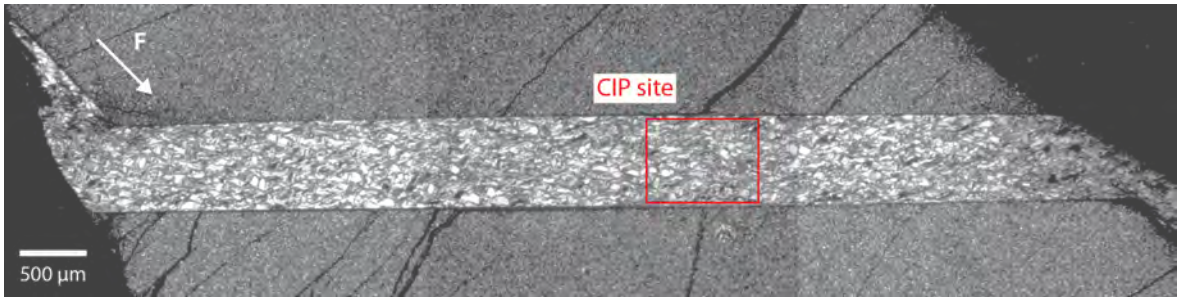

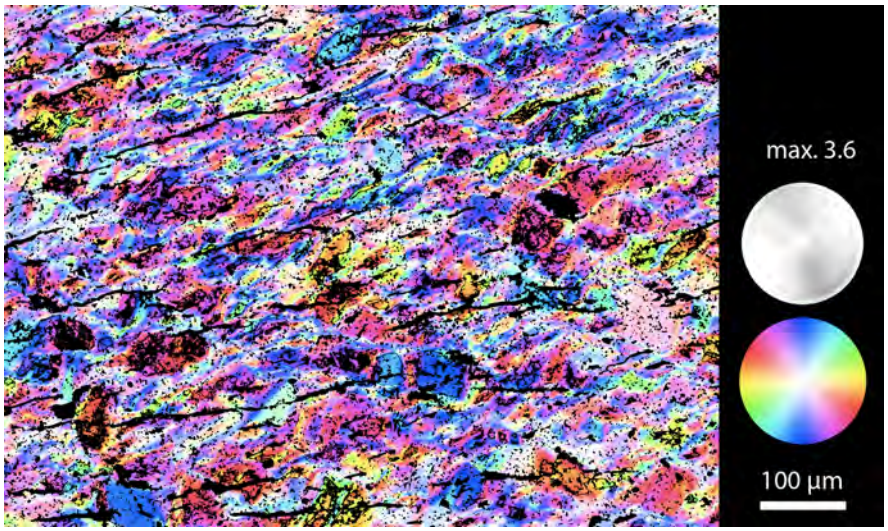

C-axis orientation image of CIP site

380BR

T = 700 °C
P_c = 1.5 GPa
stopped after 1 hour at PT conditions

Overview of the sample (crossed polarised light):

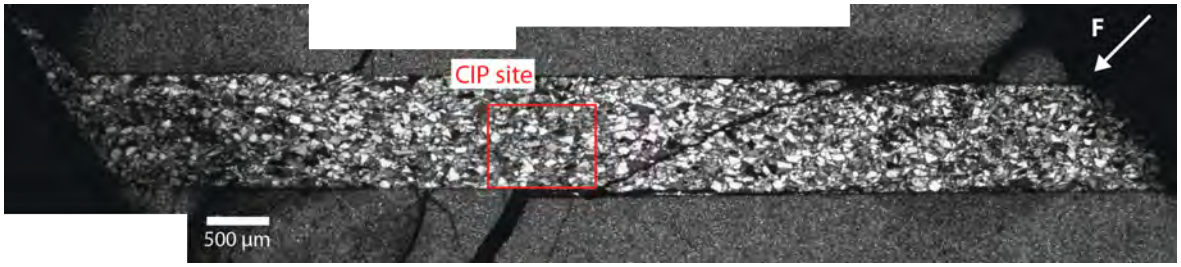

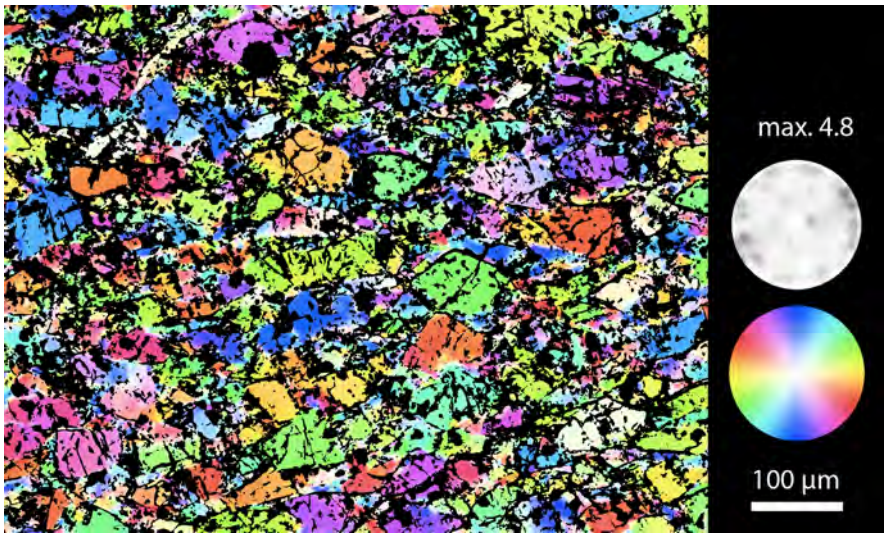

C-axis orientation image of CIP site

383BR

T = 700 °C
P_c = 1.5 GPa
$\dot{d} = 1.5 \cdot 10^{-8}$ ms^{-1}

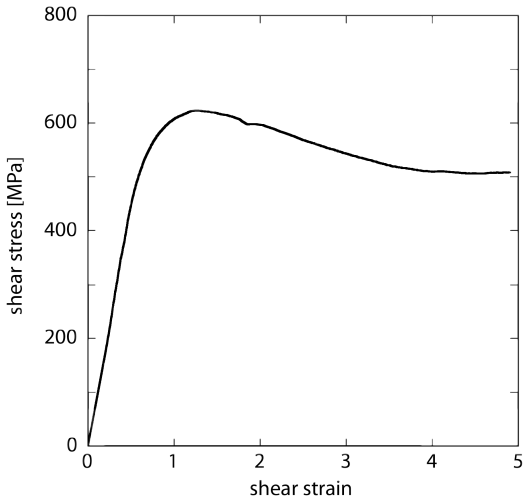

Overview of the sample in (a) crossed polarised light and as (b) BSE image:

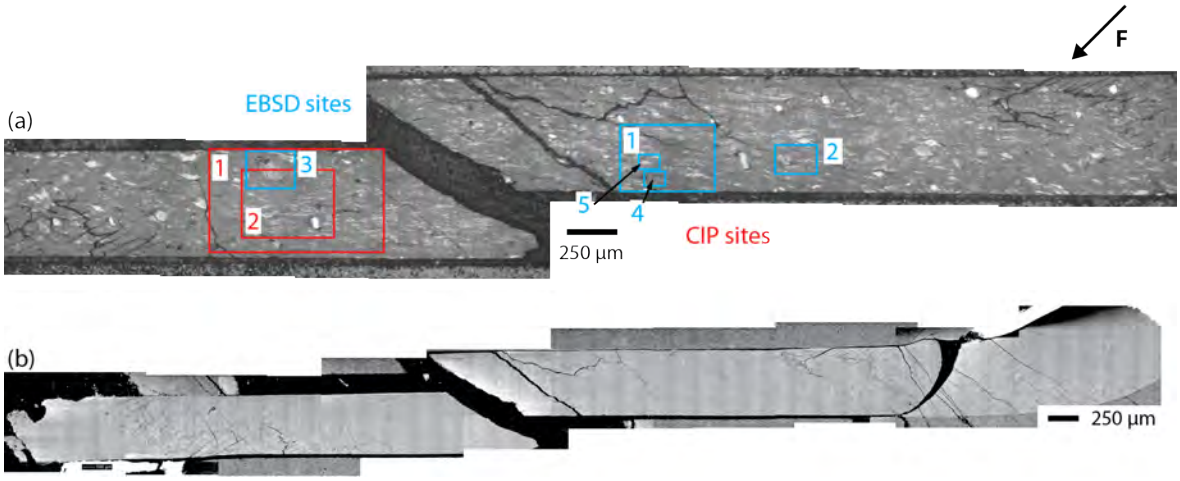

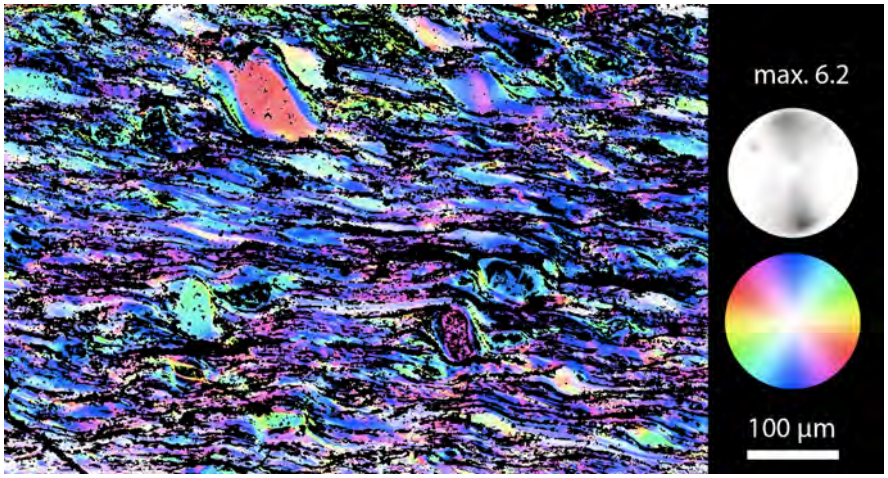

C-axis orientation image of CIP site 1

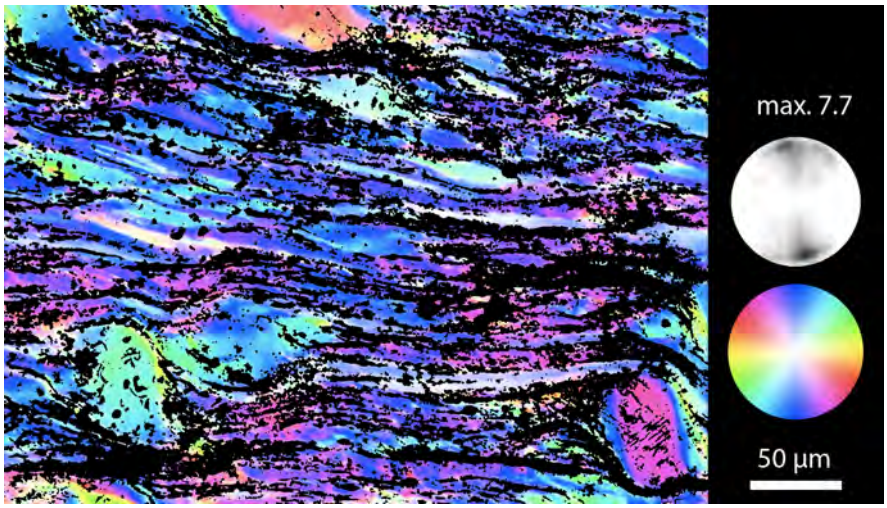

C-axis orientation image of CIP site 2

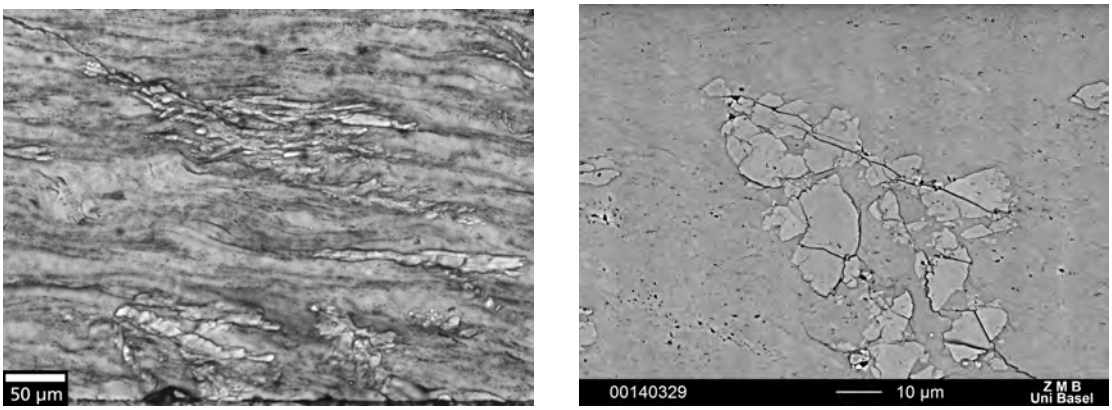

Left: Aligned coesite in foliated quartz (transmitted light). **Right:** Highly eroded coesite (BSE image).

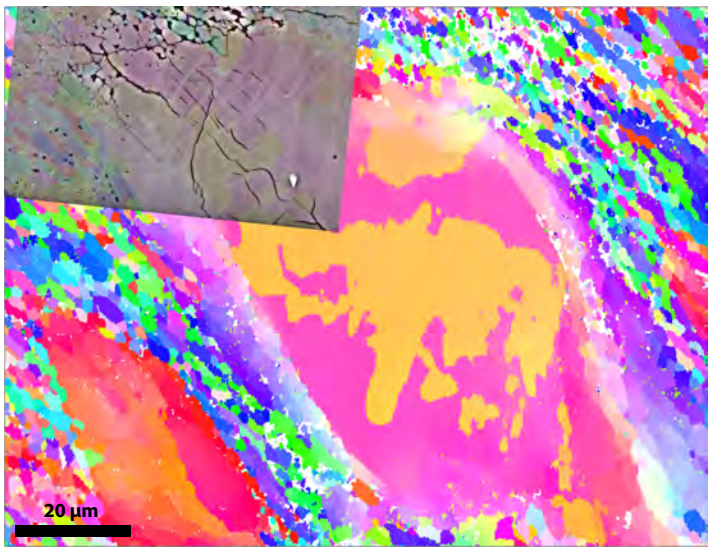

EBSD map with overlying BSE image of deformation lamellae that are only visible in the BSE image.

EBSD site 1:

IPF colouring in y direction for quartz. Black colour indicates non-quartz pixel (non-indexed or coesite).

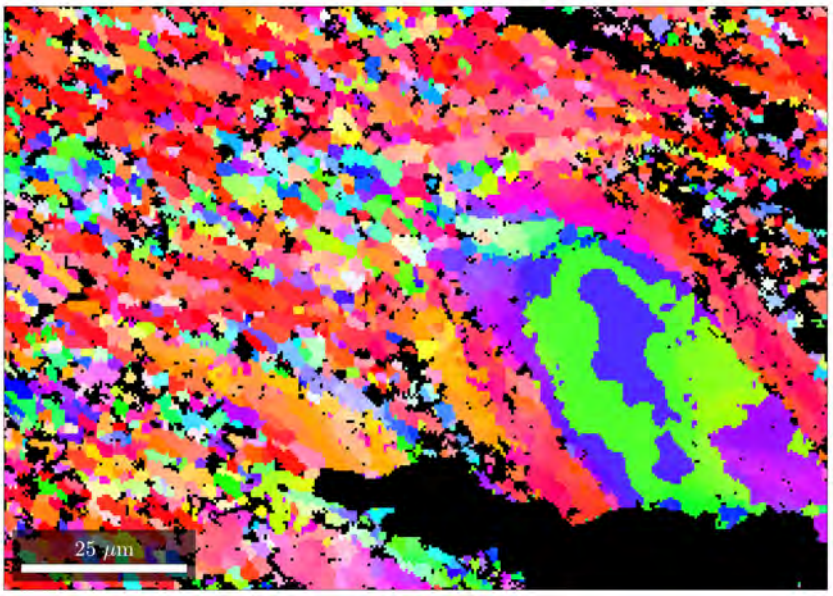

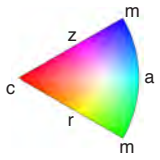

Associated pole figures for quartz.

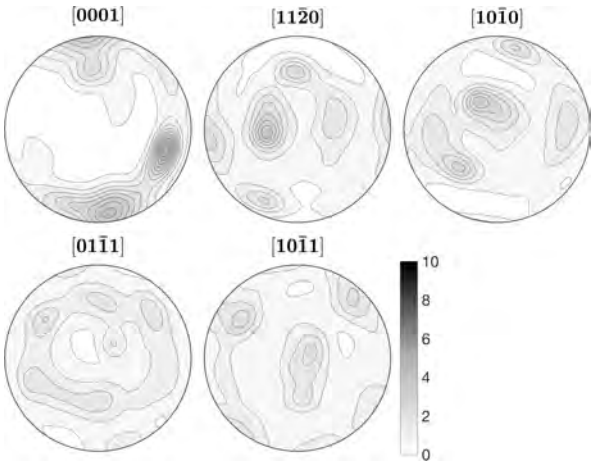

Corresponding EBSD map with IPF colouring in y direction for coesite. Black colour indicates non-coesite pixel (non-indexed or quartz).

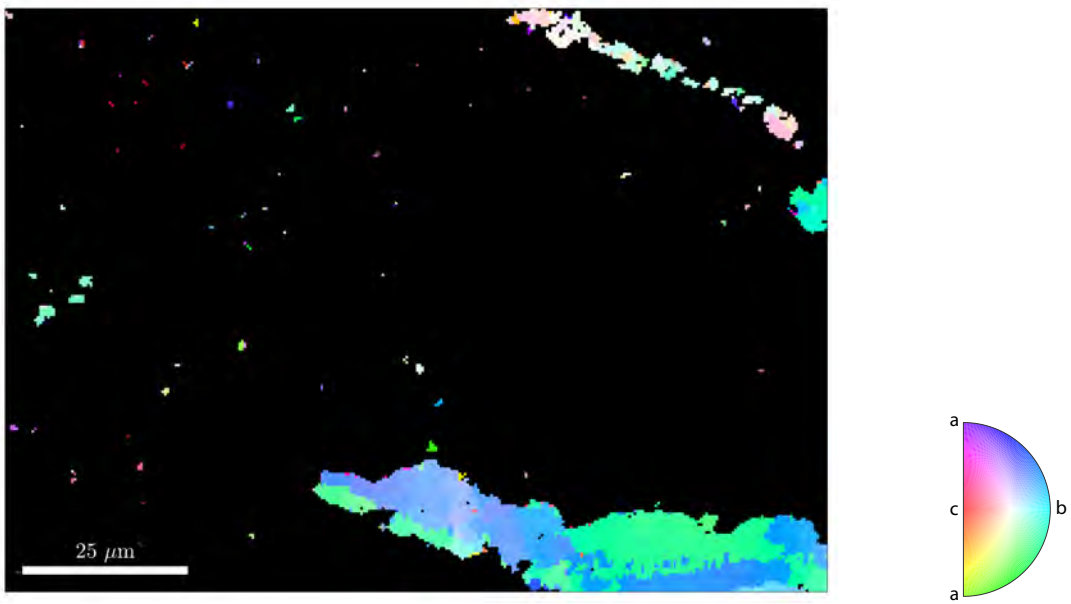

Associated pole figures for coesite.

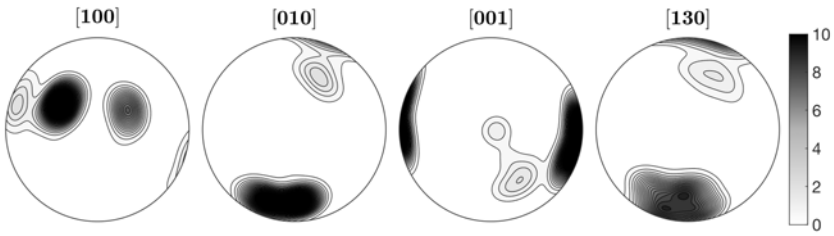

386BR

T = 800 °C
P_c = 0.5 GPa
$\dot{d} = 1.5 \cdot 10^{-8}$ ms^{-1}

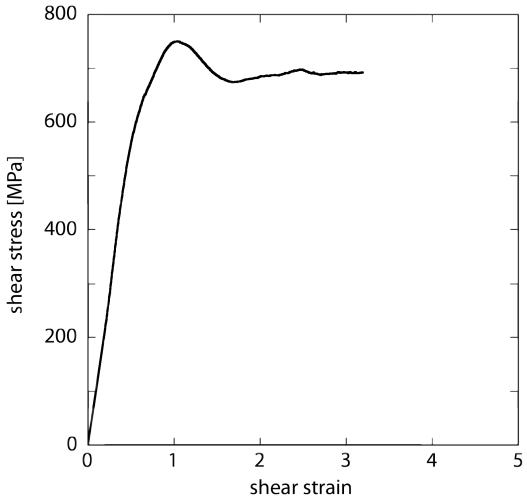

Overview of the sample (reflected light):

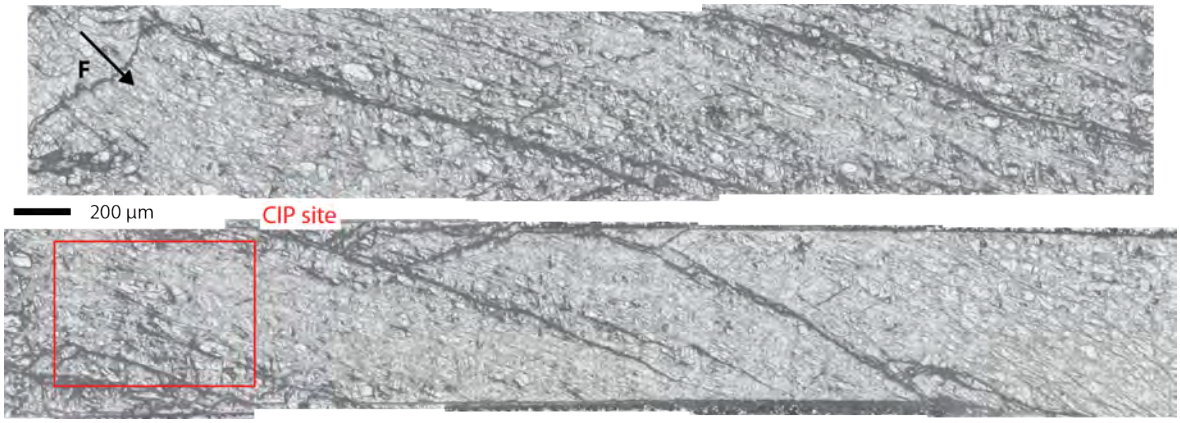

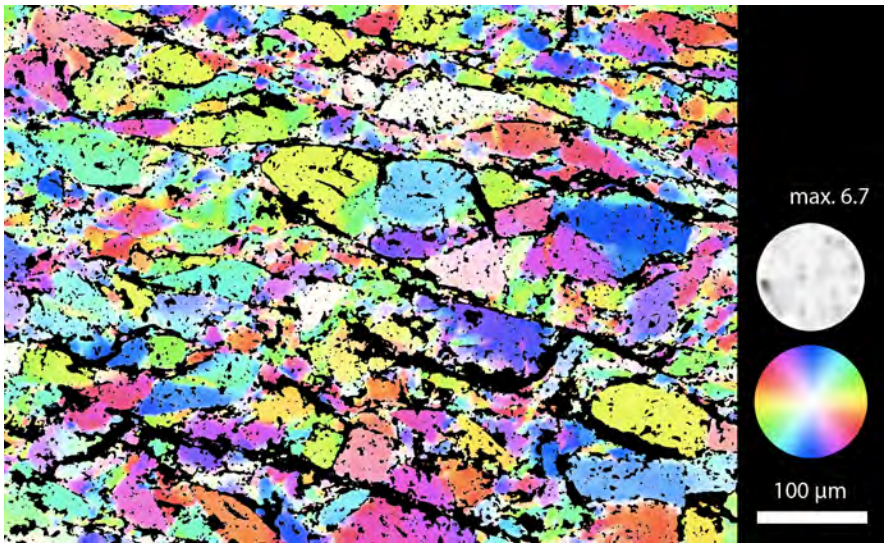

C-axis orientation image of CIP site

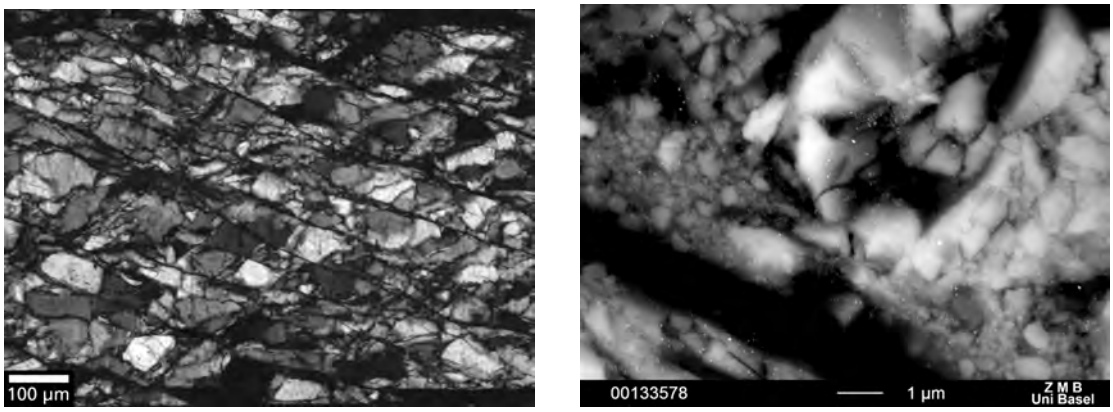

Left: Through-going R Riedel shear (crossed polarised light). **Right:** Comminution along R Riedel shear (BSE image).

388BR

T = 800 °C
P_c = 1.5 GPa
$\dot{d} = 1.5 \cdot 10^{-8}$ ms^{-1}

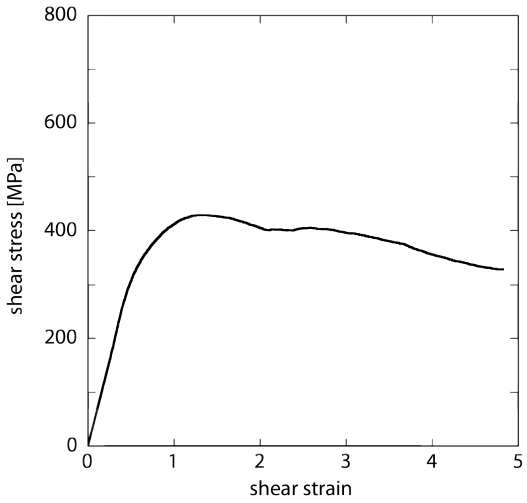

Overview of the sample (crossed polarised light):

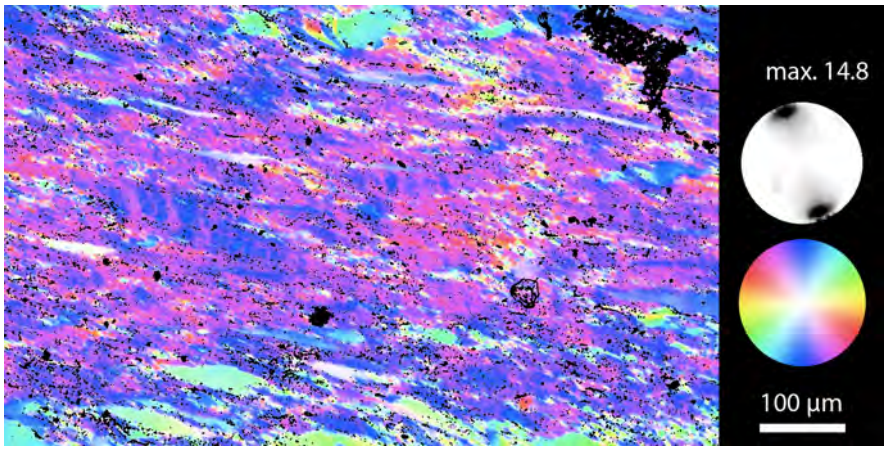

C-axis orientation image of CIP site 1

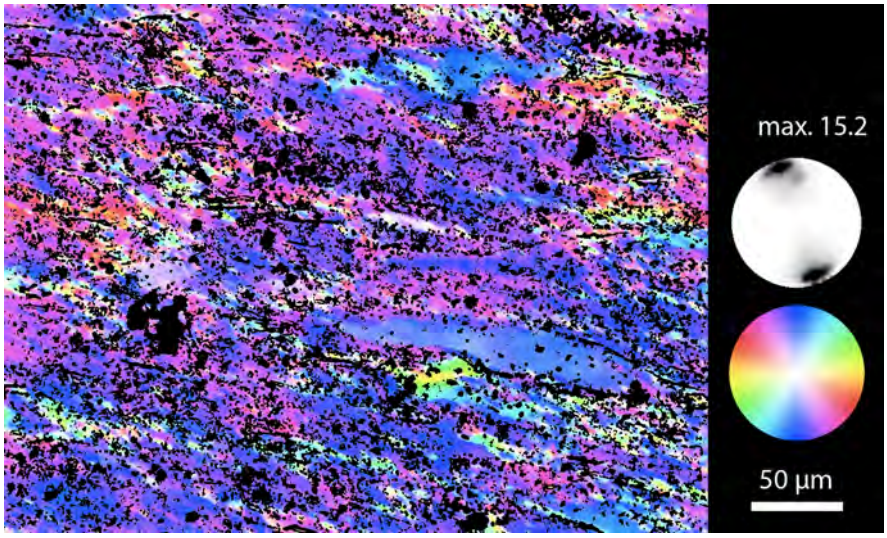

C-axis orientation image of CIP site 2

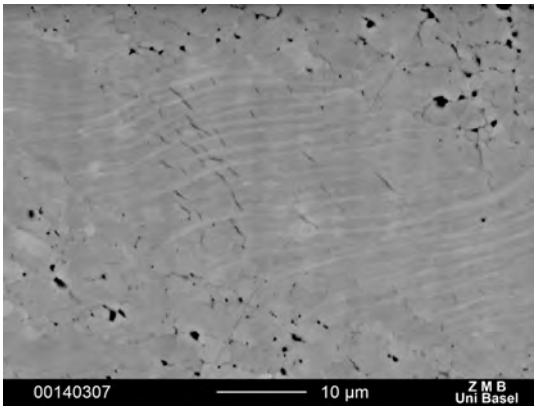

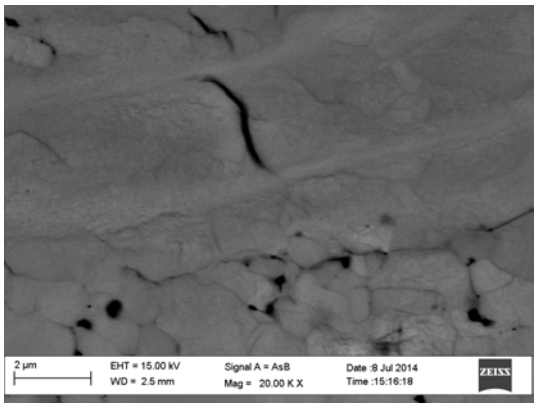

Left: Wavy deformation lamellae in elongated clast. **Right:** Tiny unloading crack between deformation lamellae. (BSE images)

EBSD site 2:

IPF colouring in y direction, black colour indicates non-indexed pixels.

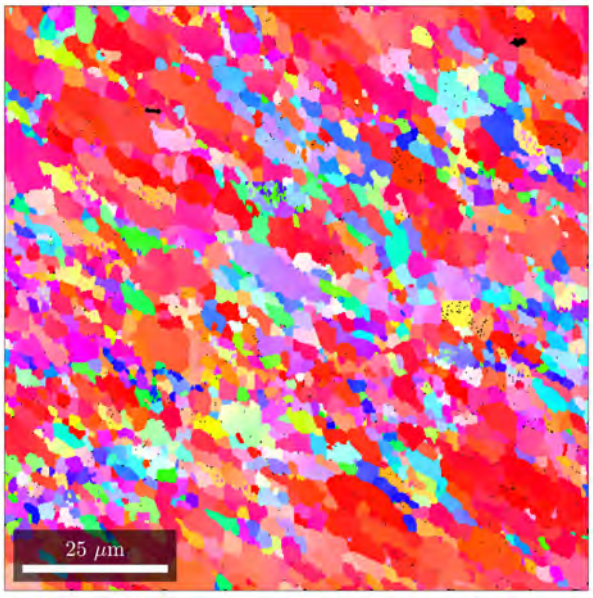

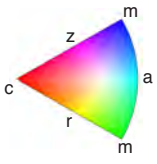

Associated pole figures.

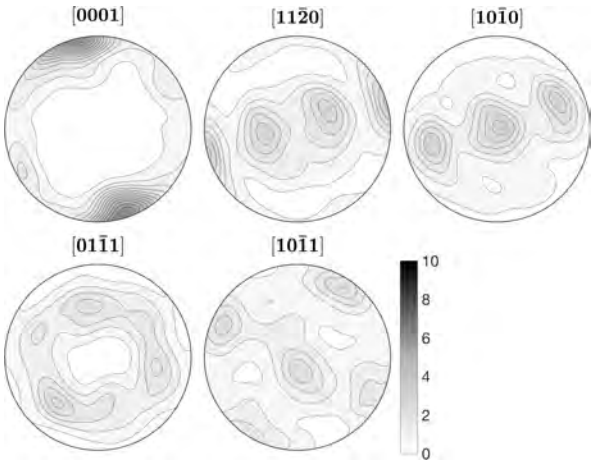

412BR

T = 900 °C
P_c = 1.5 GPa
$\dot{d} = 1.6 \cdot 10^{-8}$ ms^{-1}

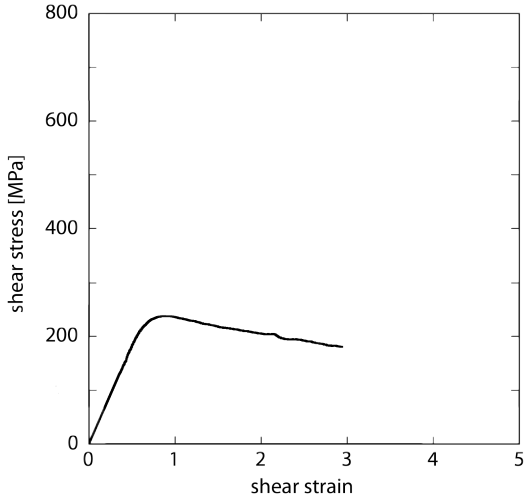

Overview of the sample (crossed polarised light):

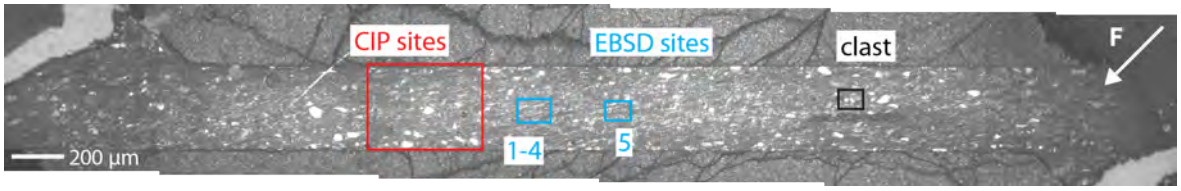

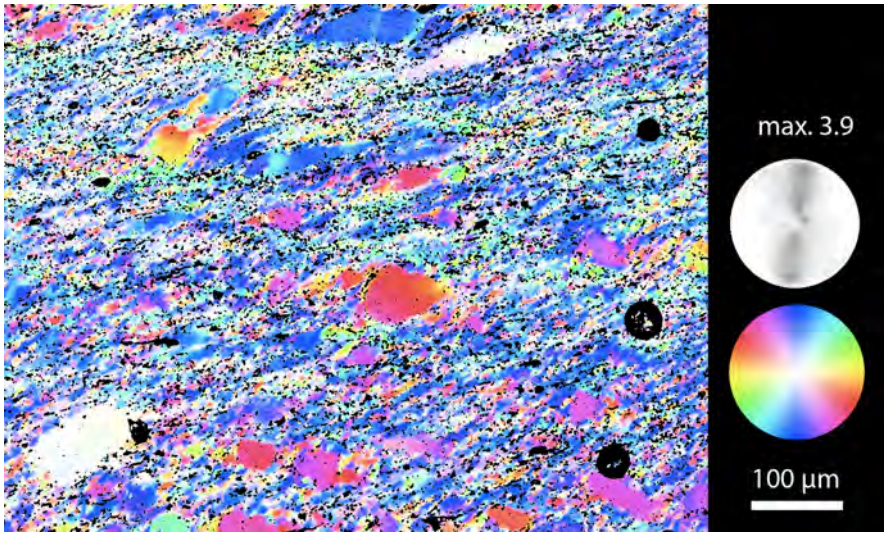

C-axis orientation image of CIP site

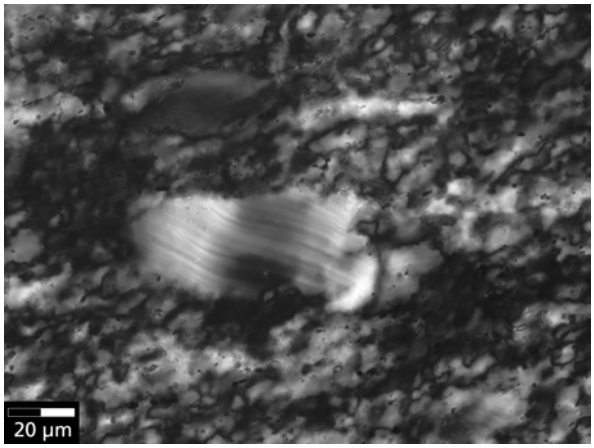

Clast with banded undulous extinction and deformation lamellae (crossed polarised light).

EBSD site 5:

IPF colouring in z direction, black colour indicates non-indexed pixels.

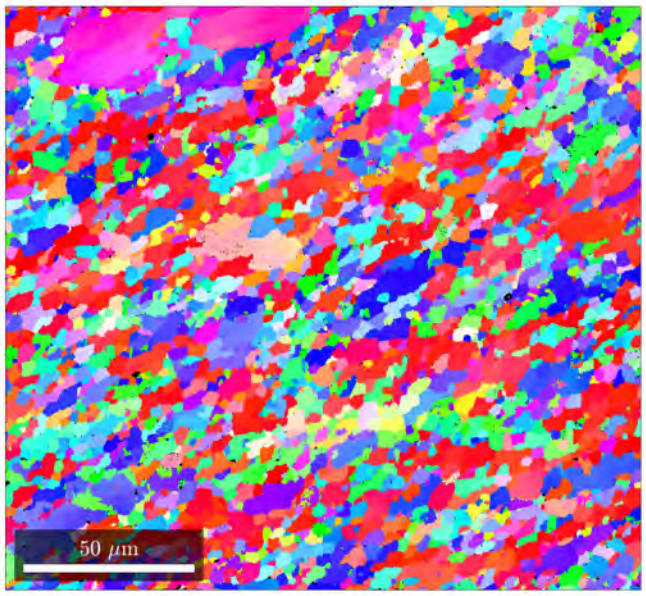

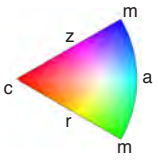

Associated pole figures.

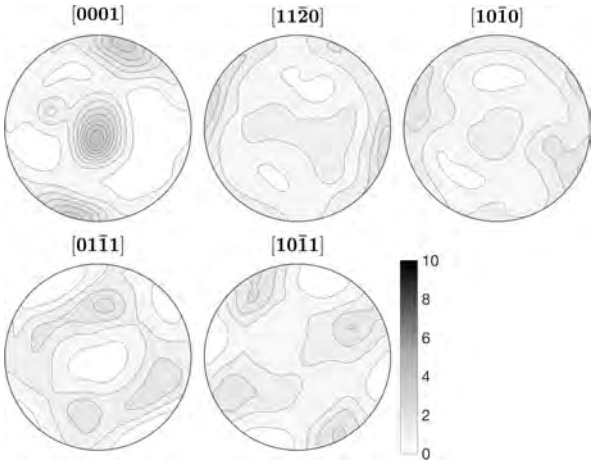

415BR

T = 600 °C
P_c = 1.5 GPa
$\dot{d} = 1.1 \cdot 10^{-8}$ ms^{-1}
hot pressed for 20 h
at 1000 °C, 1.5 GPa

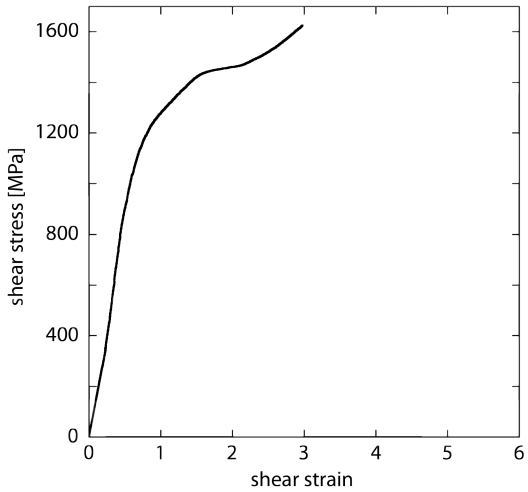

Overview of the sample (crossed polarised light):

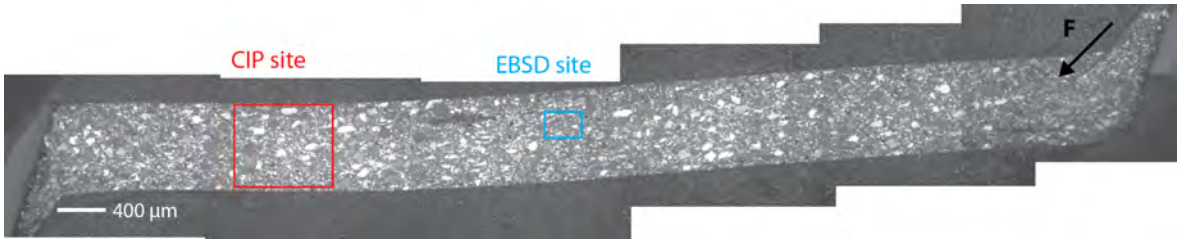

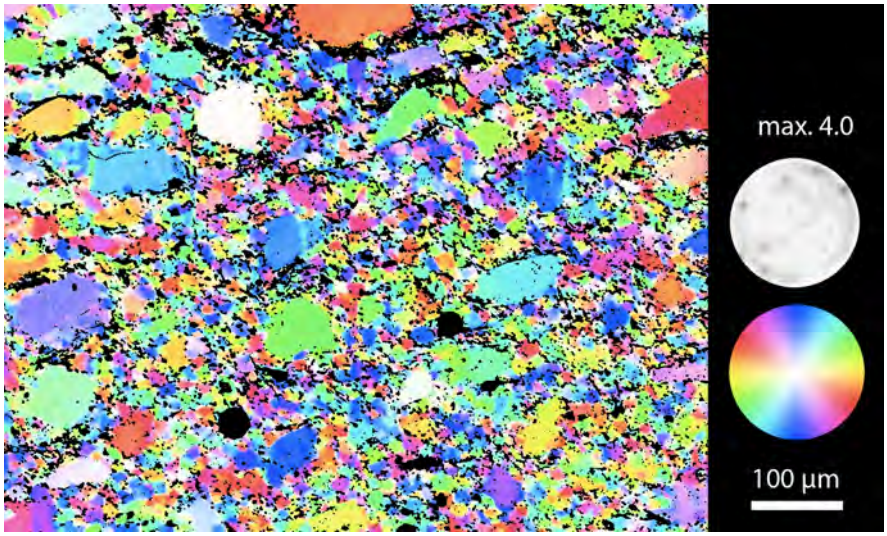

C-axis orientation image of CIP site

EBSD site:

IPF colouring in y direction, black colour indicates non-indexed pixels.

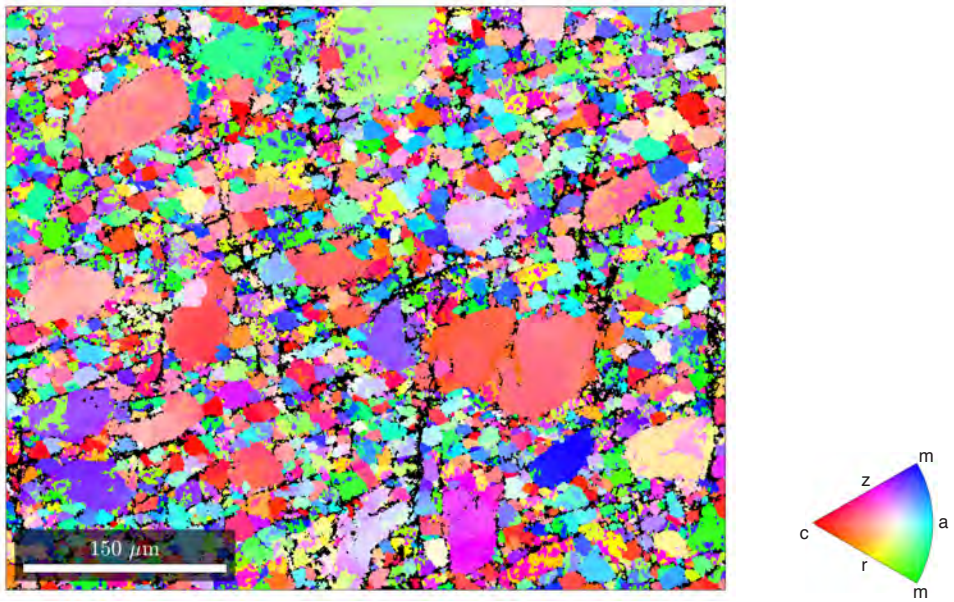

Associated pole figures.

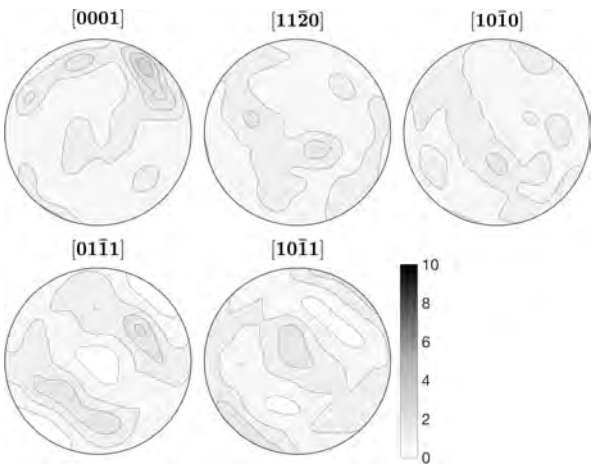

417BR

T = 1000 °C
P_c = 1.5 GPa
hydrostatic for 20 h

Overview of the sample (crossed polarised light):

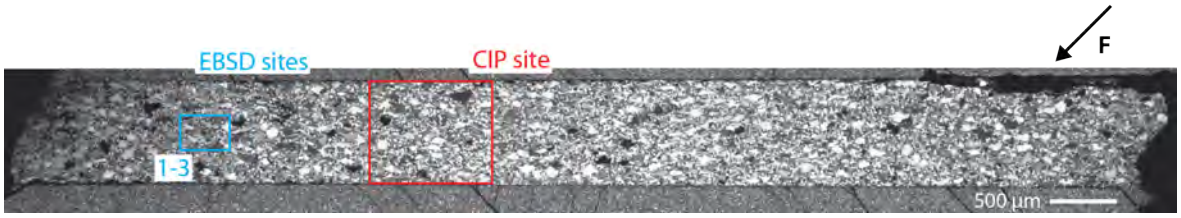

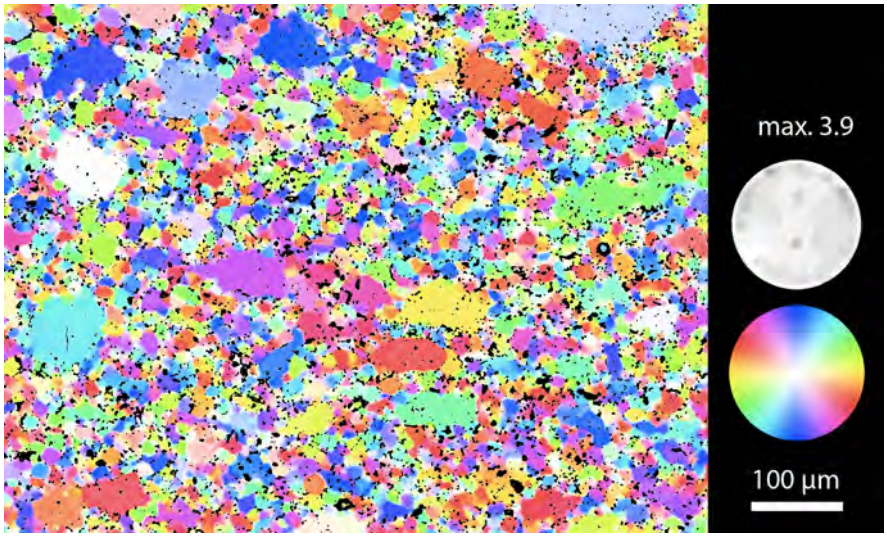

C-axis orientation image of CIP site

EBSD site:

IPF colouring in y direction, black colour indicates non-indexed pixels.

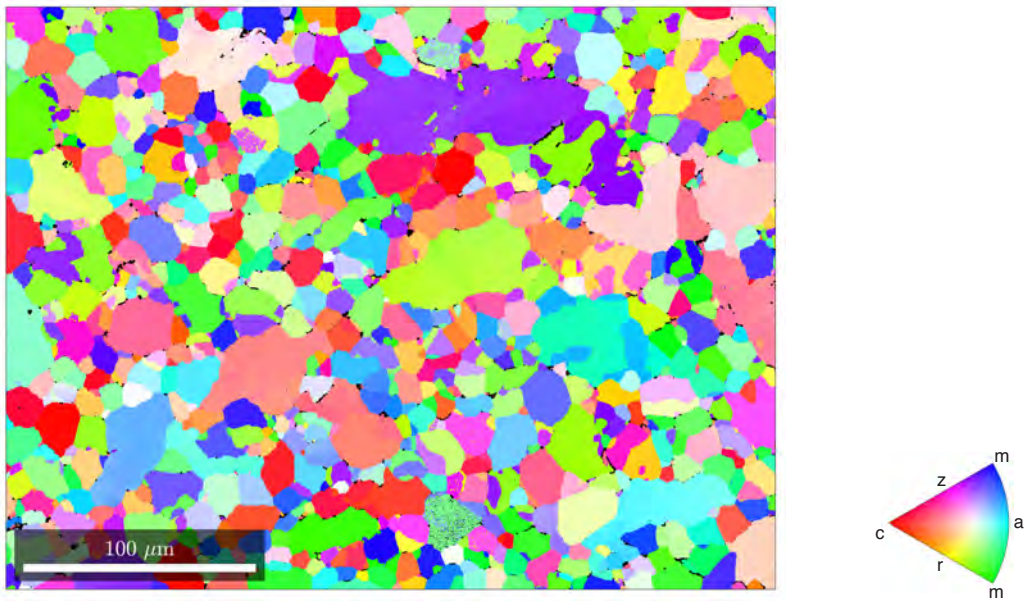

Associated pole figures.

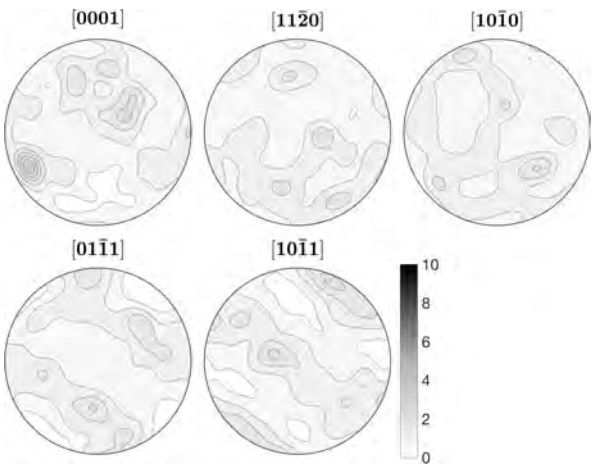

419BR

T = 800 °C
P_c = 1.5 GPa
$\dot{d} = 1.6 \cdot 10^{-8}$ ms^{-1}
hot pressed for 20 h
at 1000 °C, 1.5 GPa

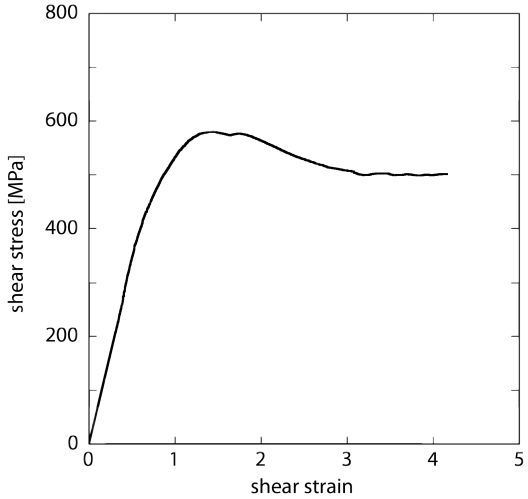

Overview of the sample (crossed polarised light):

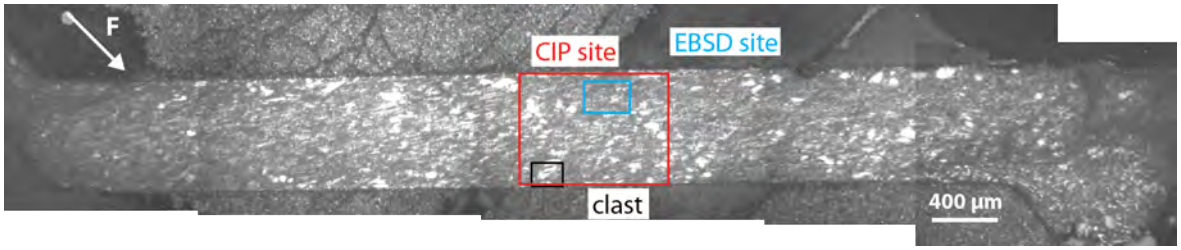

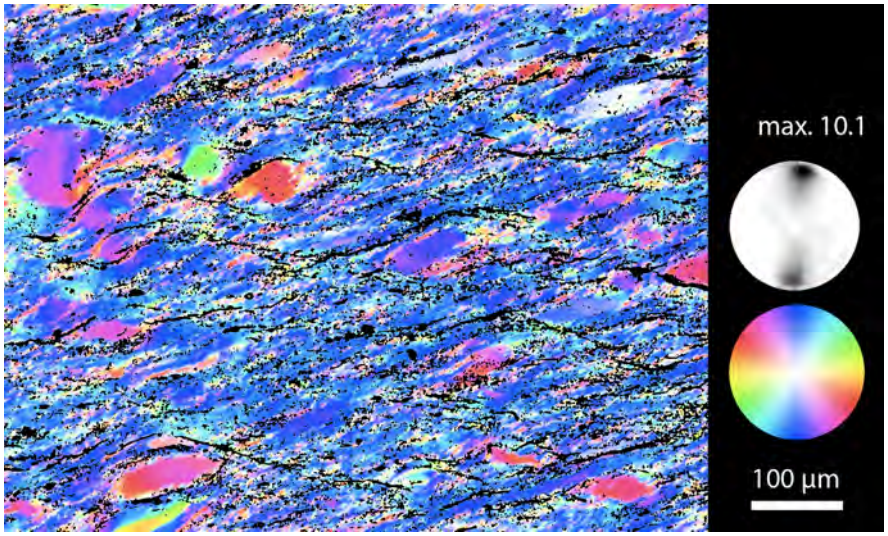

C-axis orientation image of CIP site

Elongated clast with mantle (crossed polarised light).

EBSD site:

IPF colouring in y direction, black colour indicates non-indexed pixels.

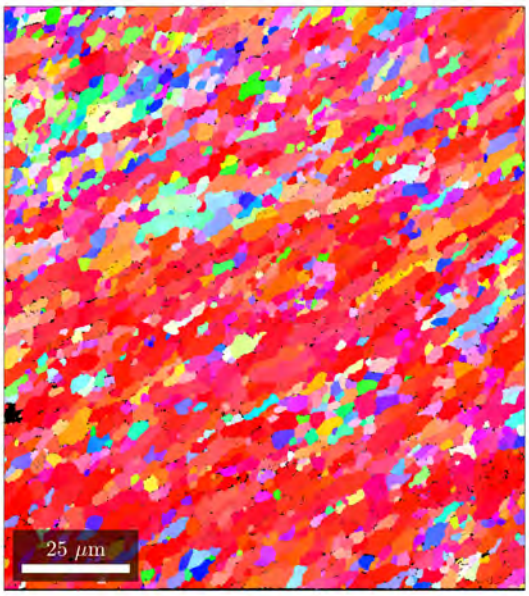

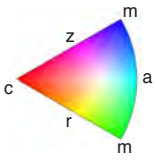

Associated pole figures.

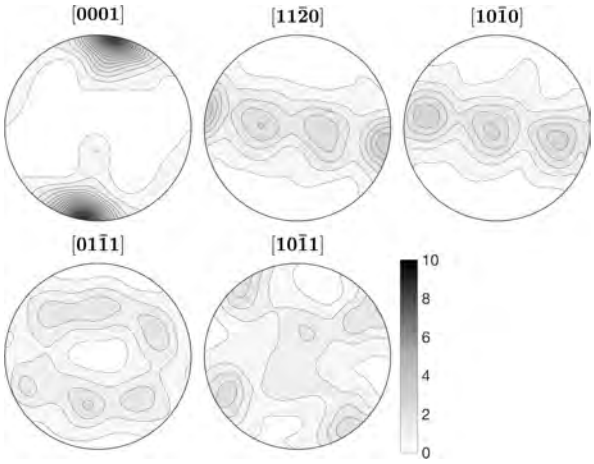

435BR

T = 650 °C
P_c = 1.5 GPa
$\dot{d} = 1.2 \cdot 10^{-8}$ ms^{-1}

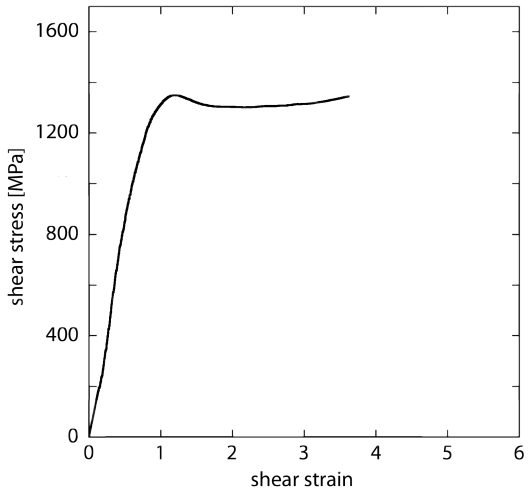

Overview of the sample (crossed polarised light):

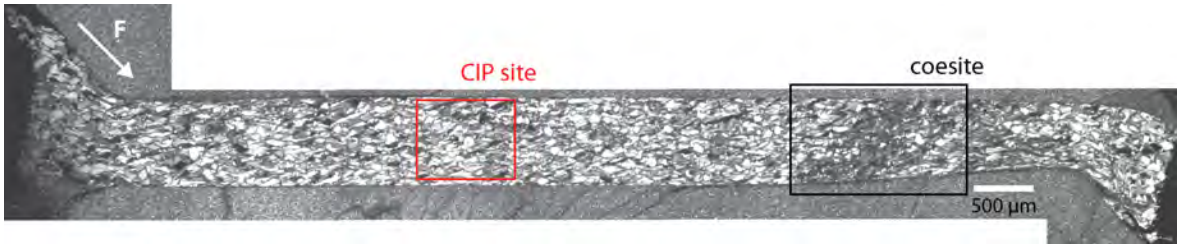

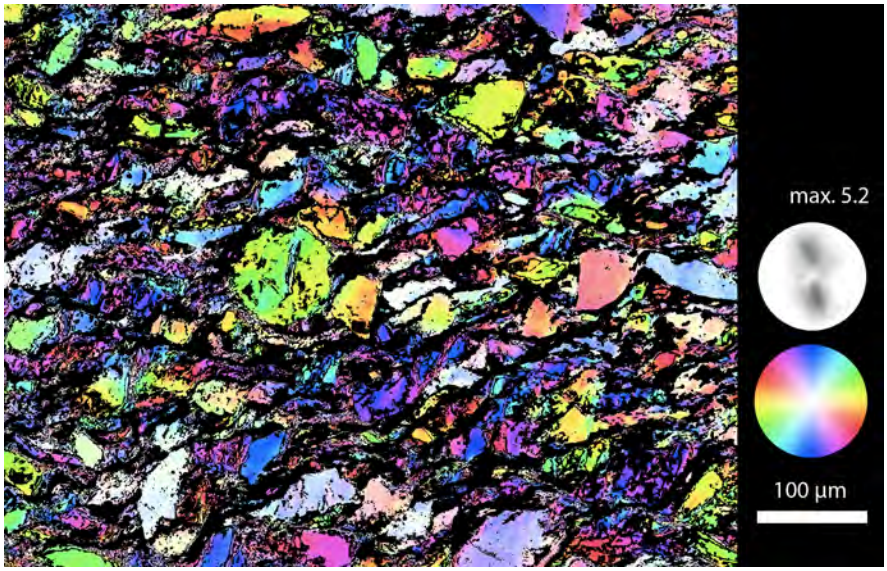

C-axis orientation image of CIP site

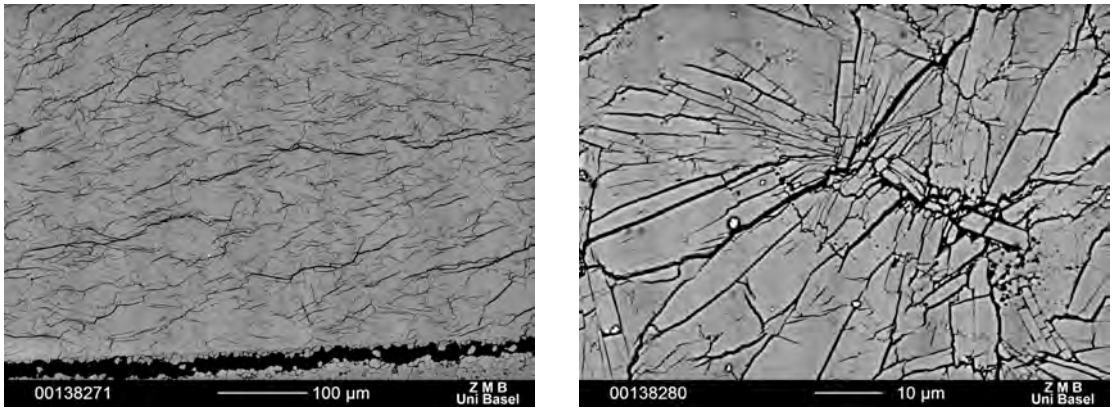

Left: Zone with high amount of coesite. **Right:** Multiple coesite grains growing from single nucleation sites, forming rare spherulitic structure. (BSE images)

437BR

T = 700 °C
P_c = 1.5 GPa
$\dot{d} = 1.2 \cdot 10^{-8}$ ms^{-1}

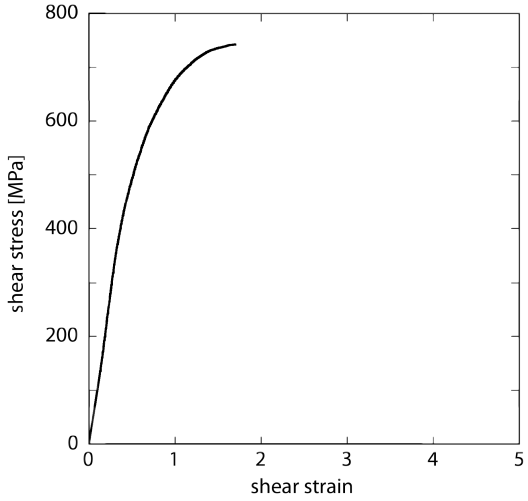

Overview of the sample (crossed polarised light):

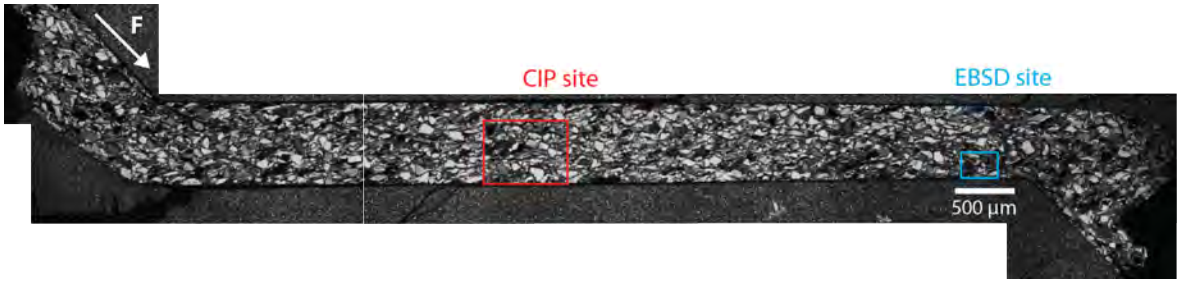

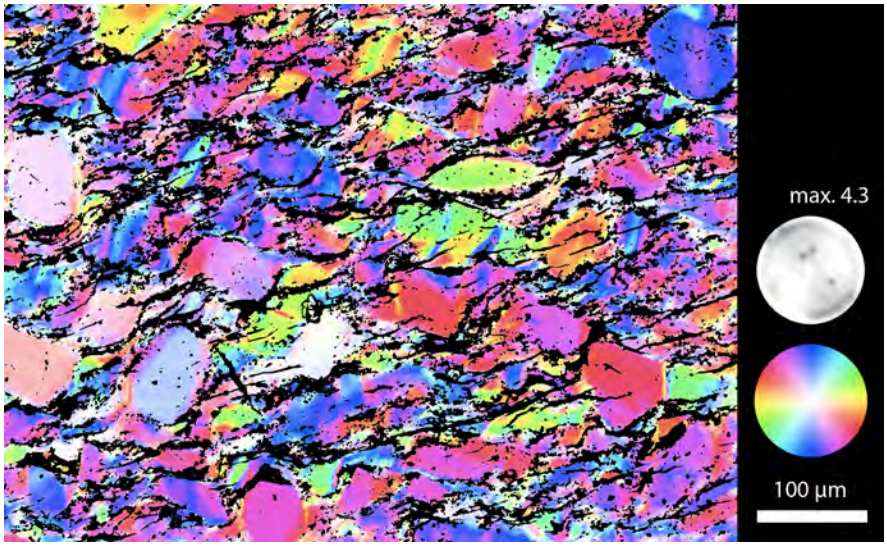

C-axis orientation image of CIP site

EBSD site:

IPF colouring in y direction, black colour indicates non-indexed pixels.

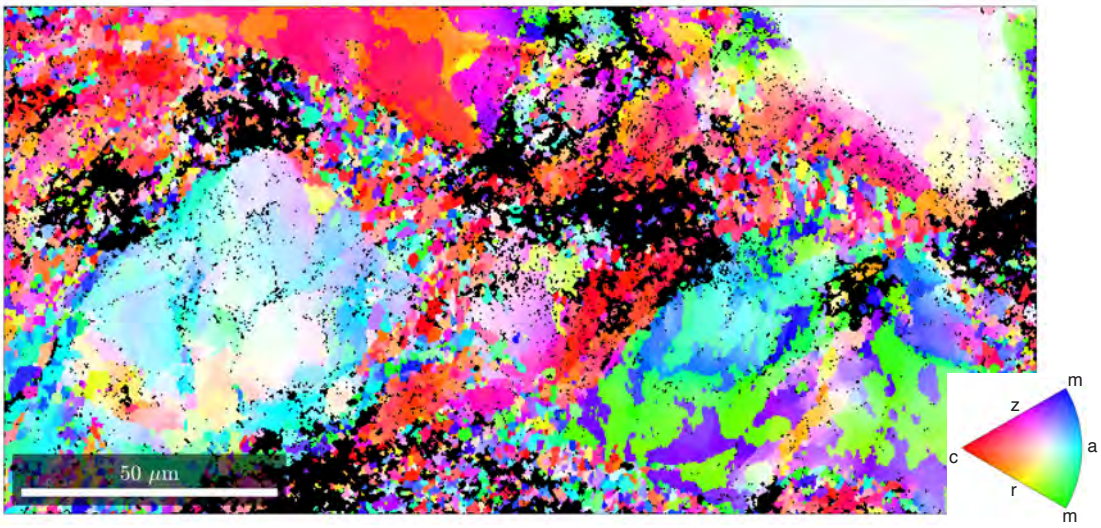

Associated pole figures.

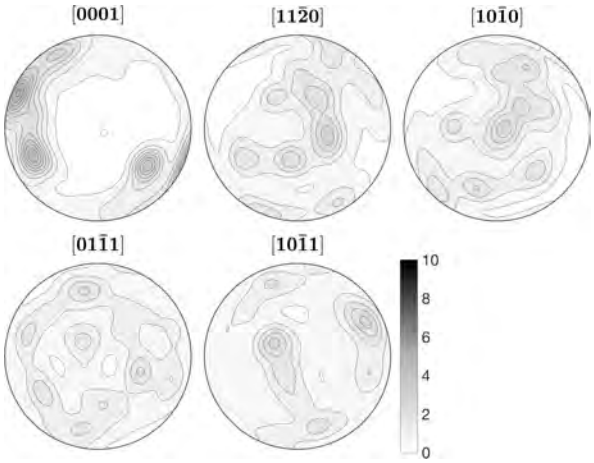

439BR

T = 800 °C
P_c = 1.5 GPa
$\dot{d} = 1.3 \cdot 10^{-8}$ ms^{-1}

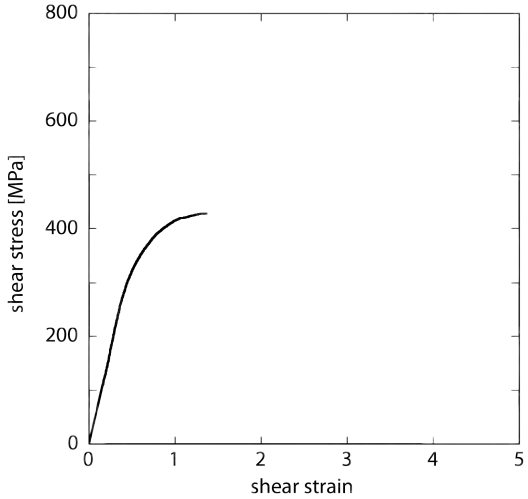

Overview of the sample (crossed polarised light):

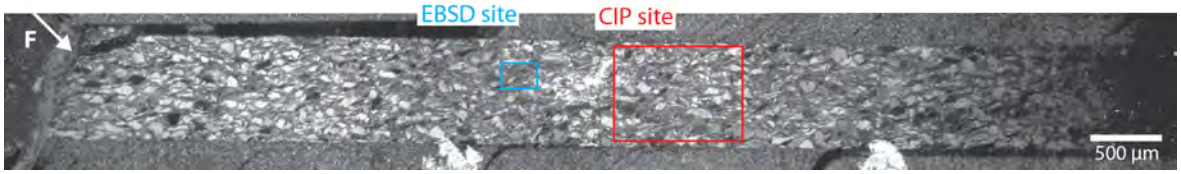

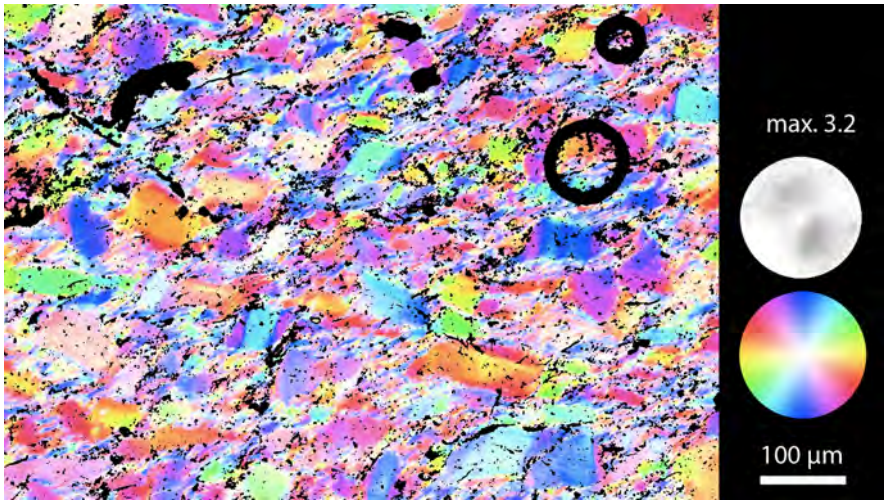

C-axis orientation image of CIP site

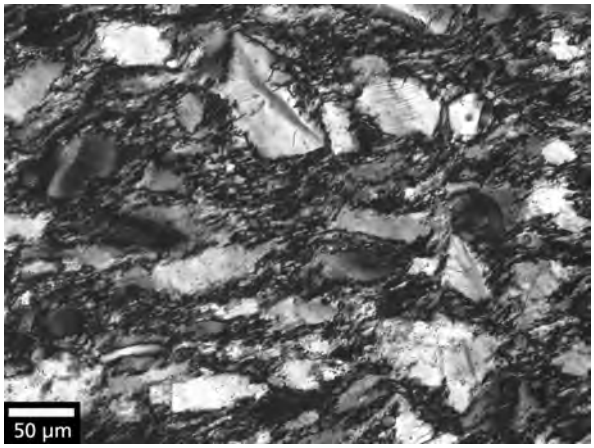

Several core mantle structures and clasts with deformation lamellae (crossed polarised light).

EBSD site:

IPF colouring in y direction, black colour indicates non-indexed pixels.

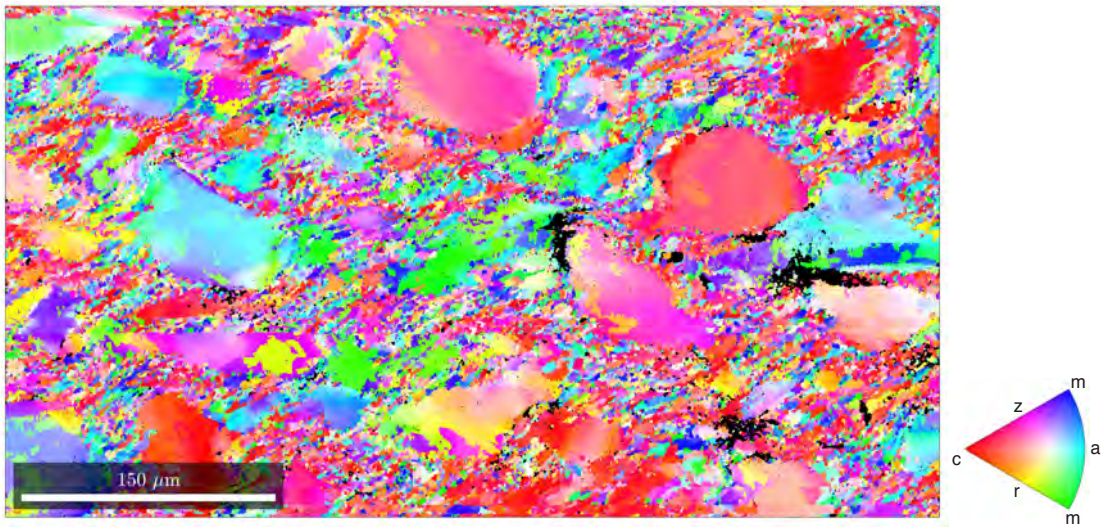

Associated pole figures.

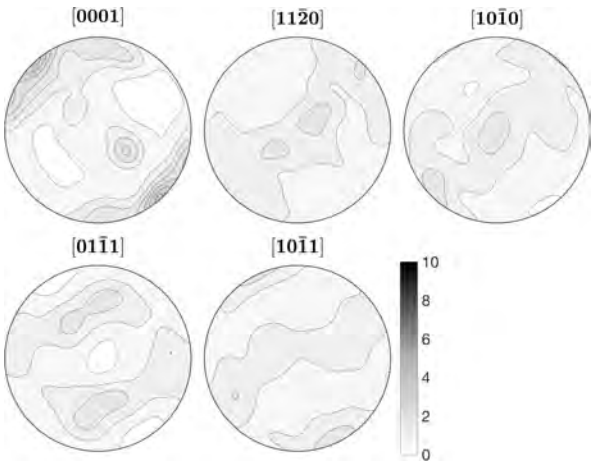

445BR

T = 800 °C
P_c = 1.5 GPa
$\dot{d} = 1.6 \cdot 10^{-8}$ ms^{-1}
7-11µm fraction

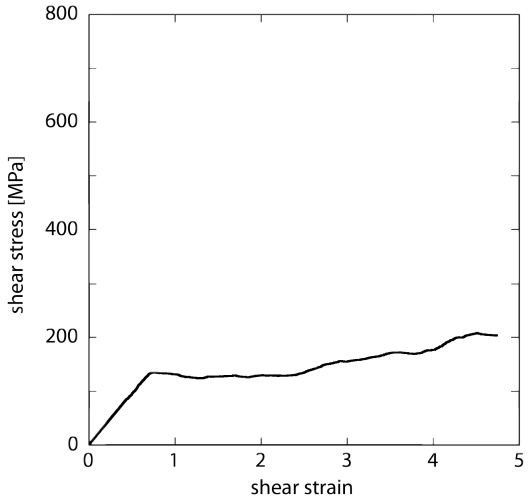

Overview of the sample in (a) crossed polarised lightand as (b) BSE image:

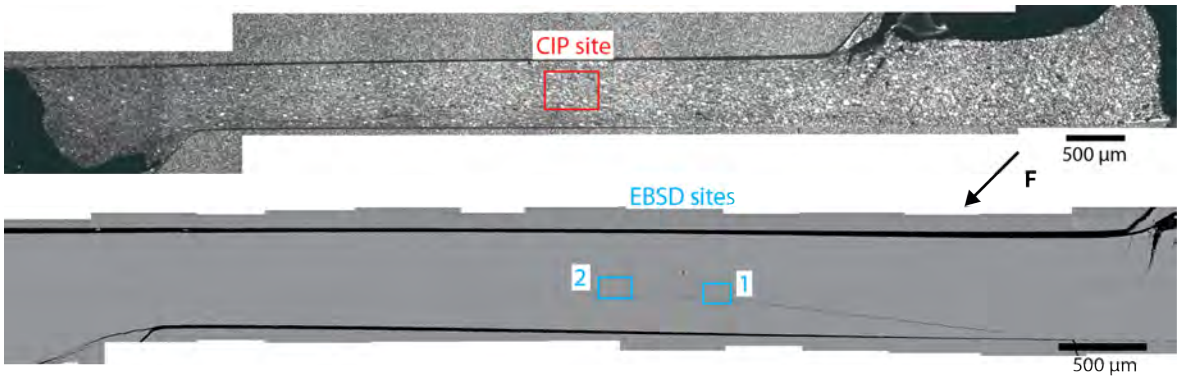

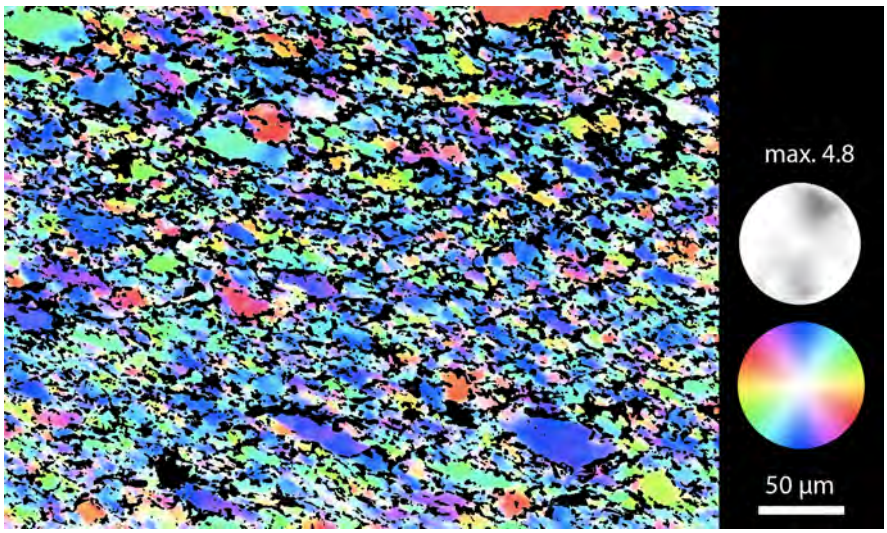

C-axis orientation image of CIP site

EBSD site 2:

IPF colouring in y direction, black colour indicates non-indexed pixels.

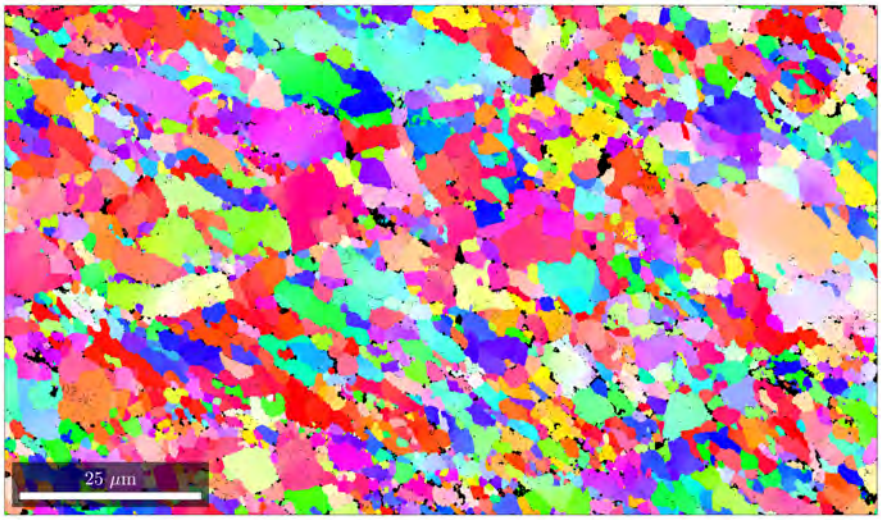

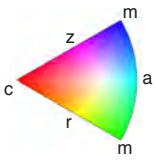

Associated pole figures.

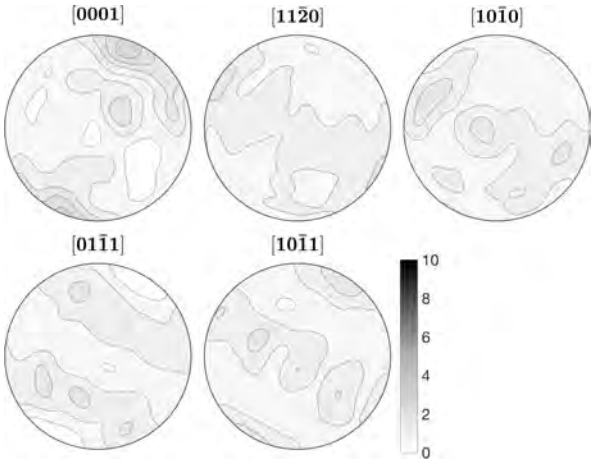

447BR

T = 800 °C
P_c = 1.5 GPa
$\dot{d} = 15 \cdot 10^{-8}$ ms^{-1}

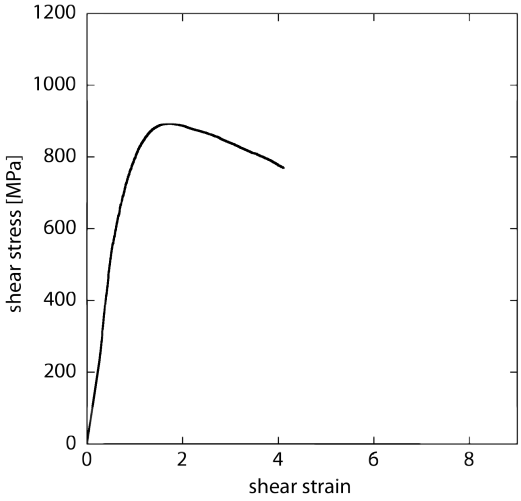

Overview of the sample (crossed polarised light):

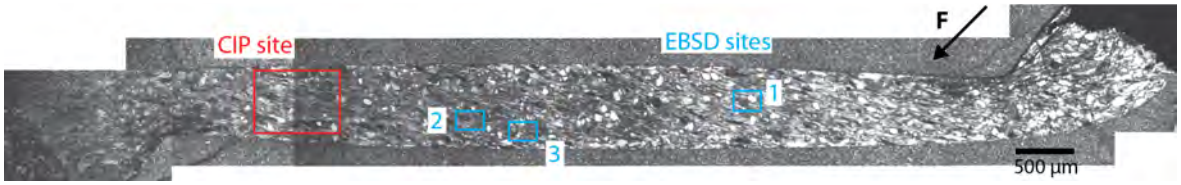

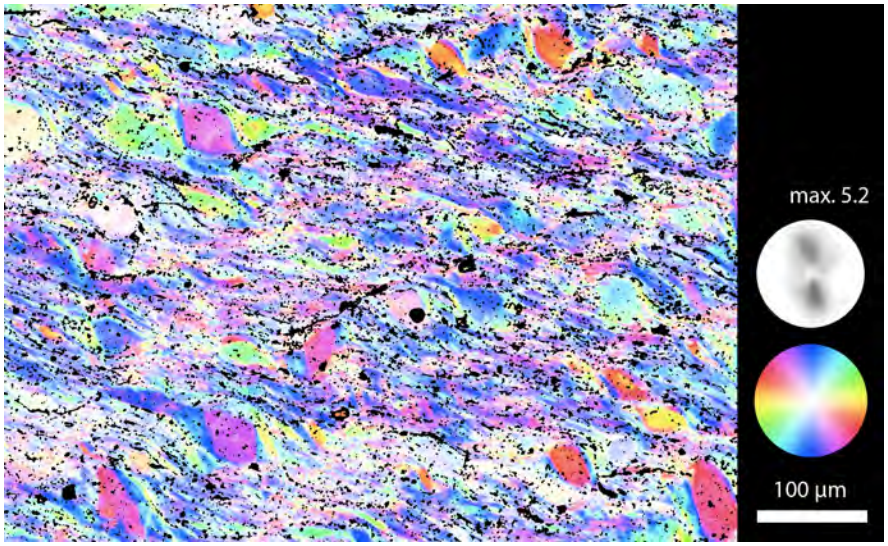

C-axis orientation image of CIP site

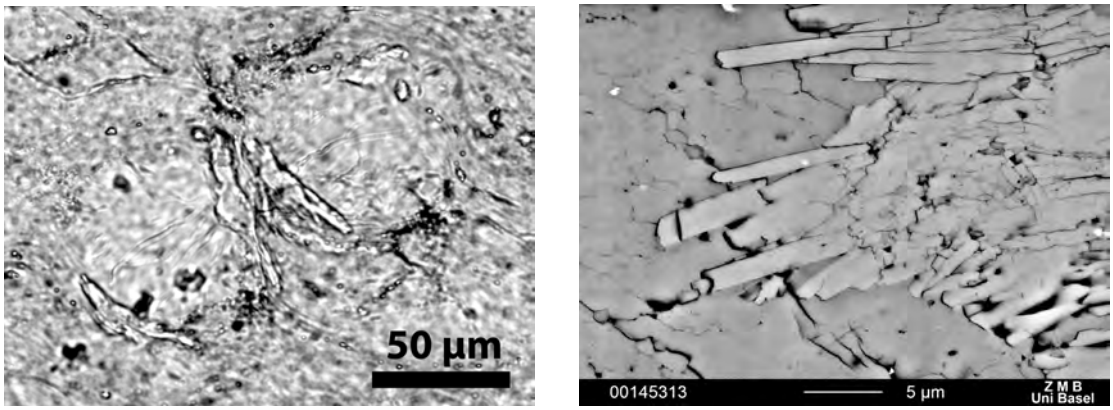

Left: Coesite (higher birefringence) in between two quarzt clasts (transmitted light). **Right:** Accumulation of coesite grains with elongated tabular shapes (BSE image).

EBSD site 1:

IPF colouring in y direction for quartz. Black colour indicates non-quartz pixels (non-indexed or coesite).

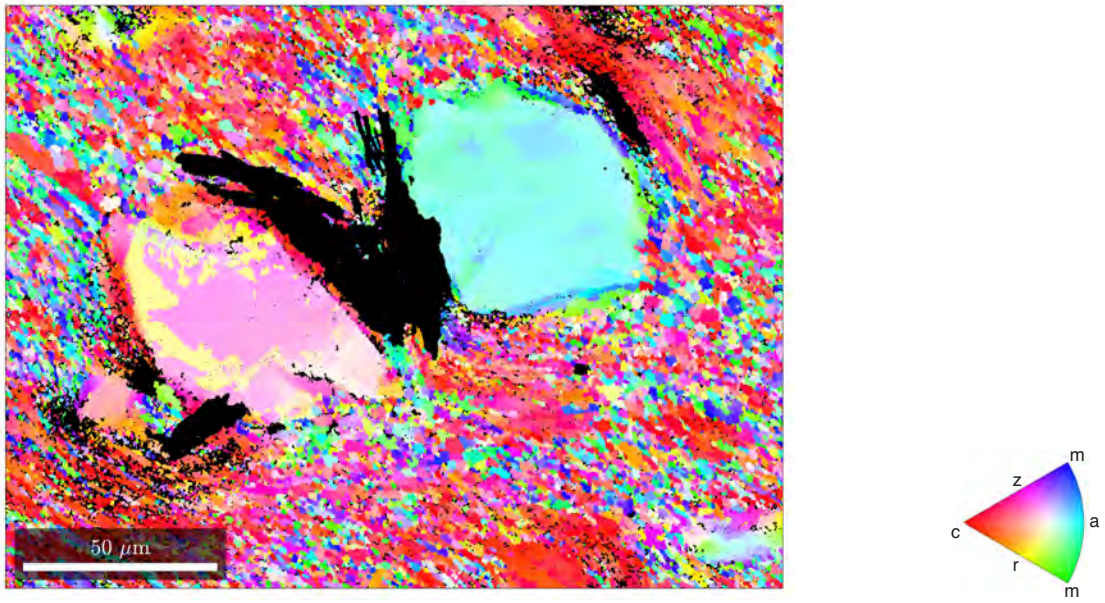

Associated pole figures for quartz that are dominated by the clasts in the centre of the map.

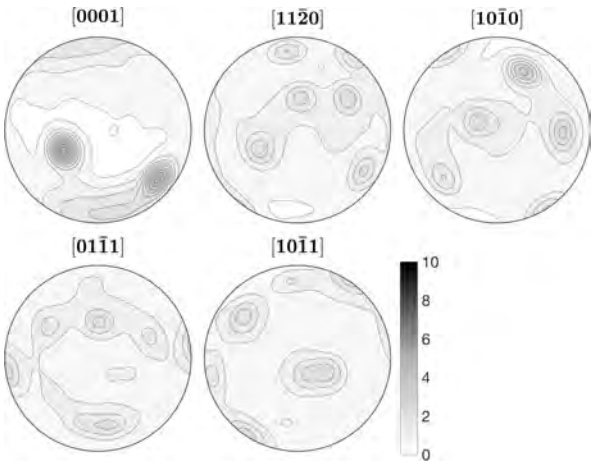

EBSD site 1:

Corresponding EBSD map with IPF colouring in y direction for coesite. Black colour indicates non-coesite pixels (non-index or quartz).

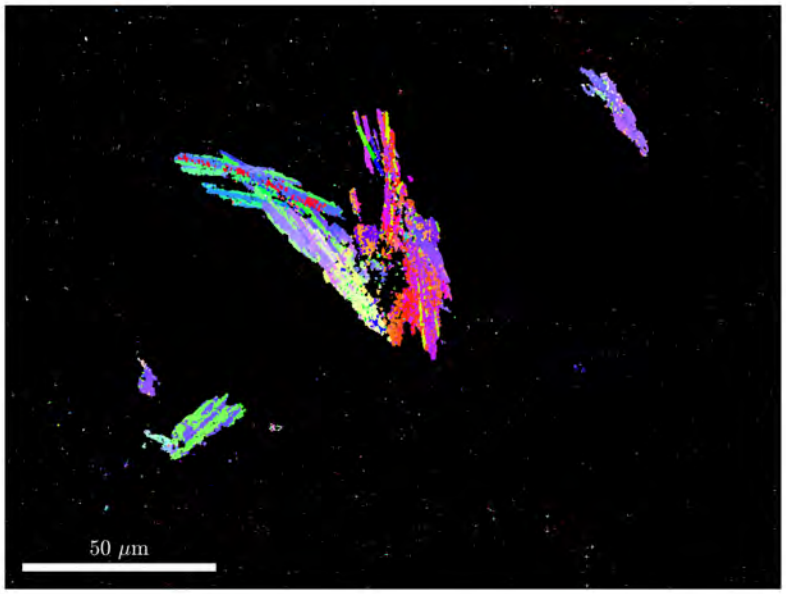

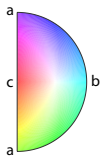

Associated pole figures for coesite.

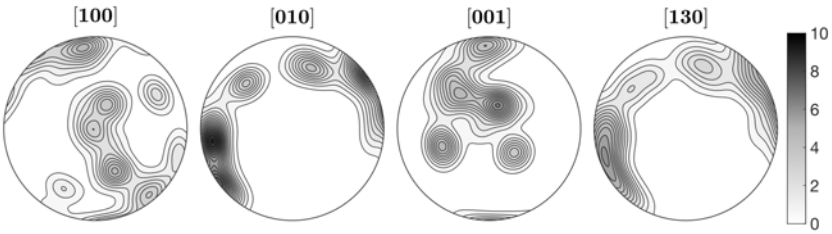

448BR

T = 800 °C
P_c = 1.0 GPa
$\dot{d} = 1.6 \cdot 10^{-8}$ ms^{-1}

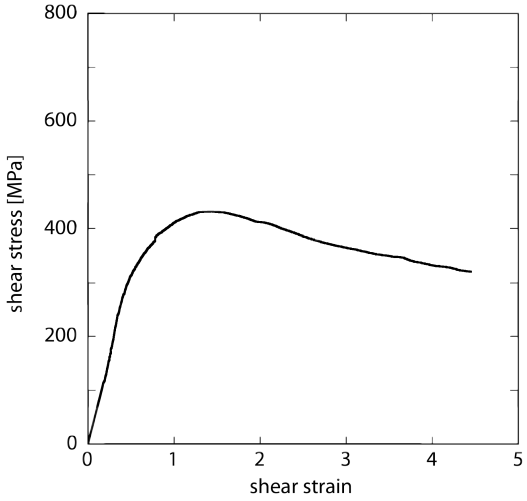

Overview of the sample (crossed polarised light):

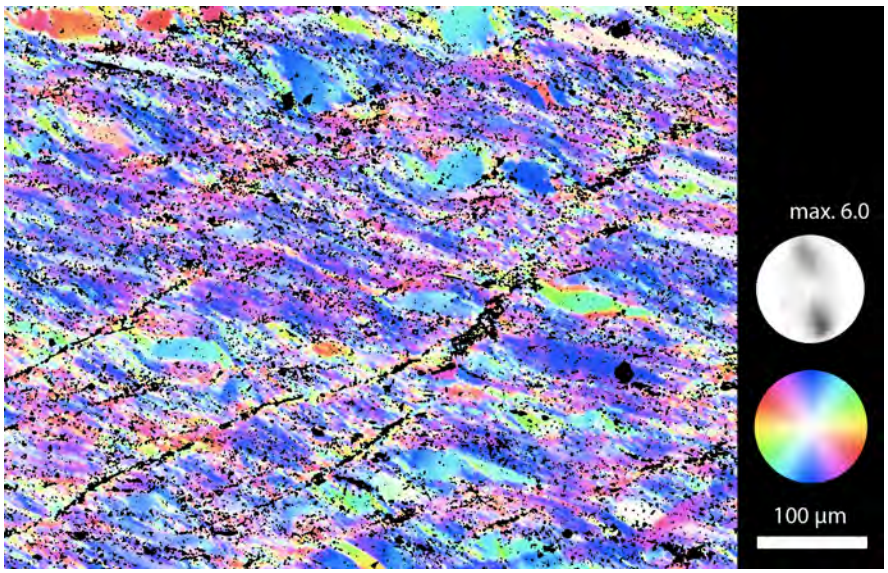

C-axis orientation image of CIP site

EBSD site 1:

IPF colouring in y direction, black colour indicates non-indexed pixels.

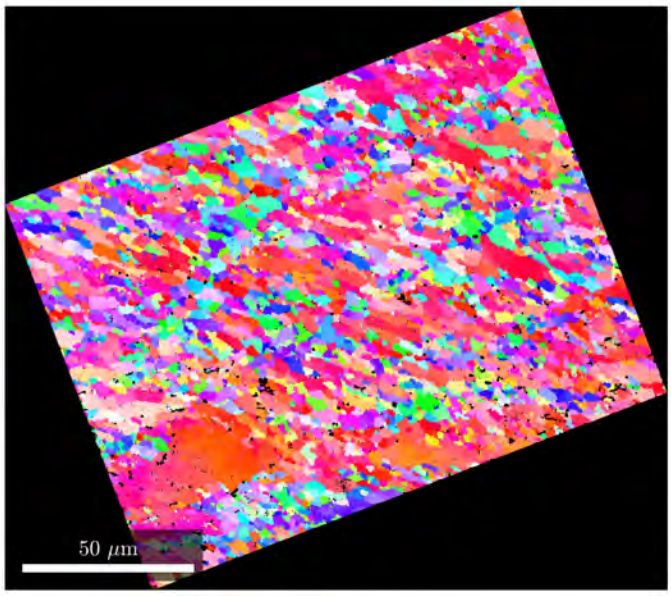

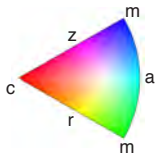

Associated pole figures.

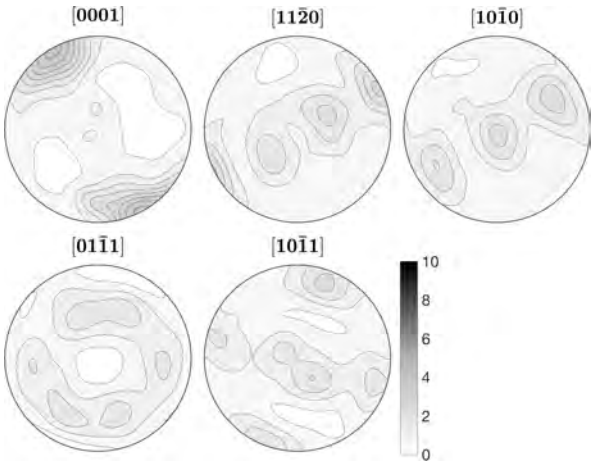

450BR

T = 500 °C
P_c = 1.5 GPa
$\dot{d} = 1.2 \cdot 10^{-8}$ ms^{-1}

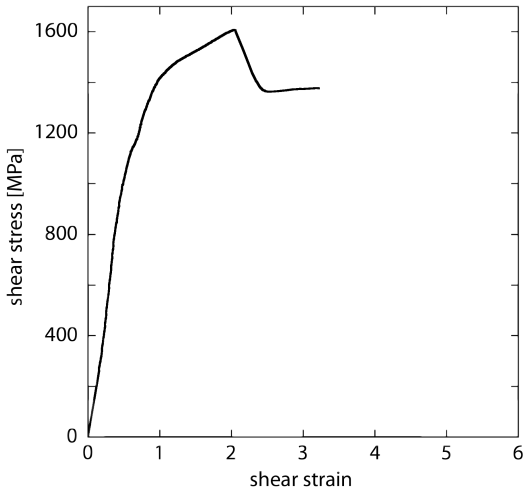

Overview of the sample in (a) crossed polarised light and as (b) BSE image:

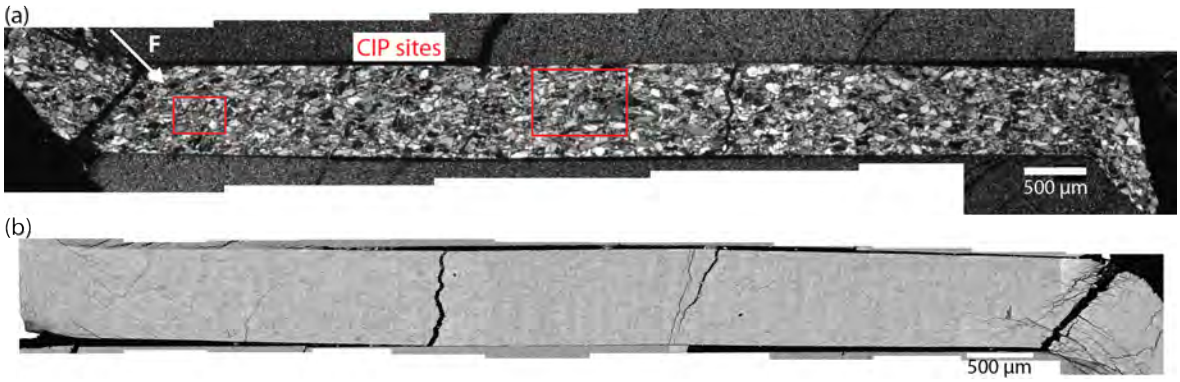

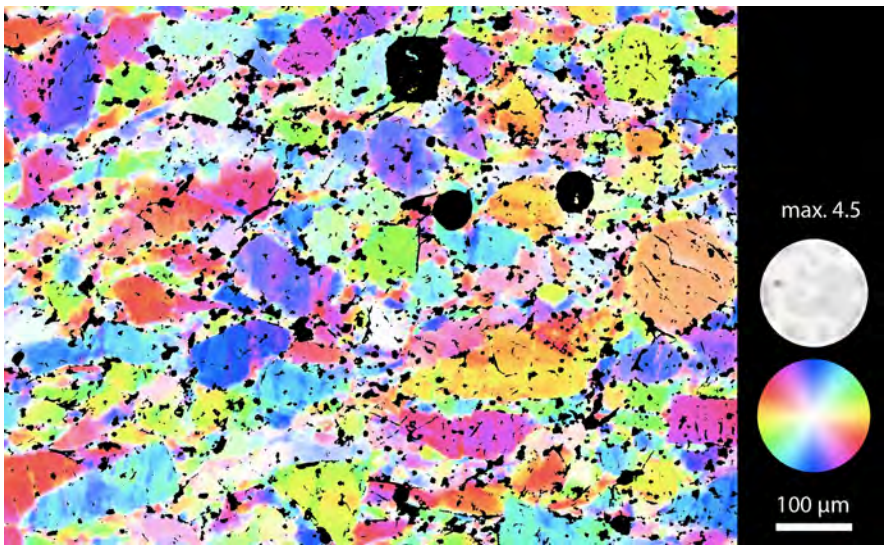

C-axis orientation image of CIP site

452BR

T = 700 °C
P_c = 1.0 GPa
$\dot{d} = 1.4 \cdot 10^{-8}$ ms^{-1}

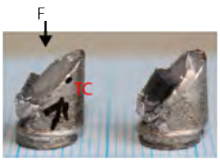

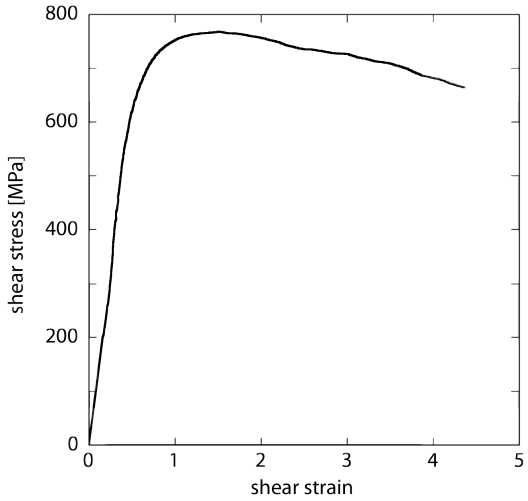

Overview of the sample (crossed polarised light):

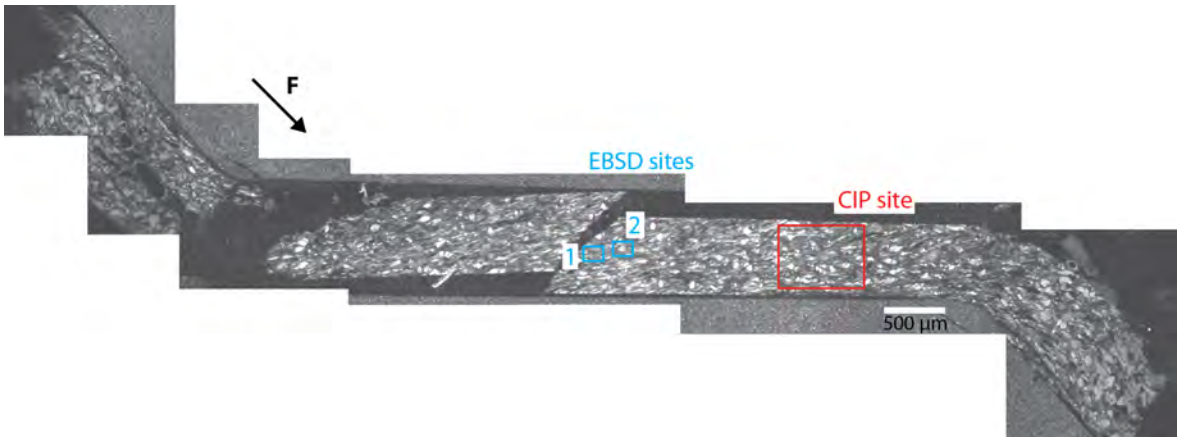

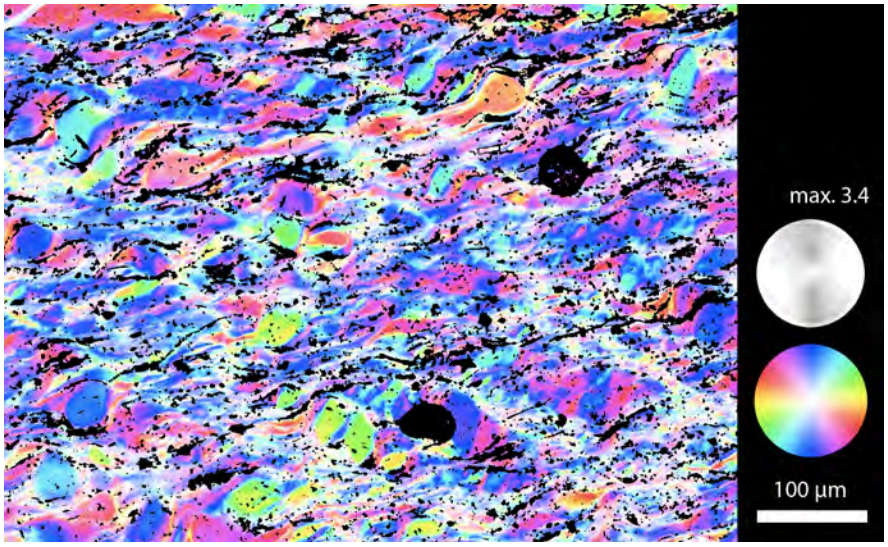

C-axis orientation image of CIP site

EBSD site 2:

IPF colouring in y direction, black colour indicates non-indexed pixels.

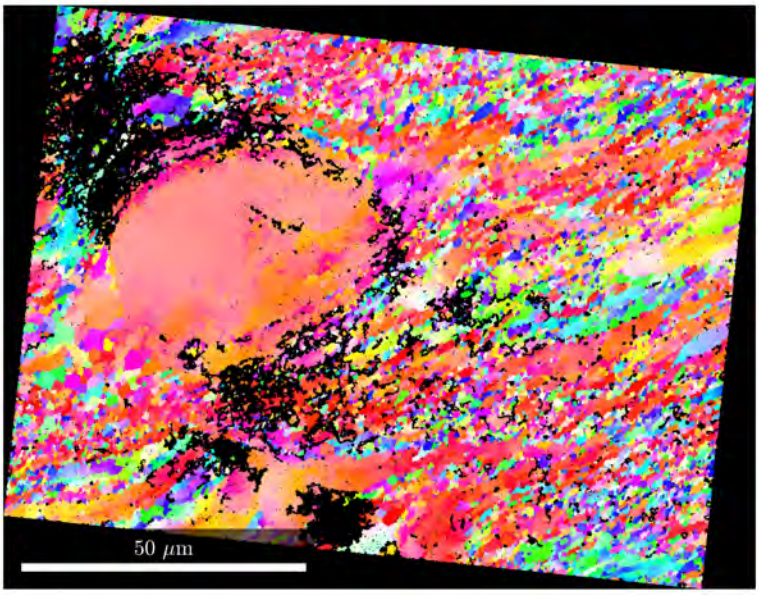

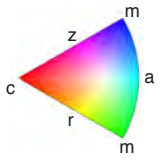

Associated pole figures. The large clast dominates the pole figures.

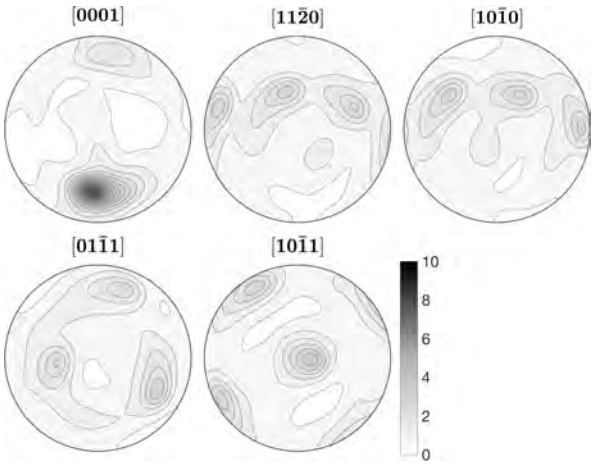

479BR

T = 600 °C
P_c = 1.5 GPa
$\dot{d} = 1.2 \cdot 10^{-8}$ ms^{-1}

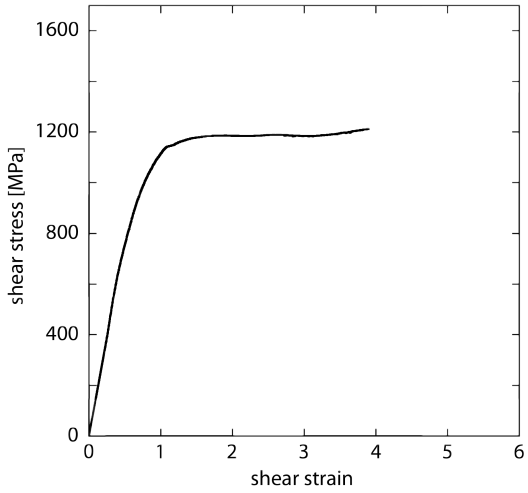

Overview of the sample (crossed polarised light):

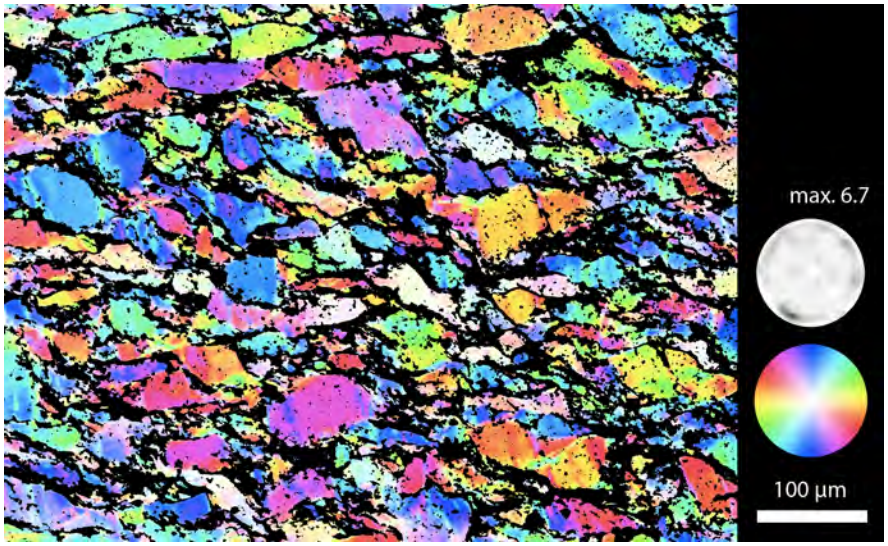

C-axis orientation image of CIP site

487BR

T = 800 °C
P_c = 1.5 GPa
hydrostatic for 25 h

Overview of the sample (crossed polarised light):

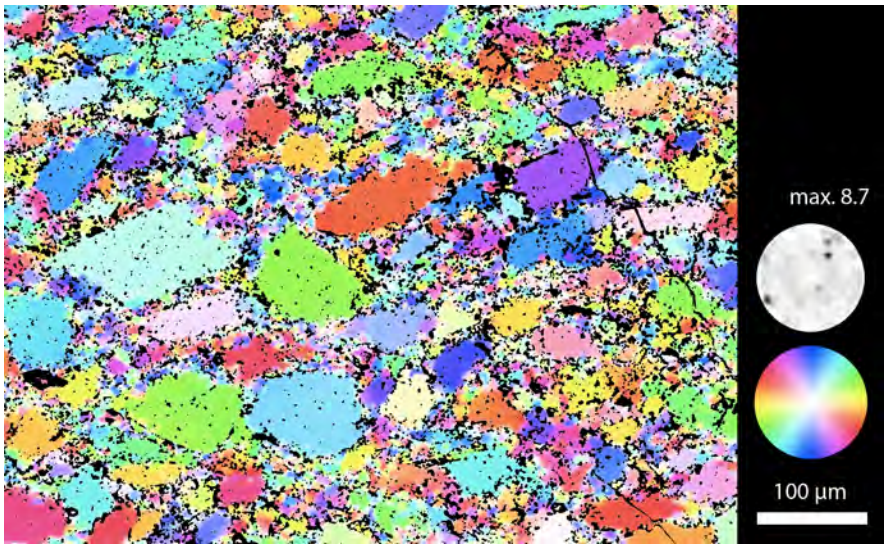

C-axis orientation image of CIP site

EBSD site 2:

IPF colouring in y direction, black colour indicates non-indexed pixels.

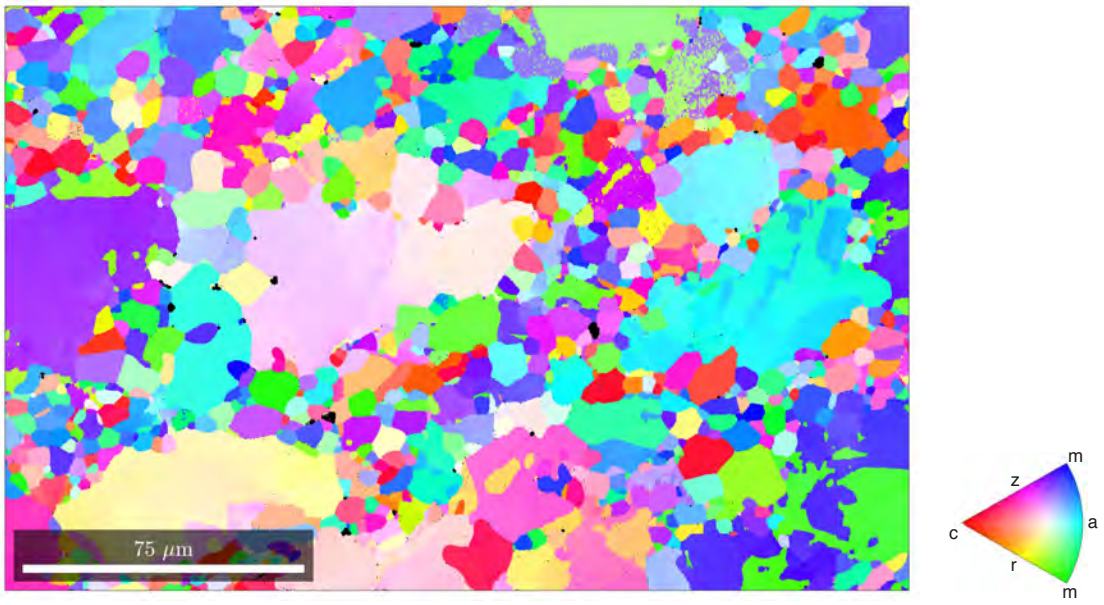

Associated pole figures.

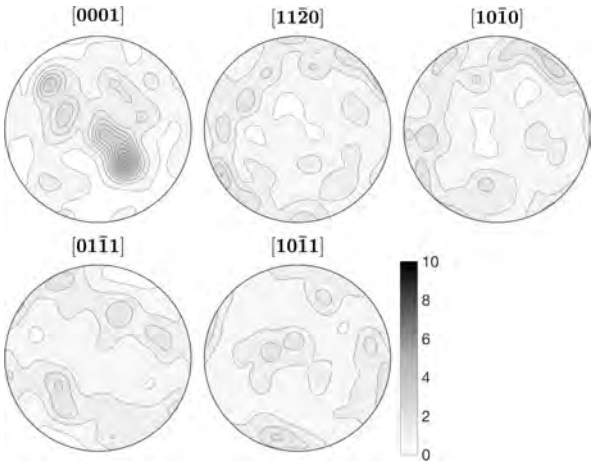

493BR

T = 700 °C
P_c = 1.5 GPa
$\dot{d} = 1.5 \cdot 10^{-8}$ ms^{-1}
hot pressed for 20 h
at 1000 °C, 1.5 GPa

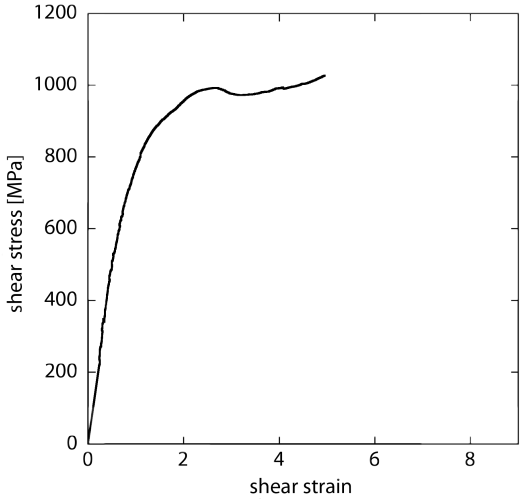

Overview of the sample (reflected light):

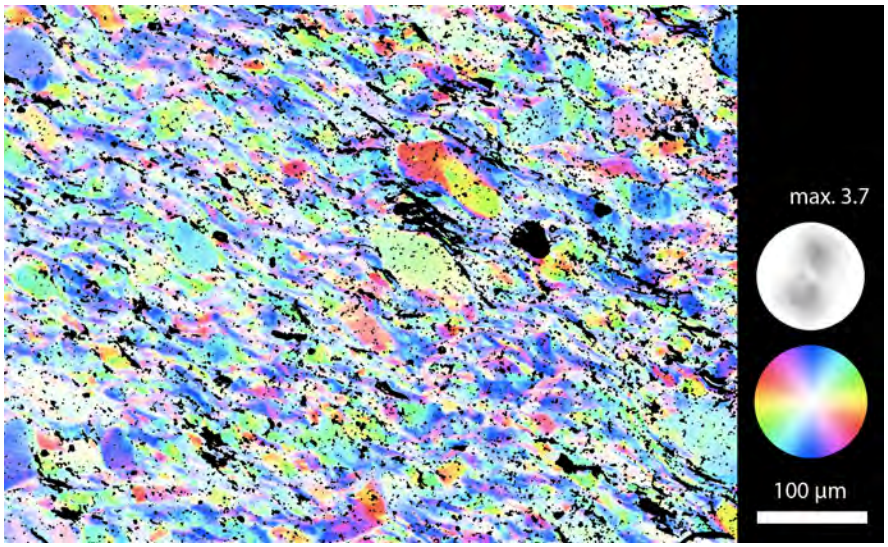

C-axis orientation image of CIP site

EBSD site 1:

IPF colouring in y direction for quartz. Black colour indicates non-quartz pixel (non-indexed or coesite).

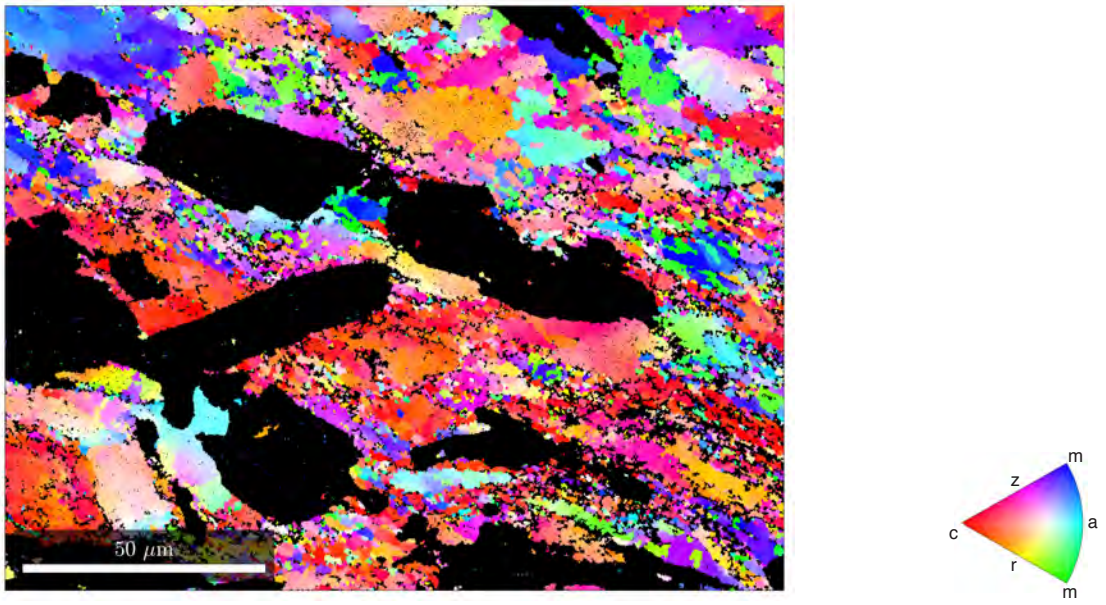

Associated pole figures for quartz.

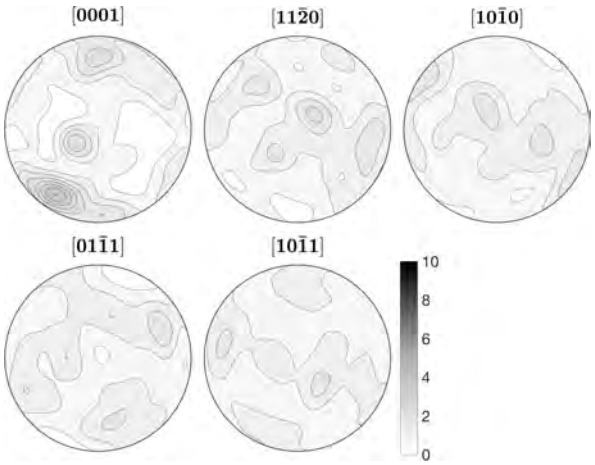

Corresponding EBSD map with IPF colouring in y direction for coesite. Black colour indicates non-coesite pixel (non-indexed or quartz).

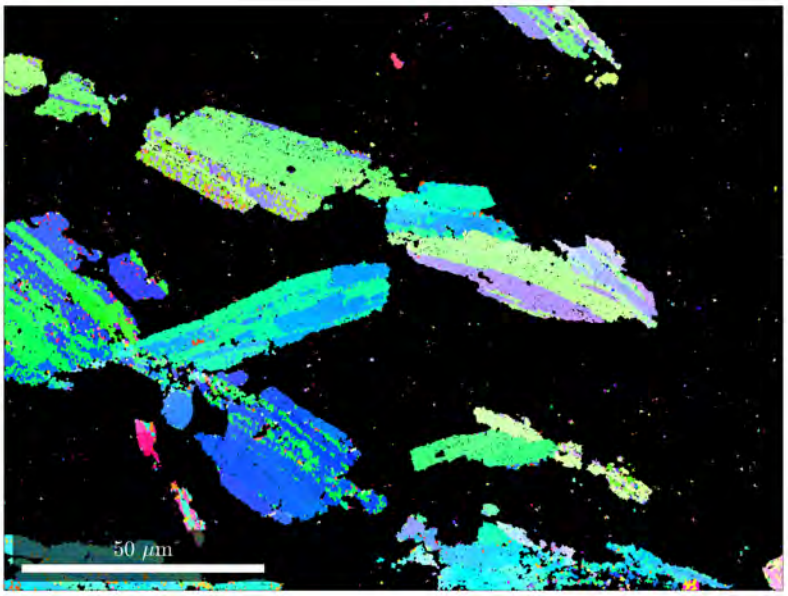

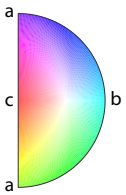

Associated pole figures for coesite.

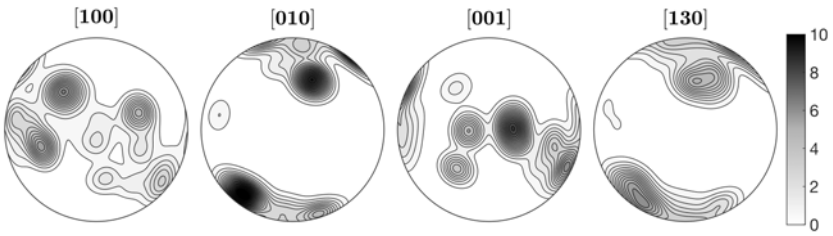

494BR

T = 650 °C
P_c = 1.0 GPa
$\dot{d} = 2.6 \cdot 10^{-8}$ ms^{-1}

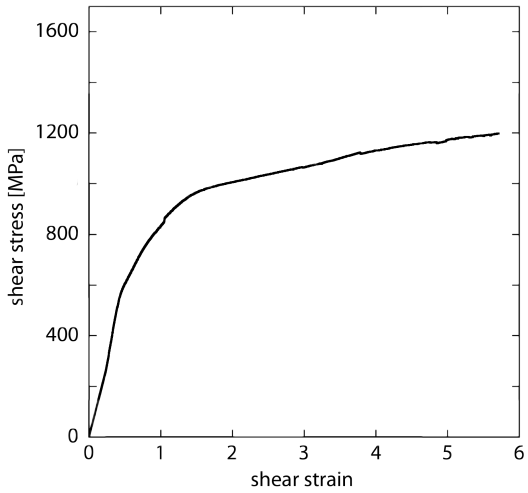

Overview of the sample (reflected light):

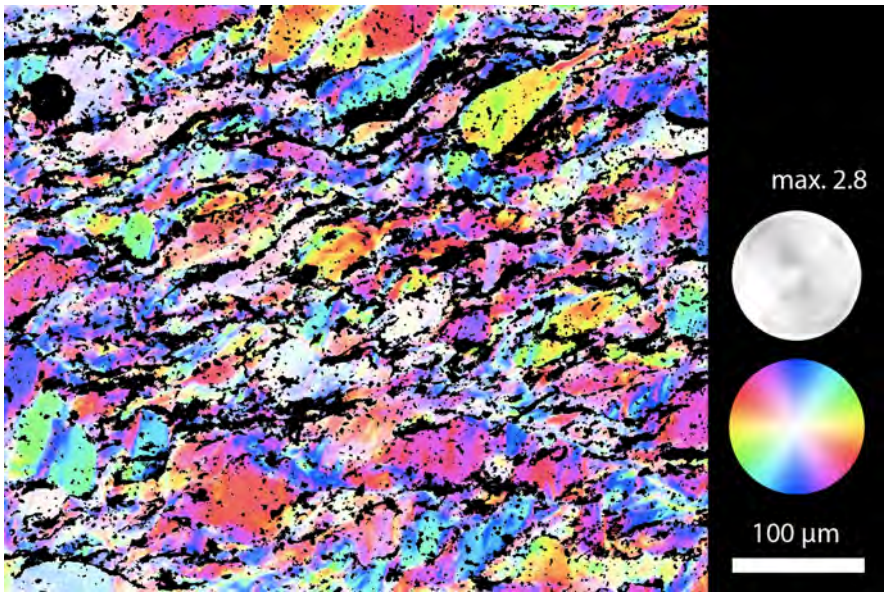

C-axis orientation image of CIP site

495BR

T = 750 °C
P_c = 1.5 GPa
$\dot{d} = 15 \cdot 10^{-8}$ ms^{-1}

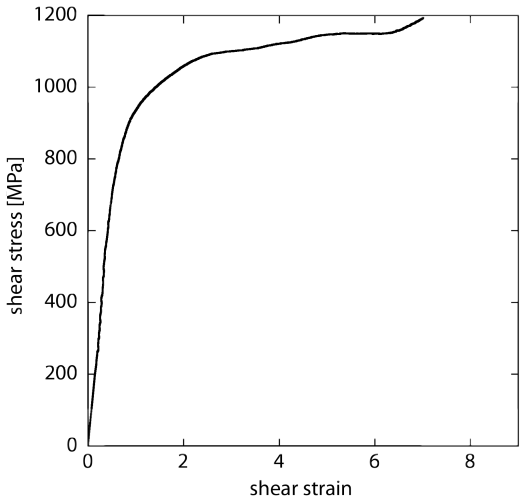

Overview of the sample (a) reflected light and (b) close-up of the central part:

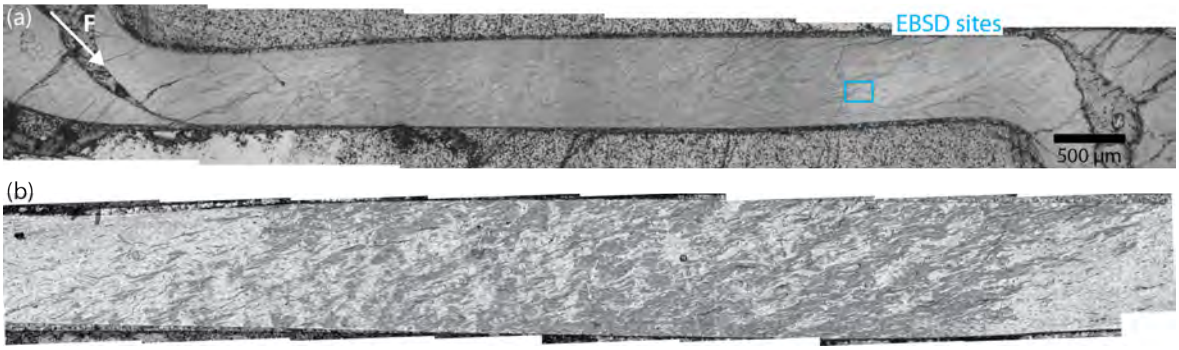

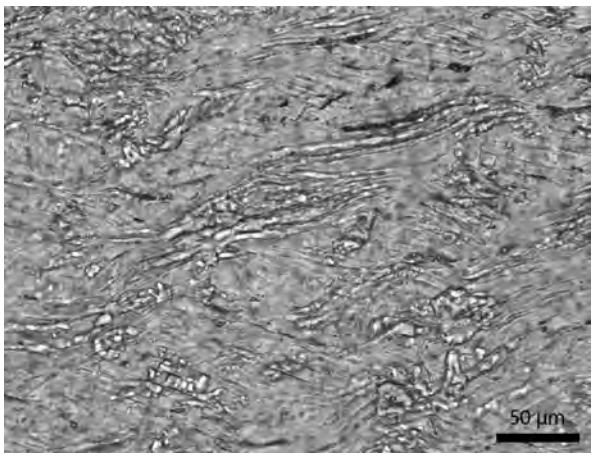

Coesite with slightly higher birefringence between quartz (transmitted light).

499BR

T = 900 °C
P_c = 1.5 GPa
$\dot{d} = 110 \cdot 10^{-8}$ ms^{-1}

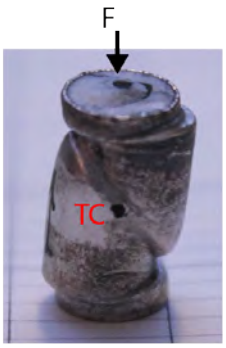

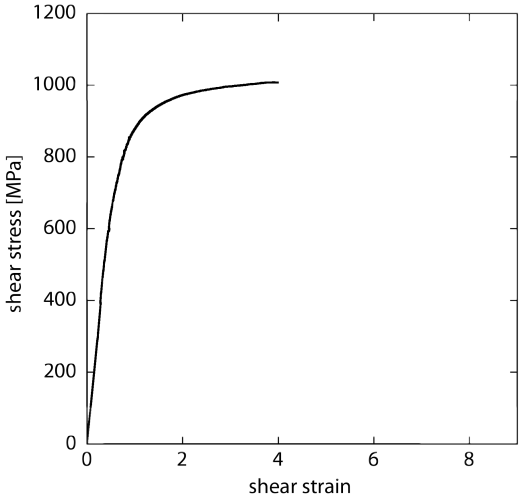

Overview of the sample (reflected light):

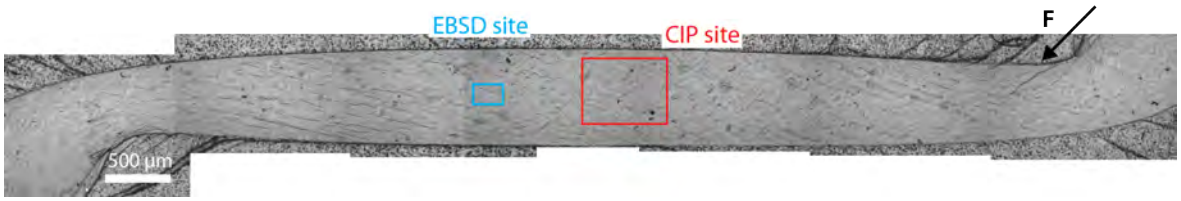

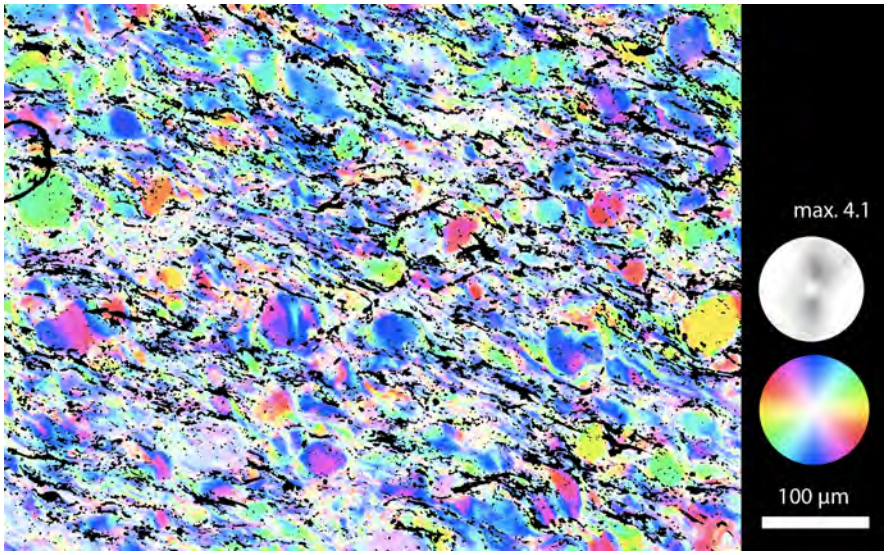

C-axis orientation image of CIP site

EBSD site:

IPF colouring in y direction, black colour indicates non-indexed pixels.

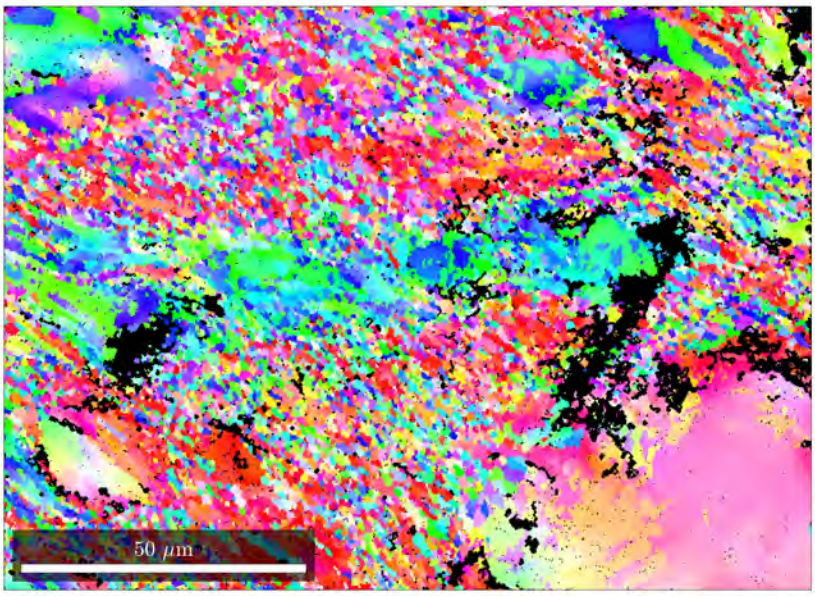

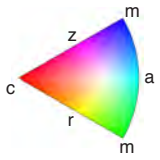

Associated pole figures. The large clast in the lower right is clearly visible in the *c*-axes pole figure.

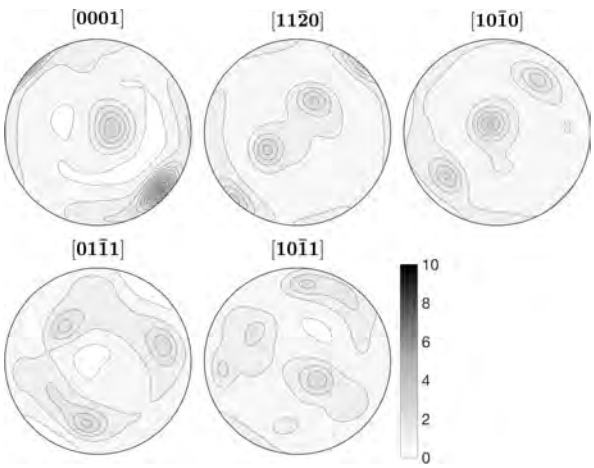

500BR

T = 650 °C
P_c = 1.5 GPa
$\dot{d} = 0.21 \cdot 10^{-8}$ ms^{-1}

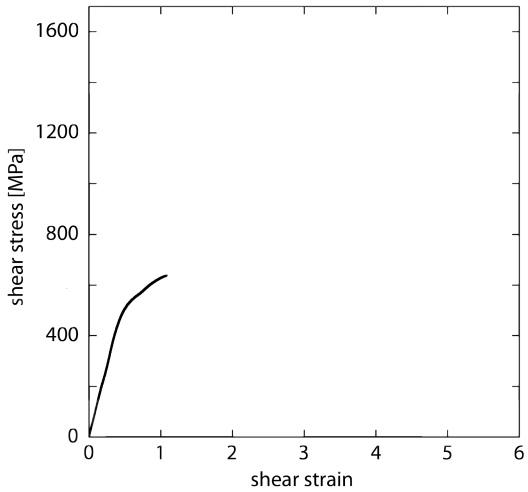

Overview of the sample (reflected light):

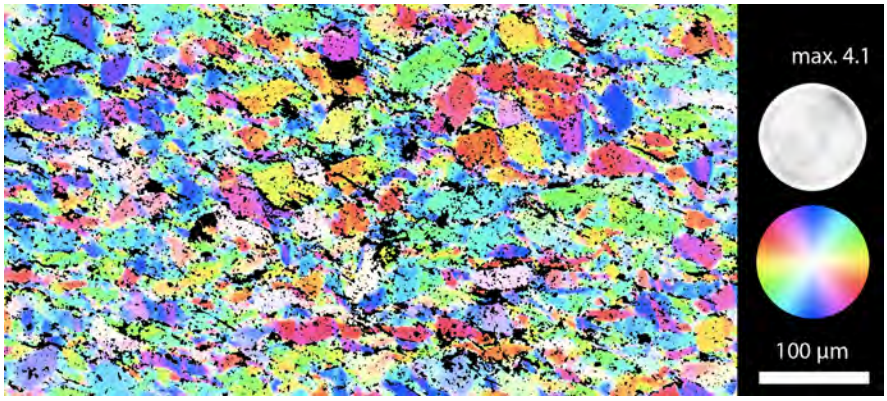

C-axis orientation image of CIP site

EBSD site:

IPF colouring in y direction, black colour indicates non-indexed pixels.

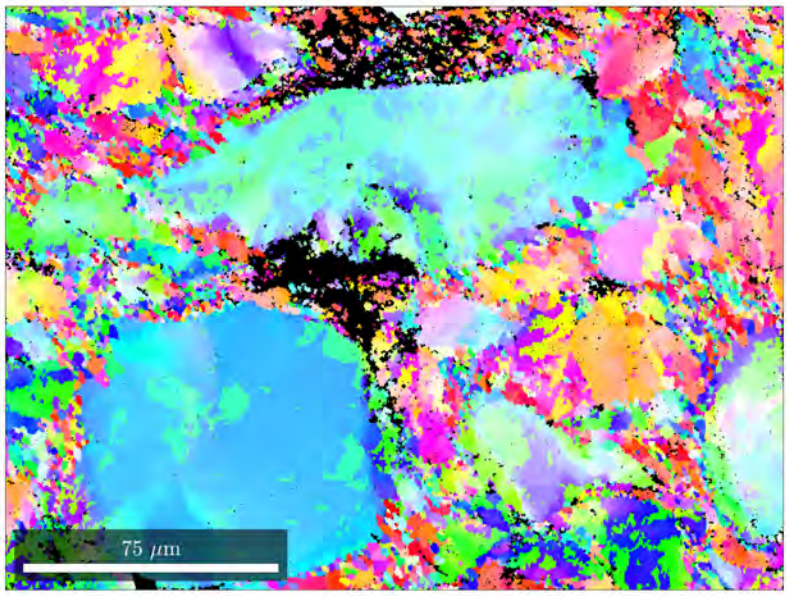

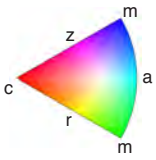

Associated pole figures. The two large clasts dominate the pole figures.

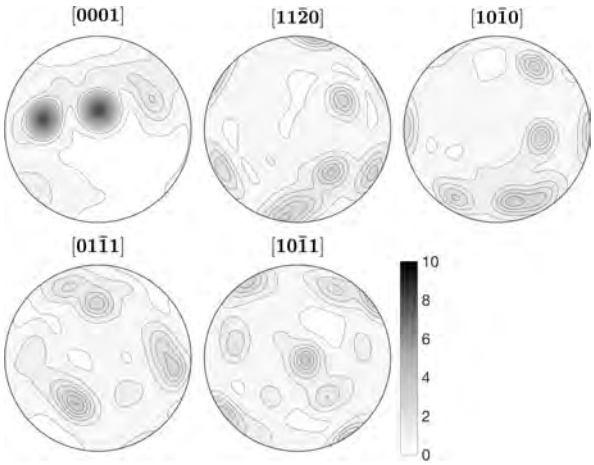

E Workflow in the laboratory

In the course of this PhD a detailed procedure for carrying out experiments including the preparation of the individual pieces (Fig. E.0-1) was composed. Thereby, existing descriptions for the preparation of salt and lead pieces have been updated. For each experiment, the measurements of all assembly pieces and the conditions of each experimental stage are recorded (Fig. E.0-2).

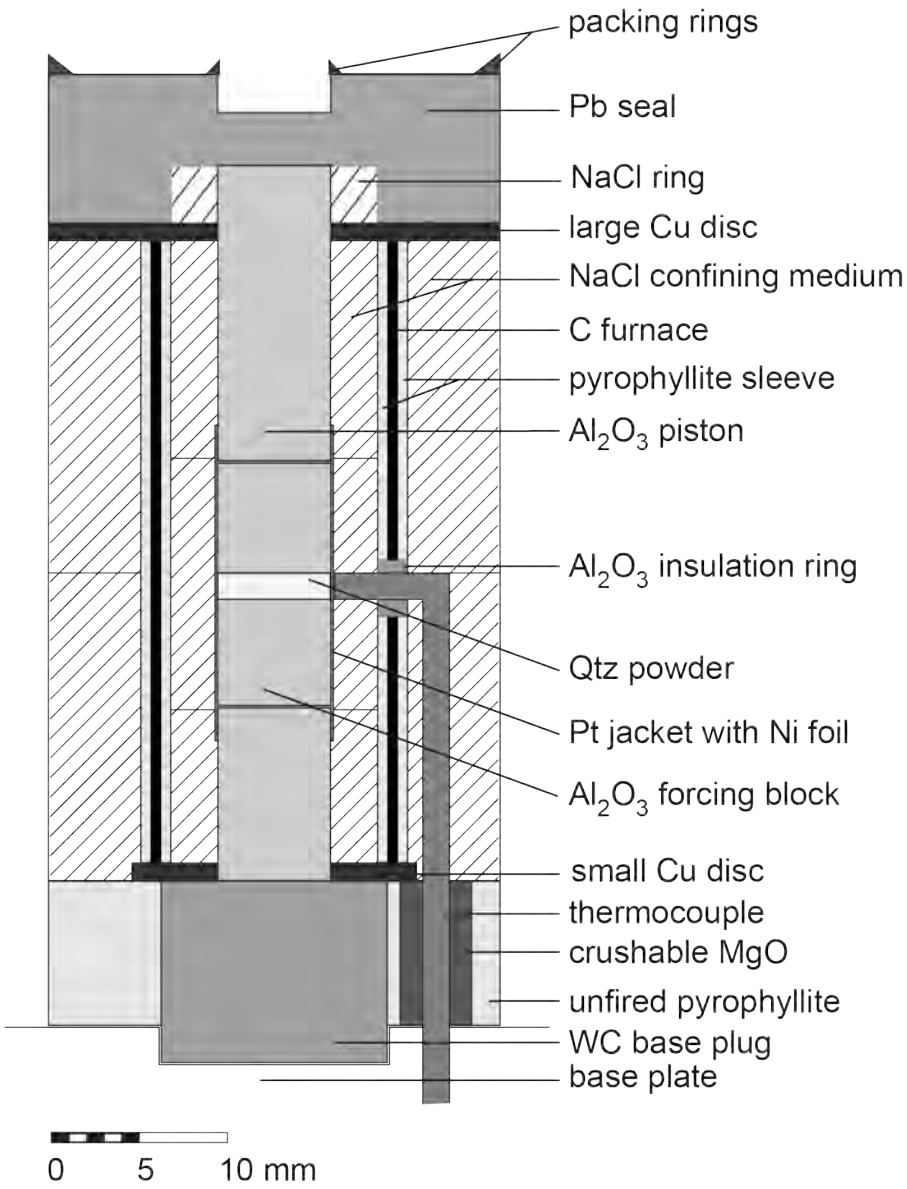

Fig. E.0-1: Sample assembly of a solid medium Griggs-type deformation apparatus.

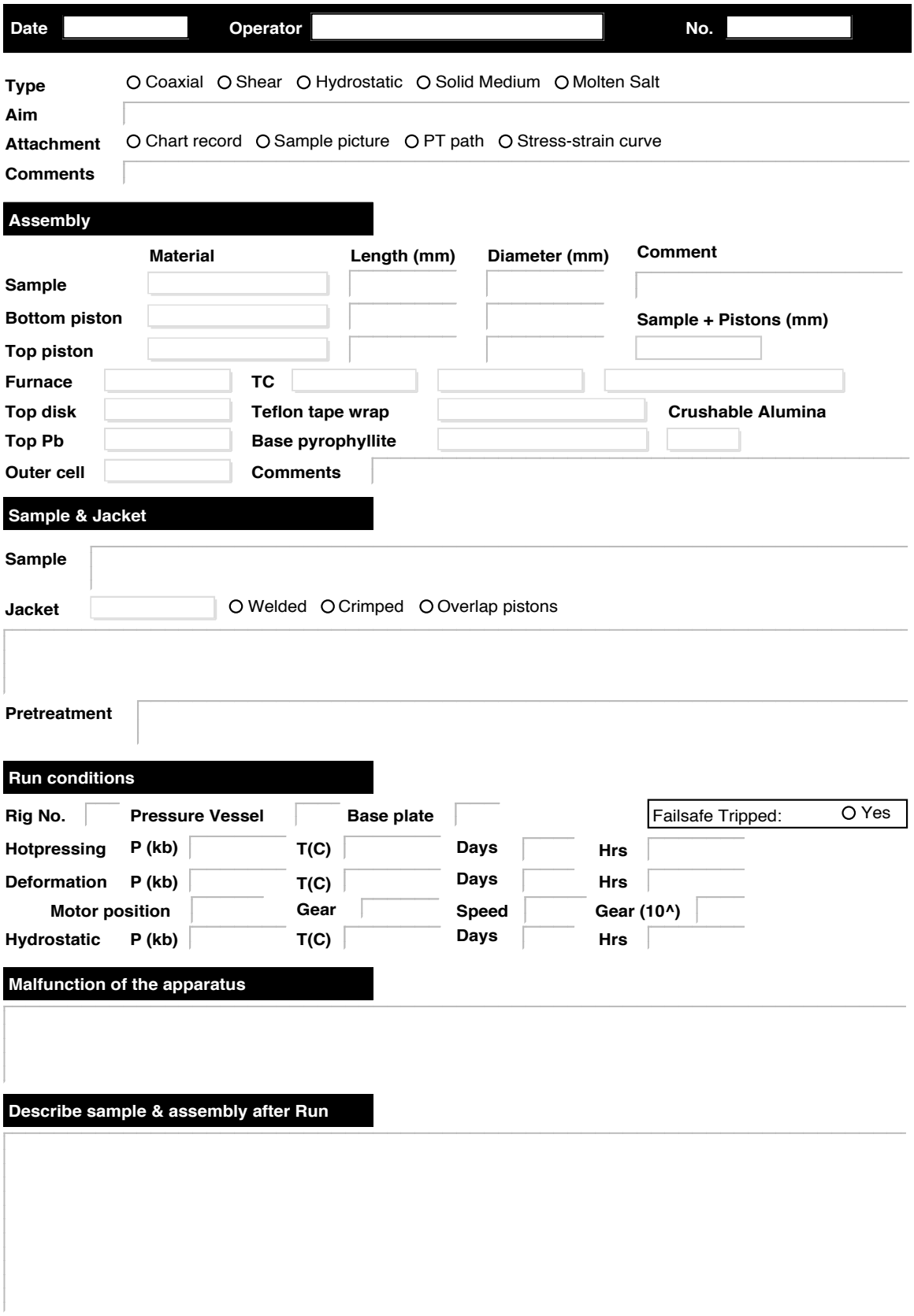

Fig. E.0-2: Template for a protocol that is kept for each experiment.

Other remarks

Output values & PT path

Zero Start Values		Scale (mv/V FS)	Pump	
P (mv/V)		Pressure		
F (mv/V)		Force		
Dx (mv/V)		Displacement		

Furnace Power		Pressure	Force	Temperature	
A (old:psi)	V	mV	mV	°C	%op

E.1 Sample assembly

E.1.1 Sample jacket

Forcing blocks for shear samples: An alumina piston (diameter ∼6.33 mm) is cut with the good diamond saw blade (length ∼12.0 - 12.5 mm). Fasten the alumina rod in the sample holder with the setscrew. The long end should be on the left side. Towards the end of the cutting, the piston breaks off and leaves a small ledge at the piston end or the long end of the rod.

The ends of the piston should be plane-parallel (difference less than 2-3 µm). The diamond-grinding wheel is used to flatten and grind the ends. The piston is put into the small holder and the screws are tightened. The holder is put into the tilting holder and fastened (watch out - do not tighten the screw to much, because that may counteract the tightening of the small screws). Before starting the grinder, it has to be made sure that the piston is not too close to the diamond wheel (it should almost pass the wheel) and the valve has to be openfor the cooling water. Move the piston back and forth a few times with a slow rocking motion until the grinding sound becomes less audible. The exact length and the diameter of the piston are measured with the micrometer and noted.

Afterwards cut the piston in a 45° angle in the saw using the appropriate holder. Afterwards the surfaces have to be polished with the 240-grit sandpaper (or by hand with the roughest grinding material on the grinding machine in the other building). The length of both pre-cut pistons is measured again by trying to hold them together as if not cut.

Pt-jacket: The Pt jacket consists of a ∼18.5 mm long tube (outer diameter 6.9 mm; length calculation: length of the pre-cut pistons, add 2 mm for 0.1 g sample material and 2 mm on each side for the end cups = 4 mm, Fig. E.1-1). The tube is cut with the tube cutter. Mark the length of the jacket with the scalpel. Stick the cylindrical rod into the Pt-tube, put both pieces into the tube cutter. Then tighten the screw (not too much - try not to leave deep groves in the rod!) and turn the tube and rod in the cutter until the jacket is separated from the tube.

For the cups two Pt discs are punched out of the Pt foil with the largest piston (Pt foil 0.13 mm thick, already annealed at 900 °C for an hour). The discs are die-shaped to cups with the "cup" piston (not the "6.3-cup"!) and the die pieces. Then, all Pt pieces are annealed at 900 °C for at least one hour in the furnace (large lab) to remove work hardening for handling and the experiment.

The edges of the cups need to be ground flat with a metal file. Afterwards one cup is fit into the Pt tube, holding the metal rod in the tube to avoid pushing the cup too deeply into the tube. Then file the matching surfaces of the cup and the tube even and flat. If there are irregularities in the cups and differences in length the weld will not be tight. Then the cup can be welded with the Pt tube (program P2; see instructions for welding).

There is some space between the inner diameter of the Pt jacket and the sample piston (forcing block). To ensure a good fit, a nickel sleeve (thickness 0.025 mm) is wrapped around the lower forcing block once and inserted into the Pt jacket together with the lower forcing block. The overlapping area should be at the future position of the thermocouple (TC). Then, 0.1 g of the powder are put into the jacket and carefully compacted with the 45° brass piston tool. The TC position is marked at the upper side of the upper sample piston. The required amount of water (e.g. 0.2 µl i.e. 0.2 wt-%) is added on the lower side of the piston before putting it into the Pt jacket (Fig. E.1-1). After marking the TC position at the Pt jacket with a scalpel, the upper cup is inserted into the jacket and both are placed in the brass holder for welding. The brass holder should be stored in the refrigerator before welding to minimise the water loss due to heating. After grinding the edges of the cup and jacket both can be welded together. The upper side of the jacket is marked with a scalpel and a pen (make an arrow) and the total length is measured.

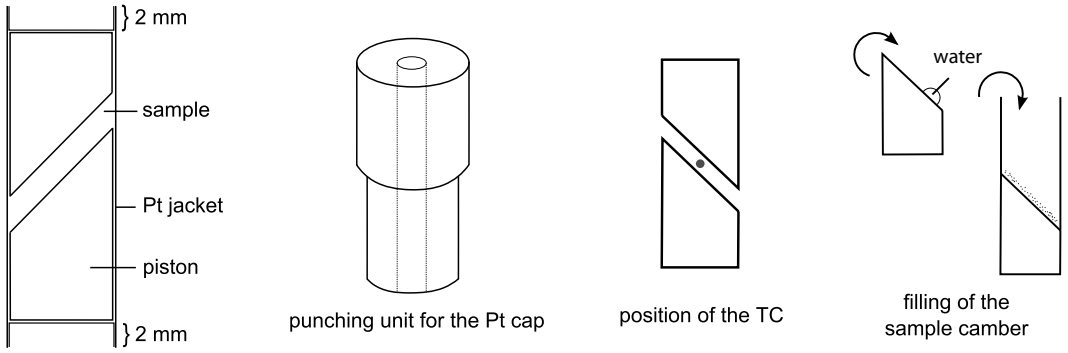

Fig. E.1-1: Sketch of the Pt jacket, the punching unit for Pt cups, the TC position and the filling of the sample chamber.

Drying the sample: If a dry sample is required the assembly of the jacket is the same as described above. The lower piston, the nickel foil, the sample material and the upper piston (naturally without any water) are placed in the jacket and the upper cup is welded but a small part is left unwelded (∼1 mm). There, a hole between the jacket and the cap is carefully opened with a thin needle. The vacuum system has to be arranged (motor, vacuum pump, glass tubes, valves, vacuum measuring device, lightly grease the contacts) and fit in the HTM Loba furnace. The glass should not touch the furnace tube! The jacket is inserted in the quartz glass tube (cleaned with ethanol on the outside) and the tubes are carefully inserted in the furnace. Make sure that the sample is in the middle of the furnace (measuring point of the temperature - see marking on the glass tube). Afterwards the motor for the vacuum and the measuring device are started. Control the valves (vacuum around $1.4{\cdot}10^{-4}$ bar)! Then, the furnace and the temperature controller (JCS-Shinko) are started (check the temperature unit!). Pressing the "loop-arrow" key and the "upward arrow" key increases the temperature. The temperature should not increase faster than 20 °C per minute (below 100 °C, setting of ΔT = 30-40 °C, above 100 °C, setting should be ΔT ∼15 °C) Leave

the furnace at the required temperature. After the sample is dried (∼24 h), the temperature is decreased (to room temperature and check the cooling rate to not exceed 20 °C min^{-1}). At room temperature the vacuum pump is stopped and the glass tubes are carefully remove from the furnace. The hole between the jacket and the cup is closed with Pt-pliers and welded.

Alumina Piston: The furnace consists of three tubes: The inner and the outer one are made of pyrophyllite. The middle one is made of graphite and it is slightly longer than the others to facilitate a good contact with the Cu discs.

The length of the furnace is ∼35.5 mm. Therefore an upper and a lower piston is needed to place the jacket in the centre of the furnace. The pistons need to be cut to the correct length using the saw and grind plan parallel (see instructions above). The length calculation for the pistons works as follows: The TC should be in the center of the sample. As the position of the TC is given by the lower outer salt piece, the bottom piston length is calculated to achieve this correct position for the sample, taking into account the sample length and the Pt cups. When the length is calculated, ∼1.5 mm is subtracted from this value, because the compaction of the salt assembly is greater than that of the sample column. The upper piston is then calculated, taking into account an additional ∼1 mm length for the piston to stick out of the upper Cu disc.

The alumina pistons are inserted at the upper and lower end of the Pt jacket added. The pistons do not fit in the cup of the jacket. Therefore the Pt welds are flattened with the Pt-pliers. By bending them slightly outwards, the piston can be fit into the cups. With the help of the brass holder (keeping the jacket together and avoiding deformation of the sample) the pistons are carefully pressed inside the cups. Afterwards, the jacket is flattened around the cups using the Pt-pliers. The TC position is marked at the upper side. Measure the total length (Fig. E.1-2).

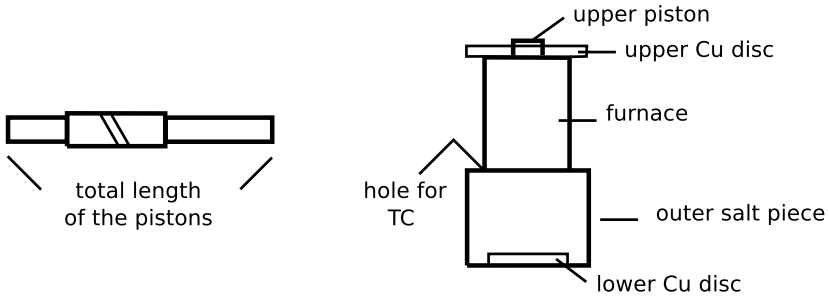

Fig. E.1-2: Length of the sample chamber and the piston to make up for the furnace length and TC position with respect to the furnace and lower salt piece.

E.1.2 Thermocouple

S-Type (Pt/Pt-Rh): The TC consists of a Pt- and a Pt-Rh-wire. The Pt-Rh wire is more elastic than the Pt wire, which can be bent more easily. They should be at least 18 cm long.

On one end they are welded together (program type S), and afterwards the welded bead is flattened with the Pt pliers. Cut its length if needed.

Mullite tubing is used for insulation. Two pieces (diameter 1.56 mm) are cut to the right length first (one 6.7 mm, the other 56 mm long) and then at a 45° angle on one side. For the 45° cut make sure that the TC holes in the tubing are in the same position on both sides and not slanted with respect to the tubing (Fig. E.1-3)! A 1 mm deep incision is cut horizontally in the perpendicular end of the shorter tube. The welding point of the wires should fit into this incision. After fitting the shorter mullite piece on the wires the TC is tested at the rig. The longer mullite piece is fit over the wires, too. Both wires are pulled tight over the two mullite pieces until they are at a right angle. Then both pieces are cemented together with the thermo-glue. First, mix part A and B of the glue using a very small amount of each component. Use the pointed scalpel to remove the powder and the liquid from the containers and to mix them on a cardboard). In addition, some thermo-glue is used to close the incision at the end of the shorter piece (make sure that there are no air bubbles underneath the glue!). Then the TC is put in the "salt"- oven for a few minutes at 110 °C.

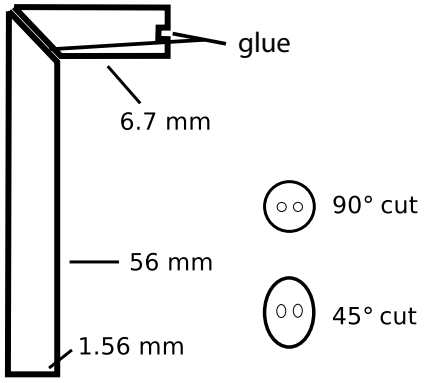

Fig. E.1-3: Dimension of the S-type thermocouple.

K-type (Cr-Al): About 30 cm of the K-type wire are cut off with the wire cutter (blue). The endings often need to be straightened. Both endings of the sheathing are peeled off with the black special peeling tool (0.62 cm diameter): top part ∼1 mm, bottom part ∼1 cm. The white powder inside the sheathing is removed at the top part with a needle. The TC wires are cut if they stick out more than 1 mm. The TC wires need to be in contact (use the needle) but should not touch the outer sheathing. The threads are welded together using program 1 (make sure that only the threads are connected with the welding machine and not the outer wire). The welded bead should lie within the sheath. If not, cut the bead with the Pt-cutter and try again. Mark the orientation of the TC wires at the sides of the sheath. Test the TC at the rig and mark the negative side (red). Stick the sheathing into the brass tool and slowly bend it around the edge in such a way that the TC wires are in a horizontal plane before and after the bending. Correct the bend with regular pliers (not the Pt-pliers!) to make it 90° and to have both sides straight to fit into the outer salt piece. The short part (from tip to outer part of the bend) should be ∼6.5 mm long. The tip of the wire is cemented with the thermo-glue

like the S-type TC (part A + part B). The glue should cover the bead, but do not have a large bead outside the wire - watch out for air bubbles, too. Dry the wire for a few minutes at 110 °C in the "salt"- oven.

E.1.3 Salt pieces

A top and bottom outer salt piece and three inner salt pieces are needed (making of the salt pieces see E.3). All salt pieces are ground with coarse sandpaper. The outer pieces have to fit into the pressure vessel and around the furnace. The inner pieces have to fit into the furnace and around the pistons and the Pt jacket, respectively. The salt can either be cut with the old saw blade (check for labels on the saw blade!) or with the jigsaw.

The inner salt piece, which fits over the jacket, has to be cut exactly to the length of the jacket. The upper and lower inner salt pieces, which fit over the pistons, also need to be cut to the right length. The set of inner salt pieces needs to be exactly of the length of the pyrophyllite tubes of the furnace, fitting the lower piston into the lower Cu disc and placing the furnace above it (do not forget the lower Cu disc while measuring!).

The outer, lower salt piece controls the length of the pistons. It should be ∼19 mm long. The calculated lengths for the pistons are:

$$\begin{aligned}\text{lower piston} &= \text{lower salt piece} + 0.5 \cdot (\text{sample} + 2 \cdot \text{Pt foil}) - \varnothing\text{TC} - 2\,\text{mm compaction}\\ \text{upper piston} &= \text{furnace} + \text{upper and lower Cu disc} + 1.5 - 2\,\text{mm to Pb} - \text{sample}\\ &\quad - \text{lower piston}\end{aligned}$$

A vertical hole has to be drilled for the TC in this bottom outer salt piece. A metal cylinder is used as template around the salt piece. Insert the salt piece with the bottom into the metal cylinder. Check that the drill bit is long enough to penetrate the whole salt piece. Then start drilling (use the wooden plate underneath; drill very slowly to avoid breaking out of the salt at the end of the hole!). While drilling lift the drill head many times to remove the salt powder from the drill hole and from the drill bit.

At the upper end of the hole in the lower salt piece, a small notch for the TC is made with a scalpel. A small Cu disc is placed below the outer, lower salt piece, the furnace and inner salt pieces are inserted, and the position for the hole of the TC is marked with pencil at the notch (Fig. E.1-2). Then, a hole for the TC is drilled through the assembly of furnace and inner salt pieces (use the wood plate) underneath the assembly.

Grind the upper salt piece to the right length. The outer upper salt piece should end at the outer furnace pyrophyllite cylinder when placed on top of the lower outer salt piece and the furnace is inserted. The inner upper salt piece also ends with the inner pyrophyllite cylinder (see above). A large Cu disc is placed on top of the salt pieces. The upper piston must fit through the hole in the disc, and the disc has to fit in the pressure vessel.

Special feature: If a K-type TC is used or the sample is hot pressed before the deformation, and the temperature is decreased later to the run conditions, an alumina ring is inserted into the furnace to protect the TC. The ring should be as thick as the furnace (∼1 mm). The hole for the ring is drilled with the larger drill bit through the pyrophyllite and the graphite (not the salt). First, the small TC hole is drilled, then the salt removed from the furnace, and then the larger hole for the ring drilled through the furnace. There should not be any leftovers of glue at the mullite tubing because the inner diameter of the alumina ring fits exactly to the diameter of the mullite piece.

E.1.4 Lead piece

A Pb piece is placed above the salt and the upper Cu disc (making of the lead pieces see E.3). Test the diameter of the Pb piece at the vessel. The Pb piece should not be thicker than 7.5 mm. A small inner salt ring (∼2 mm high) is inserted in the larger hole in the Pb pieces for higher temperatures (>700 °C). At the end the outer salt pieces and the Pb piece are wrapped in teflon band (again tested in the vessel!).

An unfired pyrophyllite base ring and the small Cu disc are placed below the furnace and salt, together with the tungsten carbide cylinder. Make sure that the better side (without pits) faces towards the base plate of the pressure vessel. A piece of crushable magnesium oxide is placed in the smaller hole of the pyrophyllite ring (cut to length with a jigsaw). A piece of Ni and Cu foil are inserted between the base plate of the pressure vessel and the tungsten carbide cylinder. Check if the pyrophyllite piece fits into the pressure vessel.

All pieces of the sample assembly are carefully put together and a large and a small packing ring are prepared. The rings often need to be ground on the pointed side. Check if the large packing ring fits into the pressure vessel and the small one over the force piston. A disc of cardboard is made for insulation between the pressure vessel and the base plate.

E.2 Experimental run

E.2.1 Installation of the sample assembly in the pressure vessel

There are three types of pressure vessels and their corresponding base plates (old US models with hooks on the sides, new models with a cooling ring on the outside, and the large "Hercules" without an outer cooling ring). The base plate is placed in the arbor press and the corresponding pressure vessel is fitted onto the moving column of the arbor press with the appropriate holder (test the screws!) and aligned with the help of the brass test piece. Afterwards the vessel is carefully raised and the screw on the arbor press is tightened.

The tungsten carbide cylinder, the pyrophyllite piece and the sample assembly (without lead piece and large Cu disc) are placed on the base plate. Use a small plastic ruler to support the sample assembly at the base. Careful with S-type TC, they break easily! With K-type TC it is necessary to carefully bend the TC sheathing while the TC is inserted into the base

plate. Afterwards, the cardboard disc for insulation is placed on the base plate (Hercules: use a small paper disc and tape around the base plate chuck for insulation). Then, the pressure vessel is carefully lowered over the assembly and the appropriate mounting devices (screws or hooks) are fixed. The upper Cu disc, the Pb piece and the large packing ring are added into the pressure vessel from above. The packing ring is carefully pressed down with the arbor press using the hydrostatic piston as a tool (Fig. E.2-1). Careful with the press - do not exert too much force on the assembly when pressing on the packing ring - you may damage the assembly!

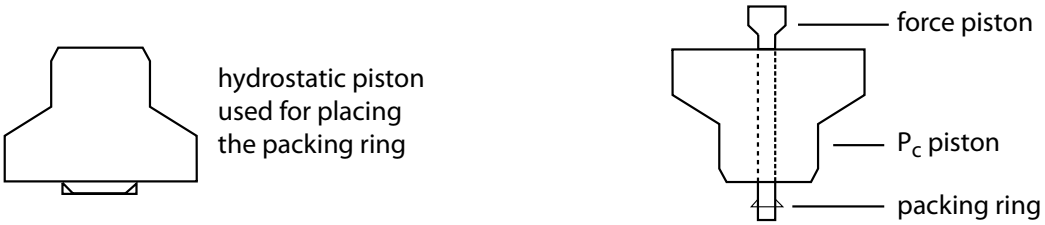

Fig. E.2-1: Fitting the large packing ring in the pressure vessel (left). Arrangement of the σ pistons and the small packing ring(right).

Remove the vessel and base plate from the arbor press, turn it around, and place it on a steel cylinder on the workbench. The base plate metal chuck is insulated with tape. Cut the extending tape with a scalpel. Lift the vessel off the steel cylinder, turn it around, and place it on the workbench. The wires of the S-type TC are fixed (both wires are covered with insulation sheathing (red - Pt, black - Pt-Rh), and small pieces of paper are added between the wires and the vessel for insulation. The TC wires are put through the slit of the base plate and fixed with paper tape at the bottom of the base plate. The K-type TC is covered on the outside with paper tape for insulation. The K-type TC is carefully bent in the slit and fixed with paper tape at the bottom of the base plate. A small wad of tape is placed in the slit over the S-type or K-type TC. Do not put the little wad directly over the hole where the TC comes through the base plate, because the TC wires will be extruded a bit during pumping! The plug for S-type/K-type TC is connected to the TC-wires. For K-type TC, remove the sheathing with the cutting tool and test for polarity with the Omega thermo controller. Small paper pieces are fixed with glue between the TC wires at the end of the K-type TC. The paper and glue should separate the threads and avoid contact with the outer wire.

The cooling plate is placed on top of the vessel (make sure the o-rings do not shift!) and fixed with screws. Subsequently, the small packing ring, the force piston and the confining pressure piston are placed on the assembly - make sure everything is well aligned (Fig. E.2-1).

E.2.2 Installation of the pressure vessel in the Griggs apparatus

The pressure vessel is placed in the rig below the hydraulic ram. The TC should not be damaged and the pistons should not crash into the ram. After switching on the main

contractor (next to the preparation table) the cooling water cycle for the hydraulic ram can be opened. The TC, the power supply for the heating element and the cooling water tubes are connected with the pressure vessel. Before opening the cooling water cycle for the pressure vessel the excess air needs to be removed from the cooling water system. Therefore the water inflow is open and the drainage tube is separated from the valve. The rig is turned on until water runs out of the tube. Pay attention when the other rig is running, especially at high temperatures! Then the tube can be connected with the valve, the water cycle can be opened and the rig is activated.

E.2.3 Setting of the recorder and the PC

The colour code for the recorders is: red - force (1), green - confining pressure (2), blue - displacement (3), black - room temperature (4, only on rig 1). The pens are inserted in the recorder and the ranges and the initial values are adjusted. The paper speed is set to 120 mm/h to see details and have enough space for comments. Then, the pens are placed on the paper ("pen lift") and the chart is started (control the amount of paper). A file is opened in LabView and a new project is started. The program starts to read the values with "operate"-"run". The initial setting is one measurement per 0.5 s (DVM interval). The interval is changed to one measurement per second for slow experiments. By starting the record you can choose the file name.

All changes of the settings should be written on the paper with time specification. Both instruments can be started when the pistons are adjusted with the oil pump and the force gears.

E.2.4 Pressurisation

After adjusting the confining pressure piston the confining pressure is increased manually. A crushing sound occurs at $\sim$0.5 kbar when the contact between the furnace and the upper Cu disc is established. The force gears has to be retraced manually as long as the force piston follows automatically the confining pressure piston (peak when the piston reaches the Pb piece). The force motor is activated (remove the wrench, contact between the equal gear wheels, after starting the furnace!) when the force piston stops following the confining pressure piston. Every 0.5 mm displacement of the confining pressure piston, the force piston should be retraced for the same amount for the next 1.5 - 2 mm. Thereafter, the tracking occurs after 0.3 mm for 2/3 of the displacement. At 1.5 kbar (depending on your pressurization curve) the temperature program is checked, the screws are removed from the base plate and the furnace is heated manually to 30 °C. The program is started and raised to 100 °C (then hold). The electric current, the voltage and the output are written down. At 1.5 kbar the P motor can be activated after closing the corresponding valve (rig 1: 11 - 12 Hz, rig 2: 24 Hz). The speed can be increased at 300 - 400 °C. The force piston should not be retraced directly

before heating since the decrease of the force cannot be controlled (no decrease when the hit point is reached). The last step of the pressurisation is the increase of the temperature to the run conditions so that the confining pressure piston is in the "pressure out" position.

E.2.5 Experiment

Before starting the experiment, the distance between the force piston and the upper alumina piston should be 1.7 mm. The current values of the force (L), the confining pressure (P), the displacement (D) and the output of the furnace (OP) are written down. Optional, the ranges and zero points have to be changed (L - 2V). The chart speed is reduced to 12 mm/h and 0.2 mm/min, respectively. The ram valve is closed at rig 2. The gear wheels of the force gear system are changed to the smallest and biggest one and the speed is adjusted at 30 to achieve a displacement rate of $10^{-8}\,\mathrm{m\,s^{-1}}$ (or a shear-strain rate of $10^{-5}\,\mathrm{s^{-1}}$). During the run L, P, D and OP values should be written down once in a while and the trend of the data should be controlled (time to hit point, differential stress etc.).

E.2.6 Quenching and removing of the sample

The chart speed is raised to $120\,\mathrm{mm\,h^{-1}}$ again and the current values are written down. The temperature program is switch from hold to run. As soon as the temperature begins to fall, the force motor is stopped and the faster speed is adjusted (equal gear wheels). Now, the ram valve (rig 2) can be open quit slowly (!). The force motor is again until the value is circa 1.5 - 2 kbar above the confining pressure. When the temperature program reaches 200 °C it is hold again and both motors are set to slowly reduce the pressure (difference of 1.5 - 2 kbar to avoid unloading cracks). At 2 kbar the last part of the temperature program is activated (cooling down to 30 °C). Afterwards the program is stopped and the output is reduced to 0. When the force and the confining pressure reach their starting values, the pistons are raised up manually. The recorder, the LabView program and the furnace are stopped (take out the pens!). Afterwards the rig can also be turned off. The water cycles are closed and the water tubes for the pressure vessel cycle are removed from the valves. The water in the system is removed with compressed air. Then, the tubes are reconnected with the valves. The water tubes, the TC and the power supply for the heating element are separated from the pressure vessel and the vessel is removed from the rig (pay attention to the pistons). The pistons and the small packing ring are carefully removed from the vessel (check for lead leaks). The cover plate, the TC insulation and the base plate are separated and the sample assembly is pressed out with the moulding press (Pb piece between the assembly and the iron piston). Clean all pieces! The pressure vessel should be stored in a drawer. The sample assembly is taken apart and the contact point of the TC at the Pt jacket is marked as well as the upper side of the sample.

E.3 Preparation of assembly parts

E.3.1 Preparation of the gouge material (<100 µm)

The sample material is broken into fragments and pestled. The fine material is screened with a 100 µm sieve. The larger fraction is slightly pestled until all the material is less than 100 µm. At the end the material is sieved with distilled water and the small fraction is collected in a beaker. Over night the particles sink but some very small particles are still in suspension. The size of them is estimated by the Stokes equation (Eq. E.1). If the particle size is less than 2 µm, the excess water can be poured, including the suspended particles. Still some of the finer particles are mixed with the more coarsed-grains material. Therefore the resulting grain size is smaller than 100 µm. The settled material is filtered with distilled water and dried at 100 °C in an oven. The dried sample is gently mixed well with a spatula and transferred in a specimen tube.

$$v_p = \frac{2r^2 g(\rho_p - \rho_f)}{9\eta}$$
$$r = \frac{9s\eta}{2tg(\rho_p - \rho_f)} \tag{E.1}$$

Example: With s = 0.10 m, η = 0.001 Ns/m^2, t = 61200 s, ρ_p = 2650 kg/m^3, g = 9.81 m/s^2 and ρ_f = 1000 kg/m^3 the maximal diameter of particles in the solution is d = 1.35 µm.

E.3.2 Salt pieces

Inner pieces: There are two sets of central columns (solid cylinders), pressing tubes and brass pieces. The columns with the large diameter are for salt pieces around the sample (3 g); those with a smaller diameter are for salt pieces around the alumina pistons (4 g). Make sure to use the right combination of central column and pressing tube.

First grind the salt with the porcelain mortar until all the crystals are crushed to a fine powder (the salt does not make a grinding sound anymore and has lost its luster - looks like caster sugar). Store it in the oven if not pressed on the same day. Clean all the pressing pieces with water and soap (not the liquid soap!) and dry it. Use a little amount of soap to grease the central column and the pressing tube. Insert the central column into the die and put the assembly under the hydraulic pump. Use the steel plates to adjust a good height for the assembly (the hydraulic ram should not travel too far down). Mix 3/4 small spatula of distilled water with the salt and put the mixture in the die (make sure that the mixture is homogeneous). The pressing tube is used to push down the salt.

Put the pressure tube in the die on top of the salt and the solid disc on top of it (Fig. E.3-1) and press carefully until 4 to 4.5 t. The hydraulic press should be in the hold-mode. Hold the pressure for several seconds. Release the pressure (switch the hydraulic press to return-mode) and put the complete assembly (central column, die, pressing tube) on the two steel plates (upright on the steel table). Use a piece of rag below the dies to prevent any damage while falling down. Be sure that the salt and inner column can be pressed out without touching the steel plates. Press the central column with the salt and the pressing tube out of the press die with the help of the brass piece (the one fitting to the pressing tube). Continue pressing until the central column falls down. This should be easy. The salt can be removed (by hand) from the central column and stored in the oven. All pieces, which were in contact with the salt, should be cleaned with water and soap and dried before pressing another salt piece. After all the work is done, clean carefully and oil (WD40) all pieces before putting them away.

Outer pieces: First grind the salt with the porcelain mortar until all crystals are crushed (the salt does not sound "grindy" anymore and has lost its luster - looks like caster sugar). Store it in the oven if not pressed on the same day. 12 g for the top piece and 12.5 g for the bottom piece (1 mm needs approximately 0.56 g salt).

Clean all the pressing pieces with water and soap and dry them. Fit the metal pieces together as show in figure E.3-2. The cylinders should be placed with their flat side towards the salt/ring. Use a little soap (Not the liquid soap!) at the inner side of the top die piece and on both sides of the cylinders to have less stick-slip when pressing the salt pieces out. Add the ring to make the bottom pieces with a recess. Put the assembly under the hydraulic pump. Use the steel plates to adjust a good height for the assembly (the hydraulic ram should not travel too far down). Add water (3/4 spatula) to the salt and stir it well in the alumina cup. Put all the salt inside the die assembly. You can use the upper cylinder to compact the salt once in a while.

Place the upper cylinder (rounded side upwards) around the central column on top of the salt inside. Press on top of the upper cylinder with the thick solid metal stamp (there should be enough salt in the die assembly that the piston does not touch the outer die piece). Press the salt with 13 t for some seconds (keep the press in hold-mode). Release the pressure (switch the hydraulic press to return-mode). Place the die assembly without the lower die piece on top of the large cylinder in such a way that the salt, the cylinder, the ring and the central column can fall out. Use a piece of rag below the dies to prevent any damage while falling down.

Press carefully until the central column falls out by itself. Then, the salt can be removed from the central column and stored in the oven. Allow at least 24 h for drying before drilling the TC hole in the bottom pieces. Place the metal plates in vertical position with the upper cylinder and central column on top of them in such a way that the central column can fall

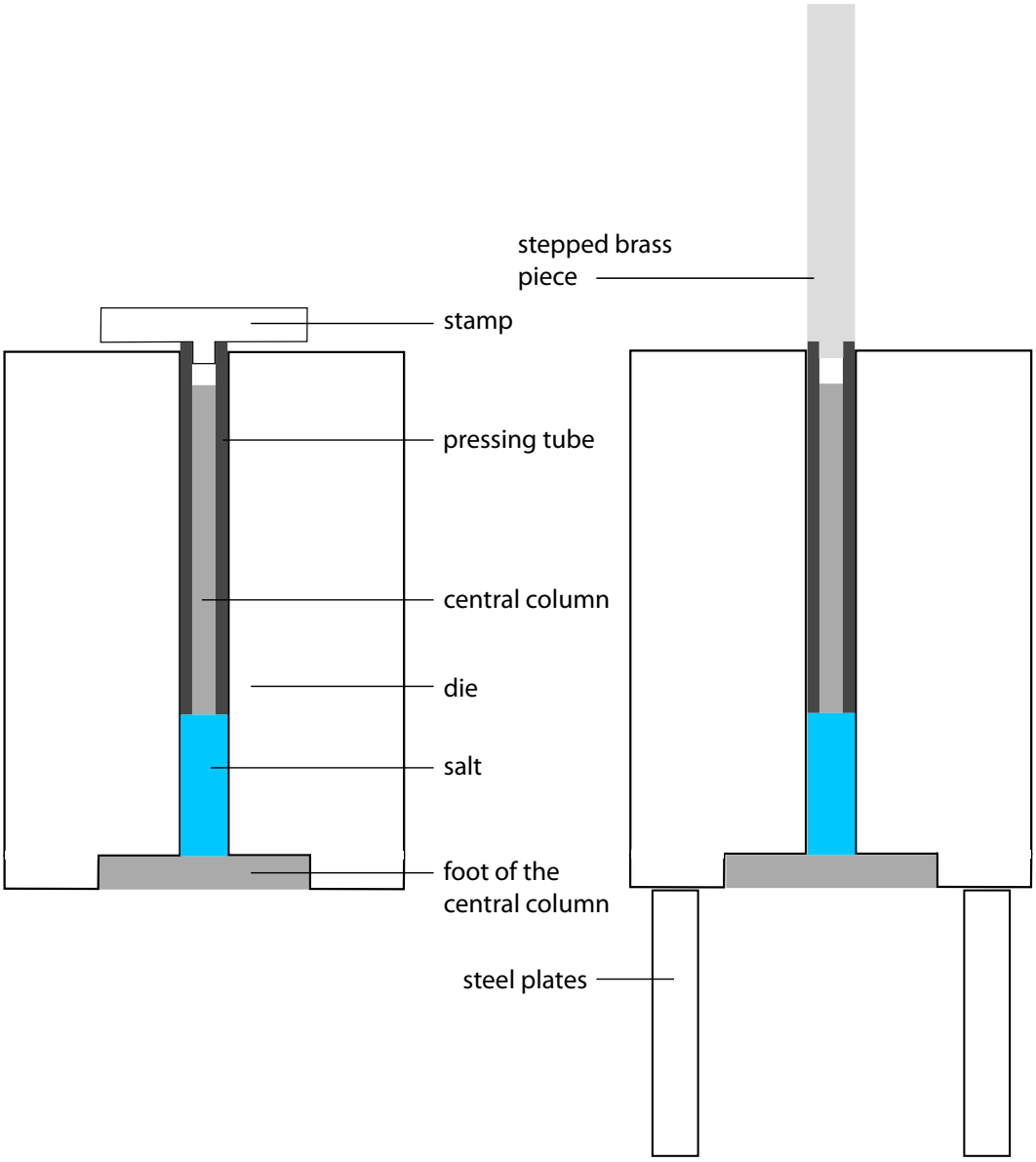

Fig. E.3-1: Assembly for preparing inner salt pieces.

down and gently press the column back. All pieces, which were in contact with the salt, should be cleaned with water and soap and dried before pressing another salt piece. After all the work is done, clean carefully and oil (WD40) all pieces before you put them away.

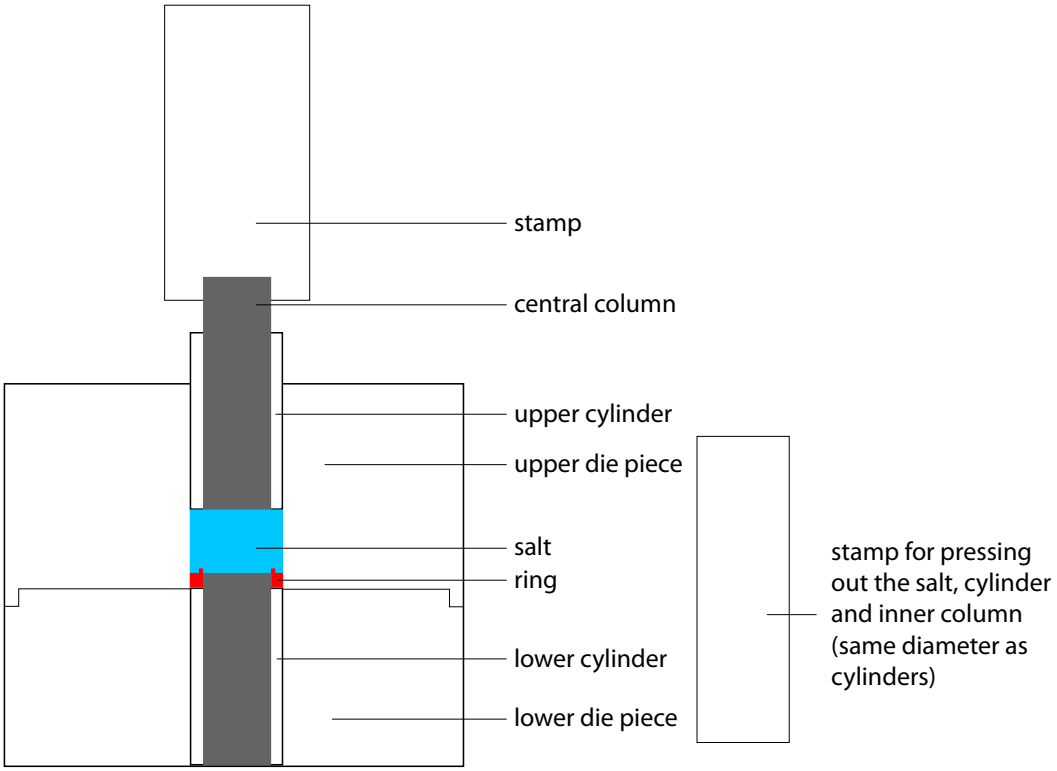

Fig. E.3-2: Assembly for preparing outer salt pieces.

E.3.3 Lead pieces

There are three metal dies (Fig. E.3-3) one fits the force piston (tallest); the other two are for the alumina piston with (wide) or without salt insert (narrow). Take the set that is appropriate for your experiments (salt insert for higher temperatures).

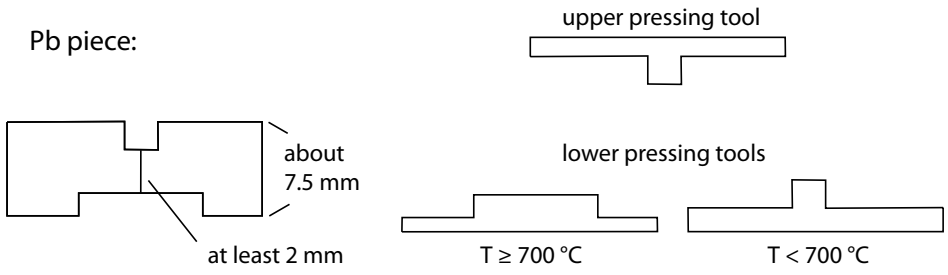

Fig. E.3-3: Dimensions of the lead piece and different metal dies.

Old Pb deposits are melted in the muffle furnace (T at 400 °C, melting point 327.5 °C). Fit the metal pieces together as shown in figure E.3-4. First, the outer ring is placed on the base plate. Then, a metal die is inserted and the liquid Pb is poured in the mould. The die press assembly is placed under the hydraulic press and the metal plates are used to adjust a

good height for the assembly. The hydraulic ram should not travel too far downwards. The other die is placed on top of the lead and pressed carefully for a minute at 4 - 4.5 t (hold-mode). Release the pressure (return-mode). The assembly is put on top of the (vertical) metal plates to press the dies and lead piece out with the press. Use a piece of rag below the dies to prevent any damage while falling down. Peel the lead out and measure the height of the lead piece. The edges have to be removed with the scalpel (store the deposits for the next pieces). Remove any lead on the pieces and store the deposits.

Wear gloves while working with lead!

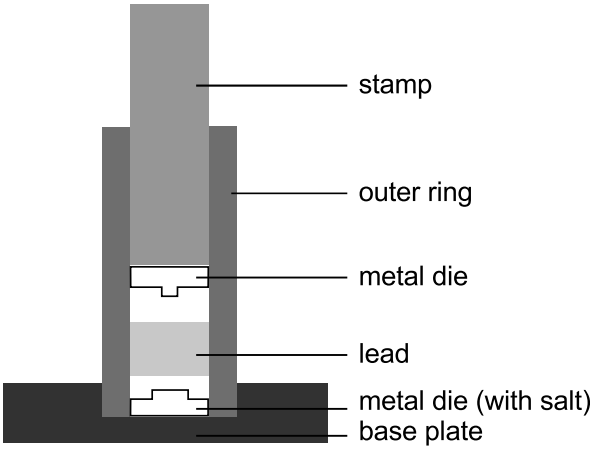

Fig. E.3-4: Assembly for preparing lead pieces.

Acknowledgement

First of all, I would like to thank my supervisors, Renée Heilbronner and Holger Stünitz, for giving me the opportunity to perform this Ph.D. studies. Their doors were always open for countless advice, discussions and any kind of support including a 24/7 emergency hotline in the lab.

Hugue Raimbourgh is thanked for jumping on my thesis in the end as second examiner.

Many thanks to Rüdiger Kilian for endless discussions and numerous computer assistance.

Lucie Tajčmanová and Evangelos Moulas are thanked for introducing me to the concepts of non-hydrostatic pressures and the effect on metamorphic reactions. In this process, a big thank you to Sebastian Cionoiu for his help with the Raman spectrometer at the ETHZ.

A huge thank you to Willy Tschudin for making excellent thin sections regardless of any special requests and Hans-Rudolf Rüegg for manufacturing parts of the sample assembly and tools for the lab. I also want to thank Trine Dahl for preparing my samples for backscatter diffraction at all times when I arrived in Tromsø. Tom Ivar Eilertsen, Eva Bieler and the team of the nano imaging lab is thanked for helping me with any kind of SEM trouble. I would not have been able to obtain such high quality data without your support.

Many thanks to Anja Thust and Matej Pec for welcoming me in Basel and in the world of experimentalists. And a big thank you to the inhabitants of the Bernoullianum.

Finally, I would like to thank Marc Riesenmann, my family and my friends - far away and close-by. They always supported me and I am very grateful for their endeavour to create necessary distractions in order to keep track of the "normal" life.